Computer Modelling Studies of MPO_4, $LiMPO_4$ and $NaMPO_4$ (M: Fe, Co, Mn) Polymorphs

By

Ndanduleni Lesley Lethole

Thesis submitted in fulfilment of the requirements for the degree of

Doctor of Philosophy (PhD)

In

Physics

In the

FACULTY OF SCIENCE AND AGRICULTURE

(School of Physical and Mineral Sciences)

At the

UNIVERSITY OF LIMPOPO

SUPERVISOR: Prof. P.E. Ngoepe

CO-SUPERVISOR: Prof. H.R. Chauke

2016

Declaration

I declare that the thesis hereby submitted to the University of Limpopo, for the degree of Doctor of Philosophy in Physics has not previously been submitted by me for a degree at this or any other University; that it is my work in design and in execution, and that all material contained herein has been duly acknowledged.

_____ _____

LETHOLE N.L. Date

Dedications

This work is dedicated to my wonderful siblings and to my parents Mr and Mrs Lethole and also to my nephews Andani Sirunwa and Oscar Lethole.

Acknowledgements

First and foremost I would like to give all the acknowledgements to the King of kings, God Almighty for his strength, health and direction when undertaking this project. ALL HONOUR AND GLORY TO HIM. Secondly, I would like to extend my words of gratitude to my supervisors, Prof. P.E. Ngoepe and Prof. H.R. Chauke for their insightful research assistance; you have been parents and role models to me. To my spiritual mentors; Ps Khangale, Ps Ndou and Dr Mabasa together with my local church Mutheiwana Assemblies of God Fellowship; it is for your guidance and prayers for me to be where I am today. To my lovely family, I say thanks a lot for your support throughout my studies at the University of Limpopo and my entire academic career. All the members of the materials modeling centre are well appreciated for their support towards the fulfilment of this project. To all members of the Mankweng Assemblies of God (Hwiti branch), thanks for keeping me discipline and loyal to God and all necessary support. The whole community of the university (students, academic and non-academic staff members) played a vital role towards education equipment and conducive studying environment. This project was carried out at the University of Limpopo Materials Modelling Centre. The National Research Foundation (NRF) is highly appreciated for funding this project.

Ndaa!

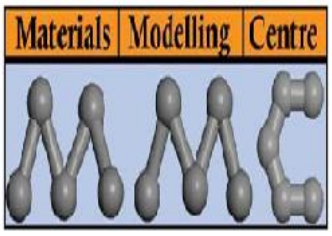

Abstract

In this work, we present first-principles calculations investigating the structural, thermodynamic, electronic and mechanical stabilities of MPO_4 and Li/$NaMPO_4$ (M: Fe, Co, Mn) polymorphs in ambient and high pressures, using density functional theory within the generalised gradient approximation. These materials are promising cathodes for rechargeable lithium and sodium ion batteries. Five structural polymorphs of MPO_4 and Li/$NaMPO_4$ with different space groups are considered in this work; namely, *$P3_121$*, *Pnma*, *Pbca*, *$P2_1/c$* and *Cmcm*. All calculations were performed using the VASP and PHONON codes as implemented in the MedeA software, employing the density functional theory with the Hubbard correction (*U*). For the exchange-correlation functional, the generalized gradient approximation of Perdew and Wang (GGA-PBE) was chosen. The equilibrium lattice constants obtained by performing full structure optimization for all MPO_4 structural polymorphs were found to be in good agreement with the available experimental and theoretical data to within 4 %.

Thermodynamic calculations on $FePO_4$ polymorphs showed that *$P3_121$*-$FePO_4$ is the most stable polymorph up 4 GPa, while the *Cmcm*-$FePO_4$ polymorph is most stable in the pressures above 4 GPa. *Pnm*a-$FePO_4$, *Pbca*-$FePO_4$ and *$P2_1/c$*-$FePO_4$ are metastable throughout the whole pressure range. For $CoPO_4$ polymorphs, it was found that *Pnma*-$CoPO_4$ is the most stable polymorph throughout the pressure range. Moreover, *Pnma*-$MnPO_4$ is most stable up to around 3 GPa, while *Cmcm*-$MnPO_4$ is most stable above this pressure for $MnPO_4$ polymorphs. The electronic density of states showed that $FePO_4$ polymorphs are insulators, due to wide band gaps, while $CoPO_4$ and $MnPO_4$ showed semiconductor and metallic characteristics, due to narrow band gaps (0.34 – 0.83 eV) and pseudo gap, respectively. Phonon dispersion curves calculations showed that *Pnma*-(Fe,Co)PO_4 and *Cmcm*-(Fe,Co)PO_4 are vibrationally stable, since we observed no soft

modes, while *P3$_1$21*-(Fe,Co)PO_4, *Pbca*-(Fe,Co)PO_4, *P2$_1$/c*-(Fe,Co)PO_4 and all $MnPO_4$ polymorphs have soft modes, a condition for mechanical instability. The corresponding mechanical elastic constants were also calculated.

Lithium insertion was found to favour polymorphs with space groups, *P3$_1$21*, *Pnma* and *Cmcm* and all $MnPO_4$ polymorphs, as the volumes changes to within 7 %, ensuring good reversibility during battery operation and long life-cycle. On the other hand, volume changed to within 14 % when sodium is intercalated. The heats of formation calculations also showed that lithium and sodium intercalation enhances the thermodynamic stability of MPO_4 structural polymorphs as the heats of formation dropped significantly during intercalation. Furthermore, electronic conductivity of $FePO_4$ was enhanced during lithium and sodium intercalation, due to the creation of spin-down 3*d* band. Elastic constants, Moduli and Pugh ratio also increased significantly during lithium and sodium intercalation. Moreover, sodium intercalation induces soft modes on *Pnma*-MPO_4, suggesting mechanical instability. The calculated voltage profiles showed that the Co-based olivines have higher insertion/removal potentials over Mn and Fe-based, respectively. The insertion/removal potentials were also found to increase with the 10 GPa pressure.

Table of contents

List of Figures

List of tables

Chapter 1

Introduction

1.1 Rationale

Over the last three decades, there has been an interesting development on lithium-ion battery technologies, which are based on the insertion/removal of lithium into structures of transition metal phosphates. The well-known material is the lithium metal phosphate ($LiMPO_4$), with M taken as Fe, Co, Mn and Ni. However, $LiNiPO_4$ will not be considered in this study, since it was found that its intercalation potential extremely exceeds the maximum value tolerated by Li electrolytes [1]. These materials are targeted for use in power tools, electric vehicles and notebook computers [2]. Lithium iron phosphate, $LiFePO_4$ also known as LFP, which was the first commercialised member of $LiMPO_4$ family is used as cathode material for lithium-ion batteries; hence the whole group of $LiMPO_4$ is referred to as lithium iron phosphate.

Lithium iron phosphate was discovered to be a promising cathode material for rechargeable lithium ion batteries by Goodenough's research group at the University of Texas in 1996 [2, 3]. $LiFePO_4$ is known for its low cost, competitive electrochemical performance, excellent thermal stability, high-energy density and high specific capacity (170 mAh/g or C/g) [4, 5]. Due to these characteristics, $LiFePO_4$ has gained some market acceptance as a cathode material for rechargeable lithium ion batteries. Most $LiFePO_4$ cells operate within a nominal voltage of 3.0 to 3.5 V, and

have a maximum operating voltage of around 4.1 to 4.2 V and a minimum operating voltage of 2.1 to 2.5 V in ambient conditions.

Apart from $LiFePO_4$, the other compounds such as $LiMnPO_4$ and $LiCoPO_4$ are also promising cathode materials, however with some limitations. In particular, the practical use of $LiCoPO_4$ was found doubtful due to poor compatibility within conventional electronic conductivity. The oxidation of the $Co^{2+/3+}$ couple normally occurred in the range of 4.8 V to 5.1 V, which exceeds the electrochemical stability of the conventional LFP based electrolytes. Moreover, $LiCoPO_4$ offers a charge/discharge capacity of 167 mAh/g [5]. On the other hand, $LiMnPO_4$ has been reported to have an operating voltage of 4.1 V, similar to that of $Li_3V_2(PO_4)_3$ component and a capacity of 170 mAh/g similar to $LiFePO_4$ [6]. A relatively high operating voltage provides a high energy density [7, 8, 9]. As a result, less attention has been devoted towards the development of 5 V $LiCoPO_4$ and 4.1 V $LiMnPO_4$ cathodes [5].

However, the major key barrier to commercialisation of these materials was their low electrical conductivity. For example, $LiFePO_4$ has poor conductivity in its pure form, greatly inhibiting high-rate applications [8] and similar problems are believed to inhibit Li exchange from $LiMnPO_4$ and $LiCoPO_4$ [10, 11]. $LiMnPO_4$ also has high ionic and electrical resistance, imposing huge challenge for battery applications [12]. However, efforts to increase the conductivity of electrodes from these materials have been made, which focused on the particle size reduction [4], intimate carbon coating [13, 14], and cat ion doping [8, 15].

Lithium cobalt oxide (LCO) has been the most successful commercial cathode for battery materials, but its usage has been limited due to scarcity of resources for cobalt and it being not friendly to the environment when overcharged. Hence, this has shifted the attention to lithium transition elements phosphates as the possible candidates for

cathode battery materials over the past few years [16]. The difference that exists between $LiFePO_4$ and $LiCoO_2$ has been that during charge/discharge of $LiFePO_4$ system, two phases are present; $LiFePO_4$ and $FePO_4$ while $LiCoO_2$ forms a $Li_{1-x}CoO_2$ solid solution. Thus, the process of discharge/charge in the $LiFePO_4$ system differs from conventional lithium ion battery positive electrode materials.

Lithium iron phosphate batteries are the cheapest and safest batteries in the market currently [17]. There are many factors that make lithium transition metal phosphate an intrinsically safer cathode material than $LiCoO_2$ and manganese spinel ($MnAl_2O_4$). The performance of these materials depends critically on the following two factors: firstly, being the reversibility of Li intercalation/removal from the host structure. This ensures multiple charge/discharge cycle (this is a compulsory condition for the battery to be reloaded). Secondly, a large value of the free energy of the lithiation-delithiation reaction, directly proportional to the intercalation voltage. In addition to these two major factors, there are also some contributing factors. The M-P-O bond is stronger than the Co-O bond; hence M-P-O bond can withstand short-circuiting and overheating better than Co-O bond. This stabilisation of the redox energies also helps fast ion migration. Only under extreme heating (generally over 800 degree Celsius) does the breakdown occur and the bond stability greatly reduces the risk of thermal runaway when compared with $LiCoO_2$. In $LiCoO_2$ battery, in particular at breakdown, lithium migrates out of the cathode cell in the non-linear expansion of the cell. This affects the structural stability of the cell and thus the battery. In LFP, lithium does not remain in the cell during breakdown. So naturally, structural stability of LFP is better as compared to LCO [18].

On the hand, Amine *et al*. revealed that lithium in a cobalt phosphate can be intercalated and extracted in a reversible way that the structure does not lose its crystal

structure during the process [5]. These results suggest a very important promise for $LiCoPO_4$ as cathode material for very high-energy density lithium battery. It is clear that there exists uncertainty with regard to the bonding and stability within the LFP battery material.

Apart from the aforementioned class of battery material (LFP and LCO), the sodium iron phosphate (NFP) are being developed as an alternative to LFP and are potential cathode material for sodium ion batteries because of the abundance of sodium. Sodium is the sixth most abundant element on earth's crust at about 2.6 % and is mainly found dissolved in the oceans and in minerals. On the other hand, lithium is on the twenty fifth position of abundance. Other advantage is that NFP offer possibility of developing much safe aqueous electrolytes that ensures sustainability and optimal safety [19, 20, 21]. Sodium ion batteries can be an excellent alternative for lithium ion batteries due to (i) good economic efficiency (ii) high abundance of sodium (iii) lower material cost (iv) fairly harmless (v) improved safety characteristics and (vi) ability to use electrolytes of low decomposition potential [22]. In this study we perform first-principles calculations within the local density approximation with Hubbard correction (LDA+*U*) to investigate the stabilities of ternaries MPO_4 and quaternaries $Li/NaMPO_4$ polymorphs in low and high pressure conditions. Lithium and sodium insertion will also be performed to determine the effect of lithium and sodium on thermodynamic, electronic and mechanical stabilities of MPO_4 systems. Moreover, their insertion/removal potentials will be determined to establish the preferential and limitations to their performance as cathode materials.

1.2 Structural Aspects

There are five known polymorphs of $FePO_4$; namely, berlinite ($P3_121$), heterosite (*Pnma*), monoclinic ($P2_1/c$), orthorhombic (*Pbca*) and high pressure (*Cmcm*). The heterosite is obtained by extracting lithium from the olivine-$LiFePO_4$ [23, 24], and is considered the most stable $FePO_4$ polymorph [17, 25]. However, around 580 ºC Yang *et al*. found the heterosite structure to transform to the berlinite phase using the differential thermal analysis (DTA) [26], while Iyer *et al*. observed the transformation to occur at 708 ºC using differential scanning calorimetry (DSC) [25]. The HP-$FePO_4$ which is isostructural to $CrVO_4$ [27] is stable in the pressures above 2 GPa [28] and finally, monoclinic and orthorhombic dehydrates are yielded by hydrothermal processes [29].

The orthorhombic structures of $FePO_4$ have space groups *Pnma* (olivine), *Pbca* and *cmcm* (HP-form), in which the transition metal (M) atoms occupy half of the octahedral sites and the phosphorus atoms occupy one-eighth of the tetrahedaral sites in a trigonal closed-packed array of oxygen atoms (see Figure 1-1). In fact the work done by Tang *et al.* highlighted that the M sites are coordinated by approximately six nearest-neighbour oxygen atoms in approximately octahedral geometry for the olivine (space group *Pnma*) and $CrVO_4$ structures (space group *Cmcm*) [17]. The quartz-like structure has a space group $P3_121$, where the M sites are coordinated by approximately four nearest-neighbour oxygen atoms in the tetrahedral geometry. The M sites in the monoclinic structure (space group $P2_1/c$) have lower symmetry and their coordination with the nearest-neighbour oxygen atoms is approximately five [16].

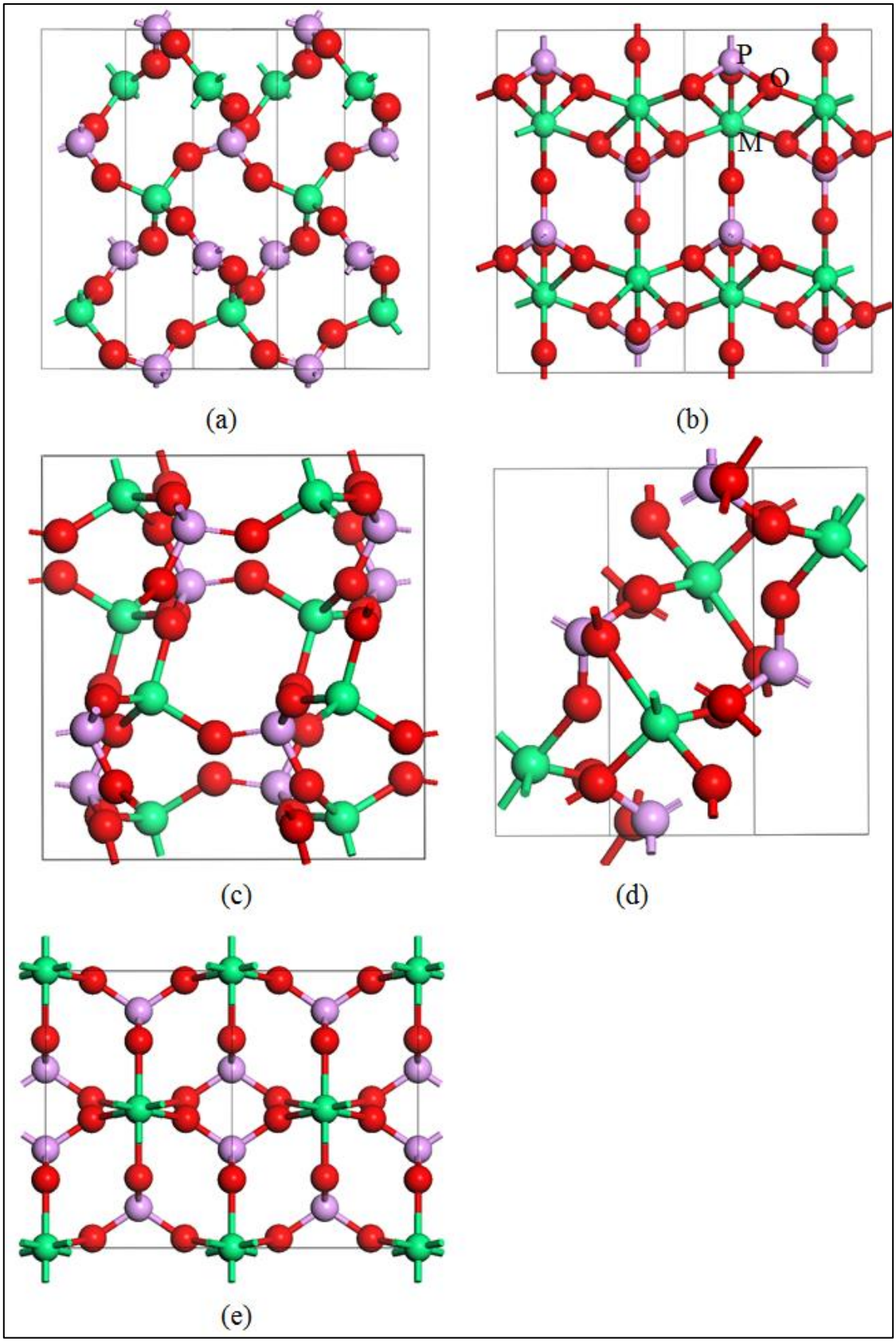

Figure 1-1 The MPO_4 polymorphs (a) *P3₁21*, (b) *Pnma*, (c) *Pbca*, (d) *P2₁/c* and (e) *Cmcm*.

In literature [29], it is often noted that the octahedral coordination of Fe stabilises in Fe^{+2} and Fe^{+3} charge states, while tetrahedral coordination stabilises only in Fe^{+3} charge state. This trend is presumably related to different crystal field splittings of the Fe *d*-states in octahedral and tetrahedral symmetries. Due to the dependency of cathode reactions on the transitions between the Fe^{+2} and Fe^{+3} charge states, it follows that the octahedral coordinated structures i.e. olivine and HP would be expected to be electrochemically active over quartz-like. However, regardless of its favourable coordination, experimental studies by Arroyo y de Dompablo *et al*. on electrochemical properties of the $CrVO_4$-like structure has shown that the Li ion mobility is not significant for technology application [30].

The oxygen sites form a nearly tetrahedral arrangement about each phosphorus site in every structure (Figure 1-1). The removal and addition of Li^+ and Na^+ ions electrons from Li/$NaMPO_4$ does not change the coordination of the structure. The remaining MPO_4 form framework yield the same structure, but with a small reduction in cell volume. The olivine, HP/$CrVO_4$ and orthorhombic forms of $LiMPO_4$ and MPO_4 have an orthorhombic system with $a=b=$c and $\alpha=\beta=\gamma=90$ degrees, whilst the quartz-like structure has a trigonal system with $a=b\neq c$ and $\alpha=\beta=90^0\neq\gamma=120$ degrees. The monoclinic system is defined by $a\neq b\neq c$ and $\alpha=\gamma=90^0\neq\beta$. The crystals with space group $P2_1/c$, *Pbca*, *pnma*, *cmcm* and $P3_121$ are listed no. 14, 61, 62, 63 and 152 in the International Tables for Crystallography, respectively.

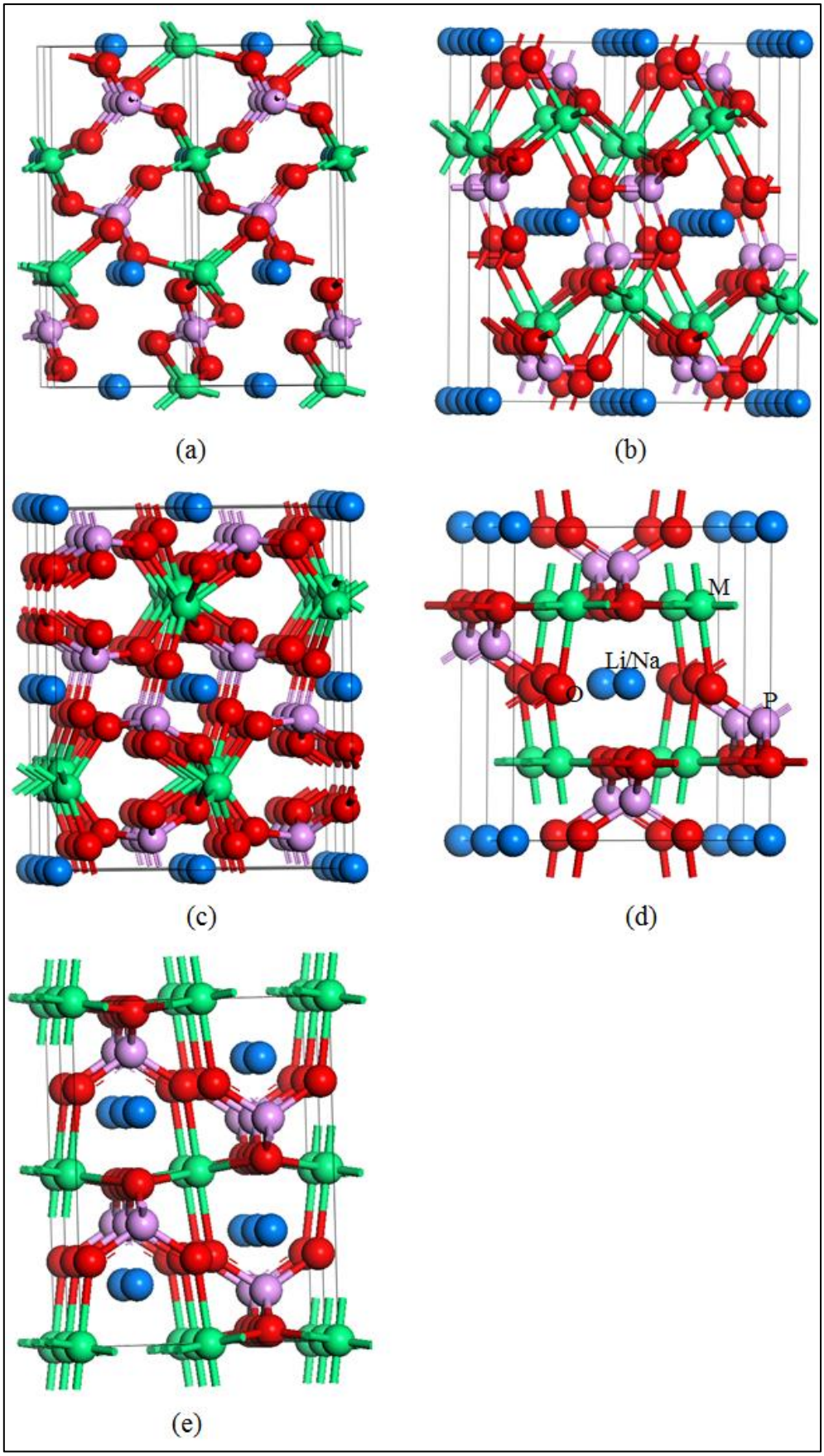

Figure 1-2 Li/NaMPO$_4$ symmetrical polymorphs (a) *P3$_1$21*, (b) *Pnma*, (c) *Pbca*, (d) *P2$_1$/c* and (e) *Cmcm*, showing Li/Na channels along the *b*-axis.

The Li/$NaMPO_4$ structures (see Figure 1-2) may be recognised by the existence of channels along *b*-axis which accommodate the mobile Li^+ and Na^+ ions. These ions are located in the space left by the PO_4 units, between the M-O layers that are blocking for the Li and Na diffusion. MPO_4 is isotructural to $LiMPO_4$ where all lithium atoms crystal sites are unoccupied. Moreover, these materials are naturally occurring [31], as supporting evidence of their structural stability. *Pnma*-$LiFePO_4$ is known as "triphylite" and has the same structure as $LiMnPO_4$ referred to as "lithiophilite" and the two forms a complete solid-solution series [31]. Various studies have successfully shown that the olivine $LiMPO_4$ can be synthesised by hydrothermal method at 150 °C [32, 33, 34]. The delithiated forms of the materials $FePO_4$ and $MnPO_4$ are known as ''heterosite'' and ''purpurite,'' respectively. The $P3_121$, *Pbca* and $P2_1/c$ polymorphs of $LiMPO_4$ are not found experimentally. For the purpose of this work these polymorphs were synthesised by inserting lithium along the *b*-axes channels of the naturally occurring delithiated forms. In the case of $NaMPO_4$, similar structures as discussed above are used. The structures are characterised by same space group, symmetry and atomic arrangements. Tables 1-1 to table 1-7 list the experimental atom positions (Wyckoff notation) and fractional coordinates for the metal phosphates under study.

Table 1-1 Fractional coordinates and atom positions of $P3_121$-$FePO_4$ [35]

Atoms	Positions	Element	X	Y	Z
Fe	3a	Fe	0.458	0.000	0.833
P	3b	P	0.458	0.000	0.333
O1	6c	O	0.413	0.311	0.398
O2	6c	O	0.414	0.260	0.880

Table 1-2 Fractional coordinates and atom positions of *Pnma*-$FePO_4$ [24].

Atoms	Positions	Element	X	Y	Z
Fe	4c	Fe	0.276	0.250	0948
P	4c	P	0.094	0.250	0.395
O1	4c	O	0.122	0.250	0.709
O2	4c	O	0.439	0.250	0.160
O3	8d	O	0.166	0.045	0.250

Table 1-3 Fractional coordinates and atom positions of $P2_1/c$-$FePO_4$ [29].

Atoms	Positions	Element	X	Y	Z
Fe	4e	Fe	0.388	0.806	0.060
P	4e	P	0.589	0.458	0.266
O1	4e	O	0.481	0.640	0.228
O2	4e	O	0.828	0.463	0.384
O3	4e	O	0.641	0.358	0.116
O4	4e	O	0.410	0.343	0.368

Table 1-4 Fractional coordinates and atom positions of *Cmcm*-$FePO_4$ [30].

Atoms	Positions	Element	X	Y	Z
Fe	4a	Fe	0.000	0.000	0.000
P	4c	P	0.000	0.354	0.250
O1	8f	O	0.000	0.246	0.050
O2	8g	O	0.247	0.465	0.250

Table 1-5 Fractional coordinates and atom positions of *Pnma*-$LiFePO_4$ [36].

Atoms	Positions	Element	X	Y	Z
Li	4a	Li	0.000	0.000	0.000
Fe	4c	Fe	0.282	0.250	0.973
P	4c	P	0.095	0.250	0.419
O1	4c	O	0.099	0.250	0.744
O2	4c	O	0.455	0.250	0.211
O3	8d	O	0.163	0.048	0.284

Table 1-6 Fractional coordinates and atom positions of *Pnma*-$LiCoPO_4$ [37].

Atoms	Positions	Element	X	Y	Z
Li	4a	Li	0.0000	0.0000	0.0000
Co	4c	Fe	0.2775	0.2500	0.9780
P	4c	P	0.0943	0.2500	0.4190
O1	4c	O	0.0972	0.2500	0.7420
O2	4c	O	0.4543	0.2500	0.2037
O3	8d	P	0.1663	0.0446	0.2817

Table 1-7 Fractional coordinates and atom positions of *Cmcm*-$LiFePO_4$ [36].

Atoms	Positions	Element	X	Y	Z
Li	4c	Li	0.000	0.676	0.250
Fe	4a	Fe	0.000	0.000	0.000
P	4c	P	0.000	0.350	0.250
O1	8f	O	0.000	0.247	0.043
O2	8g	O	0.228	0.467	0.250

1.3 Literature Review

In this section, we give a brief literature on the structural, electronic and mechanical properties from previous work for all MPO_4 and $LiMPO_4$ systems under consideration.

1.3.1 Structural Properties

The quartz-like/berlinite ($P3_121$) structure of $FePO_4$ is isostructural to $AlPO_4$. The P and Al are totally arranged in the berlinite system with alternate sheets of PO_4 and AlO_4 tetrahedra stacked in the *c*-axis (see Figure 1-1). For $AlPO_4$ and $FePO_4$, compounds have a characteristic "α-β" transformation and are found at 586 ^oC and 707

^{o}C. Ng and Calvo [35] found that the average Fe-O bond distance of 1.853 Å compares accurately with the sum of the effective ionic radii for tetrahedrally coordinated Fe^{3+} and two coordinate oxygen atoms [38, 39]. It was also found that the average P-O bond distance of 1.526 Å compared well with 1.522 Å in $AlPO_4$. The O-P-O bond angels and O-O bond distances in the PO_4 are fairly uniform. Song *et al*. showed that the bond distance of Fe-O varies from 1.81 Å to 1.96 Å, while the Fe-O tetrahedron in the orthorhombic form is more regular with all the Fe-O bonds falling within the range 1.84 Å to 1.88 Å [29].

Table 1-8 Lattice constants of the olivine *Pnma*-$LiMPO_4$ and *Pnma*-MPO_4

Structure	a (Å)	b (Å)	c (Å)	V ($Å^3$)	Ref
$LiFePO_4$	10.22	6.01	4.69	288.07	[40]
$LiCoPO_4$	10.20	5.92	4.69	283.20	[40]
$LiMnPO_4$	10.43	6.10	4.74	301.57	[36]
$FePO_4$	9.93	5.86	4.84	281.30	[41]
$CoPO_4$	10.05	5.83	4.72	275.83	[42]
$MnPO_4$	10.10	6.20	4.5.06	290.83	[38]

It has been shown recently that the $LiFePO_4$ material has an orthorhombic structure with space group *Pnma* and no impurities [31]. Similar observations were also reported by Lai *et al*. [43] and Lee *et al*. [44] in 2008. Xu and Ching did the comparative study of the electronic structure of $LiMPO_4$ and $FePO_4$ [45] and found good agreement with those in table 1-8. According to neutron-diffraction experiments performed by Santoro and Newnham, lithium transition metal phosphates have antiferromagnetic magnetic ordering [46]. $FePO_4$ also has a magnetic ordering of antiferromagnetic [24]. Other non-lithiated phosphates are considered as having the same magnetic ordering.

It should be noted however, that $MnPO_4$, $CoPO_4$, $LiMnPO_4$ and $LiCoPO_4$ systems are stable only with the *Pnma* symmetry. Furthermore, these materials were found to have

good reversibility and life cycle due to small volume changes during lithium insertion/removal; 2.2 % and 2.6 % were reported for $MnPO_4/LiMnPO_4$ and $CoPO_4/LiCoPO_4$, respectively [42].

For the purpose of the current study, all the five symmetries in MPO_4 and $LiMPO_4$ above will be considered. This will be done by replacing Fe with either Co or Mn and observe the stability of these systems for potential battery material.

1.3.2 Electronic Properties

The electronic properties of LFP are important to understand electronic contribution and electron valence state for lithium iron phosphate. The ionic state and electrical conductivity of materials are essential for Li^+ diffusion and electron transportation, respectively during the charge/discharge of the battery [47]. Chemical formula can be distinguished in terms of their electronic states, which are; lithium has +1 valence electron, iron has +2 valence electrons and phosphate has +3 valence electrons. The neutron-diffraction experiments have shown explicitly that the magnetic ordering of MPO_4 and $LiMPO_4$ is antiferromagnetic (AFM) [24, 46]. Moreover, in the literature it is often noted that the octahedral coordination of transition metal (M) is stable at its M^{+2} and M^{+3} charge states, while tetrahedral coordination stabilises only at its M^{+3} charge states [26, 29]. This trend is presumably related to different crystal field splitting of the Fe *d*-states in the octahedral and tetrahedral symmetries. Since the transitions between the Fe^{+2} and Fe^{+3} charge states is involved in the cathode reaction, it follows that the octahedral coordinated structures (olivine, orthorhombic and High Pressure) would be expected to be more electrochemically active materials.

Experimental studies of the electrochemical properties of $CrVO_4$/High Pressure structures material performed by Arroyo-de Dompablo *et al.* have shown that irrespective of its favourable Fe coordination, the Li ion mobility in this material is too small to be technologically useful [30]. Low temperature studies of the $LiMPO_4$ structures have revealed that the materials also have very interesting magnetic moments behaviour with antiferomagnetic ground-states [48, 49]. The magnetic susceptibility as a function of temperature shows that the room temperature behaviour follows a Curie-Weiss model with well-defined magnetic moments associated with the transition metal sites and a negative Curie temperature consistent with the behaviour of an antiferromagnetic material at temperature above its Neel point. The magnetic properties of these materials may not have direct technological use; but they do affect the electronic states of the materials which determine their electrochemical behaviour [48].

Zhou *et al*. investigated the electronic structure behaviour; in particular the band gap of $LiFePO_4$ and $LiMnPO_4$; their results showed that the olivine materials reveal significant band gaps of 3.7 eV and 3.8 eV, respectively. The band gaps are largely induced by strong electron correlation at the transition metals. Furthermore, band gaps of 1.9 eV and 0.5 eV were reported for $FePO_4$ and $MnPO_4$, respectively [50]. Xu and Ching reported that $LiCoPO_4$ has one more electron from the successive increase in 3*d* series than $LiFePO_4$, consequently E_F falls within the minority t_2g band resulting in a half metal with the band gap of only 0.18 eV [45]. Le Bacq and Pasturel also showed that the energy band gaps of the non-lithiated materials are smaller than the energy band gaps of lithiated compounds [51].

Crystal structure and bonding of olivines, together with the calculated band gap and conduction activation energy in $LiFePO_4$ suggest beyond doubt that olivine conduction does not occur through thermal creation of delocalised electrons across a small gap, but instead through a localised polaronic mechanism. It was also indicated that the band gap of $MnPO_4$ material shows sensitivity to the magnetic ordering, due to coupling of the magnetic ordering and the Jahn-Teller distortion. Moreover, pure $LiMnPO_4$ material has relatively poor intrinsic electrochemical conductivity [52].

Osorio-Guillen *et al*. performed analysis of electronic structure to show the characteristic features of the cathode materials in the discharge/charge phases [42]. It was found that heterosite $FePO_4$ has a band gap of 0.18 eV. This makes the material a semiconductor, which infers problems with the electronic conductivity during the battery discharge. However, this can be overcome by temperature rise. The upper valence band lies in the range -7.2 to 0.0 eV, formed by hybridization of iron *d*-states, phosphorus *p*-states and oxygen *p*-states. It was also found that $CoPO_4$ shows a metallic character, where the Fermi level lies in a band formed by hybridization of cobalt *d*-states, phosphorus *p*-states and oxygen *p*-states and $MnPO_4$ appears to be a semimetal, exhibiting a parabolic density of states curve around the Fermi level.

Tang *et al*. performed a comparison of the electronic structures of four crystalline phases ($CrVO_4$, Monoclinic, Olivine and Quartz-like) of $FePO_4$ [17] using pure LDA and GGA approximations. They found the general form of the density of states is very similar among the four materials. In their study, the $CrVO_4$-type was found to be clearly metallic with overlap of spin up electrons around the Fermi level, while the olivine and quartz have band gaps ranging 0.1 eV to 0.4 eV for olivine structure and 0.8 eV to 1.0 eV for quartz structure using LDA and GGA, respectively.

Tang and Holzawarth also performed self-consistent electronic structure calculations of $FePO_4$, $LiFePO_4$ and related materials considering no spin (NS), ferromagnetic (FM) and antiferromagnetic (AF) spin configurations [41]. Their calculations suggested that majority spin states of $FePO_4$ have substantial covalent character due to the energetic overlap of the O 2*p*-states with the Fe 3*d*-states. However, the $LiMPO_4$ materials show less covalent character such that the M 3*d*-states form narrow bands above the O 2*p* bands with relatively little mixing. The results also show that despite its reduced covalence, $LiFePO_4$ is more stable relative to $FePO_4$ and Li metal, and the approximate open circuit voltage for the cathode discharge is calculated to be ~3.2 V, which is comparable to (although smaller than) the experimental value.

1.3.3 Mechanical Properties

A better understanding of elastic properties of transition metal phosphates materials is essential in order to better control the thermodynamical properties determining their electrochemical performance. Elastic properties of quartz-like $FePO_4$ and olivines $LiMPO_4$ and MPO_4 have been investigated previously [53, 54, 55, 56]. MPO_4 is isostructural to $LiMPO_4$ where all lithium crystal sites are unoccupied. Hence it is expected that MPO_4 is softer when the crystal is distorted since the PO_4 tetrahedra and the MO_6 octahedra are able to move towards the empty space. However, Maxisch and Ceder showed that the elastic constants C_{11} and C_{66} are larger for $FePO_4$ than for $LiFePO_4$ [53]. In their study it was also shown that under a compression along the *a*-axis, the PO_4 tetrahedra are slightly rotating while moving towards the unoccupied lithium sites. As a consequence, the FeO_6 octahedra which are slightly tilted around the *b*-axis are straightened up along the *a*-axis, increasing the elastic constant C_{11} with

respect to that of $LiFePO_4$. A similar argument applies for C_{66}. Furthermore, the elastic constants C_{11} and C_{22} of $FePO_4$ and $LiFePO_4$ are significantly larger than other elastic constants, resulting in a pronounced elastic anisotropy. Moreover, the elastic constants satisfied mechanical stability conditions for both $FePO_4$ and $LiFeOP_4$. These observations were recently validated by Xie *et al*. [55].

$LiFePO_4$ exhibits smaller values for bulk, shear, and Young moduli than most transition-metal oxides [57, 58]. Furthermore, $LiFePO_4$ is a harder material than $FePO_4$ which is consistent with the prediction that lithium transport is expected to be faster in $FePO_4$ than in $LiFePO_4$ [59, 60]. Elastic properties of olivine $MnPO_4$ and $LiMnPO_4$ were recently investigated by Xie *et al.* [55]. They found that the elastic constants of $LiMnPO_4$ show similar characteristics as of $LiFePO_4$, suggesting analogy in the bonding features of the two materials. On the other hand, Wolfenstine *et al.* evaluated the mechanical properties of $LiCoPO_4$ by nanoindention to determine the elastic modulus, hardness and fracture toughness. It was discovered that the material is brittle like glass and can be used in Li-ion batteries with higher energy density [56]. Mittal *et al*. calculated elastic constants of α-quartz $FePO_4$ from the slopes of the acoustic phonon branches near the Brillloiun zone center by performing inelastic neutron scattering experiments. They found that α-quartz structure has elastic constants C_{11}=37.7 GPa, C_{33}=85.3 GPa, C_{44}=18.7 GPa, C_{66}=9.7 GPa, C_{12}=18.2 GPa, C_{13}=18.6 GPa and C_{14}=12.2 GPa and satisfy necessary stability conditions for trigonal systems [54]. The calculated bulk modulus was found to be 31.3 GPa while the experimental value is 24 GPa [61].

1.4 $NaMPO_4$ Systems

There is very limited information on sodium metal phosphates ($NaMPO_4$) in literature, as many studies have primarily focused on $LiMPO_4$ as a candidate for future batteries. This may be due to the significant discoveries and investigations on lithium ion batteries [3, 62, 63, 64, 65]. However, concerns regarding the abundance and possibilities of drastical increase in lithium ion batteries prices when demand intensifies are arising. Consequently, attention has been shifted to the more abundance and inexhaustible sodium metal phosphates, which can be found everywhere in the world [66].

$NaFePO_4$ and $NaCoPO_4$ can be synthesised by the stoichiometric reactions of $NH_4H_2PO_4$, Na_2CO_3 and $FeC_2O_4.{}_2H_2O/CoO_2O_4.2H_2O$ with the analysis of the outcome carried out by X-ray diffractometer. The X-ray diffraction (XRD) patterns refined by using space group *Pnma* of synthesised $NaFePO_4$ and $NaCoPO_4$ have shown that the materials are pure crystalline [22]. Lee *et al*. reported that $NaMnPO_4$ is synthesised by ammonium metal phosphates ($NH_4MnPO_4.H_2O$) grounded with excess sodium acetate trihydrate ($CH_3CONa.3H_2O$) heated between 65-100 ^{0}C [66]. The lattice parameters and cell volumes for olivine $NaMPO_4$ are listed in table 1-9.

Table 1-9 lattice parameters and cell volumes for olivine $NaMPO_4$.

Olivine	a (Å)	b (Å)	c (Å)	V (Å^3)
$NaFePO_4$ [67]	8.99	6.86	5.05	311.35
$NaCoPO_4$ [68]	8.88	6.79	5.03	303.38
$NaMnPO_4$ [66]	10.56	6.34	4.99	334.24

Studies done by Shakoor *et al*. [22] have shown that $NaFePO_4$ and $NaCoPO_4$ offer charge/discharge capacities of 12 mAh/g and 2.0 mAh/g, respectively, which is very less compared to $LiFePO_4$ (170 mAh/g) [4, 5], $LiMnPO_4$ (70 mAh/g) [69] and $LiCoPO_4$ (70 mAh/g) [5] and other sodium based cathode materials like $Na_{1.5}VOPO_4F_{0.5}$ (80 mAh/g) [70] and $Na_3V_2(PO_4)F_3$ (90 mAh/g) [71]. Several studies have suggested that the low capacities may be attributed to slow diffusion kinetics of sodium into the structure and the closed packed crystal structure which causes the sodium ion immobility [22, 72]. However, Fernandez-Ropero *at al*. has shown that $NaFePO_4$ has better performances at high charge rates, reaching a capacity of 70 mAh/g at charge rate C/5 (i.e. the battery should be discharged within 5 hours to preserve the life cycle) and 40 mAh/g at 2 C (i.e. at twice rated capacity) [73]. These drawbacks call for further studies on enhancement of $NaMPO_4$ electrochemical activity at room temperature to make it a good candidate for sodium ion batteries.

On the other hand, studies done by Sun and Manivannan have shown that the $NaFePO_4$ electrode is capable of maintaining capacity for a large number of cycles, despite low capacity. They found that the charge/discharge densities continued to increase for more than 300 cycles [74], making this material of good interest for large scale energy storage systems for smart grid applications [75]. Na ion batteries are also known for high density of 600 Wh/kg, which also rivals that of Li ion batteries [76]. Zhu *et al*. did a comparison of electrochemical performance of carbon coated olivine $NaFePO_4$ and $LiFePO_4$ [77]; carbon coating enhances electrochemical performance. They found that the carbon coated C-$NaFePO_4$ can deliver up to approximately 100 mAh/g of charge/discharge capacity as compared to 12 mAh/g of the pure $NaFePO_4$. Furthermore, C-$NaFePO_4$ cell retains 90 % of the capacity even after 100 cycles, which is comparable to that of C-$LiFePO_4$. The good cycling stability of C-$NaFePO_4$

is consistent with the theoretical calculations, which suggested that the olivine $NaFePO_4$ has strong P-O bonds, making it not be easily transformed into an electrochemically inactive maricite phase during cycling [72]. Previous studies have reported that the maricite $NaFePO_4$ and $NaMnPO_4$ to be the thermodynamically most stable phases over the olivine [66, 72, 78]. The maricite phosphate framework does not differ from that of the well-known $LiFePO_4$ olivine structure. However, the alkali metal (Na) occupies the M2 site and the transition metal (Mn, Fe, or Co) occupies the M1 sites which is the opposite of $LiFePO_4$. As a result, the material is characterised by edge-sharing FeO_6 octahedra, which obstructs Na ion diffusion, making the structure to electrochemically inactive and unlikely candidate for future Na ion battery development [79]. Considering that the maricite structure has been discovered not amenable for Na ion mobility, this study will primarily focus on investigating the properties of olivine structure. The development and study of the olivine $NaMPO_4$ in this study is derived from the well-established olivine $LiMPO_4$ due to the similar alkali series system.

1.5 Intentions of the Study

The use of portable electronic devices for purposes of communication, data processing and transmission, entertainment, etc. is rapidly increasing. Furthermore, the vision of massive commercial use of electrically powered vehicles is becoming more and more realistic. These developments have led to a demand for continued search of more efficient batteries with a number of crucial properties. These include a relatively flat open-circuit voltage (OCV), low cost, environmental benefit, easy to fabricate and safety in handling and operation. Rechargeable lithium batteries have proven to be one

of the most successful solutions to achieve these goals for low load applications. A crucial key towards a good battery design is concerned with the choice of cathode material.

Hence in this thesis, we investigate the properties of lithium and sodium transition metal phosphates MPO_4, $LiMPO_4$ and $NaMPO_4$ (M=Mn, Fe, Co) using first-principles density functional theory with Hubbard correction (DFT+*U*). The Hubbard *U* parameter is introduced to deal with the strongly correlated systems [55]. We employ plane-wave pseudopotential techniques as embodied in Vienna *ab-initio* simulation package (VASP) code for equilibrium ground-state properties and the PHONON code [80] for determining their vibrational frequencies. The main purpose of this work is to attain elementary and fundamental understanding on the stabilities of transition metal phosphates, especially the polymorphs of $MnPO_4$, $FePO_4$ and $CoPO_4$. We investigate stability for five structural polymorphs; namely *P3₁21*-MPO_4, *Pnma*-MPO_4, *Pbca*-MPO_4, *P2₁/c*-MPO_4 and *Cmcm*-MPO_4. The relative phase transition will also be determined with respect to change in pressure, as stabilities will be investigated in ambient (0 GPa) and high (10 GPa) pressures. Moreover, lithium and sodium intercalation will be performed in all structural polymorphs in ambient and high pressures, to determine the effect of lithium and sodium on the investigated properties of MPO_4. Previous studies have shown that lithium intercalation has a remarkable effect on the structural, thermodynamic and electronic properties of MPO_4 [45, 81, 82].

Four properties will be determined to investigate the stabilities; namely structural, thermodynamic, electronic and mechanical. In the case of structural and thermodynamic properties, the equilibrium cell parameters and heats of formation (ΔH_f) will be calculated, where the polymorph with stable equilibrium volume and

more negative ΔH_f value will be considered the most stable phase. Further investigation on stability will be performed by computing the electronic density of states (DOS), in particular observing electronic states behaviour near the Fermi level ($E-E_F=0$) with respect to the band and pseudo gaps. In order to validate our work, we will also investigate mechanical properties. We will perform first-principles phonon dispersion calculations, which play an important role in determining vibrational properties of materials. The elastic constants, bulk modulus, shear modulus and Young's modulus and anisotropy factors to evaluate the elasticity of MPO_4, $LiMPO_4$ and $NaMPO_4$ compounds will be calculated. Finally, their insertion/removal potentials will be determined and compared with the available data, contrasting between Li and Na. We will also deduce the stability trend from the thermodynamic, electronic and mechanical behaviour of the respective structural polymorphs.

1.6 Outline of the Study

The outline of the thesis is divided into seven chapters:

Chapter 1, concerns with the literature review based on applications, background information and previous studies on the structures under study. We introduce the general motivation for these structures and structural aspects of the materials under investigation i.e. the structural, electronic and mechanical properties of MPO_4 and $LiMPO_4$ polymorphs. A brief background and properties of $NaMPO_4$ are discussed. We also discuss the intensions and the motivations of the study.

Chapter 2 describes the method that has been employed in this study. Firstly, introduce density functional theory (DFT). Secondly, we discuss in detail the approximation used in this study, i.e. the generalised gradient approximation (GGA) and the local

density approximation (LDA). The plane-wave (PW) pseudopotential approach within the first-principles DFT is outlined in detail for predicting structural, electronic and mechanical properties. Lastly, we give details of the codes used and a brief theoretical background about the calculated properties, i.e. heats of formation, density of states, phonon dispersion curves and elastic properties.

Chapter 3 gives detailed results and discussions obtained using DFT+*U* technique. In this section, we present the structural, thermodynamic and electronic properties of MPO_4. The equilibrium cell parameters, heats of formation and electronic properties (spin polarised densities of states) of the polymorphs under study are discussed in details and compared with the available experimental and previous work. The trend of stability in the polymorphs of all structures is observed.

Chapter 4 brings about the mechanical properties of MPO_4 polymorphs calculation. We discuss in detail the elastic and vibrational properties i.e. elastic constants, bulk modulus and phonon dispersions, respectively. We also compare the trend of mechanical stability with the trend observed in chapter 3.

Chapter 5 presents the structural, thermodynamic, electronic and mechanical properties of $LiMPO_4$ structural polymorphs. We discuss the effect of lithium intercalation on MPO_4 and determine the stability trend within the respective $LiMPO_4$ structural polymorph.

Chapter 6 focuses on the effect of sodium interaction on structural, thermodynamic, electronic and mechanical properties of MPO_4 structural polymorphs. A comparison of $LiMPO_4$ and $NaMPO_4$ properties is also discussed. Voltage profiles of $Li/NaMPO_4$ are also presented and discussed.

Chapter 7 lastly, a brief summary and conclusion of the study is written in this chapter.

Chapter 2

Methodology

In this chapter, we discuss the quantum mechanical density functional theory (DFT) method employed in the study. The most significant advantage to DFT methods is a substantial increase in computational accuracy without the additional increase in computing time. The other advantage of DFT is that it provides some chemically important concepts, such as electronegativity, chemical potential, hardness, stiffness, response function, energetics etc. The DFT is based on the Kohn, Hohenberg and Sham theorems whereby all properties of the ground-state of an interacting electron gas are described by introducing certain functional of the electron density $\rho(r)$ [83].

Over the past few decades, DFT has been the most widely used approach to study the electronic structure of atoms, molecules and solids at ground-state level [84]. DFT approach reduces many-electron problem to an essentially single-particle problem with effective local potential. Instead of trying to solve the Schrödinger equation of interacting electrons directly, the problem is cast in a way such as to make it tractable in an approximate. We also discuss the implementation of the plane-wave pseudopotential codes, VASP and PHONON which are embedded in the MedeA software. Lastly, we give a theoretical background on the calculated properties, i.e. heats of formation, electronic density of states, phonon dispersion curves and elastic properties.

2.1 Density Functional Theory

Density functional theory is a quantum mechanical theory used in physics, chemistry and material science to study electronic structure and ground-state properties of many-body systems, particularly molecules, atoms and condensed phases. Although, DFT is based on the concept by Thomas [85] and Fermi [86], it was developed by Hohenberg, Kohn and Sham [87], using two theorems. The first theorem states that for any system of interacting particles in an external potential $V(r)$, the external potential is uniquely determined (except for a constant) by the ground state density $\rho_0(r)$ [87]. This theorem provides essential foundation for reducing many-body system by the use of functional of the electron density. The electron density thus depends only on 3 spatial coordinates, instead of 3N [87]. The second theorem gives a description that a universal functional for the energy of the density could be defined for all electron systems, whereas the exact ground state energy is the global minima for a given external potential. The density which minimises the functional is the exact ground state density [88].

DFT determines properties of many-electron systems using function of function (functional), which is dependent to the density of electrons. The DFT method was only recognised to be accurate enough for quantum chemistry calculations in the early 90s, after the enhancement of the approximations involved in the method to model the exchange and correlation interactions [89]. However, in spite of the enhancement, DFT still has difficulties to properly describe intermolecular interactions. These include the Van der Waals forces, excitations during charge transfer, transition states, global potential energy surfaces, strongly correlated systems and band gap in semiconductors [90, 91]. Kohn and Sham proved that the properties of the total

ground-state of an interacting electron gas may be described by introducing certain functional of the electron density $\rho(r)$, which depends on the positions of atoms [88].

$$E(\rho) = \int \rho(r)\upsilon_{ext}(r)dr + \frac{1}{2}\iint \frac{\rho(r)\rho(r')}{|r-r'|}drdr' + G[\rho], \qquad 2.1$$

where $\upsilon_{ext}(r)$ is the external field integrating with the field of the nuclei; the functional $G(\rho)$ comprises the kinetic and exchange-correlation energy (E_{XC}) of the interacting electrons. $G(\rho)$ is universal and is independent of the external fields. Furthermore, this expression is a minimum for the correct density function $\rho(r)$. This allowed Kohn and Sham to further develop the concept and suggested the form of [92] $G(\rho)$;

$$G(\rho) = T(\rho) + E_{xc}(\rho), \qquad 2.2$$

where $T(\rho)$ is the kinetic energy of the non-interacting electrons with density $\rho(r)$ and the functional $E_{xc}(\rho)$ encompasses the many-electron effects of the exchange and the correlation. As the exact many-body and correlation interactions are unknown, there is an approximation that the exchange-correlation is taken from the known results of an interacting electron system of constant density (homogeneous electron gas) and it is assumed that exchange and correlation effects are not strongly dependent on inhomogenities of the electron density away from the reference point r. It is therefore, necessary to determine the set of wavefunction ψ_i that minimises the Kohn-Sham energy functional. The electron density is written as follows;

$$\rho(r) = \sum_{i=1}^{N} |\psi_i(r)|^2, \qquad 2.3$$

where N represents the number of electrons. The Kohn-Sham energy function is given by a self-consistent solution;

$$\left[-\nabla^2+\sum_I \frac{2Z_I}{|r-R_I|}+\int 2\frac{\rho(r')}{|r-r'|}dr'+V_{xc}(r)\right]\psi_i=\varepsilon_i\psi_i, \qquad 2.4$$

where R_I is the position of the nucleus I of charge Z_I and ε_i are the Lagrange factors. The exchange-correlation potential, V_{xc} is written as a functional derivative;

$$V_{xc}(r)=\frac{\delta E_{xc}[\rho(r)]}{\delta\rho(r)}. \qquad 2.5$$

Though, thoroughly applicable for ground-state and the exchange-correlation energy, DFT is only known by approximation. The significance of this theory to practical uses can hardly be overemphasised. It reduces the many-electron problem to an essentially single-particle problem with the effective local potential,

$$V(r)=\sum_I \frac{2Z_I}{|r-R_I|}+\int 2\frac{\rho(r')}{|r-r'|}dr'+V_{XC}(r). \qquad 2.6$$

The most important concern when applying DFT is the way in which the functional E_{xc} is defined. The energy functional, $E_{xc}(\rho)$ for inhomogeneous electron gas can be expressed as Coulomb interaction between the electron and its surrounding exchange-correlation hole [93, 94];

$$V_{xc}[\rho]=\frac{1}{2}\int dr\rho(r)\int dr'\frac{(r,r'-r)}{|r-r'|}. \qquad 2.7$$

The major problem with DFT is that the exact functionals for exchange and correlation are not known except for the free electron gas, but this can be solved by way of approximation method. There are two commonly known approximations: namely local density approximation (LDA) and generalised gradient approximation (GGA). Figure 2-1 compares methodology for solving the Schrödinger equation and the DFT Kohn-Sham equation, respectively.

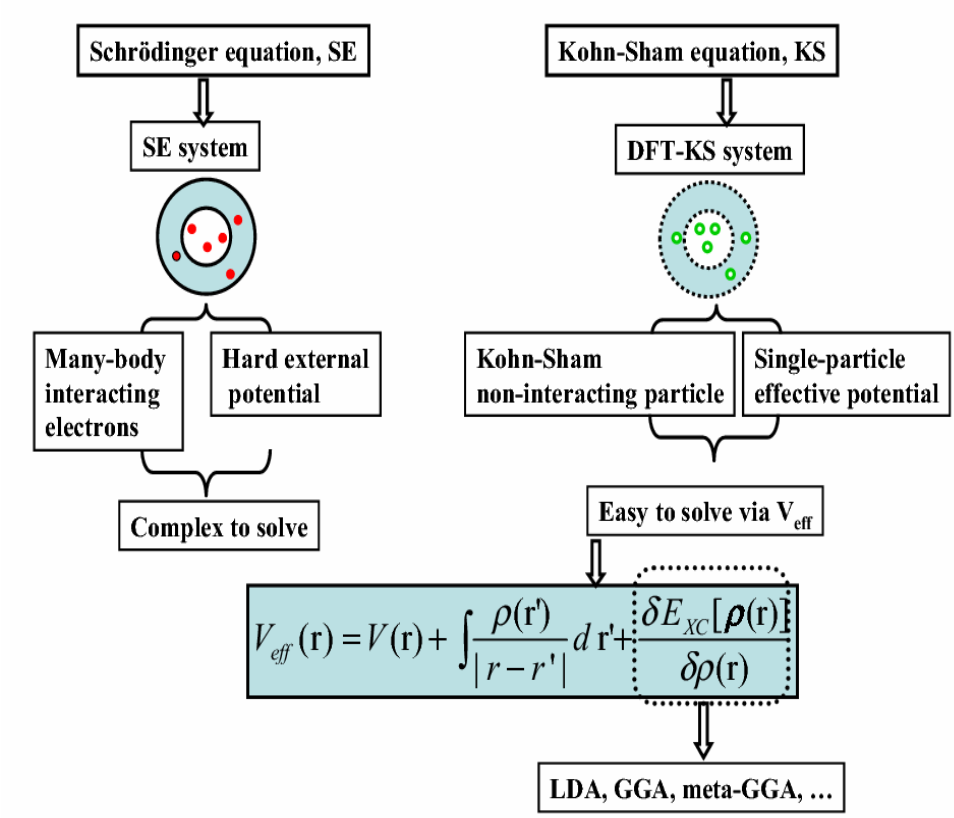

Figure 2-1 A comparison of the methodology for solving the many-body Schrödinger equation and effective one-electron Kohn-Sham equation **[95, 96]**.

2.2 Approximation Methods

2.2.1 Local Density Approximation

Local density approximations (LDA) are a set of approximations to the E_{XC} functional in DFT that are determined by the electronic density at each point in space. The LDA demonstrates that E_{XC} is similar to that for a locally uniform electron gas with similar density in regions where there is slow variation in charge density [97]. This is the most widely used approximation, whereby the E_{XC} density is locally of an inhomogeneous system substituted by that of an electron gas evaluated at local density. LDA is based

upon two basic assumptions; first being that the exchange and correlation effects are mainly from the immediate locality of point r and the second being that these exchange and correlation effects are slightly independent on the alteration of the electron density in the locality of r [98]. The fulfilment of these two conditions results same contribution from the volume element dr as if this volume element was surrounded by a constant electron density $\rho(r)$ of the same value as within dr. In this approximation, the exchange-correlation energy density of the homogeneous electron gas, $E_{XC}^{\text{hom}}(\rho_0)$ dependent on the homogeneous density ρ_0 and replaces this for the inhomogeneous system with density $\rho(r)$ by,

$$E_{XC}^{LDA}(\rho(r)) = E_{XC}^{\text{hom}}(\rho_0)|_{\rho_0} . \qquad 2.8$$

For spin-unpolarised system (where the functional depends only on the density) the LDA for the E_{XC} is written as;

$$E_{XC}^{LDA}[\rho] = \int p(r)\varepsilon_{XC}(\rho)dr, \qquad 2.9$$

and

$$\frac{\delta E_{XC}(\rho(r))}{\delta\rho(r)} = \frac{\partial[\rho(r)\varepsilon_{XC}(r)]}{\partial\rho(r)}. \qquad 2.10$$

This approximation is not effective for systems with slowly varying densities, such as the weakly perturbed electron gas, but however, also effective for systems which have very inhomogeneous electron densities such as atoms and molecules. Now, considering the exchange-correlation hole and the pair correlation function, the exchange-correlation energy density becomes;

$$\rho_{Xc}^{LDA}(r_1, r_2) = \rho(r_1)[g^{\hom}([\rho]; | r_1 - r_2 |], \qquad 2.11$$

where $g^{\hom}[\rho]$ is the coupling constant integrated pair-correlation function of the homogeneous electron gas [99]. The exchange-correlation part of the pair-correlation function which is unaffected by the coupling constant integration is given by;

$$g_{xc}^{LDA}([\rho]; r_1, r_2) = 1 - \frac{9}{2}\left[\frac{\sin(k_F(r_1)|r_1 - r_2|) - k_F(r_1)|r_1 - r_2|\cos(k_F(r_1)|r_1 - r_2|)}{(k_F(r_1)|r_1 - r_2|)^3}\right]^2, \qquad 2.12$$

where $k_F(r)$ represents the position dependent local fermi wave vector and can be written as:

$$k_F(r) = (\frac{3}{\pi})^{\frac{1}{3}}\rho(r)^{\frac{1}{3}}. \qquad 2.13$$

The E_{XC} can be fragmented into exchange and correlation terms linearly,

$$E_{XC} = E_x + E_c, \qquad 2.14$$

so that discrete expressions for E_x and E_c can be evaluated. The exchange term transforms to an analytic form for the homogeneous electron gas (HEG). Moreover, the exchange term is applied under approximation that exchange-energy within a system of inhomogeneous density is obtained by employing the HEG results pointwise, resulting in the expression [100, 101];

$$E_x^{LDA}[\rho] = -\frac{3}{4}\left(\frac{3}{\pi}\right)^{\frac{1}{3}}\int \rho(r)^{\frac{4}{3}} dr. \qquad 2.15$$

This equation satisfies the correct exchange scaling. There are corresponding equations for the correlation part of $g^{\hom}[\rho]$ and for $E_C^{LDA}[\rho]$. The LDA exchange-correlation hole is spherical around the reference electron;

$$\rho_{XC}^{LDA}(r_1, r_2) = \rho_{XC}(r_1, s), \qquad 2.16$$

where $s = | r_1 - r_2 |$ and it also satisfy the sum rule,

$$\int \rho_{XC}^{LDA}(r_1, r_2) dr_2 = 4r \int_0^{\infty} \rho_{XC}^{LDA}(r_1, s) s^2 ds = -1. \qquad 2.17$$

These equations give some significant understanding of the unlikely success of LDA in intensely inhomogeneous systems. However, the coupling constant averaged exchange-correlation hole is not spherically symmetric in these systems. As a result, the exchange-correlation hole can be adequately approximated using LDA.

The analytic expressions for the correlation energy of the HEG are only defined in the high-density and low-density limits corresponding to infinitely-weak and infinitely-strong correlation, respectively. The high-density limit of the correlation energy density is given by [100],

$$\varepsilon_c = A \ln(r_s) + B + r_s (C \ln(r_s) + D), \qquad 2.18$$

and the low limit,

$$\varepsilon_c = \frac{1}{2} \left(\frac{g_0}{r_s} + \frac{g_1}{r_s^{\frac{3}{2}}} + ... \right). \qquad 2.19$$

The Wigner-Seitz radius is related to the density as follows;

$$\frac{4}{3} \pi r_s^3 = \frac{1}{\rho}. \qquad 2.20$$

Local density approximations are of great significance as a appropriate property of any approximate E_{XC} functional in the construction of more advanced approximations to the E_{XC}, such as GGA or hybrid functionals. LDA reproduces the exact results of the HEG for non-varying densities. As a result, the LDA component explains such functional explicitly [101]. LDA properly approximates the energy of the true density

by the energy of a local constant density. However, fails to approximate in systems where the density variations are rapid such as in molecules. The local spin density (LSD) also is not accurate enough for most chemical applications, which require determination of energy differences with considerable precision. The LSD has been used to calculate the electronic structure in solid state physics for many years [102, 103]. This approximation is given by

$$E_{XC}^{LSD}[\rho_{\uparrow},\rho_{\downarrow}] = \int d^3 r \rho(r) \varepsilon_{XC}^{unif}[\rho_{\uparrow}(r),\rho_{\downarrow}(r)], \qquad 2.21$$

where $\varepsilon_{Xc}^{unif}(\rho_{\uparrow},\rho_{\downarrow})$ is the exchange-correlation energy per particle of a uniform electron gas [104, 105, 106].

2.2.2 Generalised Gradient Approximation

Although, LDA cannot adequately approximate the exchange-correlation hole, there is a way to go beyond these limitations. The most efficient way is extend the exchange-correlation functional with terms containing gradients of the electron density. These gradients measure changes of the electron density and can be used to advance the LDA. The theory of most gradient functional developed is based upon the weakly varying electron gas [99]. These approximations are called gradient expansion approximation (GEA) given as follows;

$$E_X^{GEA}[\rho] = E_X^{LDA}[\rho] + \beta \int \frac{(\nabla\rho)^2}{\rho^{\frac{4}{3}}} dr + ... \qquad 2.22$$

$$E_C^{GEA}[\rho] = E_C^{LDA}[\rho] + \int C(\rho) \frac{(\nabla\rho)^2}{\rho^{\frac{4}{3}}} dr + ... \qquad 2.23$$

where β is a constant and $C(\rho)$ is a function determined by response theory. However, the rapid variation of realistic densities in atoms and molecules obstructs any systematic improvement of GEA over the LDA. When analysis of the gradient expansion of the exchange-correlation hole is done, they show that the short range part (near the reference electron) is enhanced, but the long range is made worse [107]. The corresponding approximations of the GEA are the generalised gradient approximations (GGA), and can be written as;

$$E_{XC} = E_{XC}[\rho(r), \nabla\rho(r)], \qquad 2.24$$

which brings a significant improvements over LDA results with accuracy approaching and in some instances superior over that of correlated wavefunction methods such as MP2. GGA provides several distinct parameterisations as compared to one of LDA. A commonly used functional is the PW91 functional, proposed by Perdew and Yang [106, 108, 109]. GGA with gradient-corrected functional is given as;

$$E_{XC}^{GGA}[\rho_\uparrow, \rho_\downarrow] = \int d^3 r f(\rho_\uparrow(r), \rho_\downarrow(r), \nabla\rho_\uparrow, \nabla\rho_\downarrow), \qquad 2.25$$

This expression decreases LSD atomization energy errors by a factor of approximately 5 [110]. The most widely used GGA's are the Becke GGA [111] for the exchange energy and the exchange and correlation GGA's by Perdew [112] and Perdew and Wang [107, 113, 114, 115]. The Becker GGA correction to the LDA is of the form;

$$E_X^{GGA}[\rho_\uparrow, \rho_\downarrow] = E_X^{LDA} - \beta \int \sum_\sigma \frac{\rho_\sigma(r)^{\frac{4}{3}} x_\sigma^2}{1 + 6\beta x_\sigma \sinh^{-1} x_\sigma} d^3 r, \qquad 2.26$$

and

$$E_X^{LDA} = -C_{X\sigma} \sum \rho_\sigma^{\frac{4}{3}}(r) d^3(r), \qquad 2.27$$

where

$C_X = \frac{3}{2}\left(\frac{3}{4\pi}\right)$, $X_\sigma = \frac{|\nabla\rho|}{\rho_\sigma^{\frac{4}{3}}}$, σ denotes either electron spin-up (↑) or spin-down (↓) electron spin. β (Constant) is a parameter to obtain the correct exchange energy for the noble gas. The following correlation functional as proposed by Perdew and Wang [113] predicts correlation energies of useful accuracy for an electron gas with slowly varying density;

$$E_X^{GGA}[\rho_\uparrow, \rho_\downarrow] = \int \rho(r)\varepsilon_C(\rho_\uparrow, \rho_\downarrow)d^3r + \int \frac{C_C(\rho)|\nabla\rho(r)|^2}{de^\phi \rho(r)^{\frac{4}{3}}} d^3r, \qquad 2.28$$

where

$$d = 2^{\frac{1}{2}}\left[\left(\frac{1+\zeta}{2}\right)^{\frac{5}{3}} + \left(\frac{1-\zeta}{2}\right)^{\frac{5}{3}}\right], \qquad 2.29$$

$$\phi = 0.1929\left[\frac{C_C(\infty)}{C_C(\rho)}\right]\frac{|\nabla\rho|}{\rho^{\frac{7}{6}}}. \qquad 2.30$$

$\zeta = (\rho_\uparrow, \rho_\downarrow)/\rho$ and $C_C(\rho)$ are rotational polynomial of the density that contains seven fitting parameters. The exchange functional, written by Perdew-Burke-Ernzerhof is described in the form that contains an explicit enhancement factor over the local exchange factor, which is generally known as GGA-PBE, written as;

$$E_X^{PBE}[\rho_\uparrow, \rho_\downarrow] = \int \rho(r)\varepsilon_X^{LDA}[\rho(r)]F_{XC}(\rho, \xi, s)dr, \qquad 2.31$$

where ρ is the local density, ξ is the relative spin polarization, and $s = |\nabla\rho(r)|/(2k_F\rho)$, is the dimensionless density gradient. The factor is expressed as;

$$\left(sF_X = \left(\frac{1}{k + s^2\mu}\left(k + s^2\mu + s^2 k\mu\right)\right)\right), \qquad 2.32$$

where $\mu = \beta\left(\frac{\pi^2}{3}\right) = 0.21951$ with $\beta = 0.066725$. The correlation energy is

$$E_C^{PBE}[\rho_\uparrow,\rho_\downarrow]=\int\rho(r)\left[\varepsilon_C^{LDA}(\rho,\zeta)+H(\rho,\zeta,t)\right]dr, \qquad 2.33$$

with

$$H(\rho,\zeta,t)=\left(\frac{e^2}{a_0}\right)\gamma\phi^3\times\ln\left\{1+\frac{\beta}{\gamma}t^2\left[\frac{1+At^2}{1+At^2+A^2t^4}\right]\right\}, \qquad 2.34$$

where

$$A=\frac{\beta}{\gamma}\left[e^{\varepsilon_C^{LDA}\frac{[\rho]}{\gamma\phi^3}}-1\right]^{-1}, \qquad 2.35$$

$t=\left|\nabla\rho(r)/(2k_s\rho)\right|$ is the dimensionless density gradient,

$ks=\left(\frac{4k_F}{\pi}\right)^{\frac{1}{2}}$ is the Thomas-Fermi screening wave number and

$\phi(\zeta)=\left[(1+\zeta)^{\frac{2}{3}}+(1-\zeta)^{\frac{2}{3}}\right]$ is the spin-scaling factor.

Under uniform scaling to the high density limit, E_C^{GGA} changes to

$$-\frac{e^2}{a_0}\int d^3rn\gamma\phi^3\times\ln\left[1+\frac{1}{\chi s^2/\phi^2+(\chi s^2/\phi^2)^2}\right], \qquad 2.36$$

where $s=\left|\nabla n\right|/2k_Fn=(r_s/a_0)^{1/2}\phi t/c$ is another dimensionless density gradient.

2.3 Plane–wave Pseudopotential Method

The plane-wave pseudopotential method is a technique used to calculate the variation self-consistent solution with accuracy. This method has been advanced and perfected to reliably predict the static and dynamic properties of molecules and crystalline solids [115]. The complicated many-body problem of strongly correlated electrons and

nuclei has been mapped within the framework of the Born-Oppenheimer approximation and the DFT to a single-particle problem moving in an effective external potential for a set of fixed nuclei. The practical numerical scheme to solve the resulting single-particle Kohn-Sham equation for extended systems like crystalline solids or liquids has been developed [116]. The most common approach for solving this problem is to expand the wavefunction of the single-particle eigenstates of the Kohn-Sham equations into a set of basis functions. Then, the Schrodinger equation transforms into an algebraic equation for the expansion coefficient solved by numerical perfected method. Basically, the plane-wave pseudopotential method deals with weak pseudopotentials and performs complete structure optimization, more especially the relaxation of internal parameters. Plane-wave pseudopotential method is also able to simulate the electronic ground-states for metals, insulators and semiconductors.

2.3.1 Plane-wave Basis Sets

The plane-wave basis sets are mainly used in the calculations where boundary conditions are involved. They are usually coupled with an “effective core potential” or pseudopotential in practical performance, and are only used for valence charge density. The plane-wave basis is more efficient than the Gaussian-type basis because is guaranteed to converge to the target wavefunction. Since there is infinite number of electrons, a wavefunction is needed for each individual electron. However, the basis set required for the expansion of each wavefunction is also infinite. Bloch’s theorem, which starts with periodicity of the crystal lattice, offers solution to this problem. Bloch’s theorem defines the crystal momentum k as good quantum number and also

gives the boundary condition for the single particle wavefunction, φ_k. Bloch's theorem is often stated in an alternative form: the equation,

$$\varphi_k(r + R_L) = e^{ik.R_L}\varphi_K(r), \qquad 2.37$$

is equivalent to the statement that all eigenfunctions φ_{ki} of a single–particle Schrodinger equation with periodic potential can be written as a periodic function u_{ki} modulated by a plane-wave vector k [117], where R_L is a direct lattice vector.

$$\varphi_{kj}(r) = e^{ikr}u_{kj}(r). \qquad 2.38$$

u_{ki} can be expanded as a set of plane-wave basis,

$$u_j(r) = \sum_G C_G^j e^{iG.r}, \qquad 2.39$$

where G are reciprocal lattice vectors. The functions u_{ki} are periodic and can be expanded in a set of plane-waves. Thus the electronic wavefunction with the exponential prefactor is given as;

$$\varphi_{kj}(r) = \sum_G C_G^{kj} e^{i(K+G)r}. \qquad 2.40$$

where C_G^{kj} is the coefficient of the periodic plane-waves. As such the number of wavefunctions used is controlled by the largest wave-vector in the expansion in 2.41. This is equivalent to imposing a cut-off on the kinetic energy as the kinetic energy of an electron with wave-vector k is given by;

$$E_K = \frac{\hbar^2|K+G|^2}{2m}, \qquad 2.41$$

thus only plane-wave that obey,

$$E_K = \frac{\hbar^2|K+G|^2}{2m} < E_{cut}, \qquad 2.42$$

are included in the basis. The plane-wave set at finite cut-off energy will lead to an error in the computed total energy; hence the energy must be increased until the calculated energy has converged. It is highly advisable to use much denser k-points to reduce errors and ensure convergence. Before making use of the plane-wave expansion of the wavefunction we write the Kohn-Sham equation of density fuctional theory in the following way [115],

$$\sum\left[\frac{\hbar^2}{2m}\left|K+G\right|^2\delta_{GG}+V_{eff}(r)\right]C_{j,K+G}=\varepsilon_j C_{j,K+G}, \qquad 2.43$$

where,

$$V_{eff}(r)=V_{ext}(r)+V_H[n(r)]+V_{XC}[n(r)], \qquad 2.44$$

$V_{ext}(r)$, $V_H[n(r)]$, and $V_{XC}[n(r)]$ are Fourier transforms of the external potential of the nuclei, Hartree and exchange-correlation potentials, respectively.

2.3.2 Pseudopotentials

The pseudopotential was first introduced to practice by Hans Hellmann in 1930. In physics, a pseudopotential or effective potential is used as an approximation of complex systems. Many physical and chemical properties depend on the distribution of valence electrons, while the core electrons do not participate in a chemical bonding. The core electrons are strongly localised around the nucleus, and their wavefunction overlap less with the core electron's wavefunction of the next neighbouring atoms. Hence, the distribution of core electrons is basically the same irrespective of which chemical environment the atom is experiencing. Therefore, the core electrons are declared "frozen" and the core electron distribution is kept in the crystal environment.

This is of good advantage since few electrons have to be treated and few eigenstates of the Kohn-Sham equation have to be calculated. Secondly, the total energy scale is largely reduced by the removal of core electrons from the calculation which makes the calculation of the energy differences between atomic configurations numerically much more stable. Hence, the introduction of pseudopotential approximation is an attempt to eradicate the unsolvable complicated effects of the core electrons in motion and their nuclear with an effective potential, or pseudopotential [118, 119, 120]. Thus, the Schrodinger equation now contains a modified effective potential term instead of the coulombic potential term for core electrons. In the pseudopotential approach, only valence electrons are dealt with explicitly [121, 122, 123, 124, 125].

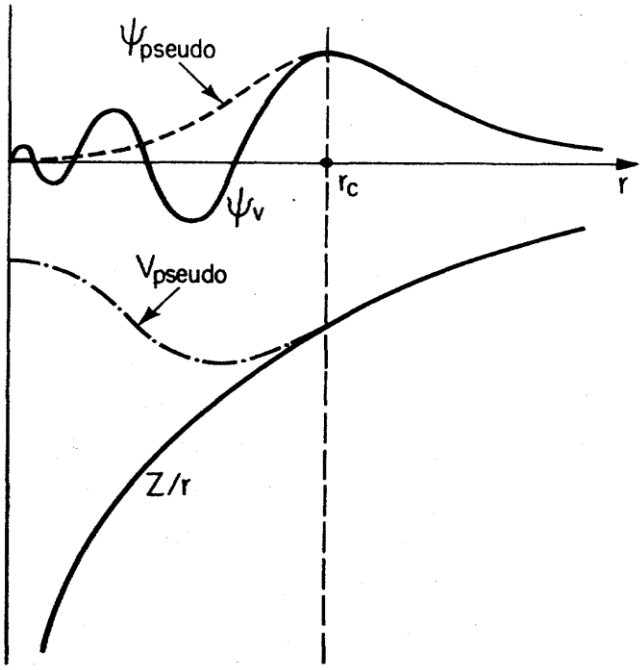

Figure 2-2 Schematic illustration of an atomic all-electron wavefunction and the corresponding atomic pseudo wave functions.

Figure 2-2 shows the schematic representation of an atomic all-electron wavefunction and corresponding atomic pseudo wavefunctions. Due to strong ionic potential, the valence wavefunctions oscillate rapidly in the region occupied by the core electrons.

Hence, the orthogonality between the core electrons and valence electrons is maintained due to these oscillations. The pseudopotential is constructed such that that the pseudo wavefunction has no radial nodes within the core region and that the pseudo wavefunctions and potential agree with the *true* wavefunction and potential outside some cut-off radius(r_{cut}). The pseudopotential also must preserve the atomic properties of the element, including phase shifts on scattering across the core. In general the pseudopotential must be non-local, i.e. it must have projectors for the different angular momentum states. The general form of the pseudopotential is

$$V_{NL} = \sum_{lm} |lm\rangle V_l \langle lm|, \qquad 2.45$$

where $|lm\rangle$ are spherical harmonics, and V_i is the pseudopotential for angular momentum (l) [117]. The majority of the pseudopotentials used in electronic structure are generated from all electron atomic calculations. Norm conserving pseudopotential is the example of non-local pseudopotential and uses a different potential for each angular momentum components of the wavefunction. However, pseudopotential that uses the same potentials for all angular momentum components of the wavefunction is called local pseudopotential. We note that between the two pseudopotential, local pseudopotential is computationally efficient than non-local pseudopotential [126, 127].

2.3.3 Norm-conserving Pseudopotentials

As outlined in section 2.3.2 above, the use of psedopotentials is crucial for performing *ab initio* calculations. Hamann *et al.* [128] proposed a norm-conserving pseudopotential type which is completely non-emperical. This type of pseudopotential allows obtaining the pseudo wavefunctions which are identical to real wavefunctions

beyond a chosen core radius, whose eigenvalue agree with the real eigenvalue. This property produces a correct description of bonding in pseudopotential calculations, and corrects self-consistent electrostatics and exchange-correlation potentials. Norm-conserving pseudopotentials also produce the scattering power of the full atom potential correctly at energies away from the bound valence state energy to first order in the energy difference. Consequently, norm-conserving pseudopotentials reproduce all-electron electronic structure calculations with high degree of accuracy [129].

2.3.4 Ultrasoft Pseudopotentials

In 1990, Vanderbilt developed a pseudopotential known as "ultrasoft pseudopotentials". Many of the modern pseudopotential calculations use this generalisation of the Kleinman-Bylander [130]. This approach is a radical departure from norm-conserving pseudopotentials discussed above, since ulrasoft pseudopotentials attain much smoother pseudo wavefunctions. In this approach, the pseudo wavefunctions are required to be equal to all electron wavefunctions outside the radius, as with the norm-conserving pseudopotentials, but inside the radius are allowed to be as soft as possible. Again the norm-conserving constraint is removed, but this also introduces some complications. However, the ultrasoft pseudopotential still able to reduce the plane-wave cut-off needed in calculations, particularly because large values of radius can be used in their scheme. The complications that result are two-fold. First of all, since the pseudo-wavefunctions are equal to the all-electron wavefunctions (and therefore have the same norm) in the interstitial, but have a different norm inside the topological complexity they are necessarily not normalised. Secondly, the pseudo charge density is not obtained by computing $\sum \varphi^* \varphi$ as with

norm-conserving pseudopotentials; this will lead to the incorrect total charge. A third, but less important, complication is that, by relaxing the norm-conservation, the resulting pseudopotentials can become less transferable. However, Vanderbilt pseudopotentials were proposed for use in large scale calculations, for which the cost of generating pseudopotentials is negligible compared with the cost of the calculations [130]. The electron density is subdivided into a smooth part that extends throughout the unit cell and a hard part localised in the core region. Ultrasoft pseudopotentials have an advantage over the norm-conserving pseudopotential.

2.4 Implementation of Plane-wave Pseudopotential Codes

In the past few decades, various plane-wave pseudopotential codes have been used to perform quantum mechanical problems. These include VASP, CASTEP, Win2k, quantum expresso. VASP [131] and PHONON [132] codes implemented in the MedeA [133] platform were chosen in this study to calculate the properties of MPO_4 and Li/$NaMPO_4$ structural polymorphs. VASP is designed to perform *ab initio* quantum mechanical calculation and molecular dynamics (MD) simulations utilizing pseudopotentials or the projector-augmented wave method and a wave basis set [131]. The approach implemented in VASP is based on the (finite temperature) local density approximation with the free energy as variational quantity and an exact evaluation of the instantaneous electronic ground-state at each MD time step. This package uses efficient matrix diagonalisation schemes and efficient Pulay/Broyden charge density mixing. These technique is highly advanced that it also avoid all the problems possibly

occurring in the original Car-Parrinello method, which is based on the simultaneous integration of electronic and ionic equations of motion. The interaction between ions and electrons is described using ultra-soft Vanderbilt pseudopotential (US-PP) [130] or by the projector-augmented wave (PAW) method. Ultra-soft pseudopontentials and projector-augmented wave allow for a considerable reduction of the number of plane-waves per atom for transition metals and first row elements. Forces and the full stress tensor can be calculated with VASP and used to relax atoms into their instantaneous ground-state. Within the VASP code, firstly a convergence test is performed to establish the suitable energy cut-off and k-points sufficient to converge the total energy of the system under consideration. Then all the properties such as heats of formation, densities of states, elastic constants and phonon dispersion curves can also be calculated.

2.5 Theoretical Background of the Calculated Properties

2.5.1 Heats of Formations

The heats of formation (ΔH_f) and associated entropies provide a fundamental understanding on stabilities of compound and as well as phase diagrams construction. The standard enthalpy of formation or standard heat of formation of a compound is the change of enthalpy that accompanies the formation of one mole of a substance in its standard state from its composite elements in their standard states (1 bar and 298 K). The heat of formation is estimated by;

$$\Delta H_f = E_c - \sum_i x_i E_i , \qquad 2.46$$

where E_c is the calculated total energy of the compound, E_i is the calculated total energy of the element i in the compound. The results of heats of formation are discussed in section 3.2. The heats of formations will be used for predicting the stability trend of the five polymorphs of MPO_4, $LiMPO_4$ and $NaMPO_4$ compounds in chapter 3, 5 and 6. They will be calculated as follows;

$$\Delta H_f(MPO_4) = {}^{1}\!/_{N}\left[E - (E_M + E_P + 4E_O)\right], \qquad 2.47$$

and

$$\Delta H_f(AMPO_4) = {}^{1}\!/_{N}\left[E - (E_A + E_M + E_P + 4E_O)\right], \qquad 2.48$$

where N is the total number of atoms in the unit cell, E is the total energy of the compound, A is either Li or Na, and M is the transition metal element. E_M, E_P and E_O are the individual total energies of M, P and O, respectively.

2.5.2 Densities of States

The density of states (DOS) of a system describes the number of states per interval of energy at each energy level that are available. The DOS indicates how densely packed quantum states are in a system. Integration of DOS over a range of energy yields a number of states;

$$N(E) = \int_{E}^{\Delta E} g(E)dE, \qquad 2.49$$

where $N(E)$ denote the carrier density and $g(E)dE$ represents the number of states between E and dE. The density of states permits integration to be done with respect to the electron energy instead of the integration over the Brillouin zone. In the case metal phosphates, the presence of suppression in the electronic density of states i.e. pseudo gap at the Fermi level is established. One question that arises in the study of complex metal phosphates systems is how the pseudo gap forms in the electronic density of states at the Fermi level and the relation of this feature to the stability of the particular structure. Pierce *et al*. [134] and Matsuda *et al*. [135] have suggested the role of pseudo gap in the structural stability by the experimental observation of very high resistivities in structurally well-ordered stable quasicrystals. Several contexts, like Hume-Rothery rule [136], Jahn-Teller effects in molecules [137], and the colouring patterns of atoms over the sites of a given lattice [138] have proposed the direct relations between the formation of a pseudo gap and stability of the structure.

In ferromagnetic Fe, Co, and Mn, the partial filling of narrow 3*d* bands following Hund's rules and high electron density of states near the Fermi level result in a spin polarised valence band [139]. Pressure has found to play an essential role in the Coulomb correlations and wavefunctions. The Coulomb correlations loose their significance due to the steady increase in electron kinetic energy versus potential energy. Furthermore, pressure enhances the overlap of the atomic wavefunctions, leading to the broadening of the *d* bands close to E_F and lowering the DOS [139]. Literature reveals that densities of states are also essential in determining the stability trend of structures with same composition with respect to the Fermi level (E_F). The theory suggests that the structure with highest density of states around the Fermi level is considered the least stable, while the structure with lowest density of states is most stable [140, 141].

2.5.3 Phonon Dispersion Curves

The phonon dispersion curves are defined as the k wave vector dependence of the frequencies $\omega(k, j)$ of the normal modes for all branches j and selected directions in the crystal. Phonon dispersion curves have an essential role in several physical properties of condensed matter physics. These include thermal conductivity, mechanical stability and electrical conductivity. They indicate an excited state in the quantum mechanical quantization of the modes of vibrations of elastic structures of interacting particles. The behaviour of phonon dispersion branches reflects specific features of the crystal structure and the interatomic interactions and, therefore, gives the most comprehensive and detailed information about the dynamical properties of crystals. The phonon vibration frequencies are calculated as follows [142, 143]:

$$\omega = \upsilon_s q \qquad 2.50$$

where υ_s is the speed and q is the wave-vector of the lattice vibrations.

In crystal where there are two or more types of atoms; two types of modes of vibrations are displayed: acoustic and optical. Optical phonons arise from out of phase vibrations between neighbouring atoms within the unit cell, while in phase vibrations give rise to acoustic phonons. Furthermore, the acoustic modes have zero frequencies at $q = 0$ (the center of the Brillouin zone (Γ), while optical modes have non-zero. The acoustic and optical split into longitudinal and transverse modes abbreviated as longitudinal acoustic (LA), transverse acoustic (TA), longitudinal optical (LO) and transverse optical (TO). A linear relationship between frequency and long wavelengths phonon wave-vector is displayed in the acoustic modes. Negative vibrational

frequencies (soft modes) indicate mechanical instability of the system, while positive vibrations show stability. Along with the Γ point, there are several points of high symmetry which are of significant interest. Table 2-1 lists and describe the critical k-points of high symmetry line in the first Brillouin zone for certain Bravais lattice of bcc, fcc and hexagonal lattices [144, 145]. Phonon dispersion curves for different crystal directions use this denotation. The denotations describe the direction and symmetry of the crystal, since different denotations are used for different symmetries.

Table 2-1 Critical k-points in the first Brillouin zone.

Symbol	Description
Γ (0,0,0)	Center of the Brillouin zone
Simple cube	
M (1/2,1/2,0)	Center of an edge
R (1/2,1/2,1/2)	Corner point
X (0,1/2,0)	Center of a face
Body-centered cubic	
H (-1/2,1/2,1/2)	Corner point joining four edges
P (1/4,1/4,1/4)	Corner point joining three edges
N (0,1/2,0)	Center of a face
Face-centered cubic	
K (3/8,3/4,3/8)	Middle of an edge joining two trigonal faces
L (1/2,1/2,1/2)	Center of a trigonal face
U (1/4,5/8,5/8)	Middle of an edge joining a trigonal and a square face
W (1/4,3/4,1/2)	Corner point
X (0,1/2,1/2,)	Center of square face
Hexagonal	
A (0,0,1/2)	Center of a hexagonal face
K (2/3,1/3,1/2)	Middle of an edge joining two rectangular faces
H (1/2,0,0)	Corner point
L (1/2,0,1/2)	Middle of an edge joining a hexagonal and a rectangular face
M (1/2,0,0)	Center of a rectangular face

2.5.4 Elasticity

Elastic properties relate to various fundamentals solid-state properties, such as equation of state, interatomic potentials, lattice constants and phonon spectra. They have vital information regarding the strength of the materials against an externally applied strain and also act as stability criteria to study mechanical stability structural transformations [146, 147]. Basically, elastic constants of a material describe its response to the external applied strain required to maintain a given deformation and provides useful information of the strength of the material, as characterised by bulk modulus (B), shear modulus (G), Young's modulus (E), Poisson's ratio (υ) and shear anisotropy factor (A).

The calculation of elastic constants was initiated by Born [148]. The Born stability criteria are a set of conditions on the elastic constants (C_{ij}) are related to the second-order change in the internal energy of a crystal under formation. However, it was later revealed that the ranges of Born stability are sensitive to the choice of coordinates [149]. It was also suggested that the Born conditions are not effective for the stressed systems and only effective for the unstressed systems [150, 151]. Barron and Klein also indicated that the normal definition of the elastic constants derived the Helmholtz free energy cannot be directly applied to the study of the stress-strain relationship of a stressed system [152].

Wang and co-workers [150, 151] demonstrated, however, that elastic constants cannot be used as stability criteria for a stressed system. They suggested the use of elastic stiffness coefficients as stability criteria for isotropic stress. For anisotropic stress, they obtained a more general form from path-dependent finite displacements. The stability criteria is framed in terms of elastic stiffness coefficients which govern the proper

relations of stress and strain at finite strain by considering both the internal and the external work done during the process of deformation [108]. This is an indication that the stability analysis can predominantly be determined by an appropriate generalization of the zero-stress elastic constants which valid for arbitrary stress.

Bulk modulus is also one of the most important parameters that characterise the physical property of a material system, because it also measures the degree of stiffness or the energy required to produce a given volume deformation, while shear modulus describes the resistance to shape change caused by shearing force; Young's modulus reflects the resistance of materials against uniaxial tensions [153]. The bulk modulus depicts the bonding characters in the material and it is usually used as an indicator for the strength and hardness of materials and is the inverse of compressibility [154].

Moreover, Pugh introduced the ratio of bulk to shear modulus (B/G) of polycrystalline phases. The ratio states that the shear and bulk moduli signifies the resistance to plastic deformation and the resistance to fracture, respectively. A high B/G value is associated with ductility, while a low B/G value is related to brittleness. The critical value separating ductility and brittleness is 1.75 [155].

2.5.4.1 Elastic Stability Criteria

Various criterion have been established to deduce elastic stability of crystals and there are different for different lattice crystals. For each material, both stress and strain have three tensile and three shear components, giving six components in total. The relationship between stress and strain is defined by a 6x6 symmetry matrix comprising 36 elements, but only 21 independent elements, such that $\sigma_1 = C_{ij}\varepsilon_j$ for stresses, σ and strain, ε. Therefore, the strain dependence of stress can be expressed as;

$$\begin{pmatrix}\sigma_x\\ \sigma_y\\ \sigma_z\\ \tau_{yz}\\ \tau_{xz}\\ \tau_{xy}\end{pmatrix}=\begin{pmatrix}C_{11} & C_{12} & C_{13} & 0 & 0 & 0\\ C_{12} & C_{11} & C_{13} & 0 & 0 & 0\\ C_{13} & C_{13} & C_{33} & 0 & 0 & 0\\ 0 & 0 & 0 & C_{44} & 0 & 0\\ 0 & 0 & 0 & 0 & C_{44} & 0\\ 0 & 0 & 0 & 0 & 0 & C_{66}\end{pmatrix}\times\begin{pmatrix}\overline{\varepsilon_{xx}}\\ \varepsilon_{yy}\\ \varepsilon_{zz}\\ \gamma_{yz}\\ \gamma_{xz}\\ \gamma_{xy}\end{pmatrix}, \qquad 2.51$$

where σ and τ represent tensile and shear stress, while ε and γ represent tensile and shear strain, respectively [155]. The structural symmetry of the crystal makes some of the matrix elements equal and others fixed at zero. Cubic crystals have three independent elastic constants (C_{11}, C_{12}, C_{44}). The bulk, shear, Young's modulus and Poisson's ratio for the cubic crystal are given by [100, 106];

$$E=\frac{9BG}{3G+G}, \qquad \nu=\frac{E}{2G-1}, \quad G_V=\left[\frac{C_{11}-C_{12}+3C_{44}}{5}\right], \quad G_R=\left[\frac{C_{44}(C_{11}-C_{12})}{4C_{44}+3(C_{11}-C_{12})}\right],$$

$$G=G_H=\left[\frac{G_V+G_R}{2}\right], \qquad B=\left(\frac{C_{11}+2C_{12}}{3}\right), \qquad C'=\frac{C_{11}-C_{12}}{2}, \qquad A=\frac{2C_{44}}{C_{11}-C_{12}},$$

$$\nu=\frac{C_{12}}{C_{11}+C_{12}}.$$

where E is the Young's modulus, ט Poisson's ratio, G isotropic shear modulus, B bulk modulus, C' tetragonal shear modulus and Zener anisotropic factor A. The Hill average, in general, is selected as the estimation of bulk modulus and shear modulus.

The requirements for the mechanical stability for cubic crystals lead to the following necessary conditions for stability on the elastic constants [111];

$(C_{11}-C_{12})>0$, $(C_{11}+2C_{12}>0)$, $C_{11}>0$, $C_{44}>0$.

The single shear modulus for the {100} plane along the [010] direction and for the {110} plane along the [110] direction in a cubic crystal are given by C_{44} and G, respectively. The elastic moduli for hexagonal crystal are given as follows [156];

$$B_V = \frac{2}{9}\left(C_{11} + C_{12} + 2C_{13} + \frac{1}{2}C_{33}\right), \tag{2.52}$$

$$G_V = \frac{1}{30}\left(C_{11} + C_{12} + 2C_{33} - 4C_{13} + 12C_{44} + 12C_{66}\right), \tag{2.53}$$

$$B_R = \frac{(C_{11} + C_{12})C_{33} - 2C_{12}^{24}}{C_{11} + C_{12} + 2C_{33} - 4C_{13}}, \tag{2.54}$$

$$G_R = \frac{5}{2}\frac{[(C_{11} + C_{12})C_{33} - 2C_{12}^2]C_{55}C_{66}}{3BvC_{55}C_{66} + [(C_{11} + C_{12})C_{33} - 2C_{12}^2]^2(C_{55} + C_{66})}. \tag{2.55}$$

On the other hand, Young's modulus is calculated by;

$$E_X = \frac{\left[C_{33}\left(C_{11} + C_{12}\right) - 2C_{13}^2\right]\left(C_{11} - C_{12}\right)}{C_{11}C_{33} - C_{13}^2}, \tag{2.56}$$

$$E_Z = \frac{\left[C_{33}\left(C_{11} + C_{12}\right) - 2C_{13}^2\right]}{C_{11} - C_{12}}, \tag{2.57}$$

$$\nu = \frac{C_{13}}{\left(C_{11} + C_{12}\right)}. \tag{2.58}$$

E_X characterises the Young's modulus along the [100] and [010] directions, while E_Z characterises Young's modulus along the [001] direction. Young's modulus (E) is defined as the ratio between stress and strain and is used to provide a measure of the stiffness of the solid; that is stiffness of materials increases with the value of E. Poisson's ratio (υ) refers to the ratio of transverse contraction strain to longitudinal extension strain during stretching, thus reflecting the stability of the crystal against shear. Hence, higher the Poisson's ratio is the better ductility the crystalline metal has

at low temperatures. On the other hand, the anisotropy factors are calculated as follows;

$$A_1 = \frac{2C_{44}}{C_{11} - C_{12}} = \frac{C_{44}}{C_{66}}, A_2 = \frac{C_{33}}{C_{11}}, A_3 = \frac{C_{12}}{C_{13}}. \qquad 2.59$$

For the hexagonal system to be elastically isotropic, the three anisotropy ratios (A_1, A_2 and A_3) must be simultaneously equal to one [106]. The elastic anisotropy A determines the possibility of inducing micro-cracks in materials [157, 158]. If the material is completely isotropic, the value of A will be equal to unity, whereas values smaller or larger than 1 measure the degree of elastic anisotropy. Thus the resultant macroscopically measurable quantities obtained for materials are the shear modulus, Young's modulus corresponding to the stress–strain ratio in the case of tensile forces, bulk modulus, Poisson's ratio and the anisotropy factor, which are all important for technological and engineering applications.

Hexagonal crystals, contains five independent elastic constants, $C_{11}, C_{12,} C_{13}, C_{33}$ and C_{44}. C_{11} and C_{13} correspond to longitudinal modes along the [1000] and [0001] directions, respectively. The requirements for mechanical stability in a hexagonal structure lead to the following restrictions on the elastic constants [158];

$C_{11} > 0,\ \ C_{11} - C_{12} > 0, C_{44} > 0,\ C_{11} + C_{12} - \frac{2C_{13}^2}{C_{33}} > 0$ and $C_{66} = \frac{C_{11} - C_{12}}{2} > 0$.

C_{44} and $C_{66} = (C_{11} - C_{12})/2$ can be determined from the speed of sound of transverse modes propagating along the [0001] and [1000] directions, respectively [159].

Orthorhombic crystal systems comprise nine independent elastic constants, $C_{11}, C_{12,} C_{13}, C_{22}, C_{23}, C_{33}, C_{44}, C_{55}$ and C_{66}. Elastic constants, C_{11}, C_{22} and C_{33} indicate the degree of directional resistance to linear compressions of *a*, *b* and *c*, respectively.

While C_{44}, C_{55} and C_{66} measure shear resistance to the {100}, {010} and {001} planes, respectively [160]. Elastic moduli derived from these elastic constants are [161];

$$B_V = \frac{1}{9}\left(C_{11} + C_{22} + C_{33}\right) + \frac{2}{9}\left(C_{12} + C_{13} + C_{23}\right), \quad 2.60$$

$$B_R = \left[\left(S_{11} + S_{22} + S_{33}\right) + 2\left(S_{12} + S_{13} + S_{23}\right)^{-1}\right], \quad 2.61$$

$$G_V = \frac{1}{15}(C_{11} + C_{22} + C_{33} - C_{12} - C_{13} - C_{23}) + \frac{1}{5}(C_{44} + C_{55} + C_{66}), \quad 2.62$$

$$G_R = 15\left[4\left(S_{11} + S_{22} + S_{33}\right) - 4\left(S_{12} + S_{13} + S_{23}\right) + 3\left(S_{44} + S_{55} + S_{66}\right)\right]^{-1}, \quad 2.63$$

$$B_H = \frac{1}{2}\left(B_R + B_V\right), \quad 2.64$$

$$G_{\mathrm{H}} = \frac{1}{2}\left(G_R + G_V\right), \quad 2.65$$

$$E_H = \frac{9B_H G_H}{G_H + 3B_H}, \quad 2.66$$

where V, R, H is the Voigt, Reuss and Hill, and S_{ij} is the inverse matrix of the elastic constants matrix C_{ij}, which is given by [162];

$$S_{11} = \frac{\left(C_{22}C_{33} - C_{23}^2\right)}{\left(C_{11}C_{22}C_{33} + 2C_{12}C_{13} + C_{23} - C_{11}C_{23}^2 - C_{22}C_{13}^2 - C_{33}C_{12}^2\right)}, \quad 2.67$$

$$S_{12} = \frac{\left(C_{13}C_{23} - C_{12}C_{33}\right)}{\left(C_{11}C_{22}C_{33} + 2C_{12}C_{13}C_{23} - C_{11}C_{23}^2 - C_{22}C_{13}^2 - C_{33}C_{12}^2\right)}, \quad 2.68$$

$$S_{13} = \frac{\left(C_{12}C_{23} - C_{22}C_{13}\right)}{C_{11}C_{22}C_{33} + 2C_{12}C_{13}C_{23} - C_{11}C_{23}^2 - C_{22}C_{13}^2 - C_{33}C_{12}^2}, \quad 2.69$$

$$S_{22} = \frac{\left(C_{11}C_{33} - C_{13}^2\right)}{\left(C_{11}C_{22}C_{33} + 2C_{12}C_{13}C_{23} - C_{11}C_{23}^2 - C_{22}C_{13}^2 - C_{33}C_{12}^2\right)}, \quad 2.70$$

$$S_{23} = \frac{\left(C_{12}C_{13} - C_{11}C_{23}\right)}{\left(C_{11}C_{22}C_{33} + 2C_{12}C_{13}C_{23} - C_{11}C_{23}^2 - C_{22}C_{13}^2 - C_{33}C_{12}^2\right)}, \quad 2.71$$

$$S_{33} = \frac{\left(C_{11}C_{22} - C_{12}^2\right)}{\left(C_{11}C_{22}C_{33} + 2C_{12}C\ C_{23} - C_{11}C_{23}^2 - C_{22}C_{13}^2 - C_{33}C_{12}^2\right)}, \qquad 2.72$$

$$S_{44} = \frac{1}{C_{44}}, \qquad 2.73$$

$$S_{55} = \frac{1}{C_{55}}, \qquad 2.74$$

and ,

$$S_{66} = \frac{1}{C_{66}}. \qquad 2.75$$

Then, we can obtain other mechanical properties for orthorhombic systems such as Poisson coefficient, compressibility and Lamé constants using the following equations [163];

$$\upsilon_X = \frac{1}{2}\left[\frac{B_X - \left(2\diagup 3\right)G_X}{B_X + \left(1\diagup 3\right)G_X}\right], \qquad 2.76$$

$$\mu_X = \frac{E_X}{\left[2\left(1+\upsilon_X\right)\right]}, \qquad 2.77$$

$$\lambda_X = \frac{\lambda_X E_X}{\left[\left(1+\upsilon_X\right)\left(1-2\upsilon_X\right)\right]}. \qquad 2.78$$

For orthorhombic crystal, the mechanical stability conditions are given by [164];

$C_{11} + C_{12} + C_{33} + 2C_{12} + 2C_{13} + 2C_{23} > 0$, $C_{22} + C_{33} - 2C_{13} > 0$, $C_{11} > 0$, $C_{22} > 0$, $C_{33} > 0$, $C_{44} > 0$, $C_{55} > 0$, $C_{66} > 0$.

The anisotropy arises from shear anisotropy as well as from the anisotropy of linear bulk modulus. The shear anisotropy factors for orthorhombic systems are given as follows:

$A_1 = \frac{4C_{44}}{(C_{11} + C_{33} + 2C_{13})}$ For {100} shear planes in $\langle 010 \rangle$ and $\langle 011 \rangle$ directions,

$A_2 = \frac{4C_{55}}{(C_{22} + C_{33} - 2C_{23})}$ for the {010} shear planes in $\langle 001 \rangle$ and $\langle 101 \rangle$ directions, and

$A_3 = \frac{4C_{66}}{(C_{11} + C_{22} - 2C_{12})}$ for the {001} shear planes in $\langle 010 \rangle$ and $\langle 110 \rangle$ directions [162].

Moreover, Chung and Buessem introduced a more comprehensive concept of measuring elastic anisotropy where the percentage anisotropy in compressibility and shear is defined as [165]:

$A_B = \frac{B_V - B_R}{B_V + B_R}$ and $A_G = \frac{G_V - G_R}{G_V + G_R}$, respectively.

where, *B* and *G* are the bulk and shear modulus, whereas subscripts *V* and *G* represents the Voigt and Reuss bounds. For these two expressions, a value of 0 % represents elastic isotropy and a value of 100 % is the largest possible anisotropy.

Quartz crystals possess trigonal symmetry and have six independent elastic constants; namely $C_{11}, C_{12}, C_{13}, C_{14}, C_{33}$ and C_{44}. C_{66} is a dependent elastic constant given by $\frac{1}{2}(C_{11} - C_{12})$. Moreover, Ledbetter and Kim described the most troublesome elastic constant C_{14} as the order parameter for beta-alpha phase transformation in their unpublished work [166]. This elastic constant complicates the mathematical analysis for relating macroscopic-vibration resonance frequencies. However, the condition C_{14} =0 leads to a rise in symmetry to hexagonal and five independent elastic constants. The Born criterions for trigonal systems are given by [167];

$$B_1 = C_{11} - |C_{12}| > 0, \tag{2.76}$$

$$B_2 = (C_{11} + C_{12})C_{33} - 2C_{12}^2 = 2((C_{11} - C_{66})C_{33} - C_{13}^2 > 0, \tag{2.77}$$

$$B_3 = (C_{11} - C_{12})C_{44} - 2C_{14}^2 = 2(C_{66}C_{44} - C_{14}^2) > 0. \tag{2.78}$$

No acoustic mode can produce the strain required by the criterion B_2. On the other hand, B_3 is associated with two different eigenvalues corresponding to different acoustic modes. A decrease of the B_3 value under compression denotes the existence of a mechanical instability correlated with the presence of a soft acoustic shear mode in the phonon spectrum at the Γ point of the Brillouin zone [168, 169]. This phenomenon is known as "rigidity catastrophe". The criterion B_1 expresses that the sample volume cannot collapse when compressed and the bulk modulus is given as follows [167];

$$B_0 = \frac{C_{33}(C_{11} + C_{12}) - 2C_{13}^2}{C_{11} + C_{12} + 2C_{33} - 4C_{13}} = \frac{B_1}{C_{11} + C_{12} + 2C_{33} - 4C_{13}}. \tag{2.79}$$

Monoclinic crystal systems show large number (thirteen) of independent elastic constants, $(C_{11}, C_{12}, C_{13}, C_{15}, C_{22}, C_{23}, C_{25}, C_{33}, C_{35}, C_{44}, C_{46}, C_{55}, C_{66})$. The general resultant elastic moduli for Voigt and Reuss approaches are given as follows [170];

$$B_V = \frac{1}{9}(C_{11} + C_{22} + C_{33}) + \frac{2}{9}(C12 + C_{23} + C_{13}), \tag{2.80}$$

$$G_V = \frac{1}{15}(C_{11} + C_{22} + C_{33}) - \frac{1}{15}(C_{12} + C_{23} + C_{13}) + \frac{1}{5}(C_{44} + C_{55} + C_{66}), \tag{2.81}$$

$$B_R = [(S_{11} + S_{22} + S_{33}) + 2(S_{12} + S_{23} + S_{13})]^{-1}, \tag{2.82}$$

$$G_R = \left[\frac{4}{15}(S_{11} + S_{22} + S_{33}) - \frac{4}{15}(S_{12} + S_{23} + S_{13}) + \frac{1}{5}(S_{44} + S_{55} + S_{66})\right]^{-1}. \tag{2.83}$$

The Hill approach is approximated as the average of the Voigt and Reuss, i.e.

$B_H = \frac{B_R + B_V}{2}$ and $G_H = \frac{G_R + G_V}{2}$ for bulk and shear, respectively.

The Young's modulus, E and Poisson's, υ ratio can be calculated as follows [170]:

$$E = \frac{9GB}{3B + G},\ \upsilon_x = \frac{3B_x - 2G_x}{2(3B_x + G_x)}.$$

A monoclinic phase is considered stable if the following mechanical stability criteria are satisfied [171];

$$C_{11} > 0, C_{22} > 0, C_{33} > 0, C_{44} > 0, C_{55} > 0, C_{66} > 0, \left(C_{35}C_{55} - C_{35}^2\right) > 0,$$

$$\left(C_{44}C_{66} - C_{46}^2\right) > 0, \left[C_{11} + C_{22} + C_{33} + 2\left(C_{12} + C_{13} + C_{23}\right)\right] > 0,$$

$$\left(C_{22} + C_{33} - 2C_{23}\right) > 0, \quad \left[C_{22}(C_{33}C_{55} - C_{35}^2) + 2C_{23}C_{25}C_{35} - C_{23}^2C_{55} - C_{25}^2C_{33}\right] > 0,$$

$$\{\ 2\left[C_{15}C_{25}\left(C_{33}C_{12} - C_{13}C_{23}\right) + C_{15}C_{35}\left(C_{22}C_{13} - C_{12}C_{23}\right) + C_{25}C_{35}\left(C_{11}C_{23} - C_{12}C_{13}\right)\right] -$$

$$\left[C_{15}^2\left(C_{22}C_{33} - C_{23}^2\right) + C_{25}^2\left(C_{11}C_{33} - C_{13}^2\right) + C_{35}^2\left(C_{11}C_{22} - C_{12}^2\right) + C_{55}g\right]\ \} > 0$$

where $g = C_{11}C_{22}C_{33} - C_{11}C_{23}^2 - C_{22}C_{13}^2 - C_{33}C_{12}^2 + 2C_{12}C_{13}C_{23}$.

In order to calculate the anisotropy of monoclinic phase, we make use of the universal anisotropy index proposed by Ranganathan and Ostoja-Starzewski [172]. This universal anisotropy index is applicable to crystals with any symmetry;

$$A^U = 5\left(\frac{G_V}{G_R}\right) + \frac{B_V}{B_R} - 6. \qquad 2.84$$

The universal anisotropy index is equal or greater than zero. For locally isotropic single crystals A^U is indistinguishably zero; any deviation from zero defines the extent of anisotropy and accounts for both the shear and the bulk contributions unlike all other existing anisotropy measures. Thus, A^U represents a universal measure to quantify the single crystal elastic anisotropy. The different in values of Voigt and Reuss approaches result in deviation of the universal elastic anisotropy index from zero.

Lastly, the tetragonal crystals have six independent elastic constants $(C_{11}, C_{12}, C_{13}, C_{33}, C_{44,} C_{66})$ [110, 166]. The corresponding elastic moduli derived from these elastic constants are;

$$B = \frac{1}{9}(2C_{11} + C_{33} + 4C_{13} + 2C_{12}), \quad 2.85$$

$$G = \frac{1}{15}(2C_{11} + C_{33} - C_{12} - 2C_{13} + 6C_{44} + 3C_{66}), \quad 2.86$$

$$E = C_{33} - 2\nu C_{13}, \quad 2.87$$

$$\nu = \frac{C_{13}}{C_{11} + C_{12}}. \quad 2.88$$

While the anisotropy factors are given by [162];

$A_1 = \frac{4C_{44}}{C_{11} + C_{33} - 2C_{13}}$. along {100} and

$A_2 = \frac{2C_{66}}{C_{11} - C_{12}}$ along {001} plane

The corresponding necessary conditions for mechanical stability criterion are [93]:

$C_{44} > 0$, $C_{66} > 0$, $C_{11} > 0$, $C_{33} > 0$, $C_{11} - C_{12} > 0$, $(C_{11} + C_{33} - 2C_{13}) > 0$,

$(2C_{11} + C_{33} + 2C_{12} + 4C_{13}) > 0$.

Chapter 3

Structural and Electronic Properties of MPO_4 Polymorphs

In this chapter, we present first-principles DFT+*U* results performed on five polymorphs of MPO_4 (M=Fe, Co and Mn). Structural and thermodynamic properties, such as equilibrium lattice constants and heats of formation will be evaluated and discussed in details. Furthermore, the electronic properties will also be analysed and discussed, in particular the electronic density of states (DOS). The effect of pressure on structural and electronic density of states will be determined at different pressures, from 0 GPa to 10 GPa. We will also correlate the equilibrium cell volume and heats of formation to mimic the stability trend.

The lattice constants and heats of formation calculations play an important role in determining the structural stability of the crystal. These are determined by performing structural optimization allowing lattice and cell volume to change. Structural optimization calculation is performed to achieve the minimum total energy or ground-state before any properties can be calculated. The calculation of total energy, density of states and pressure dependence are performed using the VASP code, which is discussed in details in chapter 2. In the next sections, we present the lattice constants, heats of formation and electronic DOS of five polymorphs of MPO_4 with different space groups, namely; $P3_121$, *Pnma*, *Pbca*, $P2_1/c$ and *Cmcm*, beginning with the convergence parameters.

3.1 Convergence of Energy Cut-off and k-points

3.1.1 Cut-off Energy

In order to determine the appropriate cut-off energy, single point energy calculations were performed for different kinetic energy cut-offs at fixed 4x6x6 *k*-mesh within GGA-PBE using VASP code for the heterosite $FePO_4$ (space group *Pnma*). In Figure 3-1 we show the curve of total energy per atom against cut-off energy for *Pnma*-$FePO_4$. The cut-off energy of 500 eV was chosen, since the energy gave a constant slope (zero slopes) at that point [173].

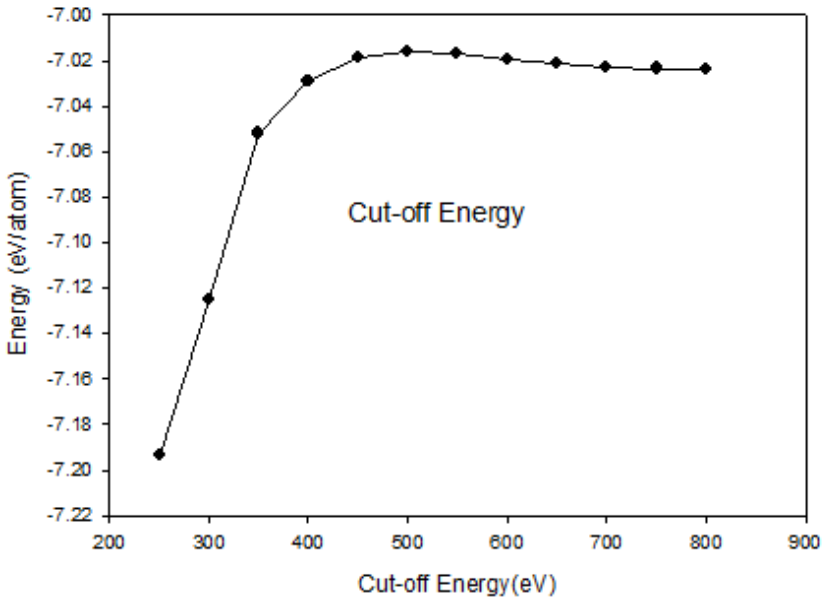

Figure 3-1 Total energy per atom versus energy cut-off for *Pnma*-$FePO_4$.

3.1.2 k-points

In this section, we show the convergence of the total energies with respect to the *k*–point sampling set size, as illustrated in Figure 3-2.

We have carried out total energy calculation at fixed cut-off energy of 500 eV (as determined in section 3.1.1) for *Pnma*-$FePO_4$ structure. The total energy with respect to the number of *k*-points was considered converged when the energy change per atom (between two consecutive points) was within 1 meV per atom. The k-point mesh of 4x6x6 was chosen for *Pnma* $FePO_4$, since we found that the structure has already converged at 4x6x6 and that similar energies are obtained at large k-mesh, however the calculations are time converging. As such the least converged k-mesh of 4x6x6 is sufficient to converge the total energy of the $FePO_4$ polymorphs. The cut-off energy of 500 eV and k-point mesh of 4x6x6 will be applied to the MPO_4 and Li/$NaMPO_4$ polymorphs, and the equivalent amount of k-point mesh of 6x6x6 for *Cmcm* and $P2_1/c$ symmetries.

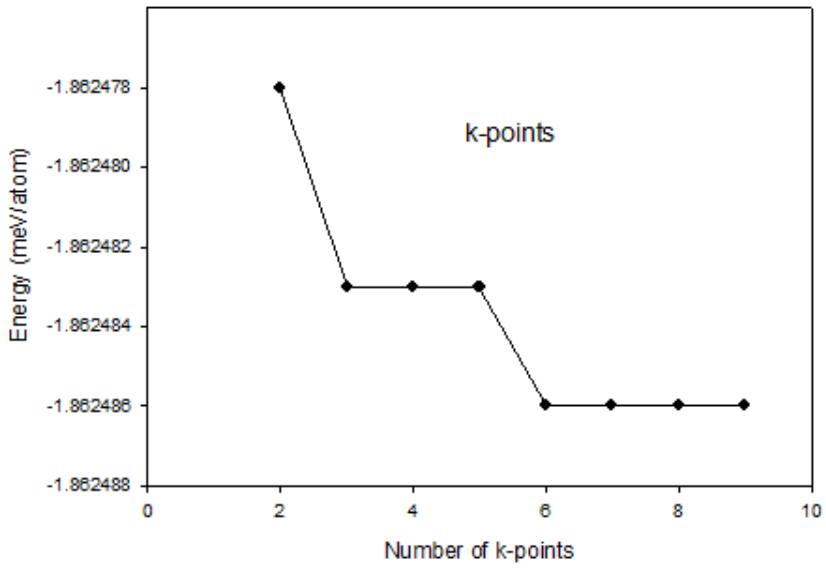

Figure 3-2 Total energy (meV/atom) versus number of k-points for *Pnma*-$FePO_4$.

3.2 Structural and Thermodynamic Properties

In order to determine the equilibrium structural properties, we performed geometry optimisation calculations within the GGA-PBE, with Hubbard *U* correction (*U*=5.5 eV) using cut-off energy of 500 eV. The equilibrium lattice constants were determined from the relaxed structures. The optimised atomic coordinates corresponding to the lattice parameters calculated with the VASP code for the LDA+*U* functional are listed in appendix A, tables 7-1 to 7-33. The experimental or previous results are also listed. We note that our calculated coordinates are in good agreement with the experimental and previous measurements within ±0.008 difference in fractional units, except for *Pnma*-$MnPO_4$ and few of the O positions in the monoclinic and orthorhombic structures. Our calculated differences are in good agreement with the results found by Tang *et a*l [17]. The differences in fractional coordinates suggest that the modelling strategy is robust and able to reproduce real systems. Moreover, the differences are within the experimental uncertainty as confirmed by also comparing coordinates for the olivine structure determined by X-ray [174] and neutron [24] diffraction.

3.2.1 $FePO_4$ Polymorphs

Table 3-1 lists the calculated and experimental lattice parameters, cell volume and heats of formation for the optimised five $FePO_4$ polymorphs. It can be clearly seen that our DFT+*U* calculations overestimate the experimental values for berlinite ($P3_121$), monoclinic ($P2_1/c$) and orthorhombic (*Pbca*) phases, while they underestimate for the heterosite (*Pnma*) and high pressure (*Cmcm*) phases. We note that the trigonal berlinite $FePO_4$ polymorph gave lattice parameters that are in good agreement to the

experimental data. The calculated lattice parameters (a=b=5.11 Å; c=11.38 Å) are in good agreement to the experimental results (a=5.12 Å; c=11.33 Å) [175, 176]. We also note that the calculated volume (257.23 Å^3) is well predicted and compares well to the experimental value (257.00 Å^3), to within 0.10 %, which is accepted for DFT for transition metal phosphates [9, 177, 178]. It was also noted that the trigonal berlinite *P3$_1$21*-$FePO_4$ has the least volume size as compared to the other polymorphs. The orthorhombic $FePO_4$ polymorphs also give lattice parameters and cell volumes that correspond well with the experimental values. We note that, the heterosite *Pnma*-$FePO_4$ polymorph gave lattice parameters; a=9.88 Å, b=5.82 Å and c=4.82 Å, which correspond to the cell volume of 277.22 Å^3. The cell volume is in good agreement with the available experimental value of 281.30 Å^3, to within 2 % [41].

Furthermore, the lattice parameters a, b and c values are in good agreement with the results by Maxisch and Gerband [53] calculated by using a similar GGA+U approach to within 1%. On the other hand, the orthorhombic *Pbca*-$FePO_4$ polymorph also shows lattice parameters; a=8.78 Å, b=9.23 Å, c=9.54 Å corresponding to a cell volume of 773.31 Å^3. The calculated cell volume overestimates the experimental value by approximately 3 %, which is still accepted for DFT calculations [29]. We also note that the *Pbca*-$FePO_4$ polymorph has the largest volume size amongst the considered $FePO_4$ polymorphs. The orthorhombic *Cmcm*-$FePO_4$ polymorph also shows lattice parameters and cell volume that are in good agreement to the experimental values. We note that lattice parameters; a=5.32 Å, b=7.76 Å and c=6.52 Å correspond to a volume of 269.00 Å^3, showing good agreement to the previously reported calculated value of 269.70 Å^3 [179]. These parameters are also in good agreement with the available experimental data (a=5.24 Å; b=7.78 Å; c=6.33 Å and the volume is 257.55 Å^3) [30, 179].

Lastly, the monoclinic $P2_1/c$-$FePO_4$ shows calculated lattice parameters of (a=5.56 Å, b=7.49 Å, c=8.11 Å) and cell volume of 335.77 $Å^3$, which correspond well to the experimental values (5.48 Å, 7.48 Å, 8.05 Å) and 329.97 $Å^3$, respectively. We note that our calculated volume slightly overestimates the experimental by approximately 2 %, which is still within the admitted range of errors of the first-principles methods. Moreover, we note that $P2_1/c$-$FePO_4$ has second largest volume size, followed by *Pbca*-$FePO_4$. The volume size trend of $FePO_4$ polymorphs is summarised as follows:

$$Pbca > P2\_1/c > Pnma > Cmcm > P3_121$$

From the above discussion, it should be noted that the DFT+U calculation methods allow a correct prediction of the lattice parameters and cell volume to within 3 %, which is a typical DFT+U transition metal phosphates calculation [177, 178, 180].

Table 3-1 Calculated and experimental lattice parameters, cell volume and heats of formation of $FePO_4$ polymorphs in ambient pressure. The experimental values are given in parentheses.

Structure	Berlinite	Heterosite	Orthorhombic	Monoclinic	HP
Space group and number	$P3_121$ (152)	*Pnma* (62)	*Pbca* (61)	$P2_1/c$ (14)	*Cmcm* (63)
a (Å) *b* *c* V ($Å^3$)	5.11 (5.12)[a] 11.38 (11.33)[a] 257.23 (257.00)[a]	9.88 (9.93)[b] 5.82 (5.86)[b] 4.82 (4.84)[b] 277.22 (281.30)[b]	8.78 (9.17)[c] 9.23 (9.46)[c] 9.54 (8.68)[c] 773.31 (752.35)[c]	5.56 (5.48)[c] 7.49 (7.48)[c] 8.11 (8.05)[c] 335.77 (328.51)[c] β=96.20°	5.32 (5.23)d 7.76 (7.78)d 6.52 (6.64)d 269.00 (269.70)d
ΔH_f (kJ/mol)	-871.34	-856.51	-867.76	-870.27	-854.00

[a] [176] [b] [41] [c] [29] [d] [30]

The heats of formation (ΔH_f), which is the enthalpy change when one mole of a compound is formed from the elements in their stable states, is essential in determining structural stabilities of different crystal structures; the lower the heat

formation the more stable is the structure. The heats of formation are calculated by subtracting the elemental total energies from that of the compound; for example the heat of formation of $FePO_4$ is calculated as follows;

$$\Delta H_f\left(FePO_4\right) = \left[E - \left(E_{Fe} + E_P + 4E_O\right)\right]. \qquad 3.1$$

where N is the total number of atoms in the unit cell, E is the total energy of the compound $FePO_4$. E_{Fe}, E_P and E_O are the elemental total energies of Fe, P and O, respectively. The predicted ΔH_f values of $FePO_4$ polymorphs in ambient pressure are calculated and compared in table 3-1. Our DFT+*U* results show that the *P3₁21*-$FePO_4$ polymorph gives the lowest heat of formation of -871.34 kJ/mol, while *Cmcm*-$FePO_4$ gives the highest heat of formation of -854.00 kJ/mol. These heat of formation values suggest that the *P3₁21*-$FePO_4$ polymorph is most stable i.e. energetically favourable and *Cmcm*-$FePO_4$ is least stable, while *Pbca*-$FePO_4$, *P2₁/c*-$FePO_4$ and *Pnma*-$FePO_4$ are intermediately metastable, respectively. The ambient pressure stability trend of $FePO_4$ polymorphs can be summarised as follows:

$$P3_121 > P2\_1/c > Pbca > Pnma > Cmcm$$

This sequence of stability is in principle consistent and in agreement with the synthetic routes that are carried out to form specific polymorphs. The heterosite form (*Pnma*-$FePO_4$) is the fourth in stability, which is not surprising, since it can only be prepared by chemical delithiation of olivine-$LiFePO_4$ [173]. Chemical delithiation is a well-known soft-chemistry method to produce metastable phases which are not obtainable by other means.

In figure 3-3, we compare the lattice parameters cell volumes and densities for $FePO_4$ polymorphs at a pressure range of 0 to 10 GPa. We observe that as the pressure is

increased from 0 to 10 GPa, the lattice parameters and cell volumes decrease, thus the structure successively undergoes compressive deformation.

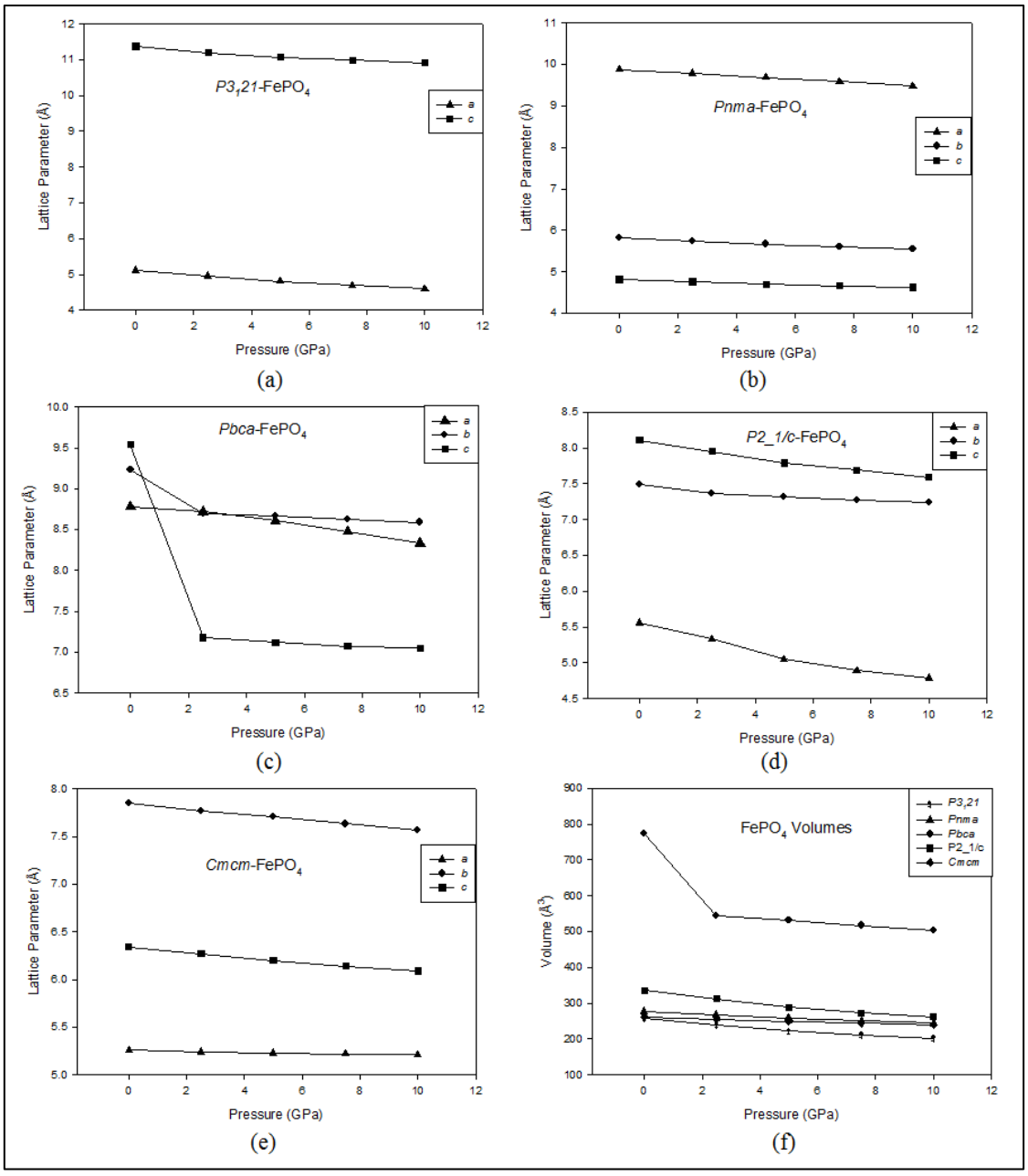

Figure 3-3 Plots of lattice constants versus pressure for $FePO_4$ polymorphs.

Interestingly, the rate of decrease in the lattice parameters and cell volumes with pressure is minimal and almost constant at all pressure intervals. However, the *b* and *c* parameters for *Pbca*-$FePO_4$ decrease abnormally at the pressure interval 0-2.5 GPa, suggesting weak stiffness along the *b* and *c*-axis. We note the change of 0.54 Å and

2.36 Å for *b* and *c*, respectively. Consequently, the cell volume decreases (figure 3-3(f)) most in this interval. It is also important to note that the volume contraction at the designated pressure range shows that the orthorhombic *Pbca*-$FePO_4$ and monoclinic *$P2_1/c$* -$FePO_4$ are more compressible over the trigonal *$P3_121$*-$FePO_4$, orthorhombic *Pnma*-$FePO_4$ and *Cmcm*-$FePO_4$, respectively.

In order to show the stability trend precisely, we have plotted the results in Figure 3-4. As indicated in discussion above, the trigonal *$P3_121$*-$FePO_4$ is thermodynamically more stable in ambient pressure and orthorhombic *Cmcm*-$FePO_4$ is least stable, while orthorhombic *Pbca*-$FePO_4$, monoclinic *$P2_1/c$*-$FePO_4$ and orthorhombic *Pnma*-$FePO_4$ are metastable, respectively. It is observed from Figure 3-4 that the trigonal *$P3_121$*-$FePO_4$ polymorph is most stable up to 4 GPa; while the orthorhombic *Cmcm*-$FePO_4$ polymorph becomes most thermodynamically stable above 4 GPa. This is in good agreement with the DFT+*U* calculation recorded by Arroyo y de Dompablo [173]. Furthermore, the order of decrease in heats of formation also agrees well with the prediction by Arroyo y de Dompablo *et al*. which suggests that *Pnma*-$FePO_4$ is metastable throughout the pressure range [173] and confirms that pressure favours metastable and high coordinated materials [181]. Orthorhombic *Pnma*-$FePO_4$, *Pbca*-$FePO_4$ and monoclinic *$P2_1/c$*-$FePO_4$ remain metastable in the whole pressure range. It can be observed that $FePO_4$ polymorphs have close heat of formation values in the region 3.8-4.5 GPa, making synthesis approaches in this range of pressure very appealing to seek for new $FePO_4$ polymorphs. The new stability trend in 10 GPa is as follows:

$$Cmcm > Pnma > Pbca > P2\_1/c > P3_121$$

Generally, we noted that highly correlated and metastable materials are energetically favourable in high pressures.

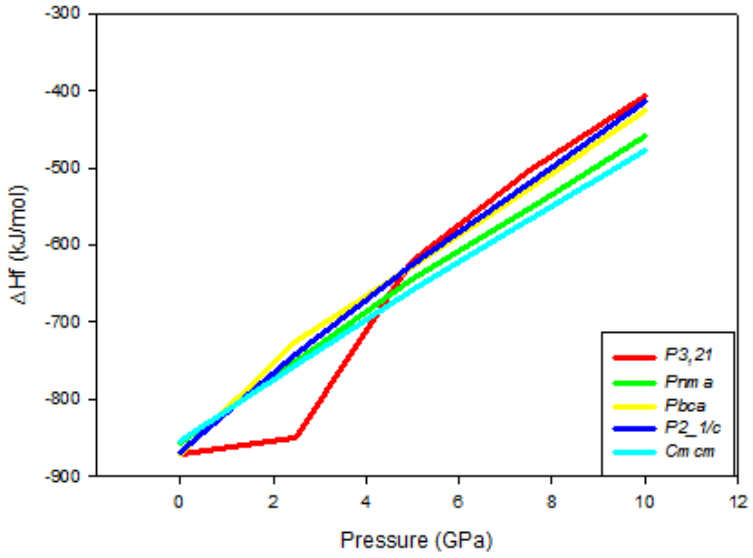

Figure 3-4 Calculated of heats of formation versus pressures for $FePO_4$ polymorphs.

3.2.2 $CoPO_4$ Polymorphs

In table 3-2, we list calculated lattice parameters, cell volumes and heats of formation for $CoPO_4$ polymorphs; the available experimental values are given in parentheses. In the similar manner to $FePO_4$, we discuss the equilibrium lattice constant and stability trend when Fe is substituted with Co. It is noted that the trigonal $P3_121$-$CoPO_4$ has lattice parameters; a=5.18 Å and c=11.19 Å, resulting in an equilibrium cell volume of 260.28 $Å^3$ in ambient pressure. To the best of our knowledge, there are no reported experimental data of $P3_121$-$CoPO_4$ polymorph, only the *Pnma*-$CoPO_4$ has been reported.

We see that our DFT+U calculations predict the cell parameters of the orthorhombic *Pnma*-$CoPO_4$ to within 5 % agreement with the experimental data [42], which is an acceptable approximation for density function theory in transition metal phosphates

[180, 177, 178]. The calculated lattice parameter *a* (9.65 Å) underestimates the experimental value (10.05 Å) by 4.08 %, while cell parameters *b* (5.93 Å), *c* (4.86 Å) and V (277.72 $Å^3$) overestimate experimental values; *b*=5.83 Å, *c*=4.70 Å and V=275.70 $Å^3$ by 1.57 %, 3.24 % and 0.69 %, respectively. Our calculations are also in good agreement with the experimental X-ray diffraction (XRD) and cyclic voltammetry values obtained by Amine *et al*. (*a*=10.09 Å; *b*=5.85 Å; *c*=4.72 Å; V=278.6 $Å^3$) [5].

Fully relaxed cell parameters for orthorhombic *Pbca*-$CoPO_4$, monoclinic *P2₁/c* - $CoPO_4$ and orthorhombic *Cmcm*-$CoPO_4$ are also listed in table 3-8. However, our DFT+*U* calculations gave reasonable cell parameters for *Pbca*-$CoPO_4$, *P2₁/c*-$CoPO_4$ and *Cmcm*-$CoPO_4$ which are compared to the $FePO_4$ polymorph. Lastly, we note that *P3₁21*-$CoPO_4$ (260.28 $Å^3$) and *Pbca*-$CoPO_4$ (769.49 $Å^3$) have smallest and largest equilibrium cell volume, while *P2₁/c*-$CoPO_4$ (341.31 $Å^3$), *Pnma*-$CoPO_4$ (277.72 $Å^3$) and *Cmcm*-$CoPO_4$ (263.01 $Å^3$), are intermediary, respectively. The volume size trend is similar to $FePO_4$ polymorphs and can be summarised as follows:

$$Pbca > P2\_1/c > Pnma > Cmcm > P3_121$$

Table 3-2 Calculated and experimental lattice parameters, cell volume and heats of formation of $CoPO_4$ polymorphs. The experimental values are given in parenthesis.

Space group	*P3₁21*	*Pnma*	*Pbca*	*P2₁/c*	*Cmcm*
a (Å)	5.18	9.65 (10.05)[a]	8.66	5.51	5.29
b		5.93 (5.83)[a]	9.46	7.62	7.77
c	11.19	4.86 (4.70)[a]	9.39	9.08	6.41
V ($Å^3$)	260.28	277.72 (275.70)[a]	769.49	341.31	263.01
				β=63.47°	
ΔH_f (kJ/mol)	-692.52	-680.59	-693.86	-688.63	-695.59

[a] [42]

The heats of formation, (ΔH_f) for $CoPO_4$ polymorphs were calculated to examine the stability of its polymorphs and are listed in table 3-2 above. Our DFT+*U* calculations show that $CoPO_4$ polymorphs yield larger heat of formation values compared to $FePO_4$ polymorphs. We note that *Cmcm*-$CoPO_4$ shows the least heat of formation value (-695.59 kJ/mol), suggesting that it is the most stable polymorph in ambient pressure. This is contrary to the prediction in $FePO_4$ polymorphs where *Cmcm*-$FePO_4$ was least stable in ambient pressure. Furthermore, it can be seen that *Pnma*-$CoPO_4$ is least stable with in ambient pressure, since it has lowest heat of formation value (-680.59 kJ/mol). Orthorhombic *Pbca*-$CoPO_4$ (-693.86 kJ/mol), trigonal *P3₁21*-$CoPO_4$ (-692.52 kJ/mol) and monoclinic *P2₁/c*-$CoPO_4$ (-688.63 kJ/mol) polymorphs are intermediately stable, respectively. It should be noted that the ΔH_f values are closer to each other, showing a strong competition of stability. The stability trend is as follows in ambient pressure:

$$Cmcm > Pbca > P3_121 > P2\_1/c > Pnma$$

Figure 3-5 presents the lattice parameters and cell volumes of $CoPO_4$ polymorphs against pressure. Similarly to $FePO_4$ polymorphs, the lattice constants general decrease with pressure for $CoPO_4$ polymorphs. However, there are anomalies observed for different polymorphs. We note that the *c* parameter increases in the intervals 2.5-5 GPa and 5-7.5 GPa for the *P3₁21*-$CoPO_4$ (figure 3-5 (a)), suggesting distortion at high pressures. For *Pnma*-$CoPO_4$ (figure 3-5(b)), we note that the lattice constants *b*, *c* and V expand in the pressure range 5-7.5 GPa and shrink considerably at 7.5-10 GPa, suggesting that similarly to *P3₁21*-$CoPO_4$, *Pnma*-$CoPO_4$ also undergo distortion in high pressures. Similar distortions are observed for the *Pbca*-$CoPO_4$ and *P2₁/c*-$CoPO_4$ polymorphs; *Pbca*-$CoPO_4$ polymorph shrinks substantially along the *c* in the pressure

range 0-2.5 GPa, while the *c* parameter for *P2₁/c*-$CoPO_4$ expands considerably at pressure interval 7.5-10 GPa. As a result, it is evident in figure 3-5(f) that *Pbca*-$CoPO_4$ is the most compressible polymorph.

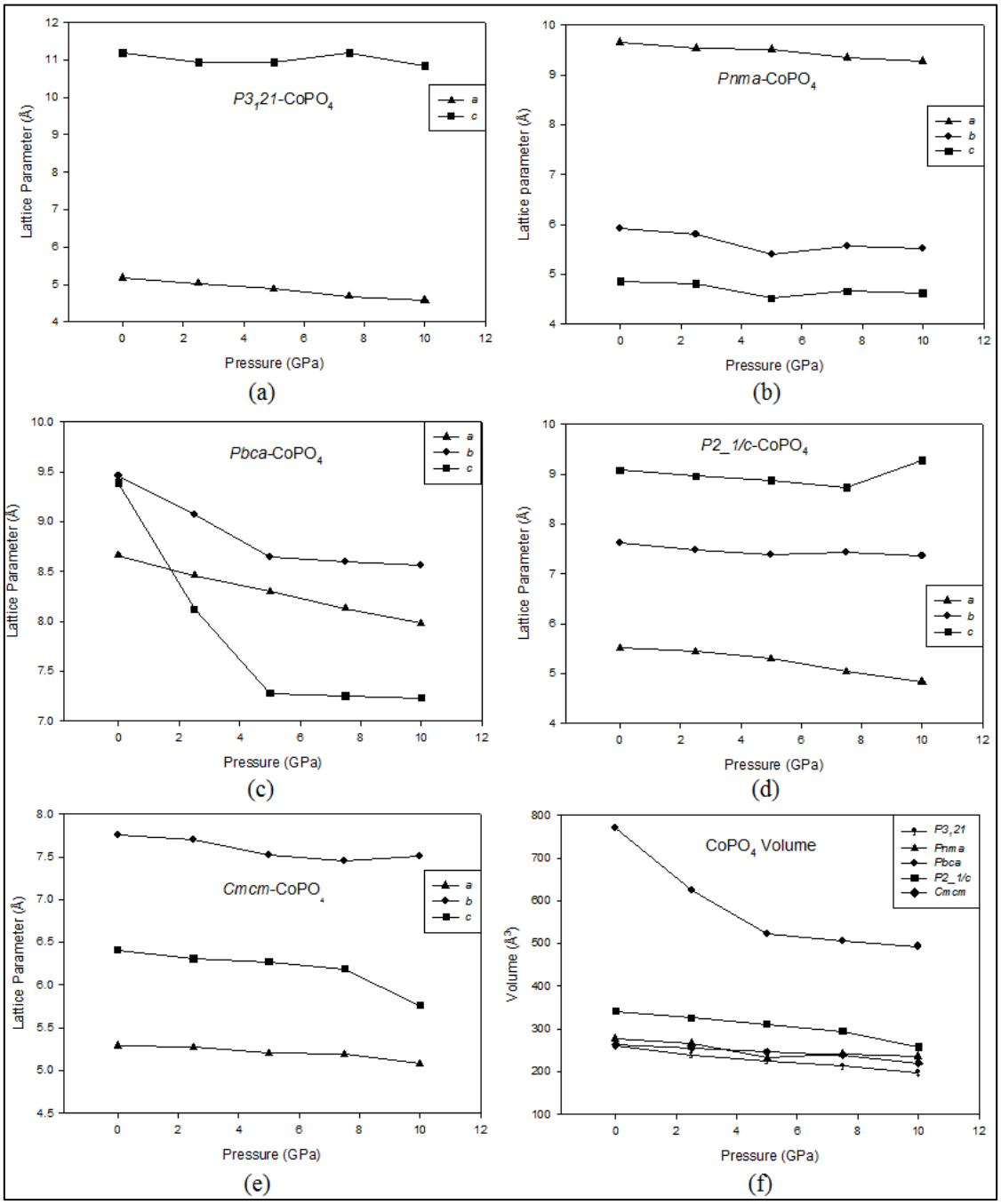

Figure 3-5 Plots of lattice constants versus pressure for $CoPO_4$ polymorphs.

Figure 3-6 shows the variation of heats of formation with pressure for $CoPO_4$ polymorphs. We note a remarkable shift on the stability trend in higher pressures. Firstly, we note that the *Pnma*-$CoPO_4$ becomes more stable compared to *P3₁21*-$CoPO_4$, *P2₁/c*-$CoPO_4$ and *Pbca*-$CoPO_4$, respectively at approximately 2 GPa. On the other hand, *P2₁/c*-$CoPO_4$ is favourable over *P3₁21*-$CoPO_4$ at around 9 GPa; hence, *P3₁21*-$CoPO_4$ is least stable in 10 GPa. Interestingly, we observe that *Cmcm*-$CoPO_4$ is energetically favourable throughout the pressure range. *P2₁/c*-$CoPO_4$ and *Pbca*-$CoPO_4$ generally remain metastable in the whole pressure range. The stability trend in 10 GPa is as follows:

$$Cmcm > Pnma > Pbca > P2\_1/c > P3_121$$

It can be observed that $CoPO_4$ polymorphs have close heats of formation values in the region 0-2 GPa; this observation rises the interest of synthesis approaches to find other $CoPO_4$ polymorphs in this pressure range. In general, we can emphasise that highly correlated orthorhombic systems are energetically favourable in high pressures.

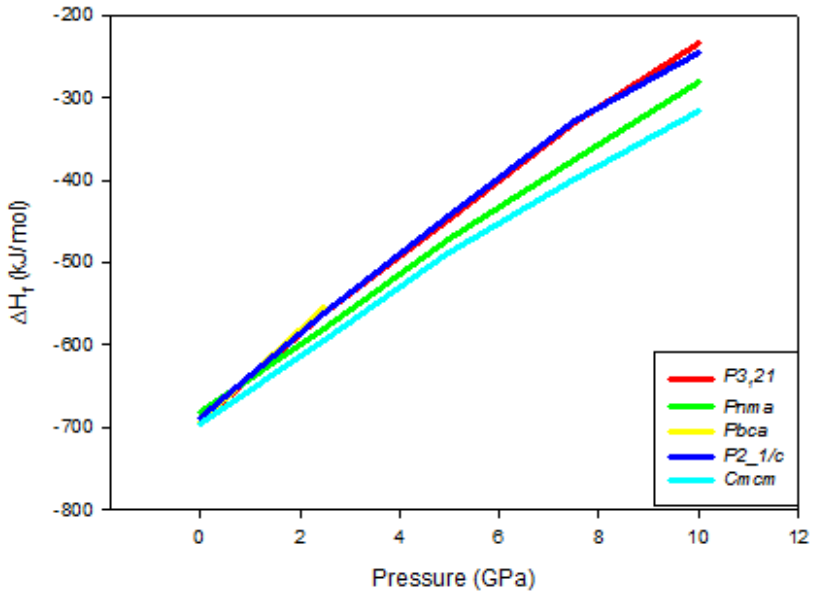

Figure 3-6 Calculated heats of formation versus pressure for $CoPO_4$ polymorphs.

3.2.3 $MnPO_4$ Polymorphs

Table 3-3 lists the equilibrium lattice parameters, cell volume and heats of formation of $MnPO_4$ polymorphs in ambient pressure. We note that the trigonal *P3₁21*-$MnPO_4$ polymorph gave lattice parameters *a*=5.07 Å and *c*=11.60 Å, corresponding to a cell volume of 258.34 $Å^3$. To the best of our knowledge, no experimental cell parameters have been recorded on this polymorph.

The orthorhombic *Pnma*-$MnPO_4$ gives lattice parameters; *a*=9.78 Å, *b*=6.01 Å and *c*=4.89 Å, which are in good agreement with previous theoretical values; *a*=9.92 Å, *b*=6.01 Å and *c*=4.93 Å [38] and; *a*=10.10 Å; *b*=6.21 Å; *c*=5.06 Å [42]. We note that our calculated cell volume (287.31 $Å^3$) is in agreement with the theoretical value (293.92 $Å^3$) to within 3 %, which is an acceptable comparison for typical DFT calculations [177, 178, 180]. Furthermore, *Pbca*-$MnPO_4$ gives lattice parameters; *a*=8.70 Å, *b*=8.89 Å, and *c*=8.59 Å corresponding to an equilibrium cell volume of 664.05 $Å^3$, which is the largest amongst $MnPO_4$ polymorphs. On the other hand, the monoclinic *P2₁/c*-$MnPO_4$ yields the subsequent largest equilibrium volume of 338.88 $Å^3$. Lastly, the orthorhombic *Cmcm*-$MnPO_4$ gives reasonable lattice parameters; *a*=5.32 Å, *b*=7.76 Å and *c*=6.52 Å corresponding to a volume of 269.06 $Å^3$. The equilibrium volume size trend of $MnPO_4$ polymorphs can be summarised as follows:

$$Pbca > P2\_1/c > Pnma > Cmcm > P3_121$$

The heats of formation are also presented in table 3-3. It is observed that *P3₁21*-$MnPO_4$ has the highest heat of formation value (-891.96 kJ/mol) value, suggesting that it is the least stable polymorph in ambient pressure.

Table 3-3 Calculated and experimental lattice parameters, cell volume and heats of formation of $MnPO_4$ polymorphs. The experimental values are given in parenthesis.

Space group	*$P3_121$*	*Pnma*	*Pbca*	*$P2_1/c$*	*Cmcm*
a (Å)	5.07	9.78 (9.65)	8.70	5.76	5.32
b		6.01 (5.62)	8.89	7.35	7.76
c	11.60	4.89 (4.78)	8.59	8.06	6.52
V ($Å^3$)	258.34	287.31 (272.96)	664.05	338.88	269.06
				β=98.17°	
ΔH_f (kJ/mol)	-891.96	-937.29	-901.55	-920.31	-933.51

[a] [38]

On the other hand, *Pnma*-$MnPO_4$ has the lowest value (-937.29 kJ/mol), indicating superiority of thermodynamic stability amongst $MnPO_4$ polymorphs. Furthermore, *Cmcm*-$MnPO_4$ (-933.51 kJ/mol), *$P2_1/c$*-$MnPO_4$ (-920.31 kJ/mol) and *Pbca*-$MnPO_4$ (-901.55 kJ/mol) are intermediately stable in ambient pressure. The thermodynamic stability trend is summarised below:

$$Pnma > Cmcm > P2\_1/c > Pbca > P3_121$$

The calculated lattice constants against pressure for $MnPO_4$ polymorphs are plotted in figure 3-7. Our results suggest that the *Pbca*-$MnPO_4$ (figure 3-7(c)) and *$P2_1/c$*-$MnPO_4$ (figure 3-7(d)) is highly susceptible to distortion under enormous pressure. We note an unsteady change in lattice parameters at different pressure intervals, especially along the *b* and *c*-axis. This suggests that the distortions will occur severely along the *b* and *c*-axis. On the other hand, the *$P3_121$*-MPO_4, *Pnma*-$MnPO_4$ and *Cmcm*-$MnPO_4$ show an expected decrease in lattice constants.

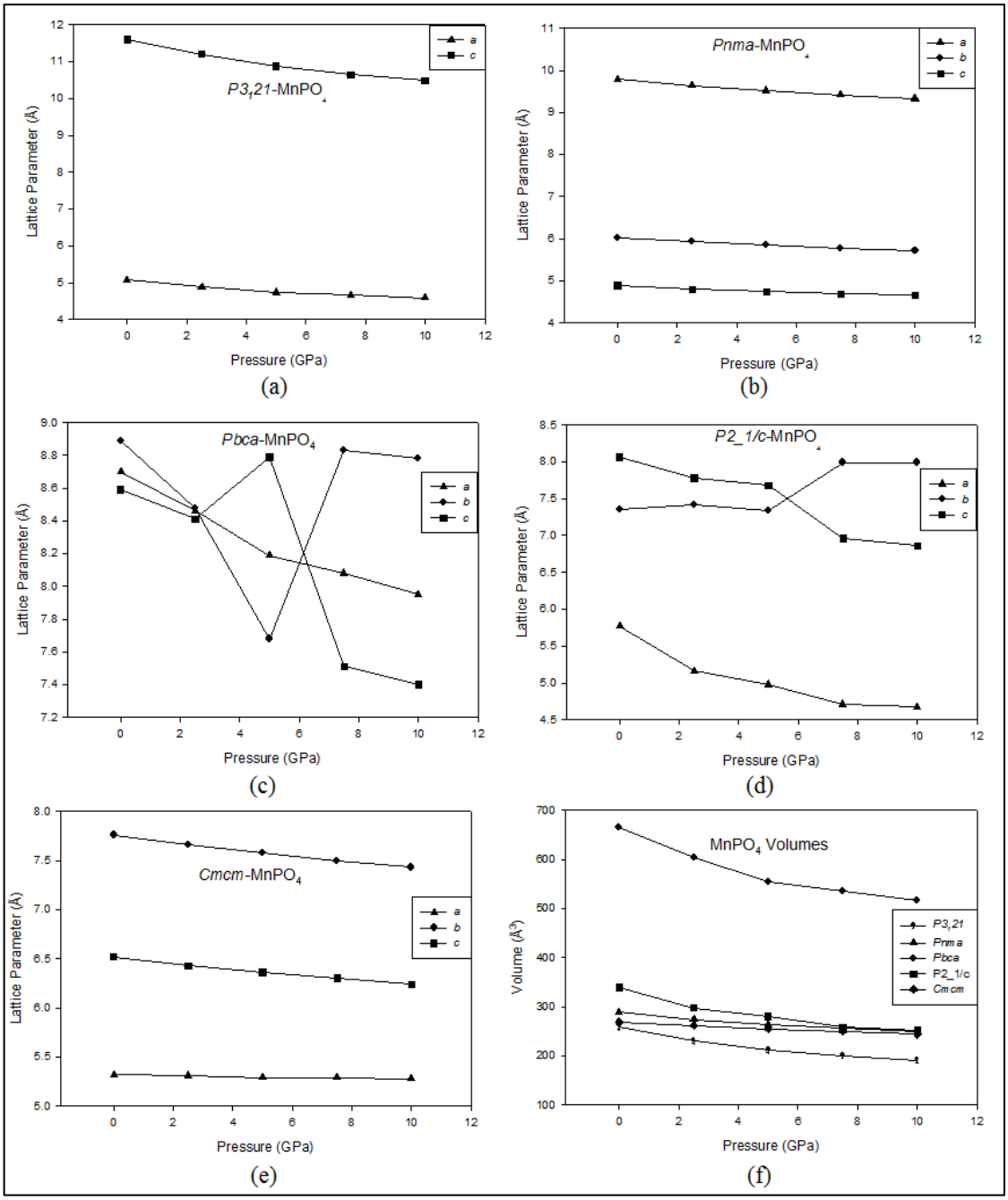

Figure 3-7 Plots of lattice constants versus pressure for $FePO_4$ polymorphs.

In figure 3-8, we present the pressure-heats of formation relationship for $MnPO_4$ polymorphs. We note that the thermodynamic stability trend is slightly altered in higher pressures. We found that *Pnma*-$MnPO_4$ is the most stable polymorph up to around 4.5 GPa; and in the pressures above 4.5 GPa, the *Cmcm*-$MnPO_4$ becomes the thermodynamically stable phase. However, *P3₁21*-$MnPO_4$ remains the least stable

polymorph, while $P2_1/c$-$MnPO_4$ and *Pbca*-$MnPO_4$ are metastable phases at the whole pressure range. The stability trend in 10 GPa is as follows:

$$Cmcm > Pnma > P2\_1/c > Pbca > P3_121$$

Similarly to $FePO_4$ and $CoPO_4$ structural polymorphs, we can deduce that orthorhombic systems are energetically favourable

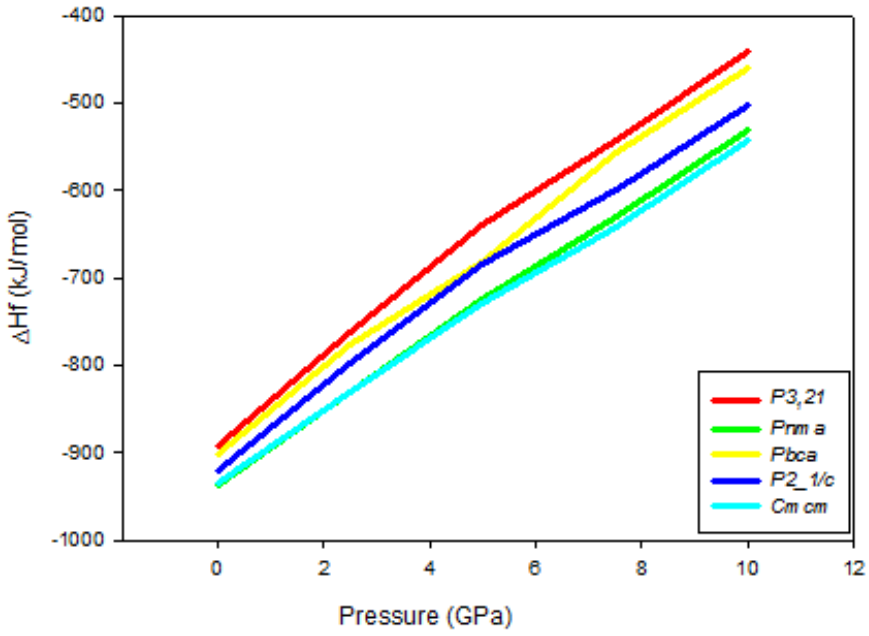

Figure 3-8 Calculated heats of formation versus pressure for $MnPO_4$ polymorphs.

3.3 Electronic Properties

In Figures 3-9 to 3-24, we show the total density of states (tDOS) and partial density of states (pDOS) of the MPO_4 polymorphs. The density of states calculations were computed using the spin polarised local denisty approximation with Hubbard corrections (LDA+*U*) in low (0 GPa) and high pressure (10 GPa) conditions, implying that the spin has been taken into consideration. The spin up states are displayed on the

positive scale while the lower spin states are seen on the negative scale of the DOS plot. The upper plots indicate total densities of states and lower plots show partial densities of states of M, P and O, respectively. The total contributions of all atoms in the structure are indicated by the tDOS, whilst the pDOS indicates the contribution of individual atoms.

The density of states spectrum for the olivine structure is consistent with recent x-ray spectroscopy measurements [182]. We note that the total and partial DOS are separated forming a band. The E_F is set at zero for all plots. The concept of Fermi level and energy band gaps are necessary to understand the stability, where the shift of the E_F with respect to the band gap plays an essential role in stability and change of coordination within the system. It can be noted that M *d*-states give a large contribution to the total density of states around the Fermi level, and minimal contribution from P and O states in all MPO_4 structural polymorphs.

3.3.1 DOS of $FePO_4$ Polymorphs

From Figure 3-9 to 3-13, it is apparent that the general form of density of states spectrum for $FePO_4$ polymorphs is uniform. It is also apparent that the hybridisation of Fe 3*d*↑ and O 2*p*↑ states predominates throughout their valence band spectra and is a distinguishable feature of all the $FePO_4$ polymorphs. The upper most states on the valence band are predominately of O 2*p* (spin up and down) and contributions from P sates, while the first states in the conduction band are basically of the Fe 3*d* spin down character. The insightful paper by Sham and Schlüter [117] has brought understanding

that an energy band gap calculated from the DFT eigenstates differs from the physical energy band gap by a self-energy correction.

Figure 3-9(a) and 3-9(b) show the total and partial density of states of the trigonal $P3_121$-$FePO_4$ in ambient (0 GPa) and high pressure (10 GPa). We note the presence of relatively wide band gaps of approximately 2.15 eV and 2.22 eV in ambient and high pressures, respectively. Tang *et al*. reported band gaps of 0.8 eV and 1.0 eV for the $P3_121$-$FePO_4$ structure in ambient pressure employing the pure LDA and GGA functionals, respectively [17]. These values are much smaller comapared to our prediction due to the use of Hubbard parammeter (*U*). Our observations are more consistent to the observed poor electrochemical activity of $P3_121$-$FePO_4$.

Moreover, previous studies have shown that DFT+*U* gives more accurate and wider band gaps for highly correlated 3*d* transition metal monoxides and phosphates over normal LDA and GGA [50, 81, 183]. The pressence of relatively wide band gaps suggests that $P3_121$-$FePO_4$ has relatively low electronic conductivity and insulator behaviour. On the other hand, the position of the Fermi level gives a clear characteristic of the material. We observe that the Fermi level lies close enough to a valence band edge that there may be a dilute number of thermally excited carriers residing near that band edge, further suggesting insulator behaviour. Moreover, we note that the 10 GPa pressure reduces the density of states, particularly the total DOS.

In the energy range ($-25 \le E \le 0eV$), the partial density of states associated with the Fe states are primarily of 3*d* character while the density of states associated with the P and O sites are primarily of 3*p* and 2*p* character, respectively. At around the Fermi level, electron population of Fe *d*-states on the valence and conduction bands dominates with the weak hybridyzation of P and O *p*-states. The total DOS peak

located at the energy value -18 eV reflect the hybridization between the O 2*s* and the P 3*p*-states. These observations show the majority spin states (↑) associated with the Fe sites separated from the minority Fe states (↓) throughout energy range. The lineshapes of partial density of states around the Fermi level are different, indicating a total difference in DOS and also suggesting weak hybridization of Fe, P and O orbital states in the total density of states. We also note the presence of spind-down Fe band in the conduction band at about 2 eV, with very minimal contribution from P and O.

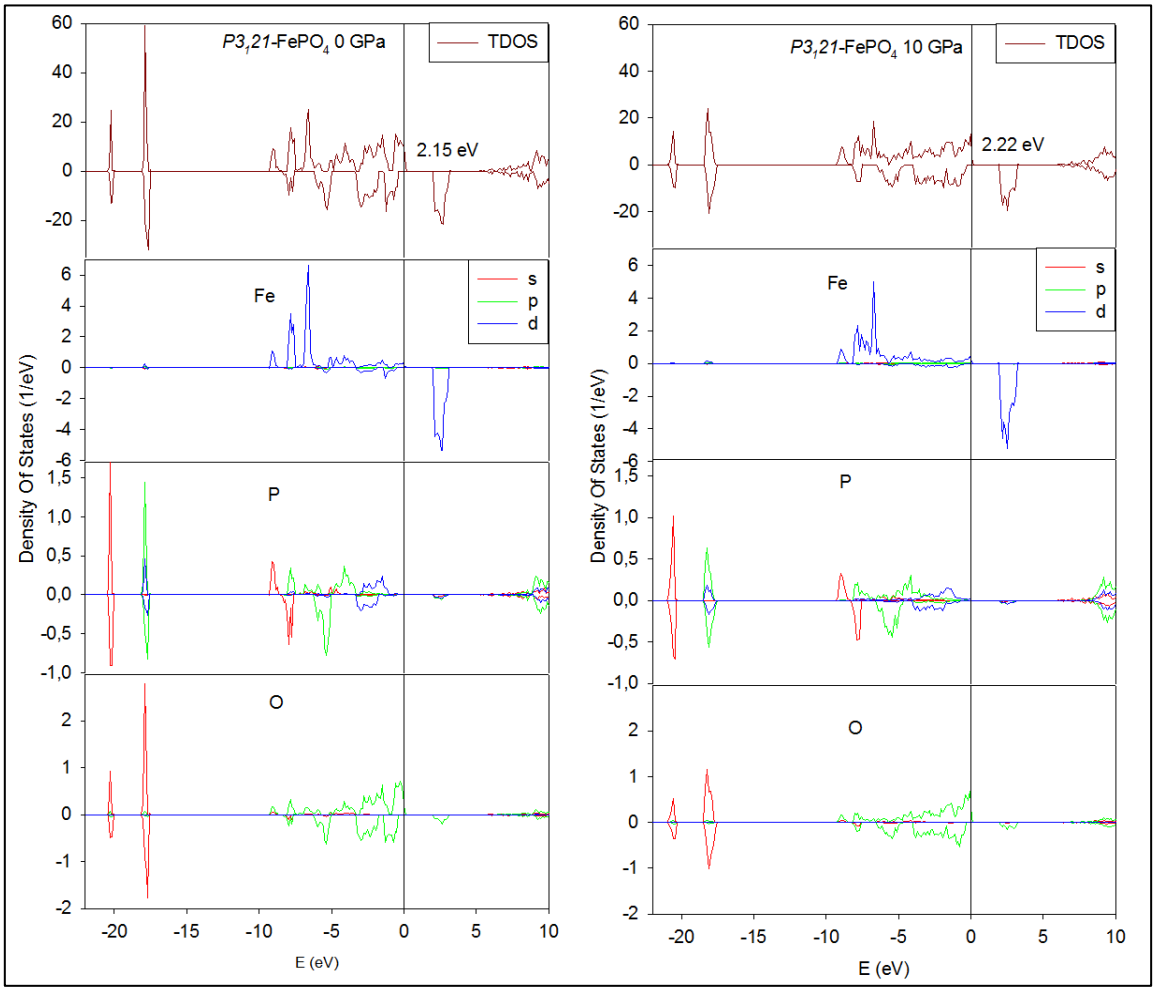

Figure 3-9 Total and partial DOS of $P3_121$-$FePO_4$ polymorph, in (a) 0 GPa and (b) 10 GPa. The Fermi level is taken as energy zero ($E-E_F=0$).

Total and partial DOS of the orthorhombic *Pnma*-$FePO_4$ polymorph in ambient and high pressures are shown in Figure 3-10(a) and 3-10(b), respectively. Similarly, to

P3₁21-$FePO_4$ polymorph, the *Pnma*-$FePO_4$ shows the majority spin states associated with the Fe states (↑) in the valence band separated from the minority Fe states (↓) in the conduction band throughout the energy range ($-10 \le 0 \le 5eV$). We note that the *Pnma*-$FePO_4$ also shows band gap. The total and partial densities of states show the Fermi level being located in the upper valence band displaying a very small E_g (↑↓) gap. The location of the Fermi level suggests that *Pnma*-$FePO_4$ also shows intrinsic insulator characteristic.

Our DFT+*U* calculations show that *Pnma*-$FePO_4$ polymorph has relatively wide band gap of about 1.81 eV in ambient pressure, which corresponds well with the results found by Zhou *et al*. [50] where the band gap was reported to be 1.90 eV. These two computational findings extremely overestimate the ferromagnetic value of 0.40 eV reported by Yamada *et al*. [8]. The total DOS shows peaks at about -22 eV and -18 eV, which emanate from the hybridisation of P 2*s* and O 3*s*; and P 3*p* and O 2*s* orbitals, respectively. We also note a strong contribution of P 3*d* and O 2*p* near the E_F. The DOS peak at about 3 eV in the conduction band is a contribution of Fe 3d (↓) orbitals. In 10 GPa, these DOS peaks become sharper, most notably at -18 eV and 3 eV, as much distribution is near the E_F, except that the peaks are slightly shifted towards the Fermi level.

An increase in pressure (10 GPa) does not perturb the octahedral coordination of the *Pnma*-$FePO_4$ polymorph. The Fermi level remains on the left of the band gap (valence band), suggesting that *Pnma*-$FePO_4$ polymorph maintains its intrinsic semiconducting behaviour; however the band gap is decreased to 1.53 eV. Moreover, the total and partial density of states, electron populations and hybridizations of states remain

relatively unchanged. This may imply that 10 GPa pressure does not enhance the overlap of atomic wavefunction in line with the theory [137].

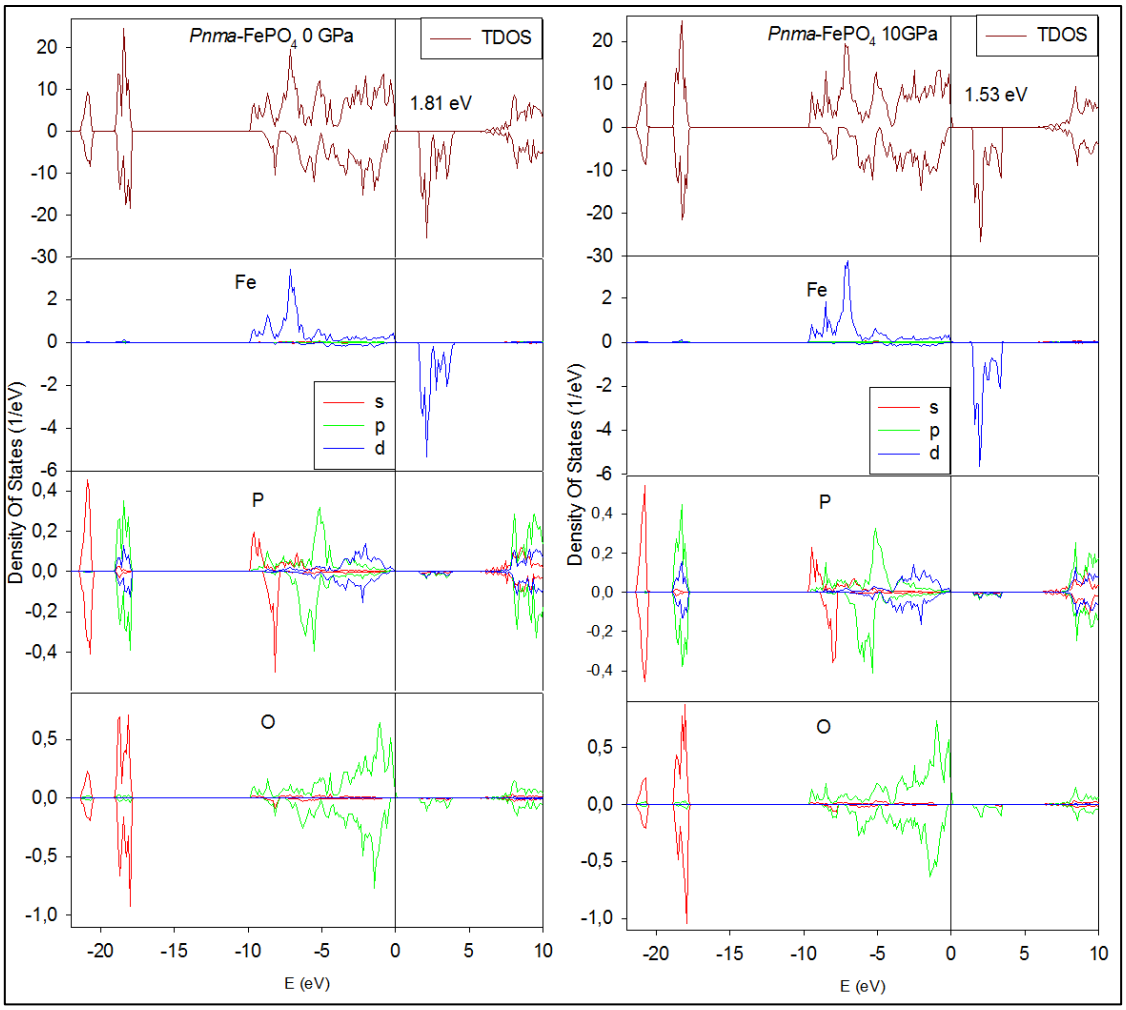

Figure 3-10 Total and partial DOS of *Pnma*-$FePO_4$ polymorph, in (a) 0 GPa and (b) 10 GPa. The Fermi level is taken as energy zero ($E-E_F=0$).

In Figure 3-11(a) and 3-11(b), we present the total and partial density of states of the orthorhombic *Pbca*-$FePO_4$ in ambient and high pressures, respectively. We note similar behaviour of DOS with the *P3₁21*-$FePO_4$ and *Pnma*-$FePO_4$; however, *Pbca*-$FePO_4$ shows semiconductor behaviour. The Fermi level is located on the edge of the upper valence band resulting to an energy band gap of 0.92 eV (Figure 3-8(a)). This energy band gap is narrower when compared to the band gaps of *P3₁21*-$FePO_4$ (2.15 eV) and *Pnma*-$FePO_4$ (1.81 eV) in ambient pressure. On the other hand, it can be

observed that the increase of pressure (10 GPa) reduces the magnitude intensity of DOS and the energy band gap to about 0.35 eV, suggesting enhancement in electronic activity.

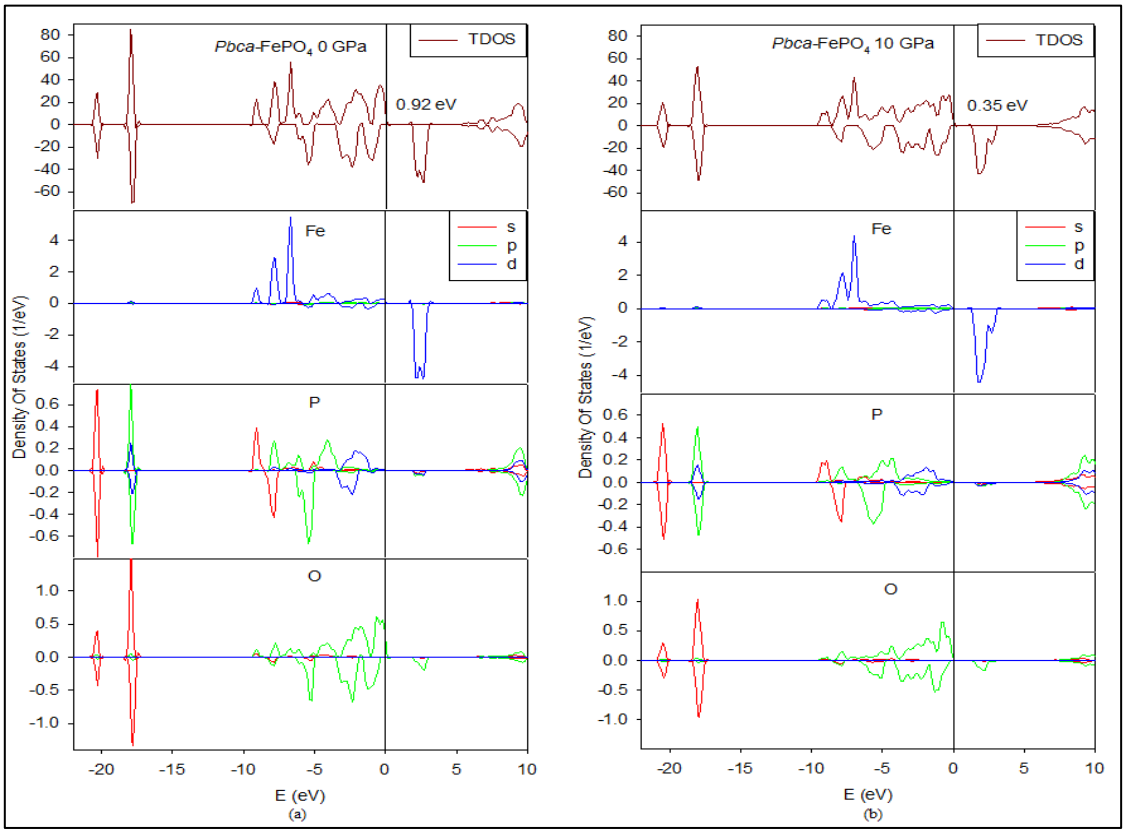

Figure 3-11 Total and partial DOS of *Pbca*-$FePO_4$ polymorph, in (a) 0 GPa and (b) 10 GPa. The Fermi level is taken as energy zero ($E-E_F=0$).

The total and partial densities of states for the monoclinic $P2_1/c$-$FePO_4$ polymorph are shown in Figure 3-12(a) and 3-12(b) in ambient and high pressures, respectively. Again, the trend of DOS is similar; however the structure display small energy band gaps of 0.70 eV and 0.84 eV in 0 GPa and 10 GPa, respectively. However, the Fermi level falls on the upper valence band states, suggesting that $P2_1/c$-$FePO_4$ is also a semiconductor. We also note that the increase in pressure to 10 GPa, increases the energy band gap slightly, making it slightly difficult for valence electrons to jump to the conduction band.

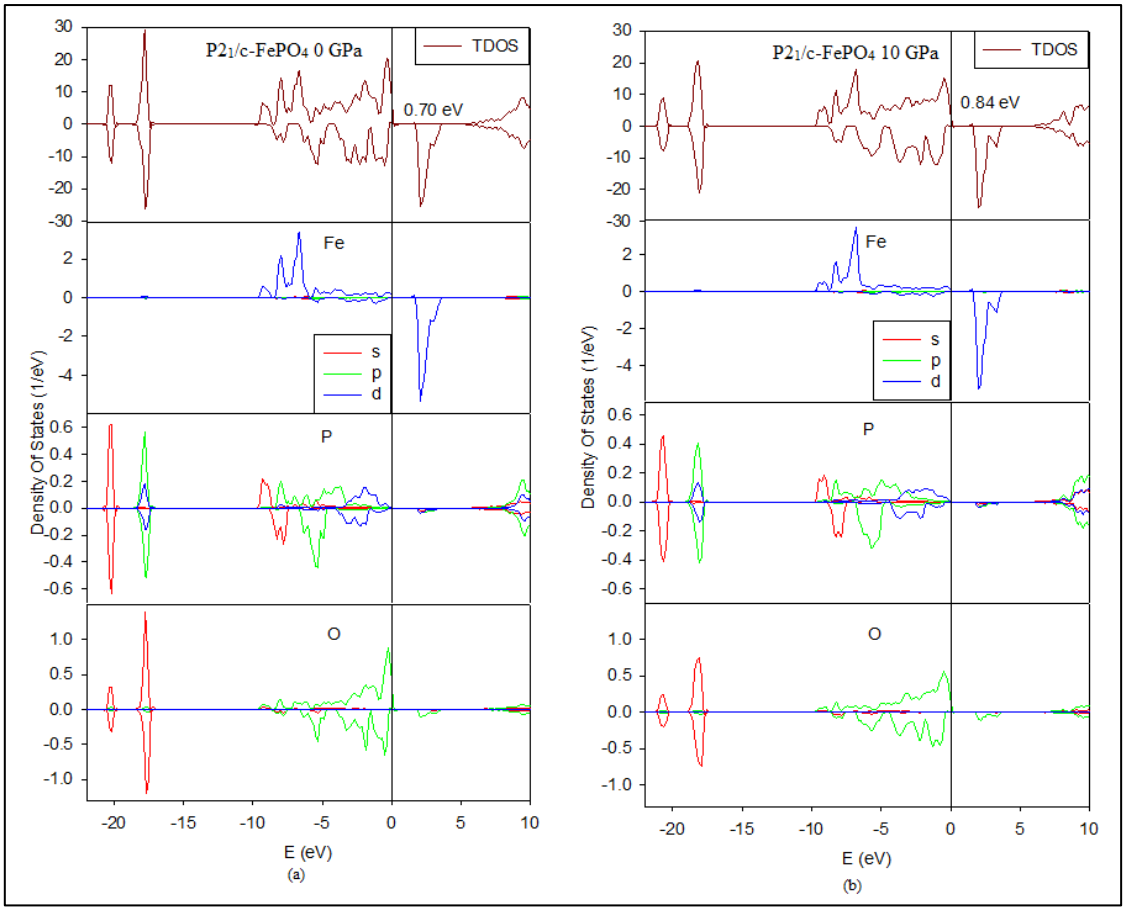

Figure 3-12 Total and partial DOS of $P2_1/c$-$FePO_4$ polymorph, in (a) 0 GPa and (b) 10 GPa. The Fermi level is taken as energy zero ($E-E_F=0$).

Figure 3-13 shows the total and partial density of states for the orthorhombic *Cmcm*-$FePO_4$ polymorph. The general form of *Cmcm*-$FePO_4$ density of states is comparable and similar to those of *Pnma*-$FePO_4$ as it shows a band gap. However, *Cmcm*-$FePO_4$ shows a slightly narrow band gap of 0.92 eV, suggesting semiconductor behaviour. The total and partial DOS of the *Cmcm*-$FePO_4$ polymorph shows the Fermi level on the left of the band gap. Our findings are contrary to the GGA results found by Tang *et al*. where *Cmcm*-$FePO_4$ was found to be clearly metallic with overlap of electrons from valence to conduction band [17]. However, our findings are in good agreement with the experimental results that suggests poor ionic conductivity and as such material to have poor electrochemical activity [8].

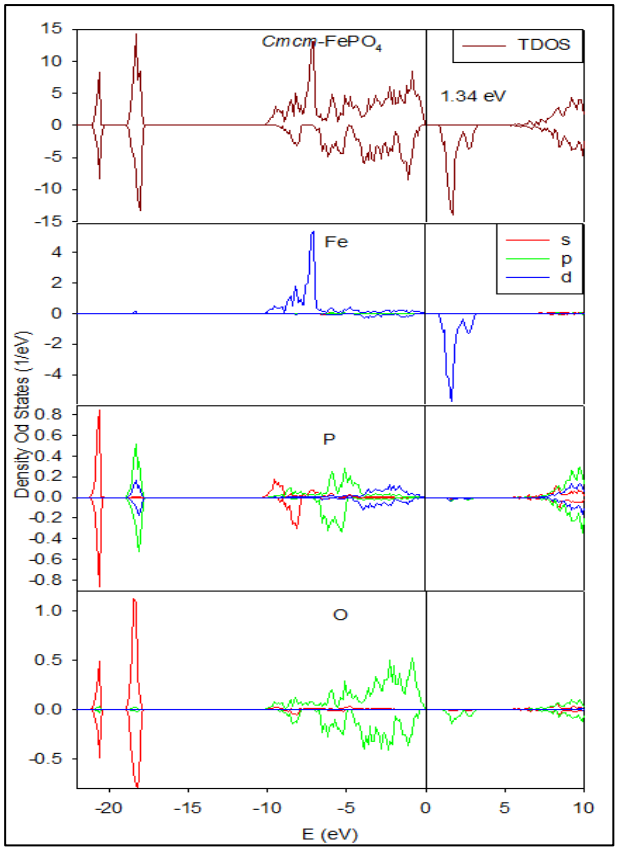

Figure 3-13 Total and partial DOS of *Cmcm*-$FePO_4$ polymorph. The Fermi level is taken as energy zero ($E-E_F=0$).

3.3.2 DOS of $CoPO_4$ Polymorphs

Figures 3-14 to 3-18 show the total and partial density of states for $CoPO_4$ polymorphs in ambient (0 GPa) and high pressure (10 GPa). There are some generic features that are common in all the densities of states of $CoPO_4$. In general, the shapes of the DOS's of $CoPO_4$ polymorphs are similar, as we observe that only spin-down (↓) electrons overlaps to the conduction band. In this energy range ($-25 \le 0 \le 10eV$), the partial densities of states associated with the Co sites are essentially of 3*d* character while the partial density of states associated with P and O are essentially of 3*p* and 2*p*, respectively. The main contribution to the valence band near the Fermi level is from

the *d*-states of Co with weak hybridisation of P and O states. We also note that the conduction band consists of the anti-bonding spin-down (↓) *d*-states of Co.

Figure 3-14(a) and 3-14(b) show the total and partial densities of states of the trigonal *P3₁21*-$CoPO_4$ polymorph in 0 GPa and 10 GPa, respectively. We observe the presence of relatively narrow energy band gap of 0.34 eV in 0 GPa. The application of 10 GPa pressure broadens the energy band gap to 0.59 eV. Similarly to *P3₁21*-$FePO_4$, 10 GPa pressure also reduces the density of states. The Fermi level falls on the left of the band gap (upper valence band). This material can be classified as a semiconductor due to the position of the Fermi level and relatively small band gaps.

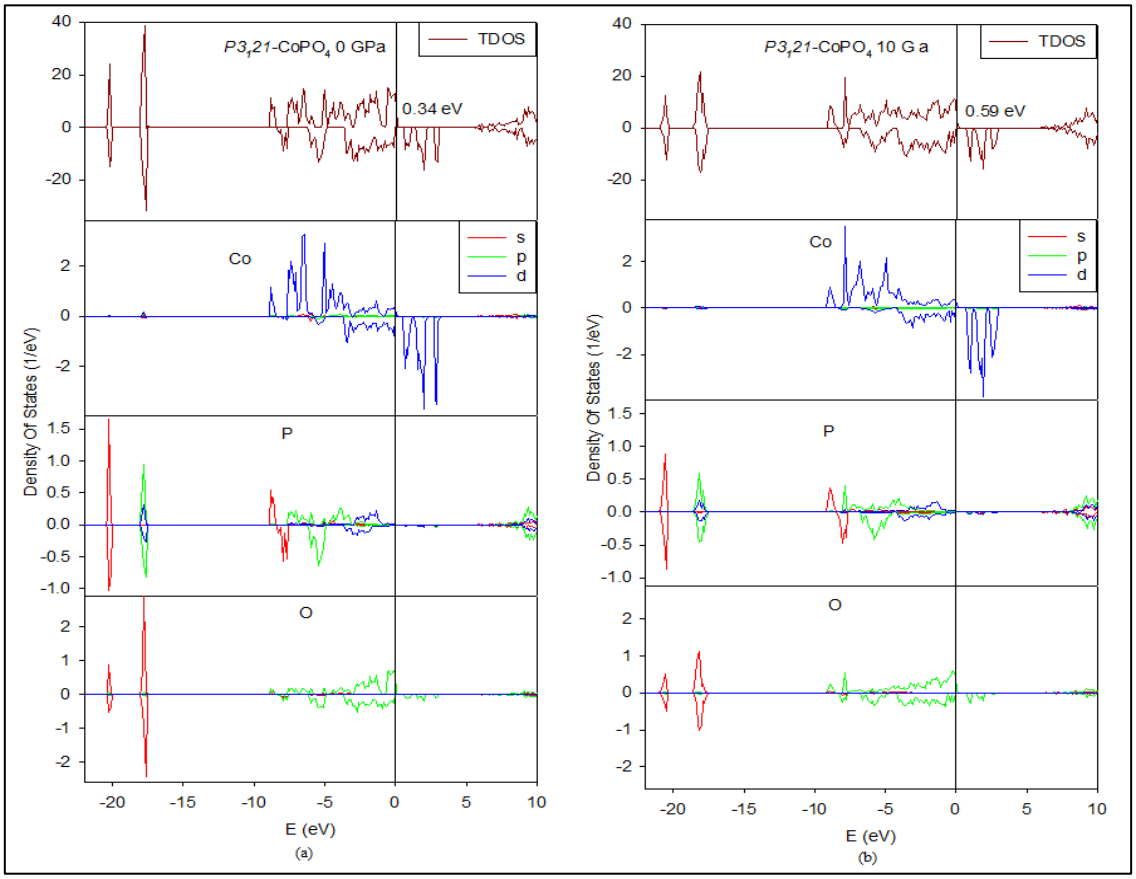

Figure 3-14 Total and partial DOS of *P3₁21*-$CoPO_4$ polymorph, in (a) 0 GPa and (b) 10 GPa. The Fermi level is taken as energy zero ($E-E_F=0$).

The total and partial densities of states of the orthorhombic *Pnma*-$CoPO_4$ in ambient and high pressures are presented in Figure 3-15(a) and 3-15(b). Similarly to other structural polymorphs, the results show systematic pattern, where the partial density of states associated with the Co site are primarily of 3*d* character while the partial density of states associated with the O and P sites are primarily of 2*p* character. We note the presence of relatively narrow energy band gaps of 0.83 eV and 0.71 eV in 0 GPa and 10 GPa, respectively suggesting semiconductor behaviour. Furthermore, the Fermi level is located on the edge of the valence band. In contrary to other structural polymorphs, 10 GPa pressure slightly increases the total density of states; mainly from the hybridisation of O 2*s* and P 2*p* states.

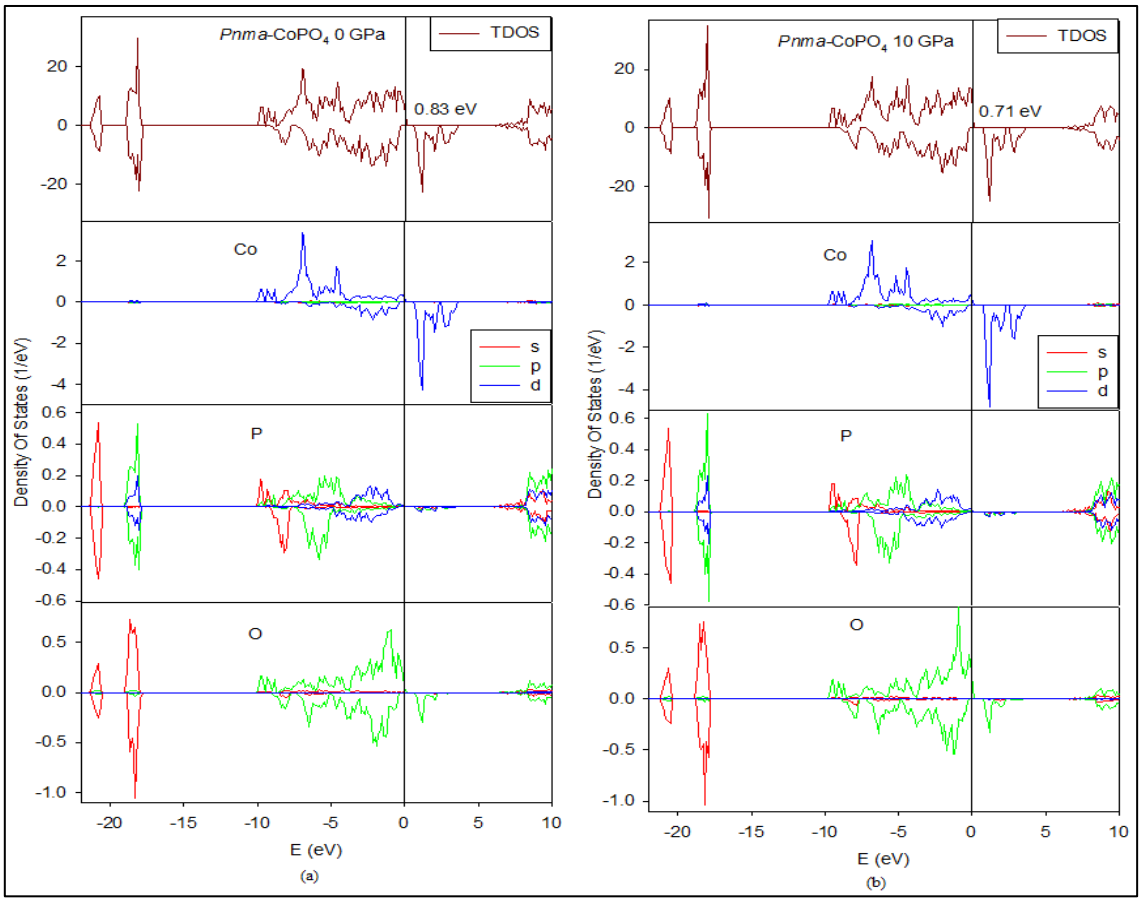

Figure 3-15 Total and partial DOS of *Pnma*-$CoPO_4$ polymorph, in (a) 0 GPa and (b) 10 GPa. The Fermi level is taken as energy zero ($E-E_F=0$).

In Figure 3-16, we present the total and partial density of states of *Pbca*-$CoPO_4$. Interestingly, we note that there exist no energy band gaps at both ambient (Figure 3-16(a)) and high pressure (Figure 3-16(b)), suggesting that valence band electrons are permissible to jump over to the conduction band; hence *Pbca*-$CoPO_4$ has good electrochemical conductivity. Furthermore, it can be noted that the Fermi level falls within the 3*d*-states, suggesting the metallic behaviour and good mechanical characteristics at both ambient and high pressures. The application of 10 GPa pressure reduces the total density of states.

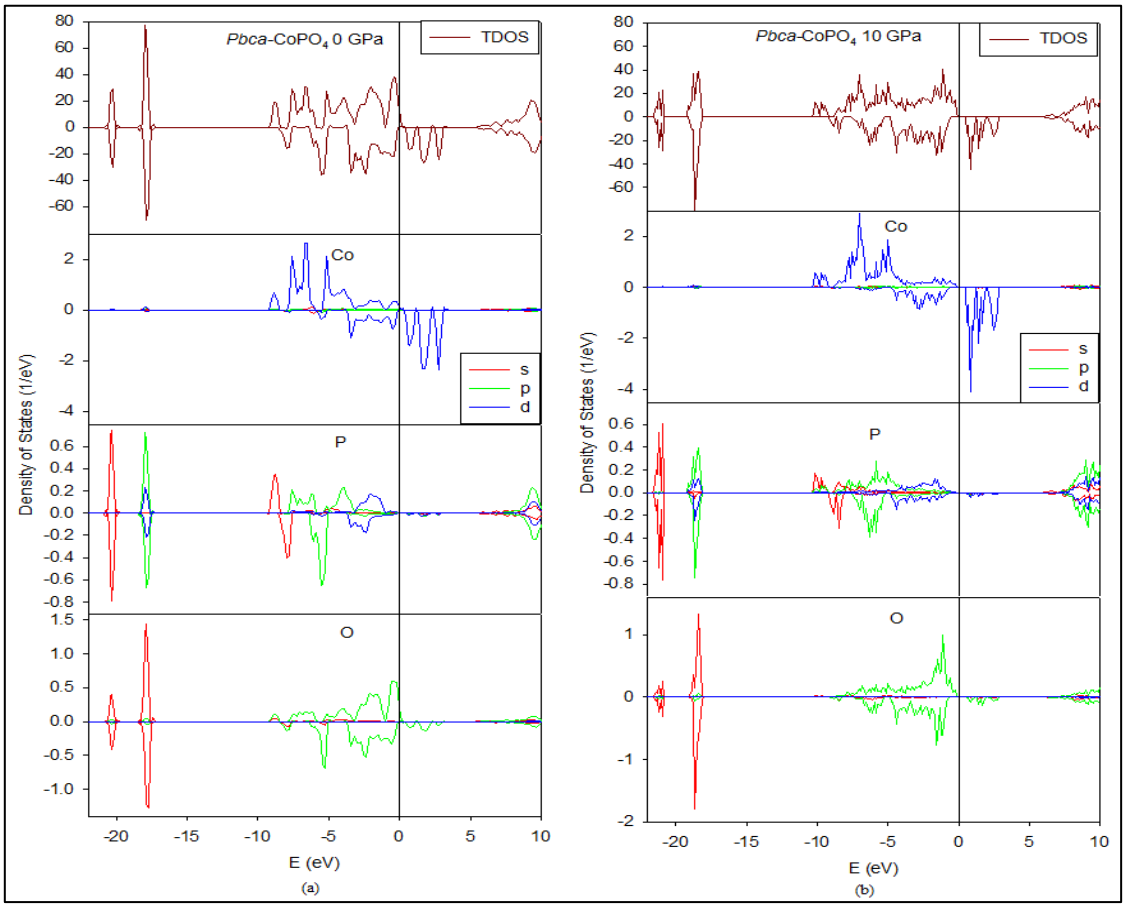

Figure 3-16 Total and partial DOS of *Pbca*-$CoPO_4$ polymorph, in (a) 0 GPa and (b) 10 GPa. The Fermi level is taken as energy zero ($E-E_F=0$).

The total and partial density of states of $P2_1/c$-$CoPO_4$ are shown in Figure 3-17. Similarly to *Pbca*-$CoPO_4$, we note that there exists no energy band gap, suggesting

metallic behaviour and good electrochemical conductivity. The Fermi level is located on the Co 3*d* band and on the upper valence band, further suggesting metallic characteristics. These features are observed at both ambient and high pressures. Furthermore, we note that pressure slightly lowers the total and partial density of states around the Fermi level.

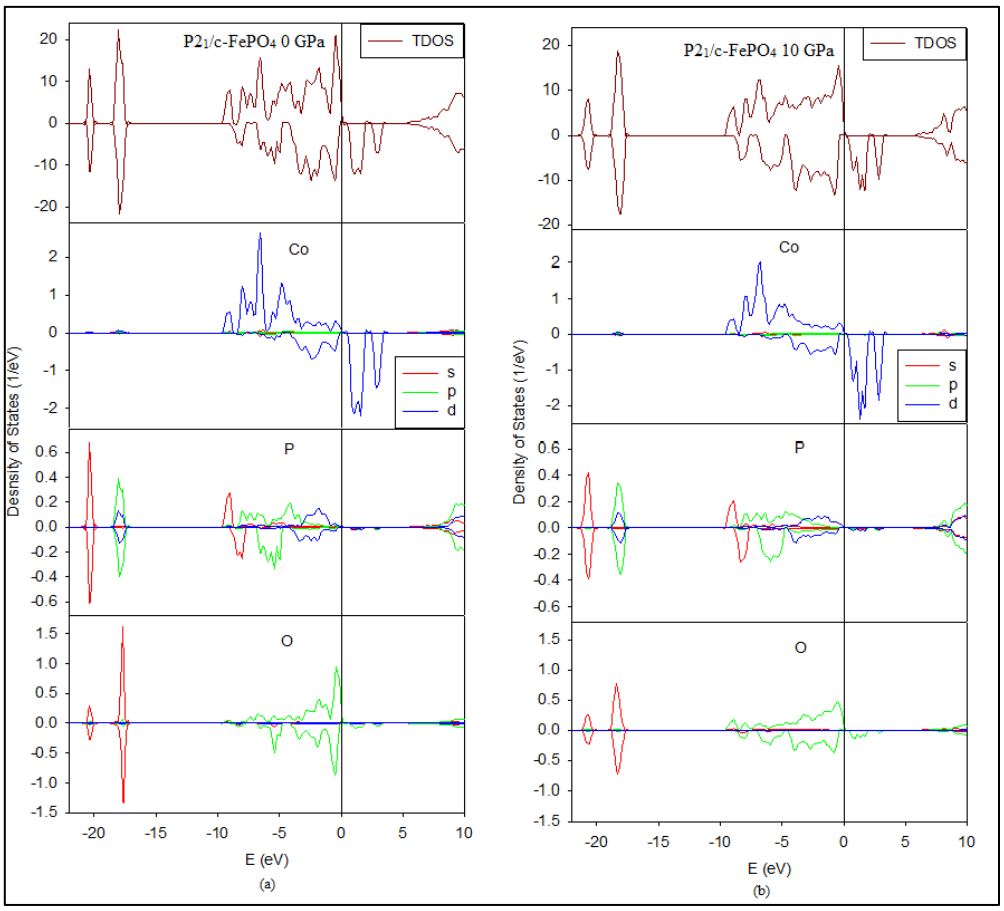

Figure 3-17 Total and partial DOS of *P2₁/c*-$CoPO_4$ polymorph, in (a) 0 GPa and (b) 10 GPa. The Fermi level is taken as energy zero ($E-E_F=0$).

Figure 3-18 shows the total and partial densities of states of *Cmcm*-$CoPO_4$ polymorph. We note that the *Cmcm*-$CoPO_4$ polymorph shows a relatively narrow band gap of 0.46 eV around the Fermi level. The Fermi level lies on the edge of the upper valence band, suggesting semiconducting characteristic.

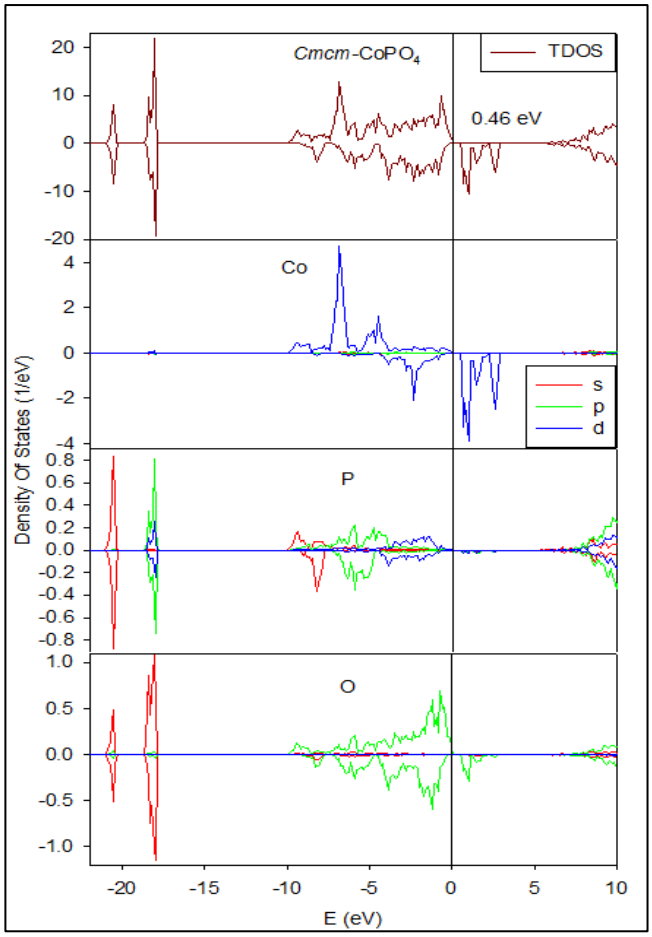

Figure 3-18 Total and partial DOS of *Cmcm*-$CoPO_4$ polymorph. The Fermi level is taken as energy zero ($E-E_F=0$).

3.3.3 DOS of $MnPO_4$ Polymorphs

Figures, 3-19 to 3-23 show the total and partial density of states for $MnPO_4$ polymorphs in ambient (0 GPa) and high pressure (10 GPa). We observe that, contrary to $FePO_4$ and $CoPO_4$ structural polymorphs; the $MnPO_4$ polymorphs show a shallow (pseudo) gap. Generally, we observe the formation of pseudo gap in conductors or metallic systems. Though the origin of pseudo gap is yet to be understood, but this phenomenon is crucial in determining stability.

In Figure 3-19, we show the total and partial density of states for $P3_121$-$MnPO_4$ polymorph in ambient (Figure 3-19(a)) and high pressure (Figure 3-19(b)), respectively. The total and partial DOS of $P3_121$-$MnPO_4$ show the existence of the shallow pseudo gap. We note that the Fermi level is located dip and on the left of the pseudo gap. The presence of a pseudo gap suggests that the electrons in the valence band are excited and not stable and are able to cross over to the conduction band. Thus the material shows metallic behaviour and good electrochemical conductivity. Similarly to other $P3_121$ symmetries, the total density states are reduced when 10 GPa is applied.

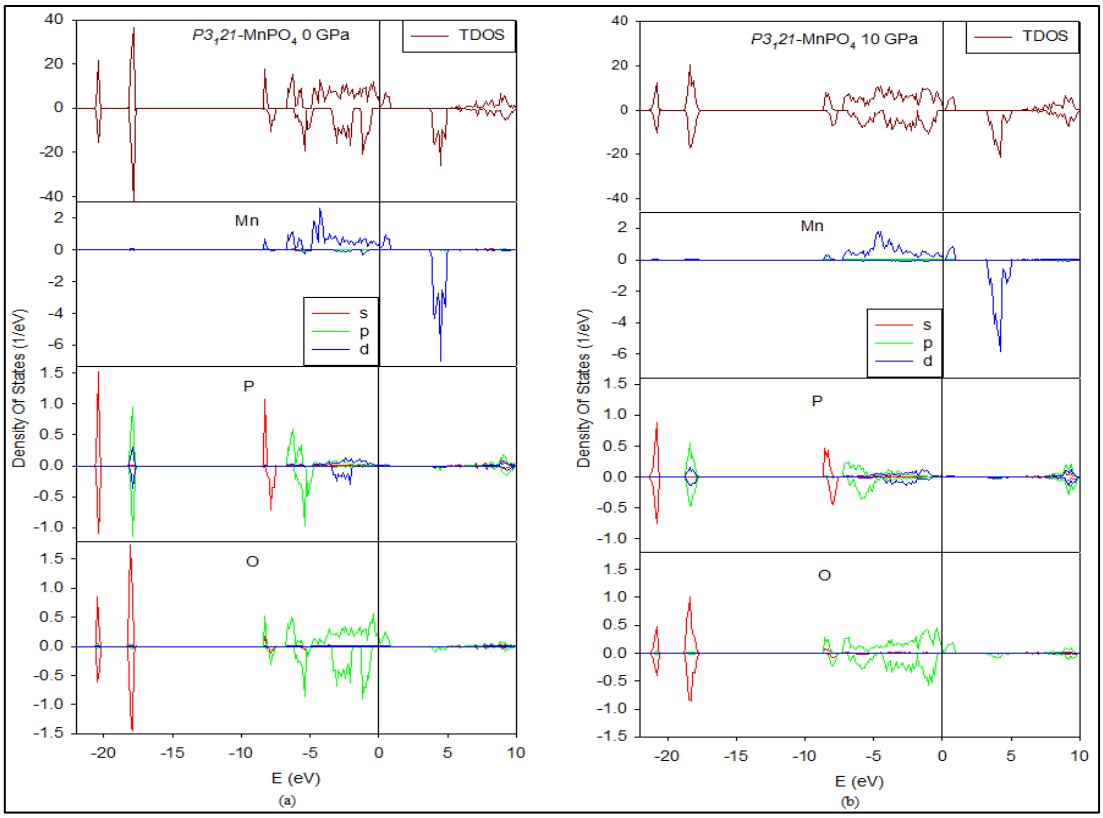

Figure 3-19 Total and partial DOS of $P3_121$-$MnPO_4$ polymorph, in (a) 0 GPa and (b) 10 GPa. The Fermi level is taken as energy zero ($E-E_F=0$).

We note that *Pnma*-$MnPO_4$ polymorph (figure 3-20) shows a shallow pseudo gap, suggesting metallic characteristics and good electrochemical activity. The Fermi level falls on the 3*d* band. Our DFT+*U* calculations slightly differ from the results reported

by Zhou *et al*. In their GGA and GGA+*U* calculations of the band gap of *Pnma*-$MnPO_4$; they found the band gap to be 0.1 eV and 0.5 eV, respectively [184]. The difference might be caused by the choice of Hubbard parameter; 5.5 eV is chosen in the work while zhou *et al*. used 4.5 [81]. Pierce *et al*. indicated that the energy band gaps for *Pnma*-$MnPO_4$ polymorph show some sensitivity to the choice of magnetic ordering, perhaps due to coupling of the magnetic ordering an the Jahn-Teller distortion [134]. Furthermore, we note that electronic density of states of *Pnma*-$MnPO_4$ changes insignificantly when 10 GPa pressure is applied.

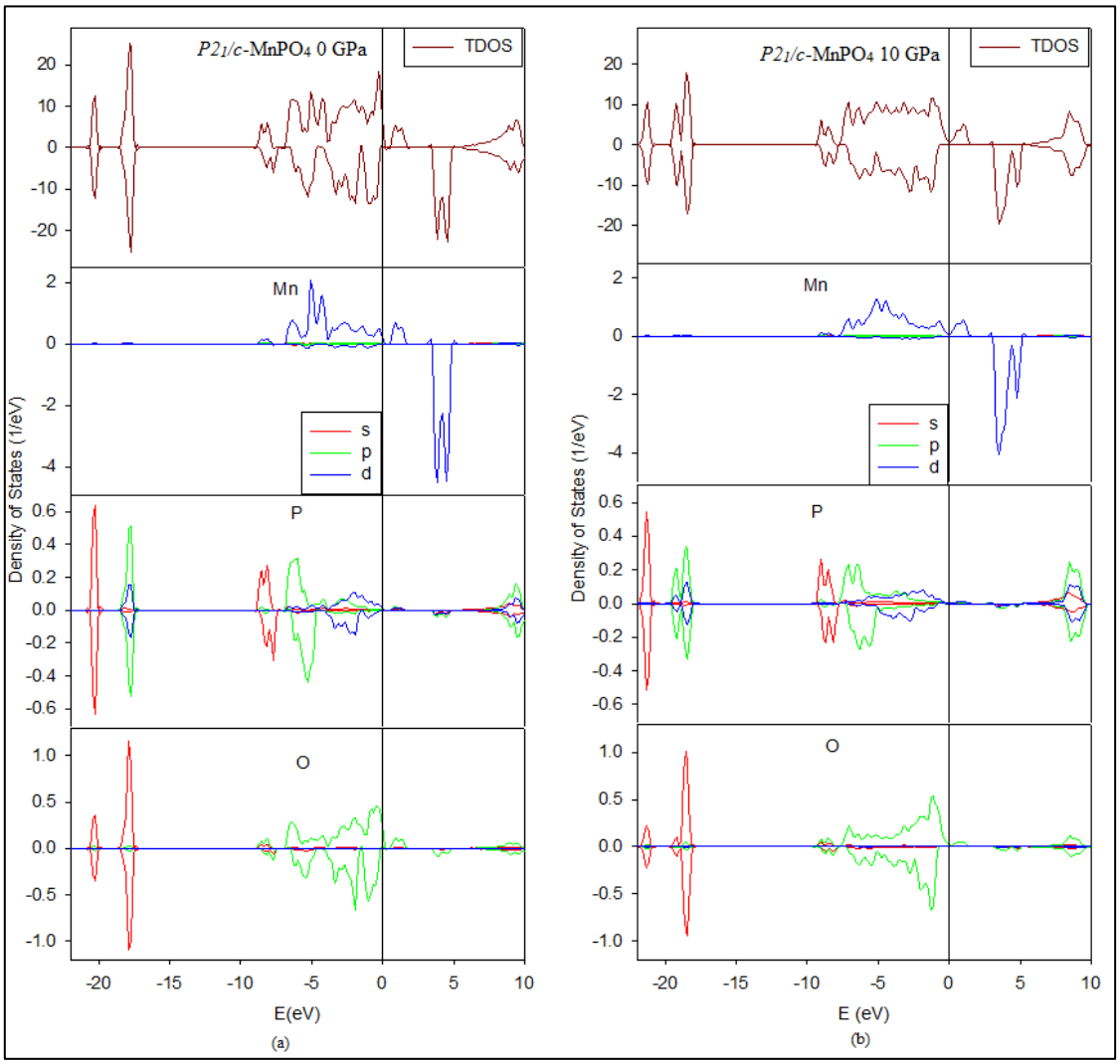

Figure 3-20 Total and partial DOS of *Pnma*-$MnPO_4$ polymorph, in (a) 0 GPa and (b) 10 GPa. The Fermi level is taken as energy zero ($E-E_F=0$).

The total and partial densities of states for *Pbca*-$MnPO_4$ are listed in Figure 3-21. In ambient pressure, we note that *Pbca*-$MnPO_4$ shows a very shallow pseudo gap and the Fermi level is located on the upper valence band, suggesting good conductivity and metallic characteristics. The application of 10 GPa pressure decreases the total and partial densities of states. Furthermore, we observe that the Fermi level remains on the upper valence band while the pseudo gap is less shallow in high pressure, suggesting that conductivity may be enhanced.

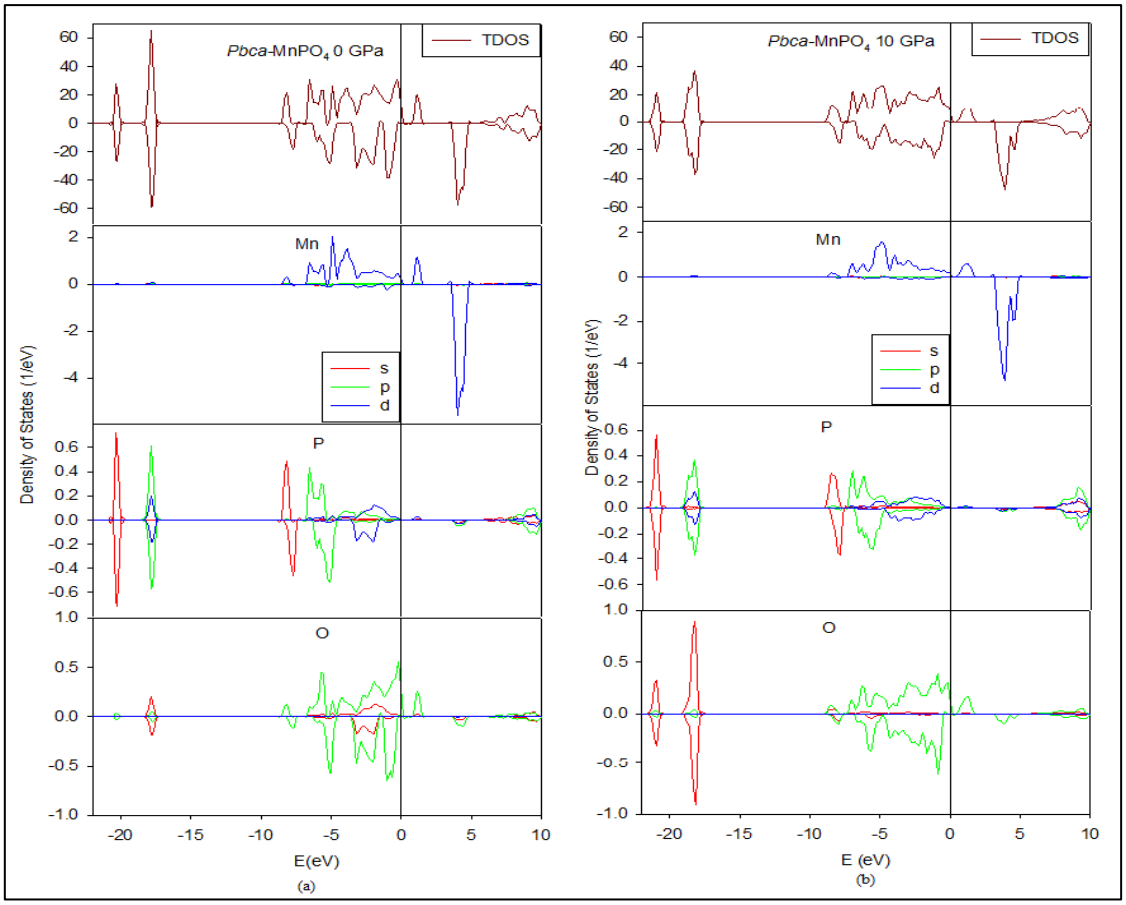

Figure 3-21 Total and partial DOS of *Pbca*-$MnPO_4$ polymorph, in (a) 0 GPa and (b) 10 GPa. The Fermi level is taken as energy zero ($E-E_F=0$).

The total and partial densities of states of $P2_1/c$-$MnPO_4$ in ambient and high pressures are presented in Figure 3-22(a) and 3-22(b), respectively. Similarly to other $MnPO_4$

polymorphs, we observe that $P2_1/c$-$MnPO_4$ shows a shallow pseudo gap in ambient pressure. The Fermi level lies on the left of the pseudo gap, suggesting metallic behaviour and conducting. The total and partial densities of states also decrease in high pressure (10 GPa). Interestingly, we observe that the Fermi level lies deep in the pseudo gap, suggesting an enhancement in conductivity. Furthermore, we note that the pseudo gap is less shallow in high pressure as observed with *Pbca*-$MnPO_4$ polymorph.

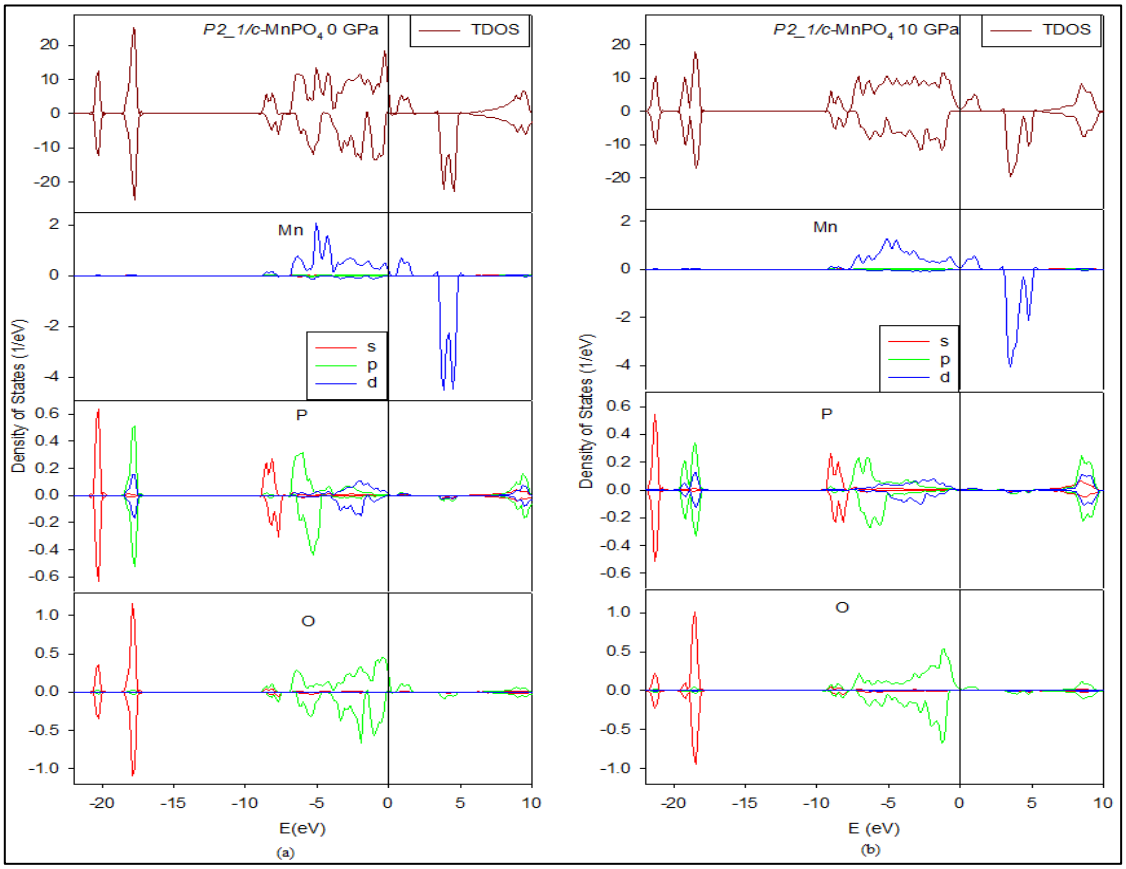

Figure 3-22 Total and partial DOS of $P2_1/c$-$MnPO_4$ polymorph, in (a) 0 GPa and (b) 10 GPa. The Fermi level is taken as energy zero ($E-E_F=0$).

In Figure 3-23 we show the total and partial DOS of *Cmcm*-$MnPO_4$ polymorph. Similarly to other $MnPO_4$ polymorphs, we note the presence of the pseudo gap. The Fermi level falls on the 3*d* band, suggesting metallic behaviour and good electrochemical conductivity.

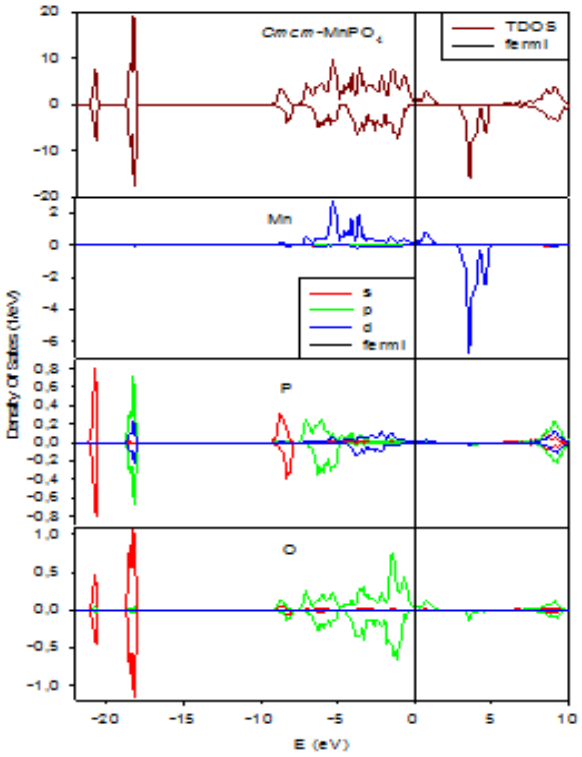

Figure 3-23 Total and partial DOS of *Cmcm*-$MnPO_4$ polymorph. The Fermi level is taken as energy zero ($E-E_F=0$).

Figure 3-24 shows the partial density of states of Fe, Co and Mn. We concentrate on the *d* electron contribution on the DOS for Fe, Co and Mn. We note a variation of peaks at the conduction band with different substitution on the metal sub lattice. All atoms display a spin down electron density distribution at the conduction band. More interestingly, at the conduction band we observe two dominant peaks of different magnitude. We observe the spin down sizes of *d*-states in the conduction bands of Fe, Mn, and Co as follows; Fe shows peaks of sizes -5.215 and -4.635 at energies 2.663 eV and 2.779 eV, respectively, Co shows peaks shorter than those of Fe; -2.123 and -1.707 at energies 2.549 eV and 2.680 eV, respectively, while Mn shows peaks of -5.215 and -4.245 at energies 3.525 eV and 3.646 eV, respectively. From the peaks of individual atoms, we can conclude that Fe and Mn show stability over Co. More important, the partial densities of states trends are consistence with the heats of

formation prediction, where it was found that $MnPO_4$ is more energetically stable. This suggests that the electron number is crucial to determine the stabilities of the systems.

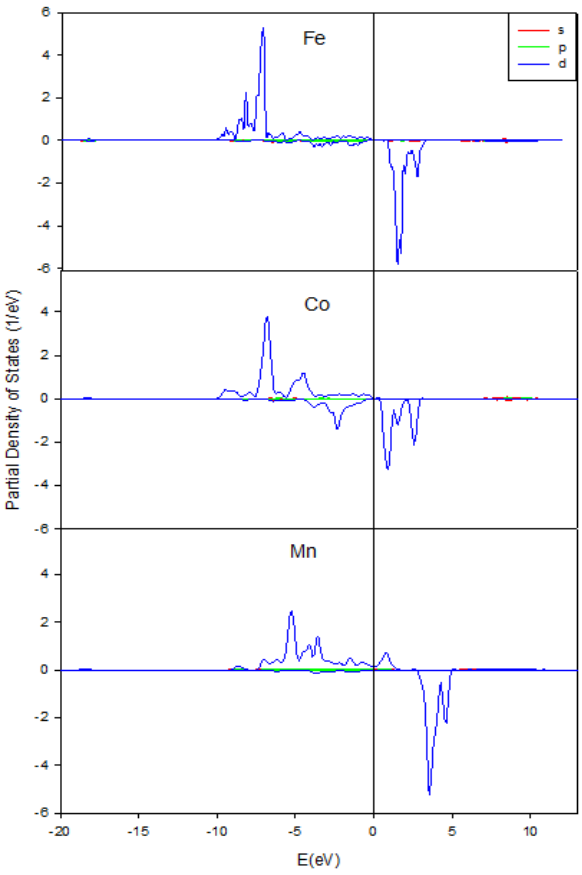

Figure 3-24 Partial density of states for *Cmcm* elements (Fe, Co and Mn).

We note several common features in density of states Figures; the MPO_4 polymorphs show that the states are distinguished into three patterns; the lower valence band, the upper valence band, and the conduction band. The partial densities of states of all three MPO_4 structures differ in bandwidths and band gaps; however all possess similar features which can be described as follows.

The peak of the lowest valence band which is predominantly composed of P-*3s* character and show hybridisation with O-*2s* electrons is located at around -20.91 eV.

The second lower valence band is predominantly O-2*s* character hybridised with P-2*p* electrons. The so called “induction” effect is responsible for there being only four 2*p* electrons for each O^{-2} ion to hybridise with the Fe 3*d*-states [17]. In fact, because of the strong spin coupling effects in Fe, the upper valence band is formed from a well hybridised configuration of O $2p^2\uparrow$ and Fe $3d^5\uparrow$/Mn $3d^4\uparrow$/Co $3d^6\uparrow$ for the majority spin; leaving the O $2p^2\downarrow$ states to form a narrower band at a similar energy for the minority spin contribution. The minority spin Fe $3d^0\uparrow$/Mn $3d^0\uparrow$/Co $3d^0\uparrow$ states form a relatively narrow band above the Fermi level. This analysis provides evidence that these materials are well approximated as closed-shell systems and well described by single Slater determinant wavefunctions [17].

Chapter 4

Mechanical Stability of MPO_4 Polymorphs

In this chapter we present first-principles DFT mechanical properties results of MPO_4 (M=Fe, Co and Mn) polymorphs. In order to investigate the mechanical stability of the different structures of MPO_4, we have evaluated their phonon dispersion curves along high symmetry directions within the first Brillouin zone and elastic properties. To the best of our knowledge, no phonon dispersion curves results on MPO_4 structural polymorphs have ever been reported to date.

4.1 Phonon Dispersion Curves

Figures 4-1 to 4-3 show the DFT+*U* calculated phonon dispersion curves for the MPO_4 polymorphs in ambient and high pressures. The $P3_121$ trigonal polymorphs has 18 atoms in a unit cell, thus there will be 54 modes of vibrations divided into 1 longitudinal acoustic (LA), 2 transverse acoustic (TA); 17 longitudinal optical (LO) and 34 transverse optical (TO). The *Pnma* and *Cmcm* orthorhombic polymorphs are composed of 24 atoms in the unit cell; hence the phonon spectra will possess 3 acoustical (1LA, 2TA) and 69 optical (23LO, 46TO) modes. The *Pbca* orthorhombic phases have 48 atoms in a crystal; hence contain 144 (3 acoustical and 141 optical) vibrational modes. Lastly, the $P2_1/c$ monoclinic phases have 24 atoms in a crystal; hence contain 72 (3 acoustical and 69 optical) vibrational branches.

We note that the phonon dispersion curves for the trigonal $P3_121$-MPO_4 polymorphs display negative frequency phonon branches (here referred to as soft modes) down to -5 THz at both ambient and high pressure. These soft modes are observed along high symmetry directions referred to as Γ (0,0,0), L (½,0,½) and Z (1,½,½) in the Brillouin zone. The presence of soft modes suggests that the $P3_121$-MPO_4 polymorph is vibrationally unstable. Similarly to the trigonal system, we observe that the orthorhombic (*Pbca*) and monoclinic ($P2_1/c$) polymorphs also show the soft modes along high symmetry lines [R (1/2,1/2,1/2), T (0,1/2,1/2), Z (0,0,1/2), Γ (0,0,0), X (1/2,0,0), S (1/2,1/2,0) and Y (0,1/2,0)] and [C (0,1/2,1/2), Y (0,1/2,0), B (-1/2,0,0), A (-1/2,1/2,0), E (-1/2,-1/2,1/2) and Z (0,0,1/2)], respectively. This is a condition for vibrational instability. However, we note that the negative vibrations are few along the centre of the Brollouin zone [Γ (0,0,0)].

On the other hand, it is clearly seen that there exists no soft modes (only imaginary modes, induced by not imposing the invariant conditions in the PHONON Code) along high symmetry lines at both ambient and high pressures for the orthorhombic (*Pnma* and *Cmcm*) polymorphs. We particularly noted that *Pnma*-$FePO_4$, *Pnma*-$CoPO_4$, *Cmcm*-$FePO_4$ and *Cmcm*-$CoPO_4$ are mechanical stable. Interestingly, we note that all $MnPO_4$ polymorphs are vibrational unstable due to the presence of the soft modes along high symmetry lines. Moreover, the application of 10 GPa pressure shifts the soft modes upward (positive frequencies) and thus enhancing vibrational stability. Particularly, we note that *Pbca*-$CoPO_4$ displays negative vibrations down to -2 THz at 0 GPa (figure 4-2 (g)), and only positive vibrations at 10 GPa (figure (4-2(h)). Contrary to other observations, we note that 10 GPa pressure does not enhance the stability of $P3_121$-$CoPO_4$ and *Pnma*-$MnPO_4$, especially along Γ (0,0,0). We note that the negative phonon vibrations remain down to -5 THz and -2 THz, respectively.

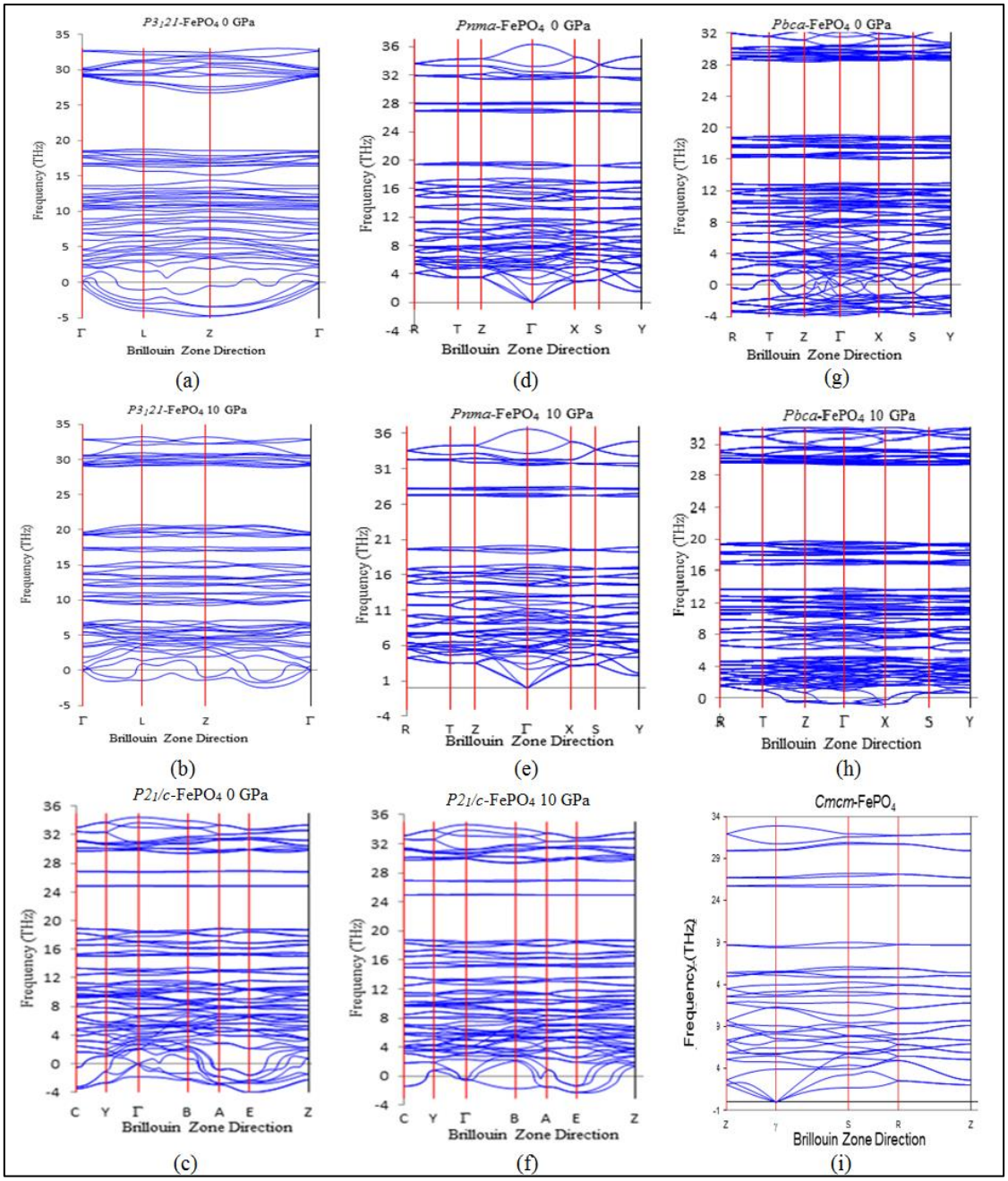

Figure 4-1 Phonon dispersion curves for $FePO_4$ polymorphs at 0 GPa and 10 GPa.

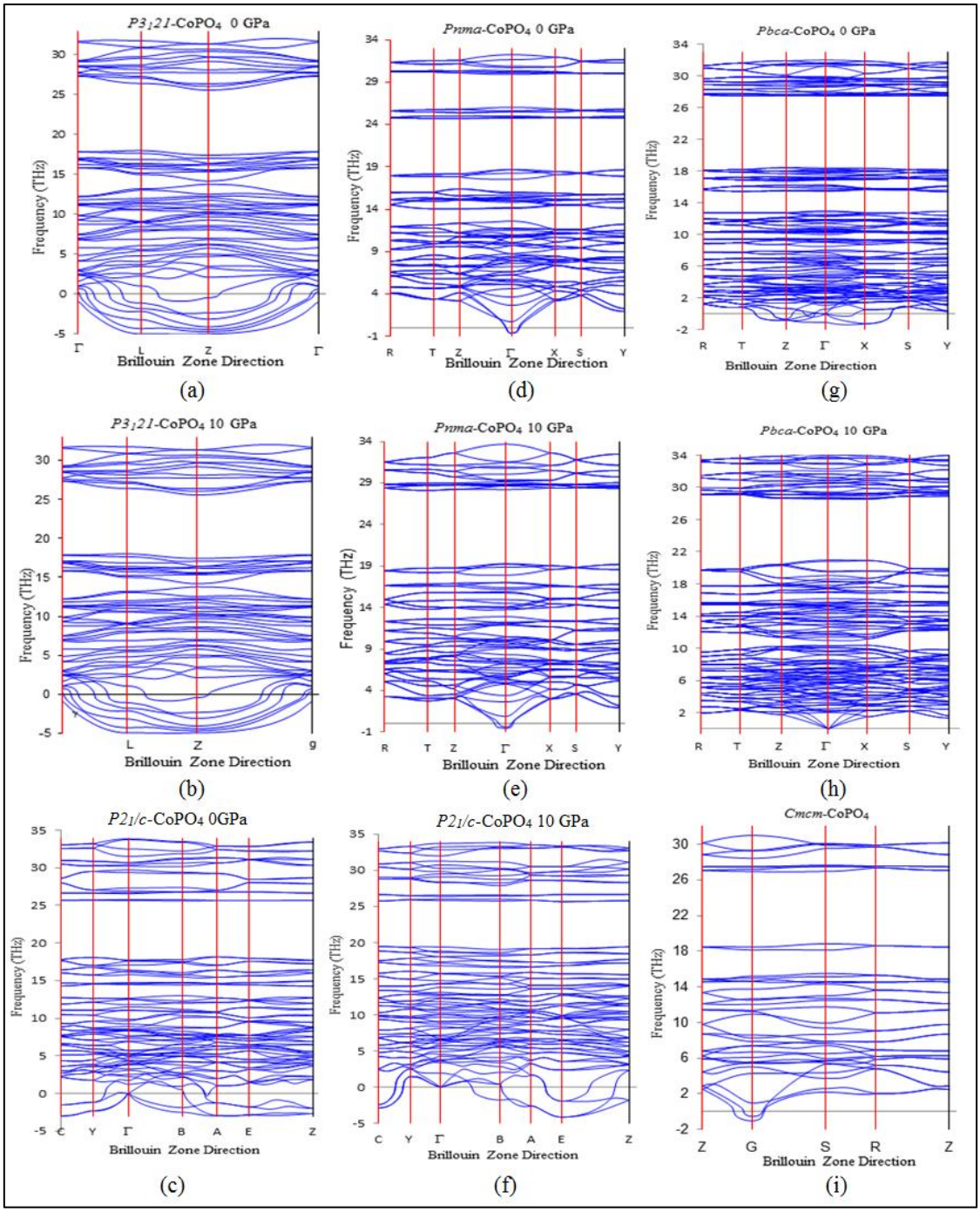

Figure 4-2 Phonon dispersion curves for $CoPO_4$ polymorphs at 0 GPa and 10 GPa.

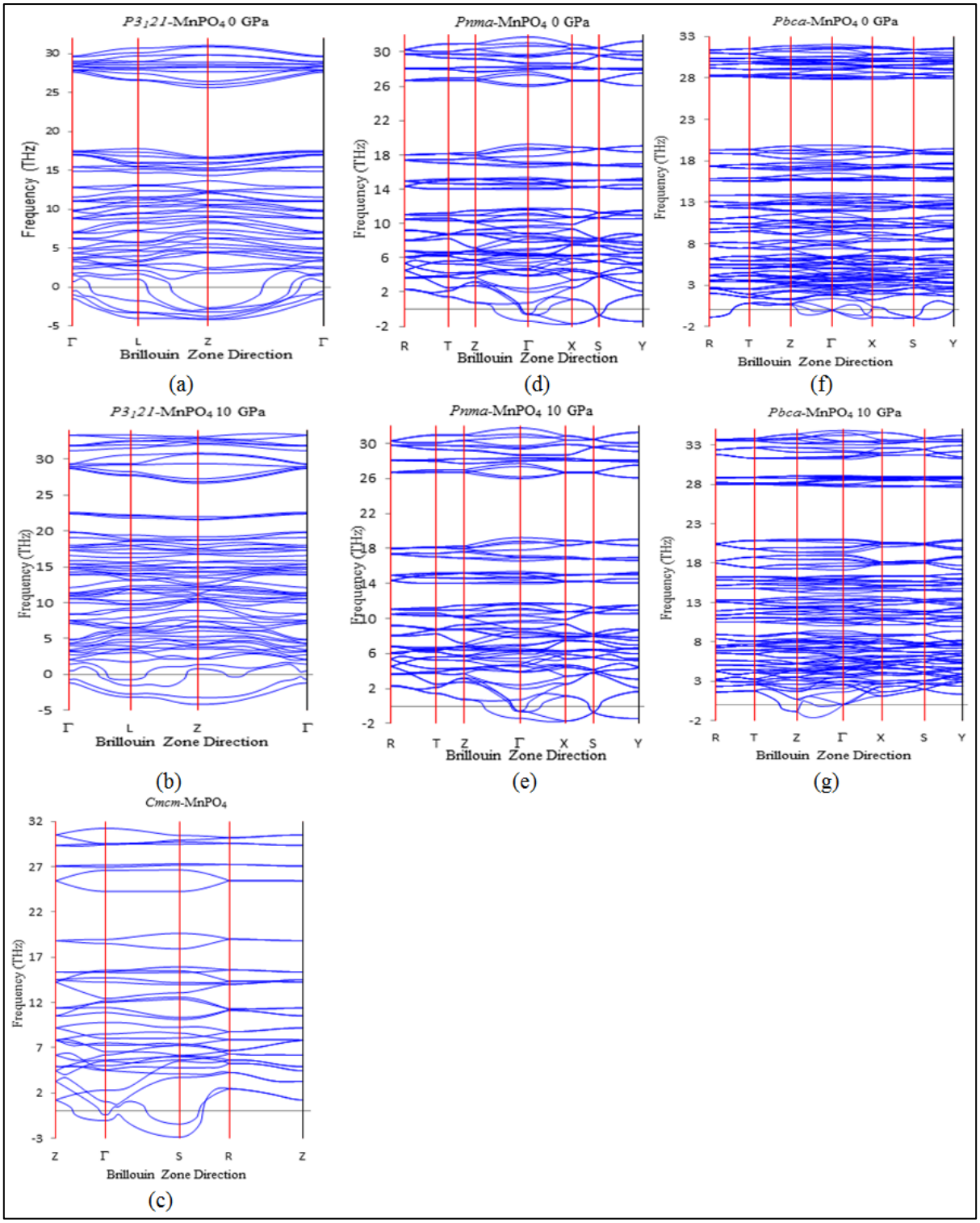

Figure 4-3 Phonon dispersion curves for $MnPO_4$ polymorphs at 0 GPa and 10 GPa.

4.2 Elastic Properties

Elastic properties are very essential for materials because they provide fundamental information on interatomic potentials and relate to various important solid state phenomena such as interatomic bonding, equations of state, phonon dispersions, heats of formations and thermal expansion [185, 186]. To further investigate the stability of MPO_4 structural polymorphs, we have calculated the elastic constants. In general, elastic constants are defined by the Taylor expansion of the total energy, derived from the energy as a function of a lattice strain as follows [187, 188, 189]:

$$U(V,\varepsilon) = U(V_0,0) + V_0\left[\sum_i \tau_i \varepsilon_i \xi_i + \frac{1}{2}\sum_{ij} C_{ij}\varepsilon_i \xi_i \varepsilon_i \xi_j\right], \qquad 4.1$$

where $U(V_0,0)$ is the energy of the unstrained system with equilibrium volume V_0, τ_i is an element in the stress tensor and ξ_i is a factor to take care of the Voigt index.

In this section we discuss the results on elastic constants, bulk, shear and Young's moduli of MPO_4 polymorphs from first-principles calculations. All calculations are performed using a plane-wave basis set with the projector augmented-wave (PAW) method [190] in the generalised gradient approximation (GGA) [178] as implemented in the VASP code [76]. Previous studies have shown that GGA+*U* are an appropriate method for predicting materials properties of oxides and phosphates containing 3*d* transition metals. *Ab initio* results obtained with GGA+*U* on phase stability, thermodynamic properties, and magnetic and electronic structure show significant better agreement with experiment than in the GGA [38, 191, 192]. Previous studies had indicated that smaller lattice parameters yield larger values of elastic constants, while larger lattice parameters give smaller elastic constants. Hence, elastic constants in 10 GPa are expected to be larger than those in 0 GPa.

4.2.1 Elastic Properties of $FePO_4$ Polymorphs

Table 4-1 lists the DFT results on elastic constants (C_{ij}), bulk (B), shear (G), Young's (E) moduli and Pugh ratio (B/G) for *P3₁21*-$FePO_4$, *Pnma*-$FePO_4$ *Pbca*-$FePO_4$, *P2₁/c*-$FePO_4$ and *Cmcm*-$FePO_4$ polymorphs. We note that the independent elastic constants for the trigonal *P3₁21*-$FePO_4$ polymorph are all positive and satisfy the necessary stability conditions, suggesting elastic stability. This is in good agreement with the experimental and calculated results found by Mittal *et al*. [54] and Labeguerie *et al*. [193]. However, the stability criteria B_3 (section 2.5.4.1) on the trigonal *P3₁21*-$FePO_4$ decreases from 1154.38 GPa to 655.85 GPa when 10 GPa pressure is introduced, denoting the existence of mechanical instability correlated with the presence of soft modes in the phonon dispersion curves. Thus rigid catastrophe phenomenon applies [167]. Gregoryanz *et al*. suggested that this B_3 type of instability emanates from the softening of C_{44} with pressure [194]. C_{44} is softened from 28.67 GPa to 17.30 GPa when pressure increases from 0 GPa to 10 GPa.

The well-studied orthorhombic *Pnma*-$FePO_4$ and *Cmcm*-$FePO_4$ polymorphs also satisfy the necessary stability condition at both 0 GPa and 10 GPa, corresponding well with the phonon dispersion curves. We note that, our LDA+*U* elastic constants overestimate GGA+*U* results found by Maxisch and Ceder [53] including the corresponding elastic moduli. Our large elastic constants and moduli is suspected to be caused by large Hubbard *U*=5.5 eV used in this study, as compared to *U*=4.7 eV used by Maxisch and Ceder [53]. This can be confirmed by the normal GGA study by Maxisch and Ceder; normal GGA results show even lower elastic constants and moduli values. The similarity between the two calculations is the trend of elastic constants values. Both calculations show C_{11} (251.32 GPa) to be largest and C_{23} (43.33 GPa) to be smallest. Robust conclusion on the

correct elastic constants and moduli is hard to make without experimental confirmations. The orthorhombic *Pbca*-$FePO_4$ and monoclinic *P2₁/c*-$FePO_4$ also satisfy the necessary stability conditions, however C_{44} is greater than the $\frac{C_{11}-C_{12}}{2}$, suggesting that there will be degeneration of transverse mode in phonon dispersion curves in the systems.

Table 4-1. DFT+*U* results on elastic constants (C_{ij}), bulk (B), shear (G), and Young's (E) moduli and Pugh ratio (B/G) for $FePO_4$ polymorphs in 0 GPa and 10 GPa.

	0 GPa					10 GPa			
C_{ij} (GPa)	*P3₁21*	*Pnma*	*Pbca*	*P2₁/c*	*Cmcm*	*P3₁21*	*Pnma*	*Pbca*	*P2₁/c*
C_{11}	62.50	251.32	49.00	145.50	249.67	89.80	230.33	112.33	121.50
C_{12}	21.33	61.50	43.92	84.58	66.67	40.90	71.42	65.83	68.58
C_{13}	35.92	88.67	0.920	90.58	28.08	49.75	80.92	90.50	76.75
C_{14}	2.00					9.75			
C_{15}				21.08					22.25
C_{22}		242.00	96.17	132.17	186.50		251.50	248.17	164.17
C_{23}		43.33	25.42	56.50	44.58		81.50	105.75	77.75
C_{25}				6.92					7.08
C_{33}	85.67	204.73	35.33	148.17	144.00	156.30	194.83	180.33	170.00
C_{35}				13.08					44.75
C_{44}	28.67	73.33	16.67	57.33	90.00	17.30	57.33	95.00	91.33
C_{46}				9.50					26.83
C_{55}		95.00	16.00	47.00	61.33		97.67	44.00	54.17
C_{66}	20.59	89.67	22.67	38.33	73.67	24.45	76.33	12.67	56.33
B_V	44.11	120.56	35.67	98.80	95.43	68.52	127.15	118.33	100.20
B_R	41.27	118.71	17.81	93.39	89.55	63.36	126.24	101.98	85.75
B_H	42.69	119.63	26.74	96.09	92.49	65.94	126.70	110.16	92.98
G_V	23.42	85.23	18.42	41.48	74.39	24.84	75.79	48.92	55.87
G_R	22.16	83.27	14.67	36.10	71.32	17.78	72.85	29.75	43.10
G_H	22.79	84.25	16.54	38.79	72.86	21.31	74.32	39.33	49.49
E_V	59.69	206.93	47.14	109.16	177.14	66.49	189.68	128.98	141.35
E_R	56.40	202.47	34.53	95.94	169.08	48.78	183.28	81.34	110.75
E_H	58.04	204.70	40.83	102.55	173.11	57.64	186.48	105.16	126.05
B/G_V	1.88	1.41	1.90	2.38	1.28	2.58	1.68	2.42	1.79
B/G_R	1.86	1.43	1.21	2.59	1.26	3.56	1.73	3.43	1.99
B/G_H	1.87	1.42	1.62	2.48	1.27	3.09	1.70	2.80	1.88

From the calculated elastic constants, the macroscopic mechanical parameters such as the bulk, shear and Young's moduli and the Pugh ratio have been determined using the Voigt-Reuss-Hill method (section 2.6.4.1 equations 2.54 to 2.59). The calculated bulk, shear and Young's modulus and Pugh ratio are summarised in table 4-1. The moduli are given for Voigt (upper bound), Reuss (lower bound) and Hill (average bound) and the values are comparable. We note that the highest bulk modulus is found for the *Pnma*-$FePO_4$ (B_H=119.63 GPa) polymorph, while *Pbca*-$FePO_4$ gives the lowest value (27.74 GPa) in ambient pressure. Thus the *Pnma*-$FePO_4$ (highest B) is the hardest while *Pbca*-$FePO_4$ is least in hardness. Furthermore, we observe that B>G, implying that the parameter limiting the stability of these polymorphs is the shear modulus [53].

On the hand, the Young's modulus is the largest for the *Pnma*-$FePO_4$ polymorph (E_H=204.70 GPa) followed by *$P2_1/c$* -$FePO_4$ (E_H=102.55 GPa), *Cmcm*-$FoPO_4$ (E_H=173.11 GPa), *$P3_121$*-$FePO_4$ (E_H=55.96 GPa) and *Pbca*-$FePO_4$ (E_H=40.83 GPa) polymorphs, respectively; hence *Pnma*-$FePO_4$ polymorph is a material with great stiffness, whilst *Pbca*-$FePO_4$ polymorph is weak in stiffness. We also note that the stiffness trend is similar to hardness trend. In addition, according to the Pugh brittle/ductility criterion [195], a parameter B/G defined. Pugh proposed that the shear modulus is relative with resistance to plastic deformation and the bulk modulus is associated with the resistance to fracture. Furthermore, if the B/G is more than the critical value (1.75), the material is ductile and if less than 1.75, the material will be brittle. From our calculations, we obtain the B/G to be greater than 1.75 for the trigonal *$P3_121$*-$FePO_4$ and monoclinic *$P2_1/c$* -$FePO_4$ polymorphs and less than 1.75 for the orthorhombic *Pnma*-$FePO_4$, *Pbca*-$FePO_4$ and *Cmcm*-$FePO_4$ polymorphs. These suggest that the trigonal and monoclinic systems of $FePO_4$ are ductile, while the orthorhombic systems are brittle.

The calculated elastic constants, resultant macroscopic moduli and Pugh ratio of $FePO_4$ in 10 GPa are also listed in table 4-1. There are several irregular changes we note on the elastic properties of $FePO_4$ polymorphs in high pressure. The effect of pressure on the elastic properties of diopside and jadeite had suggested that elastic properties values in high pressure are well compared to experimental values [196]. However, to the best of our knowledge, there are no experimental values recorded for $FePO_4$ polymorphs in high pressure. We note that $FePO_4$ polymorphs still maintain the mechanical stability in high pressure. All elastic constants satisfy the necessary conditions for stability. Furthermore, the bulk modulus is still greater than the shear modulus, suggesting that the latter is still the limiting parameter for stability.

We note that the elastic constants of the trigonal *$P3_121$*-$FePO_4$ polymorph increase in 10 GPa except for C_{44}, which decreases by 11.20 GPa. The most substantial increase is noted in C_{33}, with an increase of 64.30 GPa. Furthermore, the hardness, stiffness and ductility increase in high pressure. Moreover, we observe that the shear modulus slightly decreases when pressure is applied; further limiting the mechanical stability. The substantial difference between bulk and shear moduli leads to high Pugh ratio value; hence increasing ductility.

On the other hand, we note an inconsistent change in C_{ij}'s on the orthorhombic *Pnma*-$FePO_4$ and *Pbca*-$FePO_4$. However, similarly to *$P3_121$*-$FePO_4$, the bulk modulus and Pugh ratio increase in high pressure, consequently enhancing hardness and ductility, respectively. In contrast, the Young's modulus of *Pnma*-$FePO_4$ decreases, thus reducing the stiffness of the material. Lastly, we note that the elastic constants of monoclinic *$P2_1/c$*-$FePO_4$ generally increase in 10 GPa pressure, except for C_{11}, C_{12} and C_{13}. Contrary to other polymorphs, the average bulk (B_H) and shear (E_H) moduli slightly decrease and increase by 3.11 GPa and 0.54 GPa, respectively, thus suggesting

a trivial decrease in hardness and increase in brittleness of the material. The increase in Young's modulus also suggests that the stiffness is enhanced when pressure is applied.

In table 4-2, we compare elastic anisotropy factors and Poison ratio of $FePO_4$ polymorphs. A proper description of these factors has an essential role in engineering science and crystal physics. The shear anisotropic factors determine the degree of anisotropy in bonding between atoms in variant planes. As mentioned in section 2.6.4.1, anisotropy factors A_1, A_2 and A_3 must equate to one, otherwise any value less or greater is a measure of the degree of elastic anisotropy. The elastic anisotropy factors are calculated in 0 GPa and 10 GPa; however, to the best of our knowledge, there are no recorded experimental data to verify our calculations. The elastic anisotropy factors are entirely dependent on symmetry of crystal structures. Hence, since the lattice parameters *a*, *b*, and *c* vary when 10 GPa pressure is applied, the elastic anisotropy factors are expected to vary with pressure.

Table 4-2 Anisotropy factors and Poisson ratio of $FePO_4$ polymorphs in 0 GPa and 10 GPa.

	0 GPa					10 GPa			
Anisotropy	$P3_121$	*Pnma*	*Pbca*	$P2_1/c$	*Cmcm*	$P3_121$	*Pnma*	*Pbca*	$P2_1/c$
A_1	1.64	1.03	0.77		1.07	0.71	0.87	4.69	
A_2	1.31	1.06	0.79		1.02	1.74	1.38	1.52	
A_3	0.82	0.97	1.58		0.97	0.82	0.90	0.22	
A_B *(%)*		0.80	0.33		3.18		0.40	0.07	
A_G *(%)*		1.16	0.11		2.11		1.98	0.24	
A^U	0.39	0.14	2.28	0.80	0.28	2.07	0.21	3.38	1.65
U_H	0.39	0.22	0.24	0.32	0.29	0.28	0.26	0.34	0.23

For the trigonal $P3_121$-$FePO_4$ crystal, we note that A_1, A_2 and A_3 deviate from unity by 18.25 %, 27.14 % and 20.39 %, indicating the degree of anisotropy. However, when 10

GPa pressure is applied, we note change of 79.18 %, 27.95 % and 0.855 % for respectively, i.e. A_1 decreases by 79.18 %, while A_2 and A_3 increase by 27.95 % and 0.855 % A_1, A_2 and A_3, respectively. Thus, 10 GPa pressure converge A_1, and A_3 to unity by 14.06 % and 0.89 %, respectively, while diverge A_2 by 26.92 %. This is due to the alteration of elastic constants when pressure is applied. These suggest that *P3₁21*-$FePO_4$ is anisotropic in ambient and high pressures, since anisotropy factors are not equal to unity.

For the orthorhombic *Pnma*-$FePO_4$ crystal, we note that values of A_1, A_2, and A_3 are close to unity in ambient and high pressures suggesting that these materials are nearing isotropic, hence considered as hard material; we note values 1.03, 1.06, and 0.97 for A_1, A_2, and A_3, respectively. This is in good agreement with the bulk modulus. The anisotropy factors A_1, A_2, and A_3 change by 16.34 %, 26.62 %, and 7.27 % when 10 GPa pressure is applied for *Pnma*-$FePO_4$. We note that *Pnma*-$FePO_4$ is conceivably anisotropic by 0.79 % and 0.39 % for percentage bulk modulus anisotropy (A_B); and 1.16 % and 1.98 % for percentage shear modulus anisotropy (A_G) in 0 GPa and 10 GPa, respectively.

The other orthorhombic system, *Pbca*-$FePO_4$ shows large degree of anisotropy: we observe that values for A_1, A_2, and A_3 are 0.77, 0.79 and 1.58, respectively. The application of 10 GPa pressure enhances anisotropy of the crystal as we observe values that are far from unity i.e. 4.69, 1.52 and 0.22. Furthermore, the percentage bulk and shear moduli anisotropy show possible anisotropy of 0.33 % and 0.11 % in ambient and 0.07 % and 0.24 % in high pressure.

Furthermore, we note that the orthorhombic *Cmcm*-$FePO_4$ also nears isotropic with values 1.07, 1.02 and 0.97 for A_1, A_2, and A_3, respectively. On the other hand, the percentage bulk modulus anisotropy and percentage shear modulus anisotropy shows that *Cmcm*-$FePO_4$ is possibly anisotropic by 3.18 % and 2.11 %, respectively. We also note that the

percentage bulk modulus anisotropy is smaller than the percentage shear modulus in *Pnma*-$FePO_4$ and greater in *Cmcm*-$FePO_4$. These imply that *Pnma*-$FePO_4$ is less anisotropic in compressibility than in shear, while *Cmcm*-$FePO_4$ is less in shear than in compressibility.

The universal anisotropy index A^U, which depends both on shear and bulk contributions have been also calculated and presented in table 4-2. Our DFT+*U* results show that the orthorhombic *Pbca*-$FePO_4$ is more anisotropic (A^U=2.28), while *Pnma*-$FePO_4$ is more isotropic (A^U=0.14) in ambient pressure. *Cmcm*-$FePO_4$ (A^U=0.28), *P3₁21*-$FePO_4$ (A^U=0.39) and *P2₁/c*-$FePO_4$ (A^U=0.80) are respectively intermediately isotropic.

We note that the application of 10 GPa pressure does not alter the anisotropy/isotropy trend of $FePO_4$ polymorphs. The index values are 2.07, 0.21, 3.38 and 1.65 for *P3₁21*-$FePO_4$, *Pnma*-$FePO_4$, *Pbca*-$FePO_4$ and *P2₁/c*-$FePO_4$, respectively. The relatively significant divergence of universal anisotropy index values from zero is due to large difference between the Voigt and the Reuss values. The poison ratio $\upsilon_{H,}$ for isotropic material was also calculated from the bulk and shear moduli. The poison ratio decreases for trigonal and monoclinic systems and increases for orthorhombic systems when pressure is applied.

4.2.2 Elastic Properties of $CoPO_4$ Polymorphs

Table 4-3 lists the DFT results on elastic constants (C_{ij}'s), bulk (B), shear (G), and Young's (E) moduli and Pugh ratio for $CoPO_4$ polymorphs. We observe that all orthorhombic $CoPO_4$ polymorphs i.e. *Pnma*-$CoPO_4$, *Pbca*-$CoPO_4$ and *Cmcm*-$CoPO_4$

show positive C_{ij}'s, while the trigonal *P3₁21*-$CoPO_4$ and monoclinic *P2₁/c*-$CoPO_4$ have negative values.

Table 4-3 DFT+*U* results on elastic constants (C_{ij}), bulk (B), shear (G), and Young's (E) moduli and Pugh ratio (B/G) for $CoPO_4$ polymorphs in 0 GPa and 10 GPa.

	0 GPa					10 GPa			
C_{ij} (GPa)	*P3₁21*	*Pnma*	*Pbca*	*P2₁/c*	*Cmcm*	*P3₁21*	*Pnma*	*Pbca*	*P2₁/c*
C_{11}	40.40	196.83	48.33	148.33	226.22	110.17	272.02	163.00	135.217
C_{12}	05.45	36.58	53.17	78.58	75.88	55.25	56.95	89.17	66.75
C_{13}	20.24	68.58	16.42	90.42	59.49	74.08	96.67	98.17	87.75
C_{14}	-8.55					-19.17			
C_{15}				-5.25					23.50
C_{22}		126.50	136.83	114.50	161.75		187.89	252.33	174.67
C_{23}		29.92	32.92	60.75	53.13		47.35	114.83	83.58
C_{25}				-5.25					20.50
C_{33}	33.48	145.17	27.00	152.33	118.09	137.50	188.69	210.83	141.67
C_{35}				-16.67					49.75
C_{44}	18.76	50.00	24.00	63.33	95.16	25.67	61.89	104.67	79.33
C_{46}				0.67					23.33
C_{55}		72.00	19.00	52.17	64.72		89.46	71.33	64.17
C_{66}	17.48	65.00	19.00	37.00	65.43	27.48	73.84	58.67	54.33
B_V	22.91	82.07	46.35	97.19	98.12	84.96	116.73	136.72	103.07
B_R	22.47	76.78	21.92	91.32	89.54	81.68	110.51	130.61	85.37
B_H	22.69	79.42	34.14	94.25	93.83	83.32	113.62	133.66	94.22
G_V	15.56	59.63	19.71	42.86	66.23	26.05	74.88	68.53	53.79
G_R	10.49	57.50	15.27	37.82	60.89	13.96	72.37	62.68	39.26
G_H	13.03	58.56	17.49	40.34	63.56	20.01	73.63	65.60	46.53
E_V	38.05	144.01	51.79	112.10	162.20	70.91	185.07	176.17	137.47
E_R	27.24	138.03	37.17	99.69	148.92	39.62	178.21	162.10	102.14
E_H	32.65	141.02	44.48	105.90	155.56	55.26	181.64	169.13	119.80
B/G_V	1.47	1.38	2.35	2.27	1.48	3.26	1.56	1.99	1.92
B/G_R	2.14	1.34	1.44	2.42	1.49	5.85	1.53	2.08	2.17
B/G_H	1.74	1.36	1.95	2.34	1.48	4.16	1.54	2.04	2.02

The positive elastic constants of the orthorhombic systems satisfy the necessary conditions for stability described in section 2.6.4.1, suggesting mechanical stability of

orthorhombic systems. This is in good agreement with the phonon dispersion curves where we observed few negative vibrations along high symmetry lines for orthorhombic systems. The trigonal *P3₁21*-$CoPO_4$ system also satisfies the necessary stability criterion, however we note a negative value on C_{14} (-8.55 GPa) elastic constant. Moreover, the elastic constant C_{44} (18.76 GPa) is greater than $\frac{C_{11}-C_{12}}{2}$ (17.48 GPa), suggesting degeneration in the transverse branch in the phonon dispersion curves. These are in good agreement with the negative vibrations observed on the negative vibrations of *P3₁21*-$CoPO_4$. Lastly, we note that *P2₁/c*-$CoPO_4$ does not satisfy the necessary conditions for stability as that the criteria, $\left(C_{35}C_{55}-C_{35}^2\right)>0$ is not satisfied. This criteria give a values less than zero (-1142.80), suggesting mechanical instability. The mechanical instability is in good agreement with the soft modes observed on phonon dispersion curves.

The macroscopic bulk, shear and Young's moduli and the Pugh ratio are presented in table 4-3. It is clear to note that the Voigt, Reuss and Hill of each phase are comparable. We note that *P2₁/c*-$CoPO_4$ (94.25 GPa) polymorph gives the largest average bulk modulus value, while *P3₁21*-$CoPO_4$ gives the lowest value (22.69 GPa). Thus the *P2₁/c*-$CoPO_4$ is the hardest and *P3₁21*-$CoPO_4$ (22.69 GPa) is the least in hardness, while *Pnma*-$CoPO_4$ (79.42 GPa), and *Pbca*-$CoPO_4$ (34.14 GPa) are intermediately hard, respectively in ambient pressure. Similarly to $FePO_4$ polymorphs, we observed that the shear modulus is the limiting parameter for $CoPO_4$ stability, since it is less than the bulk modulus [53]. Moreover, the shear modulus values are positive, suggesting more mechanical stable systems. The Young's modulus suggest that the *Pnma*-$CoPO_4$ system is the stiffest (141.02 GPa), followed by the *P2₁/c*-$CoPO_4$ (105.90 GPa), *Pbca*-$CoPO_4$ (44.48 GPa) and lastly the *P3₁21*-$CoPO_4$ system (32.65 GPa).

Pugh ratio values are also listed in table 4-3. From the perspective of Pugh criteria of critical value 1.75, separating ductility and brittleness, we observe that the trigonal *P3₁21*-$CoPO_4$, orthorhombic *Pnma*-$CoPO_4$ and orthorhombic *Cmcm*-$CoPO_4$ systems are brittle, hence easy to break in ambient pressure. On the other hand, the orthorhombic *Pbca*-$CoPO_4$ and monoclinic *P2₁/c*-$CoPO_4$ systems are ductile, that is malleable in ambient pressure.

Table 4-3 also list the elastic constants (C_{ij}'s), bulk (B), shear (G), and Young's (E) moduli, and Pugh ratio (B/G) for $CoPO_4$ polymorphs in 10 GPa. The elastic properties of $CoPO_4$ in 10 GPa display an remarkable trend, particularly for *P3₁21*-$CoPO_4$ and *Pbca*-$CoPO_4$ where pressure increases all elastic constants. The *Pnma*-$CoPO_4$ is mechanically stable in 10 GPa, since it satisfy all mechanical stability criterion. This is consistent with the phonon dispersion curves as *Pnma*-$CoPO_4$ displays only positive vibrational modes. The *P3₁21*-$CoPO_4$ remains mechanically unstable in 10 GPa, due to negative C_{14} value (-19.17 GPa), corresponding well with negative vibrations. The introduction of 10 GPa pressure stabilises *P2₁/c*-$CoPO_4$, since the stability criteria $\left(C_{35}C_{55} - C_{35}^2\right) > 0$ is satisfied.

The bulk and Young's moduli of *P3₁21*-$CoPO_4$ and *Pbca*-$CoPO_4$ increase with 10 GPa pressure, suggesting that the hardness and stiffness are enhanced, respectively. On the other hand, we observe an insignificant change on the bulk modulus for *Pnma*-$CoPO_4$ and *Cmcm*-$CoPO_4$. The bulk modulus suggests that *Pbca*-$CoPO_4$ (133.66 GPa) is the harder than *Pnma*-$CoPO_4$ (113.62 GPa), *P2₁/c*-$CoPO_4$ (94.22 GPa), *Cmcm*-$CoPO_4$ (93.83) and *P3₁21*-$CoPO_4$ (83.32 GPa), respectively. On the other hand the Young's modulus suggests that *Pmna*-$CoPO_4$ (181.64 GPa) is the stiffest polymorph, while *P3₁21*-$CoPO_4$ (55.26 GPa) is the least in stiffness. *Pbca*-$CoPO_4$ (169.13 GPa), *Cmcm*-$CoPO_4$ (155.56) and *P2₁/c*-$CoPO_4$ (119.80 GPa) are intermediately stiff. The Pugh ratio suggests that *Cmcm*-

$CoPO_4$ and *Pnma*-$CoPO_4$ are brittle, while *P3₁21*-$CoPO_4$, *Pbca*-$CoPO_4$ and *P2₁/c*-$CoPO_4$ are ductile.

$CoPO_4$ polymorphs, particularly *Pnma*-$CoPO_4$ in 10 GPa have shown some controversial elastic properties and modulus; hence a proper description of anisotropy factors will be of good interest. The anisotropy factors A_1, A_2, A_3, A_B , A_G and A^U are calculated and presented in table 4-4.

Table 4-4 Anisotropy factors and Poisson ratio of $CoPO_4$ polymorphs in 0 GPa and 10 GPa.

	0 GPa					10 GPa			
Anisotropy	*P3₁21*	*Pnma*	*Pbca*	*P2₁/c*	*Cmcm*	*P3₁21*	*Pnma*	*Pbca*	*P2₁/c*
A_1	1.07	0.93	0.89		1.69	0.93	0.65	0.73	
A_2	0.83	1.27	0.78		1.49	1.25	1.00	1.22	
A_3	0.27	0.81	0.97		0.93	0.75	-5.01	0.99	
A_B *(%)*		2.73	35.78		4.57		0.95	0.02	
A_G *(%)*		1.71	12.69		4.18		-189.90	0.05	
A^U	2.44	0.23	2.57	0.73	0.53	4.37	-6.53	0.51	2.06
U_H	0.44	0.23	0.28	0.31	0.22	0.45	0.38	0.28	0.29

Generally, we observe that the anisotropy factors suggest that all $CoPO_4$ polymorphs are severely anisotropic in ambient and high pressure. The percentage modulus anisotropies A_B and A_G suggest that *Pnma*-$CoPO_4$ is possibly anisotropic by 2.73 % and 1.71 % in ambient pressure. On the other hand, we note that *Pbca*-$CoPO_4$ is abnormally anisotropic by 35.78 % and 12.69 % for A_B and A_G, respectively, suggesting susceptibility to distortions and dislocations. However, we note a negative value for the percentage shear modulus anisotropy A_G in 10 GPa; this emanate from a negative Voigt shear modulus. Furthermore, we observe that 10 GPa pressure substantially reduces anisotropy for *Pbca*-$CoPO_4$; A_B and A_G are reduced to 0.02 % and 0.05 %, respectively. On the other hand, A_B and A_G show that *Cmcm*-$CoPO_4$ is

possible anisotropic by 4.57 % and 4.18 %, respectively. We note that A_B is greater than A_G for both *Pnma*-$CoPO_4$ and *Cmcm*-$CoPO_4$ in ambient and high pressures; hence more anisotropic in compressibility than in shear. On the contrary, the A_G for *Pbca*-$CoPO_4$ is greater than the A_B in high pressure, suggesting that it is less in shear than in compressibility.

The relatively high values of A^U suggest that *P3₁21*-$CoPO_4$ is substantially anisotropic at both ambient and high pressures. Negative A^U value of *Pnma*-$CoPO_4$ in 10 GPa suggests that this phase does not exist in 10 GPa, since A^U ranges between zero and positive values. However, *Pnma*-$CoPO_4$ approaches anisotropy in ambient pressure (A^U=0.23). Furthermore, we note that *Pbca*-$CoPO_4$ and *P2₁/c*-$CoPO_4$ shows relatively low A^U values at both ambient and high pressures. Lastly, the *Cmcm*-$CoPO_4$ universal value departs from zero by 0.53. The poison ratio υ_H, for isotropic materials was also calculated from bulk and shear moduli and found to be generally increasing with pressure for $CoPO_4$ polymorphs.

4.2.3 Elastic Properties of $MnPO_4$ Polymorphs

Table 4-5 lists the DFT results on elastic constants (C_{ij}), bulk (B), shear (G), and Young's (E) moduli and Pugh ratio for $MnPO_4$ polymorphs in 0 GPa. Considering Born stability criterion of the elastic constants in trigonal, monoclinic and orthorhombic systems, it is clearly seen that all $MnPO_4$ polymorphs, except C*mcm*-$MnPO_4$ are mechanically stable in ambient pressure, since all criterion are relatively satisfied. We note a negative elastic constant C_{55}>0 (-126.02 GPa) for C*mcm*-$MnPO_4$, corresponding well with the phonon

negative vibrations. The macroscopic bulk, shear and Young's moduli were obtained using Voigt-Reuss-Hill method from our calculated elastic constants [154].

Table 4-5 DFT+*U* results on elastic constants (C_{ij}), bulk (B), shear (G), and Young's (E) moduli, Pugh ratio (B/G) $MnPO_4$ polymorphs in 0 GPa and 10 GPa.

	0 GPa					10 GPa			
C_{ij} (GPa)	*$P3_121$*	*Pnma*	*Pbca*	*$P2_1/c$*	*Cmcm*	*$P3_121$*	*Pnma*	*Pbca*	*$P2_1/c$*
C_{11}	51.79	202.83	75.83	121.33	242.76	105.17	231.17	109.50	171.17
C_{12}	25.03	43.17	24.08	54.58	55.45	56.25	80.08	71.58	99.75
C_{13}	36.59	64.92	22.33	60.67	61.60	54.92	90.75	45.17	94.25
C_{14}	04.87					-15.08			
C_{15}				25.50					31.92
C_{22}		231.50	90.33	117.67	135.33		245.00	195.83	252.2
C_{23}		25.50	34.33	54.83	40.90		78.58	75.25	125.92
C_{25}				9.750					18.58
C_{33}	84.06	106.83	45.50	125.83	128.72	131.50			154.83
C_{35}				19.25			198.83	147.67	29.08
C_{44}	21.13	31.33	28.67	70.33	97.02	24.17	44.00	38.33	44.00
C_{46}				14.00					24.67
C_{55}		71.67	18.33	38.67	-126.02		102.67	27.00	64.50
C_{66}	13.38	48.67	62.67	41.67	46.99	24.48	25.33	67.33	85.67
B_V	42.68	89.81	41.46	78.33	91.41	74.89	130.43	93.00	135.33
B_R	38.35	80.06	37.69	69.59	82.76	74.21	129.72	83.67	113.37
B_H	40.51	84.94	39.58	73.96	87.09	74..55	130.07	88.34	124.35
G_V	17.09	57.51	30.66	43.12	26.85	26.27	62.77	43.93	56.05
G_R	14.96	48.52	23.03	37.06	81.55	16.83	49.62	39.30	44.56
G_H	16.02	53.01	26.84	40.09	54.20	21.55	56.19	41.62	50.31
E_V	45.23	142.17	73.79	109.30	73.38	70.57	162.28	113.87	147.75
E_R	39.71	121.09	57.39	94.41	184.16	46.95	132.02	101.93	118.20
E_H	42.47	131.63	65.59	101.86	128.77	58.76	147.15	107.90	132.98
B/G_V	2.50	1.56	1.35	1.82	3.40	2.85	2.08	2.12	2.41
B/G_R	2.56	1.65	1.64	1.88	1.02	4.41	2.61	2.13	2.54
B/G_H	2.53	1.60	1.48	1.85	1.61	3.46	2.32	2.12	2.47

We note that the bulk's Voigt, Reuss and Hill of all phases are relatively comparable. Similarly to $FePO_4$ and $CoPO_4$ structural polymorphs, our calculated bulk modulus suggests that *Pnma*-$MnPO_4$ is the hardest material in ambient pressure, since it shows the largest bulk modulus value (84.94 GPa). However, in contrary to the observations for $CoPO_4$ polymorphs, *Pbca*-$MnPO_4$ is the least (39.58 GPa) material in hardness, while *P2₁/c*-$MnPO_4$ (73.96 GPa) and *P3₁21*-$MnPO_4$ (40.51 GPa) are intermediating materials in hardness, respectively. The trend of hardness in $MnPO_4$ polymorphs is comparable to the trend of $FePO_4$ polymorphs. Moreover, the Young's modulus suggests that the *Pnma*-$MnPO_4$ is the most stiff (131.63 GPa) polymorph, while *P2₁/c*-$MnPO_4$ (101.86 GPa), *Pbca*-$MnPO_4$ (65.59 GPa) and *P3₁21*-$MnPO_4$ (42.47 GPa) are subsequently stiff. We note that the hardness trend is different from the stiffness trend for $MnPO_4$ polymorphs.

The Pugh brittle/ductility criterion suggests that the trigonal *P3₁21*-$MnPO_4$ and monoclinic *P2₁/c*-$MnPO_4$ polymorphs are ductile, while the orthorhombic *Pnma*-$MnPO_4$ and *Pbca*-$MnPPO_4$ are brittle in ambient pressure. The elastic properties of $MnPO_4$ polymorphs in 10 GPa pressure provide a noteworthy trend. In contrary with $FePO_4$ and $CoPO_4$ structural polymorphs we note that the independent elastic constants for $MnPO_4$ polymorphs increase in 10 GPa pressure, except for C_{66} and C_{44} for *Pnma*-$MnPO_4$ and *P2₁/c*-$MnPO_4$, respectively. Moreover, we observe that all elastic constants satisfy the necessary stability conditions for four $MnPO_4$ polymorphs, suggesting mechanical stability. However, this is not in good agreement with the phonon dispersion curves. On the other hand, we note that *Cmcm*-$MnPO_4$, displays a negative C_{55} value (-126.02 GPa), which does not satisfy the stability criteria $C_{55} > 0$; hence *Cmcm*-$MnPO_4$ is mechanical unstable. We also note that C_{14} for *P3₁21*-$MnPO_4$ becomes negative in 10 GPa (-15.08 GPa), implying mechanical instability. Moreover, we observe that the respective macroscopic bulk, shear and Young's moduli also increase in 10 GPa pressure, suggesting

that the hardness and stiffness of $MnPO_4$ polymorphs are enhanced. Consequently, the Pugh ratio of ductility and brittleness rises, as we observe that all B/G values are greater than 1.75; hence all polymorphs are ductile in 10 GPa. Furthermore, it can be observed that the shear and Young's moduli of *Cmcm*-$MnPO_4$ shows irregular pattern of values, as the Voigt upper bound is less than the Reuss lower bound; the shear Voigt upper bound and Reuss lower bound values are 26.85 GPa and 54.20 GPa while the Young's Voigt upper bound Reuss lower bound values are 73.38 GPa and 184.16 GPa, respectively. Consequently, the Pugh ratio is less than 1.75; hence *Cmcm*-$MnPO_4$ is brittle.

Similarly to $CoPO_4$ polymorphs, $MnPO_4$ polymorphs have shown some discordant elastic properties, with C_{55} of *Cmcm*-$MnPO_4$ being the most notable irregularity. $MnPO_4$ polymorphs are materials with relatively low moduli and large difference between Voigt upper bound and Reuss lower bound resulting in large percentage modulus anisotropy, particularly for shear.

In ambient pressure (table 4-5), we note that all $MnPO_4$ polymorphs are relatively anisotropic. This is made evident by the anisotropy factors values which are far from unity by reasonably large variances.

Table 4-6 Anisotropy factors and Poisson ration of $MnPO_4$ polymorphs in 0 GPa and 10 GPa.

	0 GPa					10 GPa			
Anisotropy	*$P3_121$*	*Pnma*	*Pbca*	*$P2_1/c$*	*Cmcm*	*$P3_121$*	*Pnma*	*Pbca*	*$P2_1/c$*
A_1	1.58	0.63	0.69		0.78	0.99	0.71	0.44	
A_2	1.62	1.04	0.44		-2.77	1.25	1.43	0.56	
A_3	0.68	0.61	2.12		0.70	1.02	0.32	1.66	
A_B *(%)*		3.46	4.76		4.73		0.27	0.05	
A_G *(%)*		8.03	14.2		50.46		11.70	0.06	
A^U	0.83	1.05	1.76	0.94	-3.30	2.81	1.33	0.70	1.48
U_H	0.48	0.20	0.22	0.27	0.24	0.34	0.31	0.30	0.32

The percentage anisotropy in compressibility and shear show that the orthorhombic $MnPO_4$ polymorphs are less anisotropic in compressibility than in shear at both ambient and high pressures. In concurrence with the anisotropy factors, the percentage anisotropy shows that the *Cmcm*-$MnPO_4$ is largely anisotropic, as we observe the anisotropic possibility of 4.73 % and 50.46 % for bulk and shear, respectively. Therefore, shear distortions and dislocations will take place easily. Moreover, the percentage anisotropy of *Pbca*-$MnPO_4$ is substantially enhanced in high pressure. In ambient pressure A_B and A_G diverge from zero by 4.76 % and 14.21 %, while diverging by 0.05 % and 0.06 % in high pressure, respectively.

The universal anisotropy index suggests that *Cmcm*-$MnPO_4$ does not exist, since it has a negative A^U value (table 4-6). The other polymorphs i.e. *P2₁/c*-$MnPO_4$, *P3₁21*-$MnPO_4$, *Pnma*-$MnPO_4$ and *Pbca*-$MnPO_4$ are substantially anisotropic in ambient pressure, respectively. In high pressure, we note that the universal anisotropy index decreases for *Pbca*-$MnPO_4$, while increases for *Pnma*-$MnPO_4$, *P2₁/c*-$MnPO_4$ and *P3₁21*-$MnPO_4$, respectively. The Poison ratio υ_H was also obtained from the elastic moduli and presented in table 4-6. The pressure dependent Poison ratio decreases with pressure for *P3₁21*-$MnPO_4$ and increases with pressure for *Pbca*-$MnPO_4$, *Pnma*-$CoPO_4$ and *P2₁/c*-$MnPO_4$, respectively.

Chapter 5

Structural, Electronic, and Mechanical Properties of $LiMPO_4$ Polymorphs

In this chapter, we present the structural, thermodynamic, electronic and mechanical properties of $LiMPO_4$ (M=Co, Fe, Mn) structures and their respective polymorphs. Furthermore, we will deduce their respective stability trends with respect to heats of formation, density of states, elastic constants and phonon dispersion curves. We will also determine the effect of lithium intercalation on MPO_4.

5.1 $LiMPO_4$ Structural and Thermodynamic Properties

5.1.1 $LiFePO_4$ Polymorphs

In table 5-1 we compare experimental and optimised lattice parameters, cell volumes and heats of formation of $LiFePO_4$ polymorphs. It is clear that our DFT+*U* calculated values slightly underestimate the experimental lattice parameters. Consequently the calculated cell volumes are smaller than the experimental cell volumes by 0.17 % and 7.80 % for *Pnma*-$LiFePO_4$ and *Cmcm*-$LiFePO_4$, respectively. No experimental data have been recorded on the $P3_121$-$LiFePO_4$, *Pbca*-$LiFePO_4$ and $P2_1/c$-$LiFePO_4$ polymorphs. The equilibrium lattice parameters and cell volumes for $FePO_4$ polymorphs change minimally during lithium insertion, since the removal and addition

of Li^+ ions from $LiMPO_4$ does not change the coordination of the structure. Our DFT+*U* calculations indicate that the *a* and *b* become longer while *c* become shorter during Li insertion for *P3₁21*-$FePO_4$, *Pnma*-$LiFePO_4$ and *Cmcm*-$LiFePO_4$ polymorphs ($FePO_4$ lattice values are presented in chapter 3) which are consistent with experimental findings and previous calculations [192]. On the other hand, we note that the *a* and *c* contract while *b* expands for *Pbca*-$FePO_4$. We also note that *b* and *c* expand while *a* contracts for *P2₁/c*-$FePO_4$.

In ambient pressure, we note that the equilibrium cell volumes for *P3₁21*-$FePO_4$, *Pnma*-$FePO_4$ and *P2₁/c*-$FePO_4$ increase by 0.97 %, 4.86 % and 20.53 %, respectively when Li is inserted. In contrast, the equilibrium cell volumes for *Pbca*-$FePO_4$ and *Cmcm*-$LiFePO_4$ decrease by 15.78 % and 3.52 %, respectively.

Table 5-1 Calculated and experimental lattice parameters, cell volume and heats of formation of $LiFePO_4$ polymorphs in 0 GPa. The experimental values are given in parenthesis.

Symmetry	*P3₁21*	*Pnma*	*Pbca*	*P2₁/c*	*Cmcm*
a (Å)	5.41	10.38 (10.40)[a]	8.31	5.47	5.40 (5.52)[b]
b		6.06 (6.05)[a]	9.82	8.51	8.08 (8.26)[b]
c	10.24	4.71 (4.73)[a]	8.09	8.88	5.95 (6.16)[b]
V ($Å^3$)	259.69	295.98 (291.61)[a]	660.23	412.34	259.66 (280.87)[b]
				β=86.41°	
Hf (kJ/mol)	-1105.82	-1184.49	-1977.30	-1972.26	-1161.30

[a] [36] [b] [201]

In 10 GPa, we note an equilibrium volume expansion by 26.79 %, 10.43 %, 11.80 % and 2.51 %, respectively for *P3₁21*-$FePO_4$, *Pnma*-$FePO_4$, *Pbca*-$FePO_4$ and *Cmcm*-$FePO_4$, while the cell volume of *P2₁/c*-$FePO_4$ contracts by 2.12 % when Li is inserted. According to the study by Wolverton *et al*. [202], the volume of $LiCoO_2$ unit cell increases by 14 % when delithiation is complete in ambient pressure. Since volume

changes of $P3_121$-$LiFePO_4$, *Pnma*-$LiFePO_4$ and *Cmcm*-$LiFePO_4$ are less than that of $LiCoO_2$, we deduce that these $LiFePO_4$ phases are more stable during lithium insertion/extraction process than $LiCoO_2$. This minimal volume change suggests structural stability which ensures excellent tolerance of $LiFePO_4$ to the good reversibility and long life cycle [203]. We note that the volume trend of $FePO_4$ phases is slightly altered after lithium insertion; *Cmcm*-$LiFePO_4$ phase is marginally smaller than $P3_121$-$LiFePO_4$ phase in ambient pressure. The volume size trend can be summarised as follows in 0 GPa:

$$Pbca > P2\_1/c > Pnma > P3_121 > Cmcm$$

We further observe that *Pbca*-$LiFePO_4$ and *Cmcm*-$LiFePO_4$ still show largest and least volume size, respectively in high pressure. The volume size trend can be summarised as follows in 10 GPa:

$$Pbca > Pnma > P3_121 > P2\_1/c > Cmcm$$

The trigonal $P3_121$-$LiFePO_4$ phase shows lattice parameters 5.41 Å and 10.24 Å for *a* and *c*, respectively resulting in an equilibrium volume of 259.69 $Å^3$ in ambient pressure. The calculated cell volumes for *Pnma*-$LiFePO_4$ and *Cmcm*-$LiFePO_4$ underestimate the experimental data by 0.17 % and 7.85 %, respectively. The application of 10 GPa pressure on $LiFePO_4$ polymorphs shows some unexpected volume expansion and contractions (table 5-2). We note that the equilibrium cell volume of $P3_121$-$LiFePO_4$ slightly expands by 1.26 %, while the cell volumes of *Pnma*-$LiFePO_4$, *Pbca*-$LiFePO_4$, $P2_1/c$-$LiFePO_4$ and *Cmcm*-$LiFePO_4$ expectedly contracts by 7.12 %, 15.23 %, 46.56 % and 5.34 %, respectively. The percentage volume contraction indicates that $P2_1/c$-$LiFePO_4$ is the most compressible polymorphs in 10 GPa pressure. Heats of formation were calculated and presented in table 5-1 and table 5-2 in ambient and high pressures, respectively using equation 5.1.

Table 5-2 Calculated and experimental lattice parameters, cell volume and heats of formation of $LiFePO_4$ polymorphs in 10 GPa.

Symmetry	*$P3_121$*	*Pnma*	*Pbca*	*P21_/c*	*Cmcm*
a (Å)	5.18	10.02	7.90	5.53	5.31
b		5.91	9.66	6.68	7.96
c	9.79	4.58	7.44	7.40	5.82
V ($Å^3$)	227.49	271.02	567.19	256.67	246.10
Hf (kJ/mol)	-616.65	-757.95	-1046.59	-1061.89	-756.90

$$\Delta H_f\left(LiFePO_4\right)=\left[E-\left(E_{Li}+E_{Fe}+E_P+4E_O\right)\right] \qquad 5.1$$

We note that the heats of formation values decrease with Li intercalation for all polymorphs at both ambient and high pressures, thus enhancing stability of $FePO_4$ polymorphs. However, Li intercalation alters the stability trend at both ambient and high pressures. We observe *Pbca*-$LiFePO_4$ (-1977.30 kJ/mol) polymorph to be the most stable polymorph over *$P2_1/c$*-$LiFePO_4$ (-1972.26 kJ/mol), *Pnma*-$LiFePO_4$ (-1184.49 kJ/mol), *Cmcm*-$LiFePO_4$ (-1161.30 kJ/mol) and *$P3_121$*-$LiFePO_4$ (-1105.82 kJ/mol), respectively in 0 GPa. The stability trend is summarised as follows:

$$Pbca > P2\_1/c > Pnma > Cmcm > P3_121$$

In 10 GPa we note that the stability trend is slightly altered as we observe that *$P2_1/c$*-$LiFePO_4$ is the most stable polymorph with the lowest heat of formation value:

$$P2\_1/c > Pbca > Pnma > Cmcm > P3_121$$

5.1.2 $LiCoPO_4$ Polymorphs

The calculated and experimental lattice parameters and cell volumes for $LiCoPO_4$ in ambient pressure (0 GPa) are compared in table 5-3. It is observed that calculated lattice parameters *a* and *c* overestimated compared to experimental values by 2.13 %

and 0.74 %, while *b* underestimated by 0.63 % for the *Pnma*-$LiFePO_4$. Consequently, the calculated equilibrium cell volume is slightly larger than the experimental value by 2.23 %. No experimental values have been recorded so far for the other $LiCoPO_4$ polymorphs.

Our DFT+*U* calculations indicate that the *a* for $P3_121$, *Pnma* and *cmcm* symmetries and the *b* for *Pbca* and $P2_1/c$ symmetries are stretched during lithium interaction. On the other hand, the *a* for *Pbca* and $P2_1/c$ symmetries, *b* for *Pnma* symmetry and *c* for all $CoPO_4$ symmetries are contracted during lithium insertion.

Table 5-3 Calculated and experimental lattice parameters, cell volume and heats of formation of $LiCoPO_4$ polymorphs in 0 GPa. The experimental values are given in parenthesis.

Symmetry	$P3_121$	*Pnma*	*Pbca*	$P2_1/c$	*Cmcm*
a (Å)	5.26	10.42 (10.20)[c]	8.27	5.44	5.48
b		5.88 (5.92)[c]	9.69	8.45	8.25
c	10.87	4.74 (4.70)[c]	8.32	8.85	6.25
V ($Å^3$)	260.72	290.35 (283.80)[c]	667.16	406.35	282.36
				$\beta=87.53^\circ$	
H_f (kJ/mol)	-1064.22	-1097.25	-1769.37	-1768.26	-1124.58

[c] [5]

As a result the equilibrium cell volumes for $P3_121$-$LiCoPO_4$, *Pnma*-$LiCoPO_4$, $P2_1/c$-$LiCoPO_4$ and *Cmcm*-$LiCoPO_4$ expand by 0.58 %, 4.47 %, 17.41 % and 7.19 % respectively, while the cell volume for *Pbca*-$LiCoPO_4$ contracts by 14.24 %. Experimental findings also show a volume change to within 2.87 % for *Pnma*-$LiCoPO_4$ [204]. The minimal volume changes for $P3_121$-$LiCoPO_4$, *Pnma*-$LiCoPO_4$, and *Cmcm*-$LiCoPO_4$ suggest that these polymorphs are stable during the lithium insertion/extraction process and ensure excellent tolerance of good reversibility and long life cycle [203]. Interestingly, we note that the volume size trend for $CoPO_4$

polymorphs remain unchanged after lithium insertion in ambient pressure. The volume trend is summarised below:

$$Pbca > P2\_1/c > Pnma > Cmcm > P3_121$$

The effect of the external pressure (10 GPa) on lattice parameters and equilibrium cell volume of $LiCoPO_4$ polymorphs has been also investigated and presented in table 5-4. In high pressure, we note that *P3₁21*-$LiCoPO_4$, *Pnma*-$LiCoPO_4$, *Pbca*-$LiCPO_4$ and *Cmcm*-$LiCoPO_4$ expand by 12.00 %, 11.73 %, 9.43 % and 7.19 %, respectively, while *P2₁/c*-$LiCoPO_4$ contract by 4.60 %. These minimal volume changes ensure good reversibility during charge/discharge process and long life cycle [203]. The volume trend is summarised as follows in 10 GPa:

$$Pbca > Pnma > Cmcm > P2\_1/c > P3_121$$

Table 5-4 Calculated and experimental lattice parameters, cell volume and heats of formation of $LiCoPO_4$ polymorphs in 10 GPa.

Symmetry	*P3₁21*	*Pnma*	*Pbca*	*P2₁/c*	*Cmcm*
a (Å)	4.96	10.05	7.68	5.53	5.37
b		5.74	9.83	5.49	8.11
c	10.41	4.61	7.34	9.20	6.03
V (Å^3)	221.92	265.93	553.94	250.41	263.02
H_f (kJ/mol)	-581.12	-678.80	-875.77	-920.81	-707.19

The heats of formation of $LiCoPO_4$ in ambient and high pressures are calculated using equation 5.2 and are presented in table 5-3 and 5-4 respectively.

$$\Delta H_f\left(LiCoPO_4\right) = \left[E - \left(E_{Li} + E_{Co} + E_P + 4E_O\right)\right] \qquad 5.2$$

Similarly to $LiFePO_4$ polymorphs, we note that the heats of formation for $LiCoPO_4$ drops when lithium is intercalated at both ambient and high pressures, suggesting that

lithium insertion enhances thermodynamic stability of $CoPO_4$ polymorphs. However, the stability trend is altered after lithium intercalation. The heats of formation suggests that *Pbca*-$LiCoPO_4$ (-1769.37 kJ/mol) is preferred for stability over *P2₁/c*-$LiCoPO_4$ (-1768.26 kJ/mol), *Cmcm*-$LiCoPO_4$ (-1124.58 kJ/mol), *Pnma*-$LiCoPO_4$ (-1097.25 kJ/mol) and *P3₁21*-$LiCoPO_4$ (-1064.22 kJ/mol), respectively in 0 GPa. The stability trend is summarised as follows:

$$Pbca > P2\_1/c > Cmcm > Pnma > P3_121$$

The predicted heats of formation values in 10 GPa shows that *P2₁/c*-$LiCoPO_4$ (-920.81 kJ/mol) is the most stable polymorph over *Pbca*-$LiCoPO_4$ (-875.77 kJ/mol), *Pnma*-$LiCoPO_4$ (-678.80 kJ/mol) and *P3₁21*-$LiCoPO_4$ (-581.12 kJ/mol), respectively.

$$P2\_1/c > Pbca > Cmcm > Pnma. > P3_121$$

5.1.3 $LiMnPO_4$ Polymorphs

The equilibrium lattice parameters and cell volumes for $LiMnPO_4$ in ambient pressure are presented in table 5-5. Similarly to *Pnma*-$LiFePO_4$, we observe that the calculated DFT+*U* lattice parameters *a*, *b* and *c* are slightly underestimated compared to the experimental values by 3.18 %, 2.65 % and 1.62 %, respectively for *Pnma*-$LiMnPO_4$. It should be noted that the calculated equilibrium cell volume compares well with the experimental cell volume to within 7.42 %, which is accepted for DFT calculations [9, 177, 178]. We also note that the lattice parameter *a* increases for *P3₁21*-$LiMnPO_4$, *Pnma*-$LiMnPO_4$ and *Cmcm*-$LiMnPO_4$ while it is small for *Pbca*-$LiMnPO_4$ and *P2₁/c*-$LiMnPO_4$ polymorphs. In contrast to $LiFePO_4$ and $LiCoPO_4$ structures, $LiMnPO_4$ polymorphs show that the lattice parameters change by almost similar value for *b* and *c*: the *b* expands while the *c* contracts during lithium intercalation.

Table 5-5 Calculated and experimental lattice parameters, cell volume and heats of formation of $LiMnPO_4$ polymorphs in 0 GPa. The experimental values are given in parenthesis.

Symmetry	*$P3_121$*	*Pnma*	*Pbca*	*$P2_1/c$*	*Cmcm*
a (Å)	5.33	10.52 (10.86)	8.21	5.247	5.59
b		6.12 (6.28)	10.19	8.046	8.44
c	11.02	4.78 (4.86)	7.86	7.765	6.29
V ($Å^3$)	246.93	307.32 (331.22)	657.99	327.1	296.85
				β=86.23 °	
H_f (kJ/mol)	-1265.96	-1340.45	-2208.62	-2124.00	-1328.29

[d] [42]

Moreover, it is noted that the equilibrium cell volumes are slightly changed by 4.80 %, 6.79 %, 0.92 %, 3.54 % and 0.30 % for *$P3_121$*-$MnPO_4$, *Pnma*-$MnPO_4$, *Pbca*-$MnPO_4$, *$P2_1/c$*-$MnPO_4$ and *Cmcm*-$MnPO_4$, respectively. These relatively less changes of equilibrium cell volumes suggest excellent tolerance of good reversibility during lithium insertion/extraction process and long life cycle for the material [203]. On the other hand, it can be noted that the volume size trend is slightly changed during lithium intercalation; we observe smallest volume change for *Cmcm*-$LiMnPO_4$ and can be summarised as follows:

$$Pbca > P2\_1/c > Pnma > Cmcm > P3_121$$

Furthermore, we note that the equilibrium cell volumes for *Pnma*-$MnPO_4$, *Pbca*-$MnPO_4$ and *$P2_1/c$*-$MnPO_4$ slightly change by 6.48 %, 9.60 % and 1.12 % when lithium is intercalated in 10 GPa, indicating good reversibility and long life cycle in high pressure. On the other hand, the cell volume for *$P3_121$*-$MnPO_4$ changes enormously by 18.93 % when lithium is inserted. This suggests poor reversibility during operation and short life cycle. We further note that the cell volume trend remains unaltered in 10 GPa. The heats of formation for $LiMnPO_4$ polymorphs were also calculated in ambient and high pressures, respectively.

$$\Delta H_f\left(LiMnPO_4\right)=\left[E-\left(E_{Li}+E_{Mn}+E_P+4E_O\right)\right] \qquad 5.3$$

Similarly to $LiFePO_4$ and $LiCoPO_4$ polymorphs, we observe that lithium insertion significantly decrease the heats of formation values of $LiMnPO_4$ polymorphs; as a result, the thermodynamic stability trend changes. The *Pbca*-$LiMnPO_4$ shows the lowest heat of formation value (-2208.62 kJ/mol), while *P3₁21*-$LiMnPO_4$ displays the highest value (-1265.96 kJ/mol), suggesting that *Pbca*-$LiMnPO_4$ and *P3₁21*-$LiMnPO_4$ are the most and least thermodynamically stable polymorphs, respectively. Moreover, *P2₁/c*-$LiMnPO_4$ (-2124.00 kJ/mol), *Pnma*-$LiMnPO_4$ (-1340.45 kJ/mol) and *Cmcm*-$LiMnPO_4$ (-1328.29 Kj/mol) are intermediately metastable. The thermodynamic stability trend in 0 GPa is summarised as follows:

$$Pbca > P2\_1/c > Pnma > Cmcm > P3_121$$

When external pressure is applied, we note that the stability trend is slightly shifted as *P2₁/c*-$LiMnPO_4$ (-1360.65 kJ/mol) is the most stable polymorph over *Pbca*-$LiMnPO_4$ (-1272.78 kJ/mol), *Pnma*-$LiMnPO_4$ (-919.02 kJ/mol) and *P3₁21*-$LiMnPO_4$ (-753.88 kJ/mol), respectively.

$$P2\_1/c > Pbca > Pnma > Cmcm > P3_121$$

Table 5-6 Calculated and experimental lattice parameters, cell volume and heats of formation of $LiMnPO_4$ polymorphs in 10 GPa.

Symmetry	*P3₁21*	*Pnma*	*Pbca*	*P2₁/c*	*Cmcm*
a (Å)	5.05	10.12	7.62	5.47	5.47
b		5.97	10.07	6.10	8.23
c	10.46	4.63	7.41	7.50	6.12
V (Å^3)	231.14	279.76	568.72	249.72	275.09
H_f (kJ/mol)	-753.88	-919.02	-1272.78	-1360.65	-891.16

5.2 $LiMPO_4$ Electronic Density of States

The development of $LiFePO_4$ as a future cathode material for lithium ion batteries has been greatly hindered by low electronic conductivity and poor charge/discharge rate performance. Since the discovery of the conductivity hindrances, much effort has been made to improve its conductivity properties. In 2002, Chung *et al*. found that replacing a small amount of high-valence metal ions for lithium ions substantially improves the electronic conductivity of $LiFePO_4$ [10]. Shi *et al*. in 2003 further explained these observations using first-principles calculations, and proposed two mechanisms to improve electronic conductivity, i.e. the conventional *p*-type doping conductivity and electron hopping within a cluster surrounding the doping atom [205].

Jiang *et al*. showed that lithium intercalation narrows the energy band gap employing the normal GGA approach [192]. Furthermore, the study conducted by Zhou *et al*. on the electronic structure of $LiFePO_4$ and $LiMnPO_4$ has also shown that the band gap becomes wider with lithium intercalation. It was revealed that the DFT+*U* generally generates larger and more accurate band gaps and becomes narrow with the normal DFT [50].

5.2.1 $LiFePO_4$ Density of States

Figures 5-1 to 5-5 show calculated spin polarised partial and total densities of states (DOS) of $LiFePO_4$ polymorphs in ambient (0 GPa) and high pressures (10 GPa). In general, we note that for all $LiFePO_4$ polymorphs, the Fermi level falls within the Fe 3*d* band, suggesting semi-metallic characteristics. This observation is in good agreement with the DOS presented by Xu *et al*. The olivine *Pnma*-$LiFePO_4$ showed

metallic characteristics with the Fermi level falling in the majority spin band and in the t_{2g} minority spin band [206]. This is in contrast to unlithiated structural polymorphs discussed in section 3.3.1, which have the Fermi levels falling on the upper valence bands. This observation suggests that Li insertion enhances the electronic conductivity of $FePO_4$ polymorphs. It was also seen that the spin-down Fe *d*-electron below the Fermi level contributes to the spin-down energy band of $LiFePO_4$. Thus, the Fe *d*-electrons have an influence on the total densities of states. This suggests that the electronic conductivity of $LiFePO_4$ can be enhanced by introducing excessive *d*-electrons. The P and O *p*-electrons have less contribution on the total density of states, in particular around the Fermi level. From the partial densities of states, we observe that the covalent bonding between Fe 3*d* and O 2*p* orbitals is greater in $FePO_4$ polymorphs than in $LiFePO_4$ polymorphs.

First-principles study on electronic structure of $LiFePO_4$ by Jiang *et al*. [192] showed that nearly 0.21 of lithium electron is transferred to Fe atom, 0.09 electrons to O atom, but none to P atom, supposing that the radii of the Fe, O and P atoms are 0.82 Å, 1.42 Å and 0.80 Å, respectively. This suggests that lithium intercalation hardly affects the electronic structure of P atom. The distribution of Li electron was determined by constructing a virtual compound $FePO_4$-II with the same crystalline form as $LiFePO_4$ except that all lithiums are removed. Then the integral of the valence electron of each atom was calculated within $LiFePO_4$ and $FePO_4$-II.

The *P*3_121-$LiFePO_4$ polymorph shows a band gap of 1.65 eV at both ambient and high pressures (Figure 5-1). Thus, the 'rigid-band approach' applies in these structures [167], where the electronic structure is fixed and the position of the Fermi level is shifted with the increase in the number of electrons. It was also observed that in 10 GPa pressure, no significant effect are observed, since the energy band gap remains

unchanged. We note that the energy band gap becomes narrow with lithium insertion; this is due to the creation of the spin-down energy band. The delithiated $P3_121$-$FePO_4$ showed band gaps of 2.15 eV and 2.22 eV in ambient and high pressures, respectively. The location of the Fermi level on the Fe 3*d* band suggests that $P3_121$-$LiFePO_4$ has a semi-metallic characteristic. Moreover, the total density of states around the Fermi level is reduced when lithium is intercalated, indicating that lithium intercalation stabilises the structure. It is also apparent to note that the total DOS is contracted from a range of approximately $-40 \le 0 \le 60$ to approximately $-20 \le 0 \le 20$.

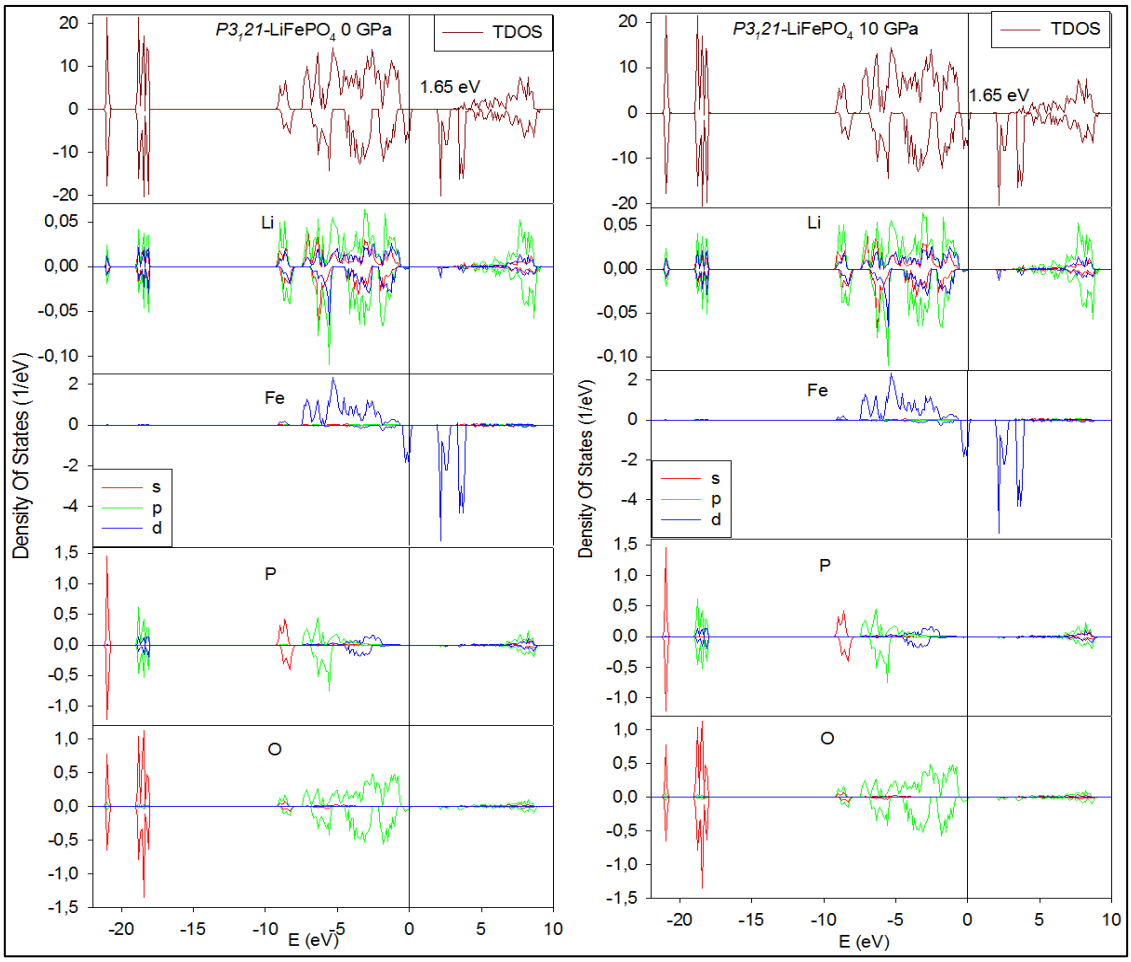

Figure 5-1 Total and partial DOS of $P3_121$-$LiFePO_4$ polymorph, at (a) 0 GPa and (b) 10 GPa. The Fermi level is taken as energy zero ($E-E_F=0$).

The total and partial DOS of *Pnma*-$LiFePO_4$ are presented in Figure 5-2. We observed band gaps of 1.86 eV and 2.10 eV in ambient and high pressures, respectively. The Fermi level is located on the spin-down Fe 3*d* band, suggesting that *Pnma*-$LiFePO_4$ has a semi-metallic behaviour, which is a good condition for electronic conductivity of this material. We note that the energy band gap becomes wide when lithium is inserted into *Pnma*-$FePO_4$ in ambient and high pressures. The band gap increases from 1.75 eV to 1.86 eV in ambient pressure and from 1.52 eV to 2.10 eV in high pressure. The predicted band gaps are in good agreement with the findings that lithiated olivines gives wider band gaps than delithiated [50, 51]. This also confirms that DFT+*U* calculations give more wider and accurate band gaps for the transition metal phosphates. On the other hand, our DFT+*U* findings dispute the normal DFT suggestion that lithium intercalation narrows the band gaps as recorded by Jiang *et al*. [192].

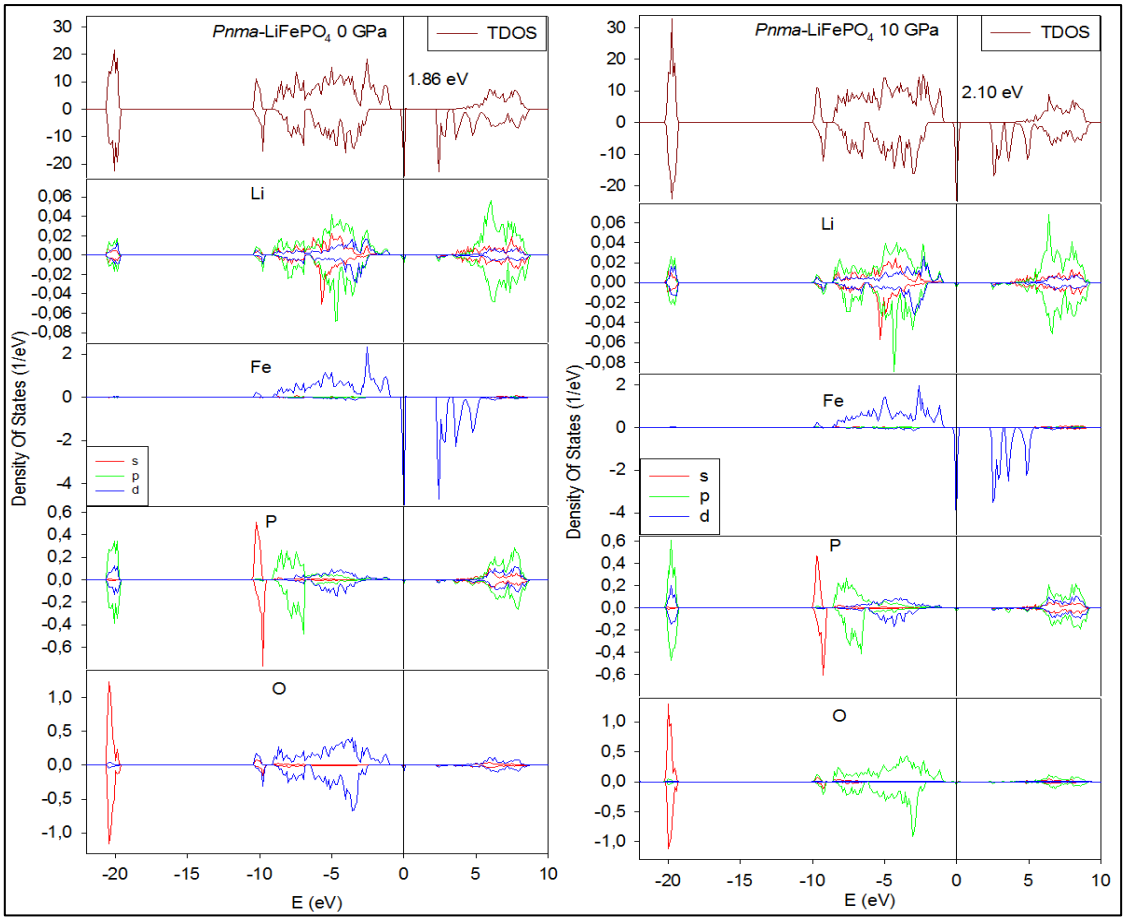

Figure 5-2 Total and partial DOS of *Pnma*-$LiFePO_4$ polymorph, at (a) 0 GPa and (b) 10 GPa. The Fermi level is taken as energy zero ($E-E_F=0$).

Figure 5-3 shows the calculated total and partial density of states for *Pbca*-$LiFePO_4$ in ambient and high pressures. In contrast, to *P3₁21*-$LiFePO_4$ and *Pnma*-$LiFePO_4$, no band gap is observed. Interesting, *Pbca*-$LiFePO_4$ shows a continuous flow of electrons from the valence band to the conduction band at both ambient and high pressures. Furthermore, the Fermi level is located on the spin-down Fe 3*d* band, suggesting that *Pbca*-$LiFePO_4$ has metallic behaviour which is good for electronic conductivity of the material. The absence of energy band gap suggests that lithium intercalation significantly enhance the electronic conductivity of the material (*Pbca*-$FePO_4$ shows an energy band gap of 0.92 eV in ambient pressure).

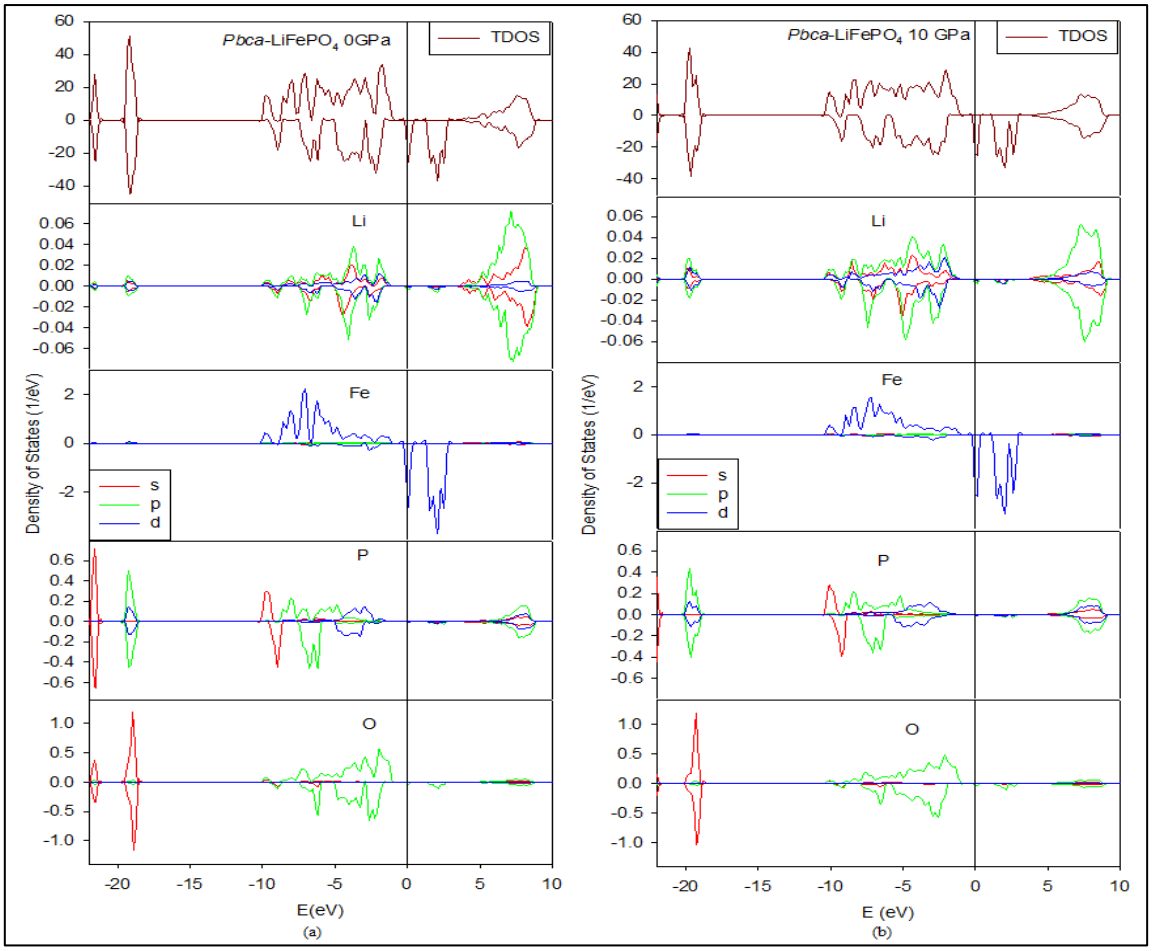

Figure 5-3 Total and partial DOS of *Pbca*-$LiFePO_4$ polymorph, at (a) 0 GPa and (b) 10 GPa. The Fermi level is taken as energy zero ($E-E_F=0$).

In Figure 5-4 we present the total and partial density of states of $P2_1/c$-$LiFePO_4$ in ambient and high pressures. Similarly to *Pbca*-$LiFePO_4$, we observe no band gap around the Fermi level, but a continuous flow of electrons from the valence to the conduction band at both ambient and high pressures. Furthermore, the Fermi level falls on the Fe 3*d* band, suggesting metallic characteristics. This again suggests that lithium intercalation plays an essential role on the enhancement of the electronic conductivity of $FePO_4$ polymorphs.

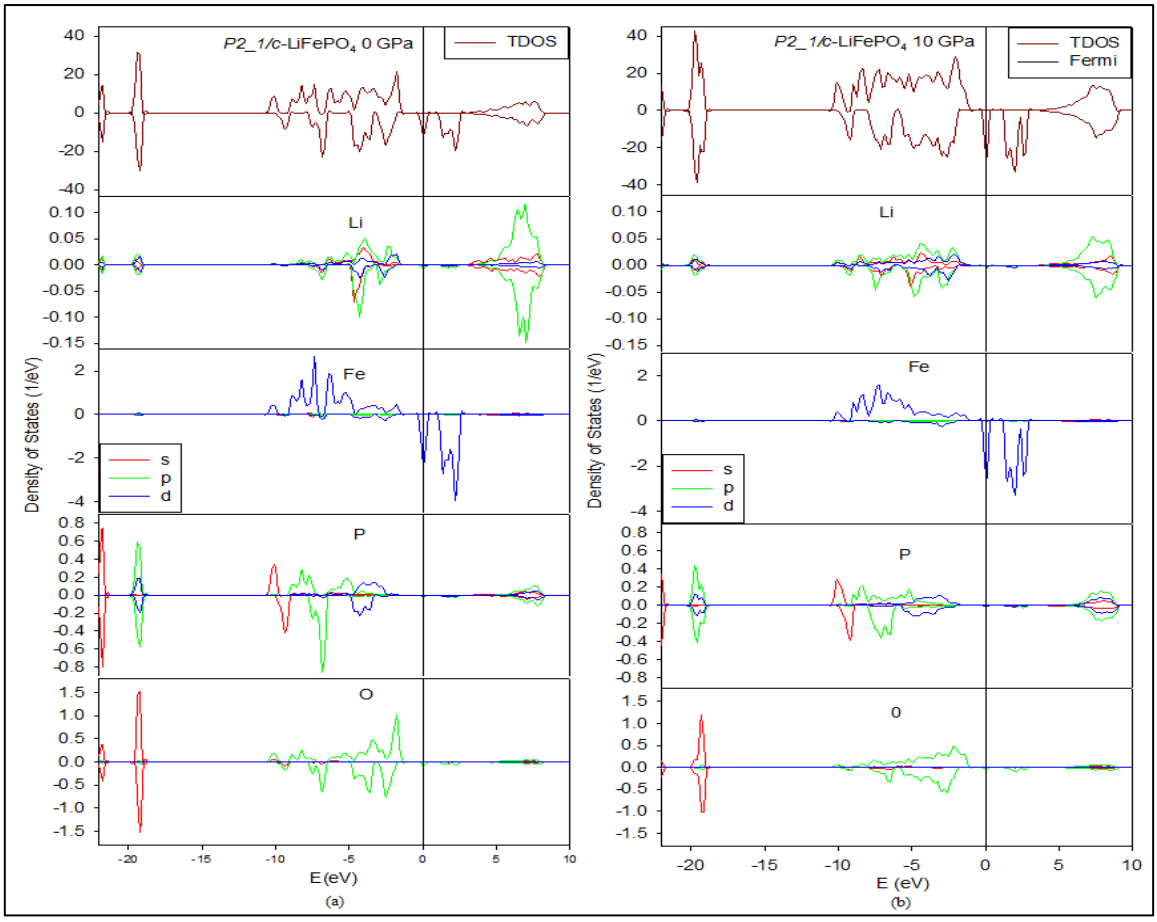

Figure 5-4 Total and partial DOS of $P2_1/c$-$LiFePO_4$ polymorph. (a) $P2_1/c$-$LiFePO_4$ in 0 GPa and (b) $P2_1/c$-$LiFePO_4$ in 10 GPa. The Fermi level is taken as energy zero ($E-E_F=0$).

Figure 5-5 shows the total and partial electronic density of states of *Cmcm*-$LiFePO_4$. We observe an energy band gap of 1.53 eV. It was noted that the Fermi level falls on the 3*d* spin-down energy band, suggesting that the material has semi-metallic characteristic. Similarly to the *Pnma*-$LiFePO_4$ polymorph, we observe that the band gap becomes wide when lithium is intercalated. The energy band gap is 1.53 eV, which is wider compared to 0.92 eV of delithiated phase.

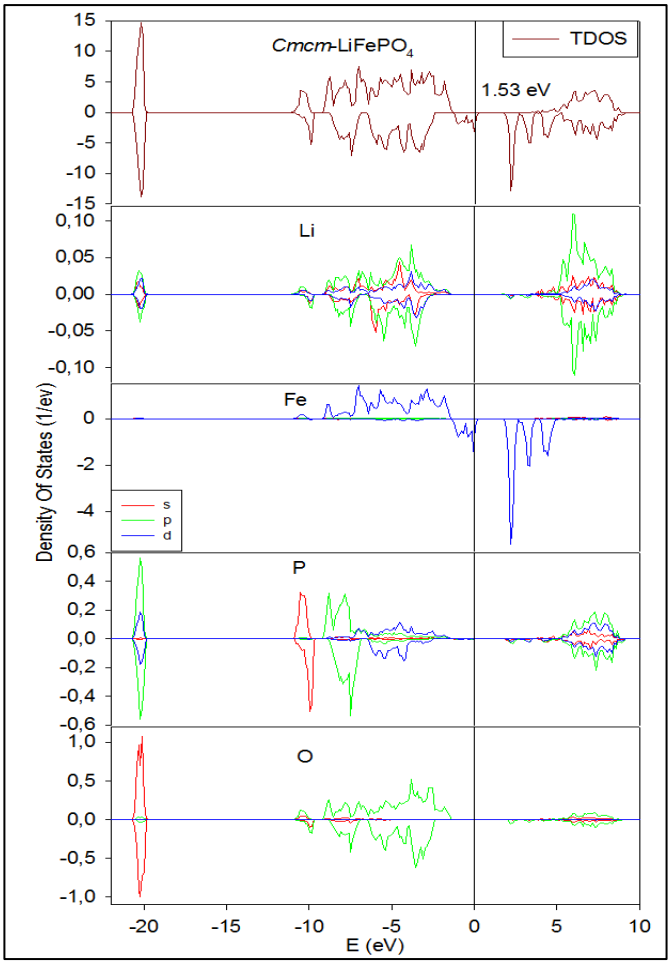

Figure 5-5 Total and partial DOS of *Cmcm*-$LiFePO_4$. The Fermi level is taken as energy zero ($E-E_F=0$).

5.2.2 $LiCoPO_4$ Density of States

In this section we discuss the spin polarised calculated LDA+*U* total and partial density of states (DOS) for $LiCoPO_4$ polymorphs in ambient and high pressures. Similarly, to $CoPO_4$ polymorphs, we note that in the energy range $-22 \le 0 \le 10$, the partial density of states associated with Co are primarily of 3*d* character, the partial density of states associated with P and O are primarily of 2*p* character. The spin-down Fe 3*d* band observed in the case $LiFePO_4$ polymorphs above is not seen in $LiCoPO_4$ polymorphs. This is due to the fact that Co has one more electron than Fe, while the spin-down LUMO peak observed in $LiFePO_4$ polymorphs is paired. The $LiCoPO_4$

polymorphs clearly shows band gaps and the Fermi level falls on the edge of the upper valence band, suggesting semi-conductor behaviour; which can result in poor electrochemical activity.

In Figure 5-6, we show the total and partial density of states for $P3_121$-$LiCoPO_4$ and observed typically large energy band gap semi-conductor behaviour. Similarly to $P3_121$-$LiFePO_4$, $P3_121$-$LiCoPO_4$ shows the same band gap value of 2.73 eV at both ambient and high pressures. Thus, the 'rigid-band approach' also applies in these structures [167], where the electronic structure is fixed and the position of the Fermi level is shifted with the increase in the number of electrons.

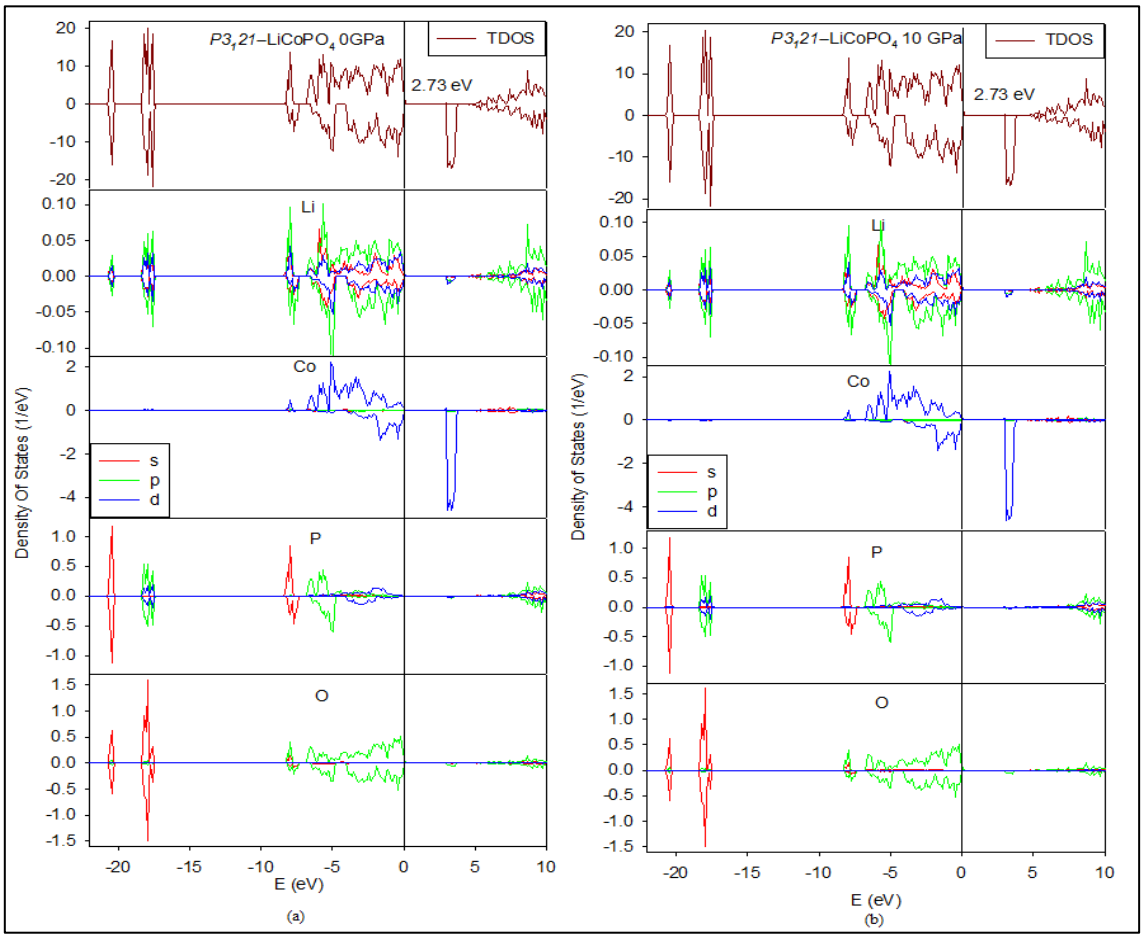

Figure 5-6 Total and partial DOS of $P3_121$-$LiCoPO_4$ polymorps, at (a) 0 GPa and (b) 10 GPa. The Fermi level is taken as energy zero ($E-E_F=0$).

We also note that the Fermi level falls on the edge of the upper valence band. It is evident that lithium intercalation expands the energy band gap of $P3_121$-$CoPO_4$ at both ambient and high pressures; $CoPO_4$ showed band gaps of 0.34 eV and 0.59 eV in ambient and high pressures, respectively. This is in good agreement with the previous DFT+*U* predictions [50]. These suggest that lithium insertion does not enhance the electronic conductivity of $CoPO_4$. Similarly to $LiFePO_4$ polymorphs, it is observed that the total and partial densities of states are reduced when lithium is intercalated. Moreover, importantly, the states around the Fermi level are also reduced, suggesting that lithium intercalation enhances electronic stability.

We further discuss the total and partial density of states of *Pnma*-$LiCoPO_4$ as shown in Figure 5-7. It is noted that *Pnma*-$LiCoPO_4$ shows a band gap of 1.62 eV in ambient pressure. Our DFT+*U* band gap highly overestimates the findings by Xu and Chung who reported a band gap of 0.18 eV [45] employing spin-polarised linear combinations of atomic orbitals method [207]. Moreover, the Fermi level is located on the edge of the upper valence band, suggesting semi-conductor characteristics. In 10 GPa pressure the energy band gap increases to 2.14 eV, suggesting that the material has an insulating behaviour and diminishing electrochemical conductivity.

We also note that lithium insertion reduces the electronic conductivity of *Pnma*-$LiCoPO_4$. The energy band gap expands from 0.83 eV to 1.62 eV and 0.71 eV to 2.14 eV in 0 GPa and 10 GPa, respectively. Similarly, to $P3_121$-$LiCoPO_4$, lithium insertion reduces the total and partial density of states, indicating that stability is enhanced, particularly states around the Fermi level. We also note the creation of spin-down *d*-orbital slightly below and on the left of the Fermi level of Co atom, which contributes to the new band gap in *Pnma*-$LiCoPO_4$. The broadening of this new band would have

caused the Fermi to fall within, thus enhancing the electrochemical activity of *Pnma*-$CoPO_4$. Hence, the electrochemical conductivity of $LiCoPO_4$ can be improved by adding excessive Co *d* electrons. The notable substantial hybridisation of Co 3*d* orbitals and O P 2*p*, and decrease in Co magnetic moment when lithium is inserted suggest a depletion of electron in the $t_{2g}\downarrow$ band during Li ion battery operation.

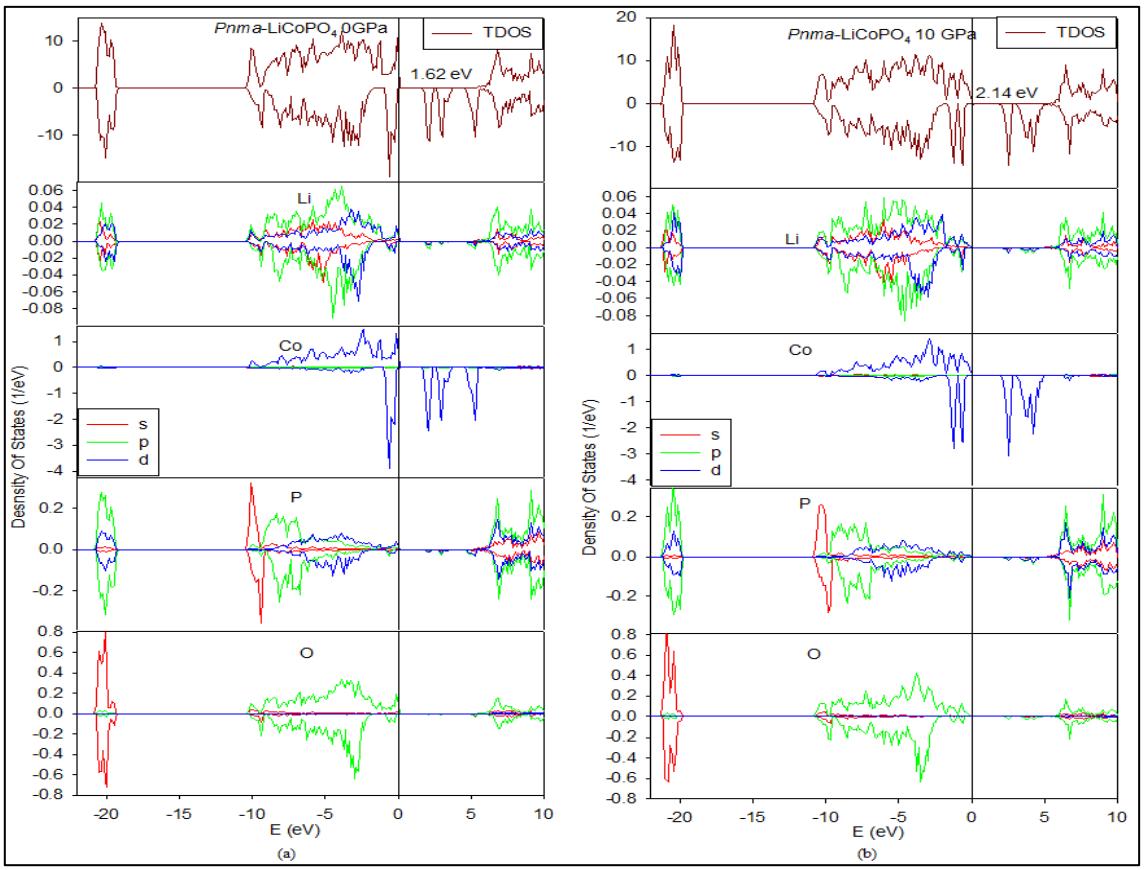

Figure 5-7 Total and partial DOS of *Pnma*-$LiCoPO_4$ polymorph, at (a) 0 GPa and (b) 10 GPa. The Fermi level is taken as energy zero ($E-E_F=0$).

The total and partial densities of states of *Pbca*-$LiCoPO_4$ are presented in Figure 5-8. We note that there exists a band gap of 2.54 eV in ambient pressure, suggesting that the material is a semi-conductor. Moreover, the Fermi level is located on the upper valence band, further confirming semi-conductor behaviour. However, the Fermi level is located on the shallow pseudo gap when 10 GPa pressure is exerted, suggesting that

pressure enhance the electronic conductivity of the this material. Moreover, the relatively wide band gap is reduced to 1.39 eV. Lithium intercalation reduces electronic conductivity of the material. This is made evident by the creation of the energy band gap, which is not observed on the delithiated form (*Pbca*-$CoPO_4$). In contrast to other structural polymorphs, the total density of states increases when lithium is intercalated, suggesting destabilisation.

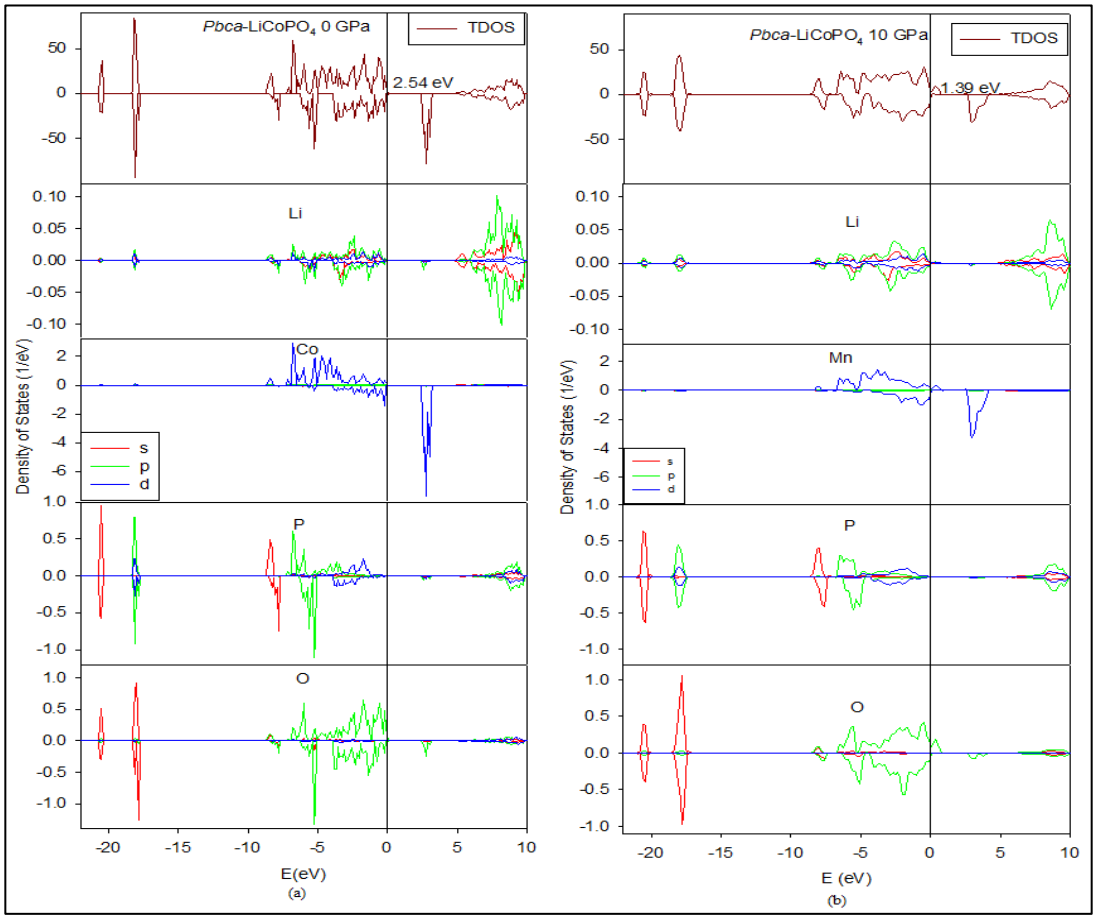

Figure 5-8 Total and partial DOS of *Pbca*-$LiCoPO_4$ polymorph, at (a) 0 GPa and (b) 10 GPa. The Fermi level is taken as energy zero ($E-E_F=0$).

In Figure 5-9, we present the total and partial density of states of $P2_1/c$-$LiCoPO_4$ in ambient and high pressures. We observe that there exists an energy band gap of 2.28 eV in ambient pressure. The Fermi level is located on the Co 3*d* band on the valence

band, suggesting that the material is semi-metallic. The application of 10 GPa pressure enhances the electrochemical conductivity as the Fermi level falls on the upper valence band and there are transfer of electron states to the conduction band. It can be noted that lithium intercalation creates an energy band gap, as the delithiated $P2_1/c$-$CoPO_4$ shows no band gap. Moreover, we note that total density of states is increased when lithium is intercalated, suggesting that lithium destabilises $P2_1/c$-$CoPO_4$ polymorph.

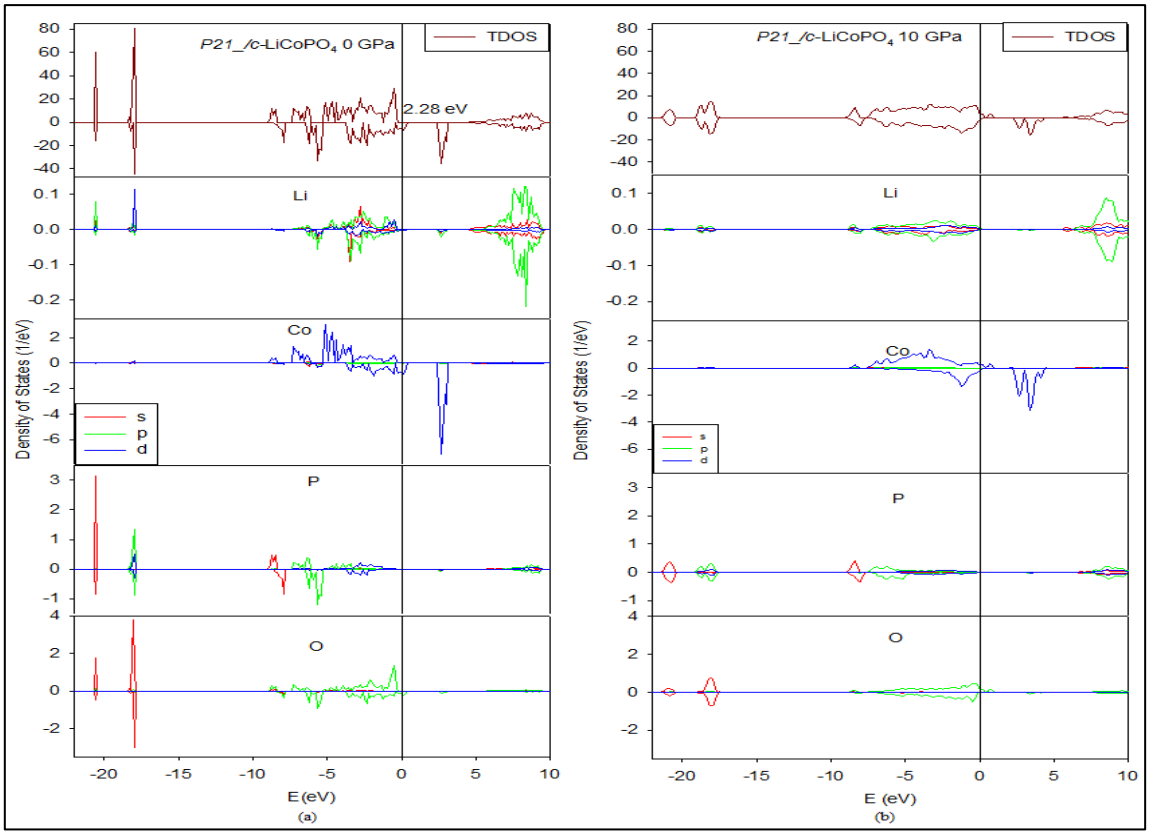

Figure 5-9 Total and partial DOS of $P2_1/c$-$LiCoPO_4$ polymorph, at (a) 0 GPa and (b) 10 GPa. The Fermi level is taken as energy zero ($E-E_F=0$).

The total and partial DOS of *Cmcm*-$LiCoPO_4$ are calculated and presented in Figure 5-10. We observe the relatively wide band gap of 1.14 eV. The energy band gap becomes wider when lithium is intercalated, as we reported 0.46 eV for *Cmcm*-$CoPO_4$. However, the Fermi level remains on the left of the band gap, suggesting insulator

behaviour. Hence, lithium intercalation reduces the electronic conductivity of *Cmcm*-$CoPO_4$ polymorph. Furthermore, the total and partial density of states are reduced when lithium is intercalated, indicating that stability is enhanced.

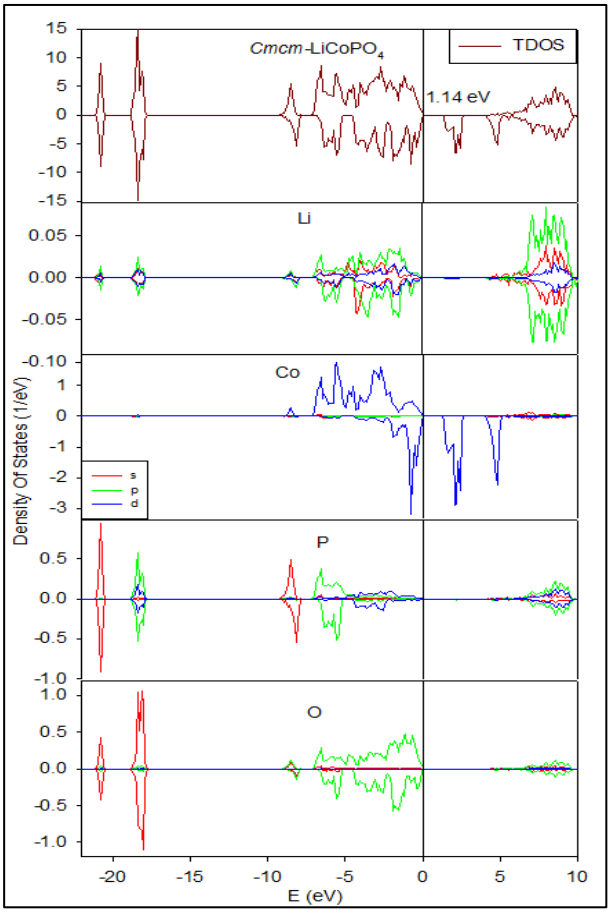

Figure 5-10 Total and partial DOS of *Cmcm*-$LiCoPO_4$ polymorph. The Fermi level is taken as energy zero ($E-E_F=0$).

5.2.3 $LiMnPO_4$ Density of States

Results for the total and partial density of states of $LiMnPO_4$ polymorphs are presented in Figures 5-11 to 5-15. There are no experimental and calculated electronic structure properties from previous recorded on $LiMnPO_4$ polymorphs, but *Pnma*-$LiMnPO_4$. Firstly, we consider the partial and total DOS of *P3₁21*-$LiMnPO_4$, in Figure 5-11. We observe a relatively wide energy band gap of 4.30 eV in ambient pressure. In

addition, the Fermi level is located on the left (upper valence band) of the band gap, suggesting that electrons are impermissible to jump over to the conduction band. The energy band gap is slightly decreased when 10 GPa pressure is applied giving rise to a relatively large value of 4.19 eV. These suggest that *P3₁21*-$LiMnPO_4$ has insulator characteristic and poor electronic conductivity. It is deduced that lithium intercalation reduces the electronic conductivity. Delithiated $MnPO_4$ shows the Fermi level is located on the pseudo gap, indicating metallic characteristic. On the other hand, lithium intercalation enhances stability, since the total density of states is reduced.

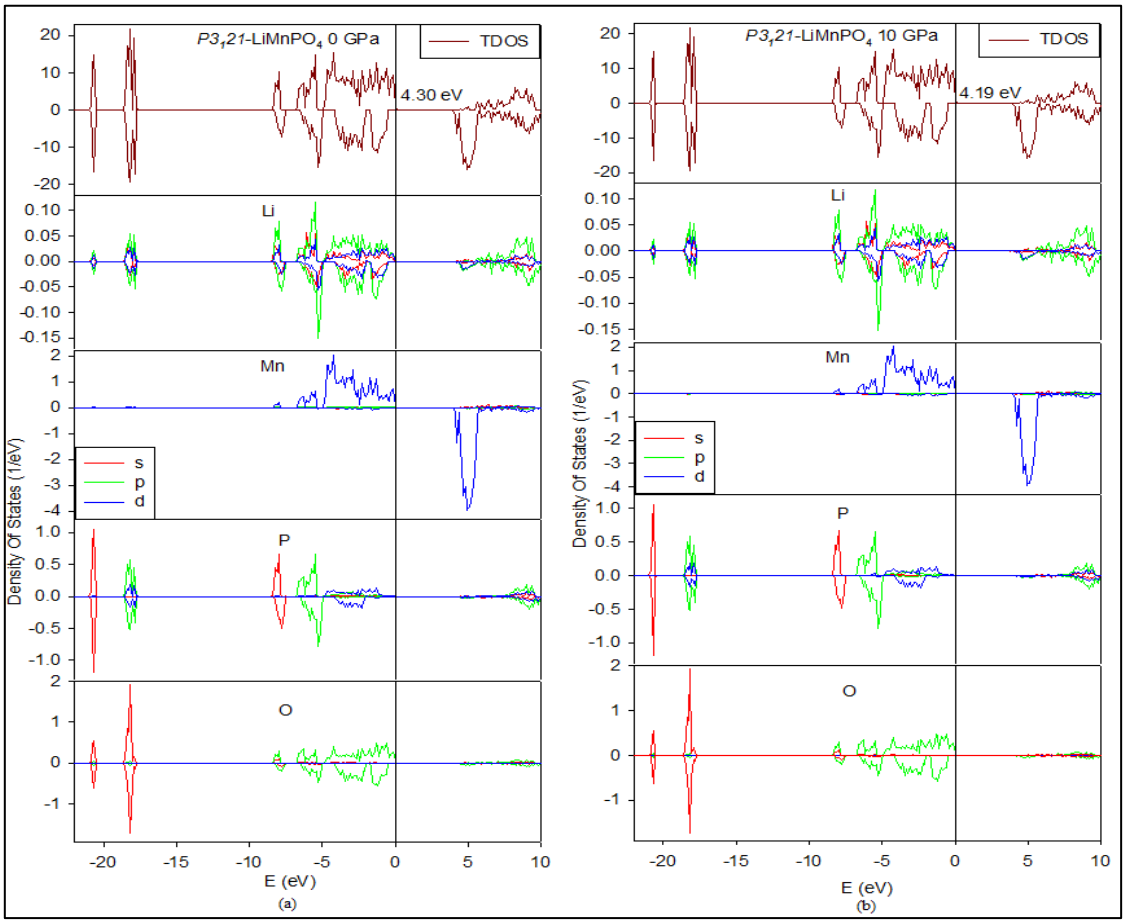

Figure 5-11 Total and partial DOS of *P3₁21*-$LiMnPO_4$ polymorph, at (a) 0 GPa and (b) 10 GPa. The Fermi level is taken as energy zero ($E-E_F=0$).

The total and partial densities of states of *Pnma*-$LiMnPO_4$ are presented in Figure 5-12. In ambient pressure, *Pnma*-$LiMnPO_4$ shows a relatively wide energy band gap of

1.98 eV. The existence of the band gap can be explained by the deformation of the oxygen octahedra surrounding the Mn sites, leading to a splitting of the spin-up e_g states. In contrast to $LiFePO_4$, we note that the density of states of $LiMnPO_4$ is not associated with the filling of the spin-down t_{2g} and leads to metallic characteristic and good electronic conductivity, since the Fermi level falls within this band. The Fermi level is located on the edge of the valence band, suggesting insulator characteristics.

The application of 10 GPa substantially expands the band gap to 4.97 eV. The Fermi level is located on the edge of the upper valence band, suggesting that electrons are impermissible to cross the potential barrier over to the conduction band, thus *Pnma*-$LiMnPO_4$ is an insulator in 10 GPa. We note that lithium intercalation creates the energy band gaps and increases the total density of states; hence reducing stability.

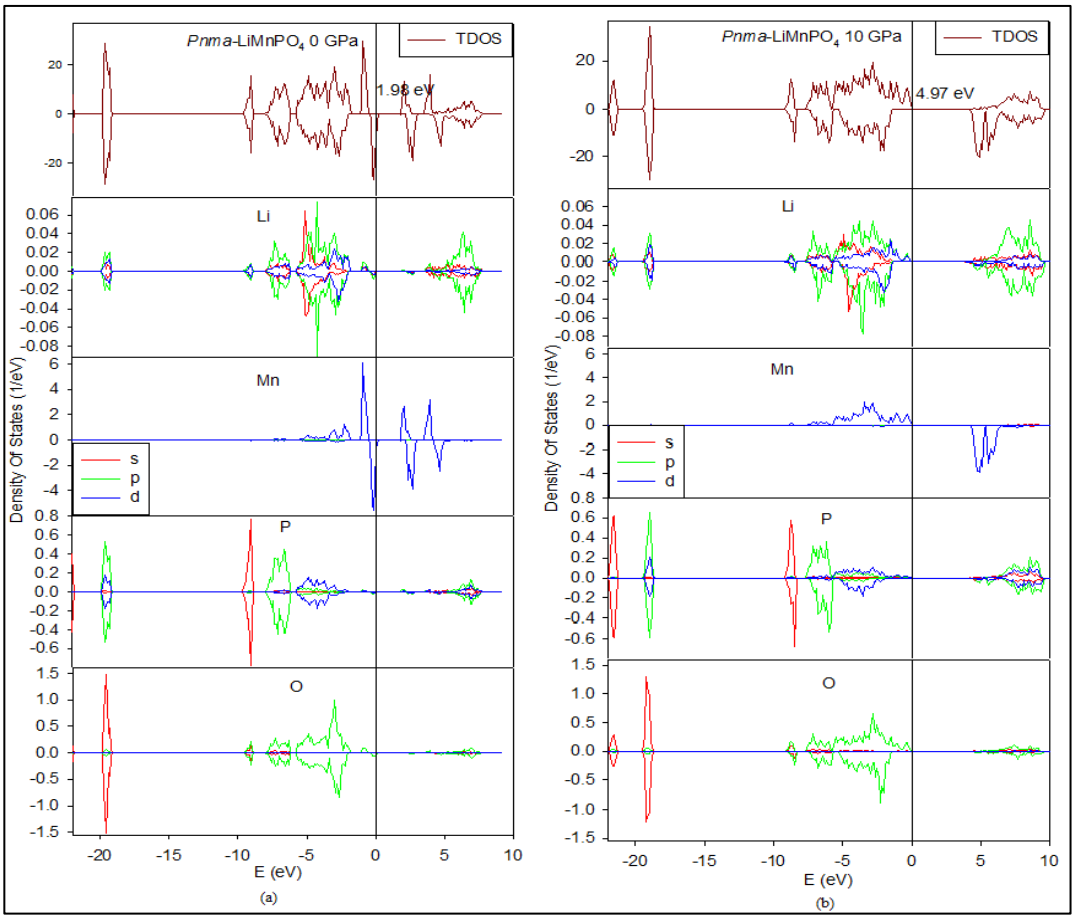

Figure 5-12 Total and partial DOS of *Pnma*-$LiMnPO_4$ polymorph, at (a) 0 GPa and (b) 10 GPa. The Fermi level is taken as energy zero ($E-E_F=0$).

Figure 5-13 shows the total and partial density of states for the *Pbca*-$LiMnPO_4$. We observe relatively wide band gaps of 3.20 eV and 3.40 eV in 0 GPa and 10 GPa, respectively. However, the location of the Fermi level, which is within the shallow pseudo gap, indicates that the electrons are permissible to cross over to the conduction band at both ambient and high pressures. Hence, *Pbca*-$LiMnPO_4$ is classified as good electronic conductor. Lithium intercalation reduces the total density of states, suggesting that stability is enhanced.

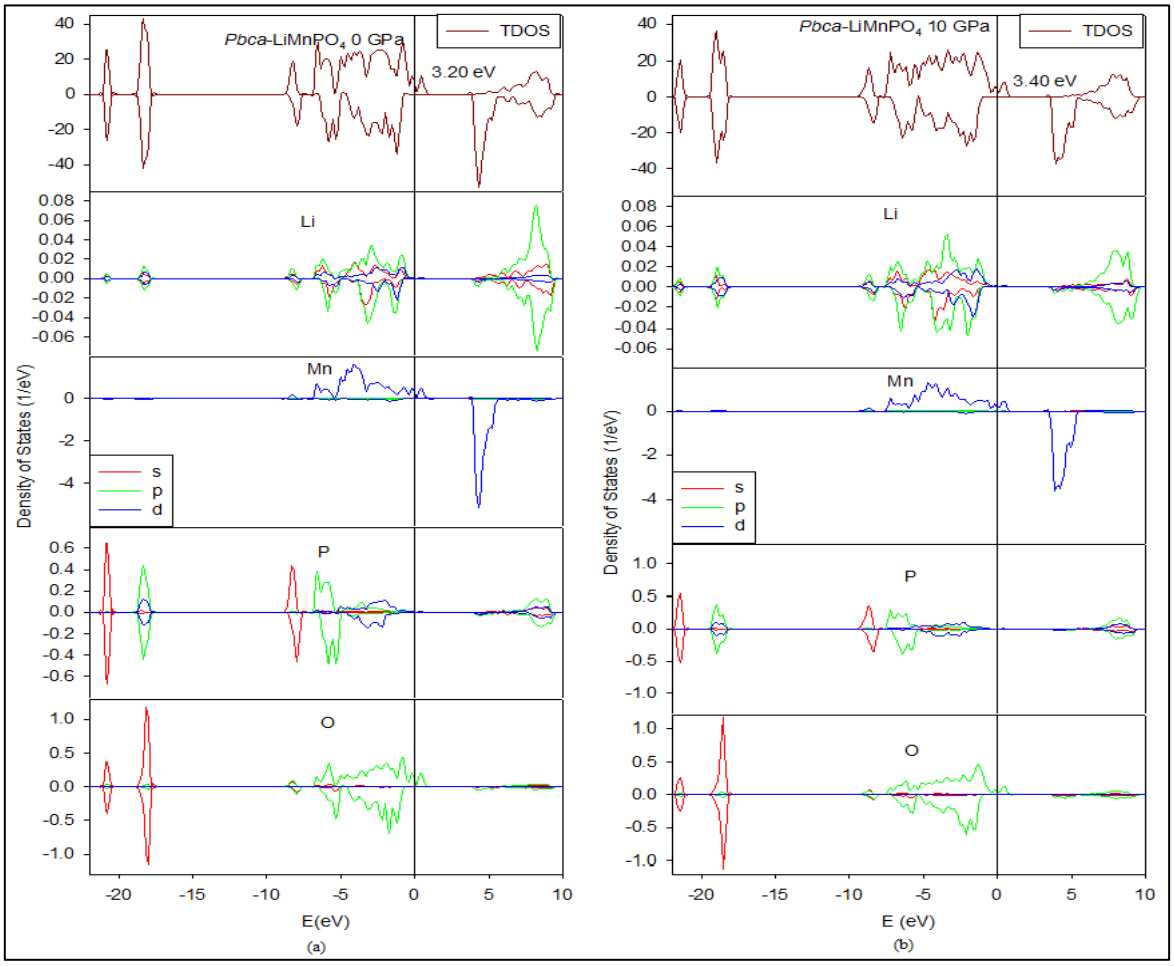

Figure 5-13 Total and partial DOS of *Pbca*-$LiMnPO_4$ polymorph, at (a) 0 GPa and (b) 10 GPa. The Fermi level is taken as energy zero ($E-E_F=0$).

In Figure 5-14, we present the total and partial density of states for the *$P2_1/c$*-$LiMnPO_4$. We note a relatively wide band gap of 3.07 eV in ambient pressure. Furthermore, the Fermi level fall on the right of a marginally shallow pseudo gap on

the valence band, indicating the electrons are permissible to cross over to the conduction band. Hence, similarly to *Pbca*-$LiMnPO_4$, *P2₁/c*-$LiMnPO_4$ is classified as a good electronic conductor. In high pressure, we note that the band gap narrows to 2.44 eV and the shallow pseudo gap is eliminated. However, the Fermi level remains on the upper valence band. Moreover, the total density of states is reduced when pressure is applied. Lithium intercalation reduces the total density of states, suggesting that stability is enhanced.

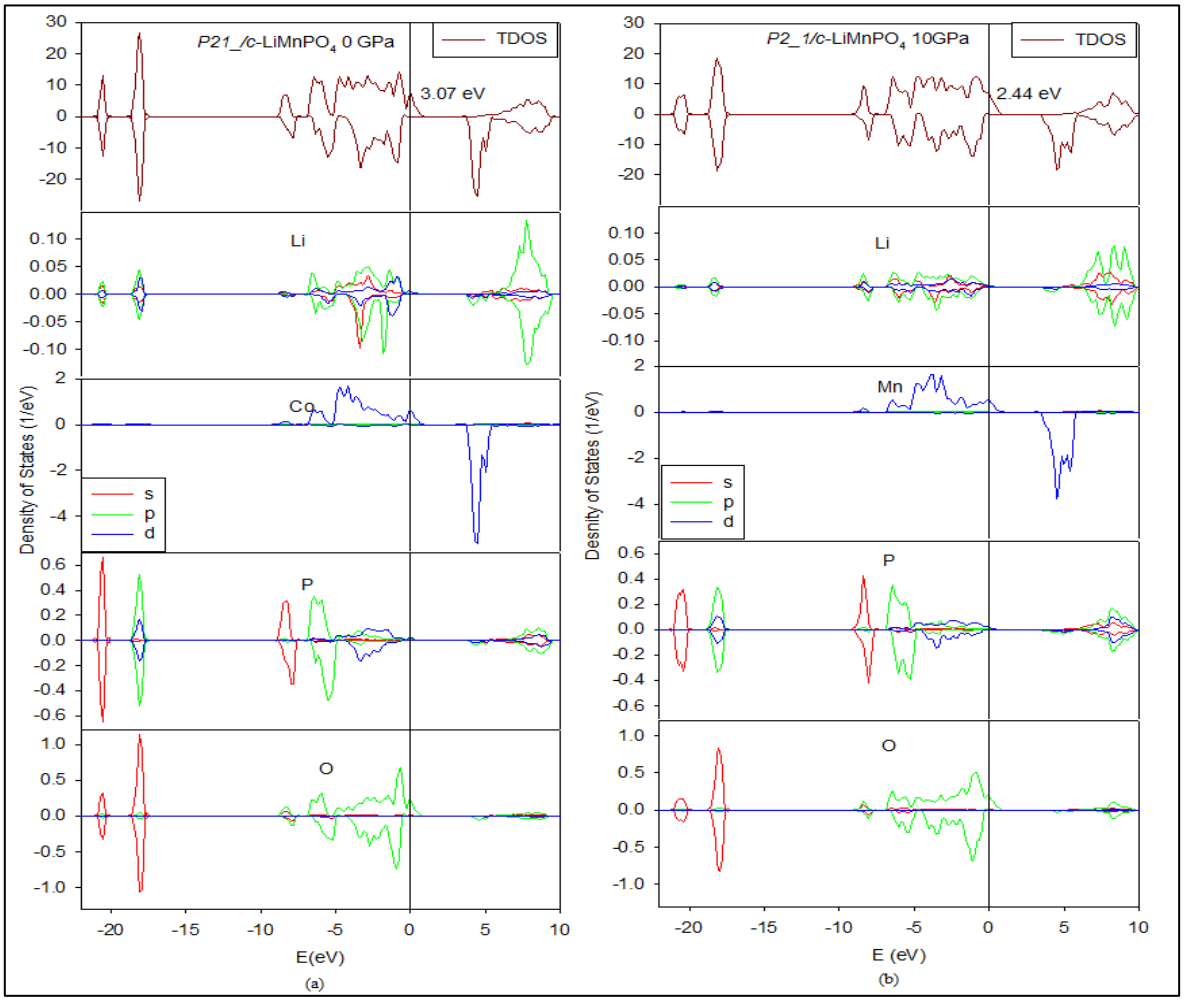

Figure 5-14 Total and partial DOS of *P2₁/c*-$LiMnPO_4$ polymorph, at (a) 0 GPa and (b) 10 GPa. The Fermi level is taken as energy zero ($E-E_F=0$).

The total and partial densities of states of *cmcm*-$LiMnPO_4$ are presented in Figure 5-15. Similarly to *P3₁21*-$LiMnPO_4$, *Cmcm*-$LiMnPO_4$ also depicts poor electronic

conductivity with a relatively large band gap of 4.24 eV. We notice that lithium insertion lowers electrochemical conductivity of *Cmcm*-$MnPO_4$ polymorph, as we observed pseudo gap on the delithiated polymorph.

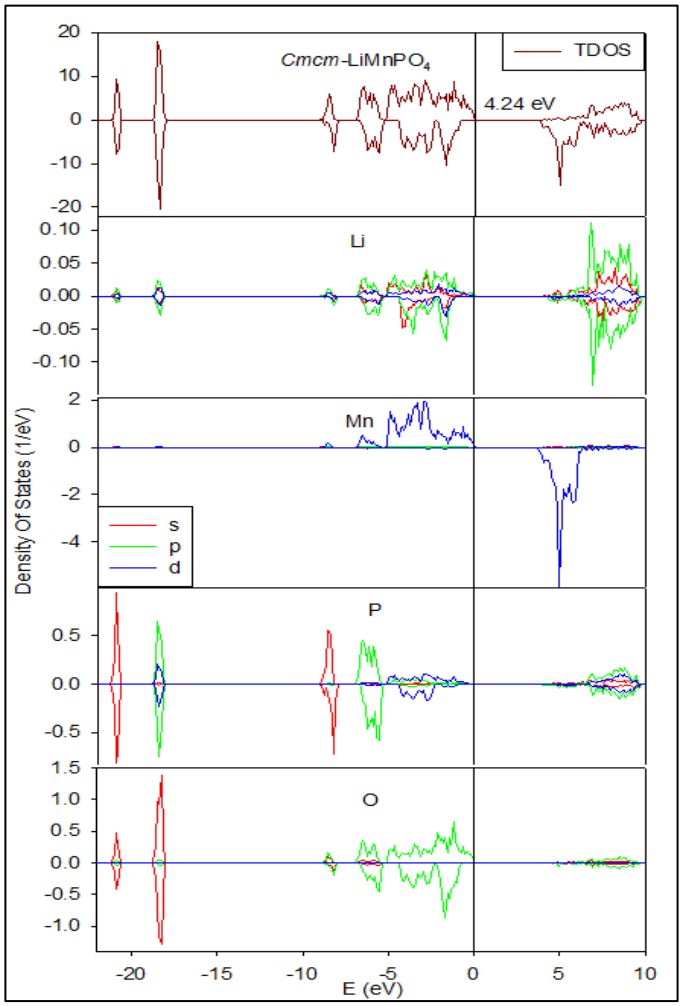

Figure 5-15 Total and partial DOS of *Cmcm*-$LiMnPO_4$ polymorph. The Fermi level is taken as energy zero ($E-E_F=0$).

5.3 Mechanical Properties of $LiMPO_4$ Polymorphs

5.3.1 Phonon Dispersion Curves

In this section, we discuss the vibrational properties of the $LiMPO_4$ polymorphs under study. The change in vibrational stability when lithium is intercalated will be of great

importance in understanding the mechanical stability, and also for determining the effect of lithium intercalation. The phonon dispersion curves were calculated using the PHONON code [80] as discussed in detail in section 2.5. The effect of pressure on vibrational stability will also be investigated. Phonon dispersion curves on $LiMPO_4$ structural polymorphs have never been investigated elsewhere, to the best of our knowledge. We note that lithium insertion increases the number of atoms per unit cell in all crystal systems. The trigonal $P3_121$ polymorphs contain 21 atoms per unit cell as such there will be 3 (1LA, 2TA) acoustic and 60 (20LO, 40TO) optical modes. The orthorhombic (*Pnma* and *Cmcm*) systems have 28 atoms in the unit cell; hence there will be 84 vibrational modes on phonon spectra; 3 (1LA, 2TA) acoustical and 81 (27LO, 57TO) optical. Lastly, the orthorhombic (*Pbca*) and monoclinic ($P2_1/c$) posses 52 and 26 atoms, resulting to 156 and 78 vibrational modes, respectively.

The phonon dispersion curves for the $LiMPO_4$ polymorphs are presented in figures 5-16 to 5-18. Similarly to the delithiated polymorphs, we observe that the phonon dispersion curves for the trigonal $LiMPO_4$ polymorphs are characterised by soft modes or negative vibrations (-5 THz) at both ambient and high pressures. The orthorhombic (*Pbca*) and monoclinic ($P2_1/c$) spectra also display mechanical instability (presence of soft modes). The negative vibrations are observed along high symmetry directions Γ (0,0,0), L (½,0,½) and Z (1,½,½). We note that no negative vibrations are observed for the orthorhombic (*Pnma* and *Cmcm*) systems, but "imaginary" vibrations along the high symmetry line, Γ (0,0,0) in the Brillouin zone direction at both ambient and high pressures. Moreover, generally, we have noted that lithium intercalation does not perturb the vibrational stability of the system, however, with few exceptions. The deliathiated $MnPO_4$ (section 4.1) displayed negative vibrations, which are not observed on the lithiated form at both ambient and high pressures (figure 5-18(d) and

(e)). Furthermore, lithium intercalation mechanically destabilise the *Pnma*-$CoPO_4$ (figure 5-17(e)) and *Pbca*-$CoPO_4$ (figure 5-17(g)) at 10 GPa. We further, observe soft modes down to -3 THz and -5 THz along high symmetry line [X (1/2,0,0), S (1/2,1/2,0) and Y (0,1/2,0)] and [R (1/2,1/2,1/2), T (0,1/2,1/2), Z (0,0,1/2), Γ (0,0,0), X (1/2,0,0), S (1/2,1/2,0) and Y (0,1/2,0)] in the Brilouin zone *Pnma*-$CoPO_4$ and *Pbca*-$CoPO_4$, respectively.

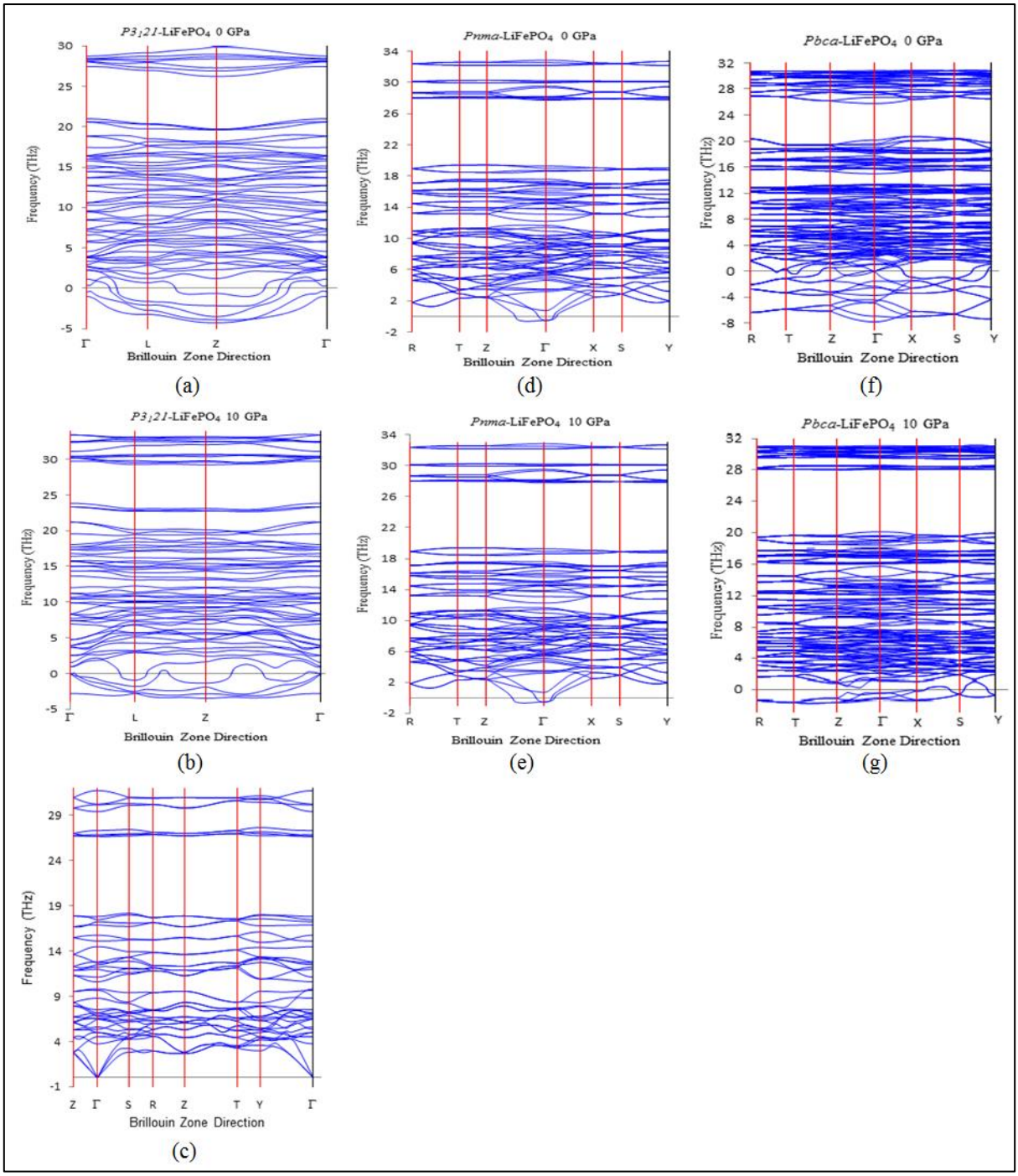

Figure 5-16 Phonon dispersion curves for $LiFePO_4$ polymorphs at 0 GPa and 10 GPa.

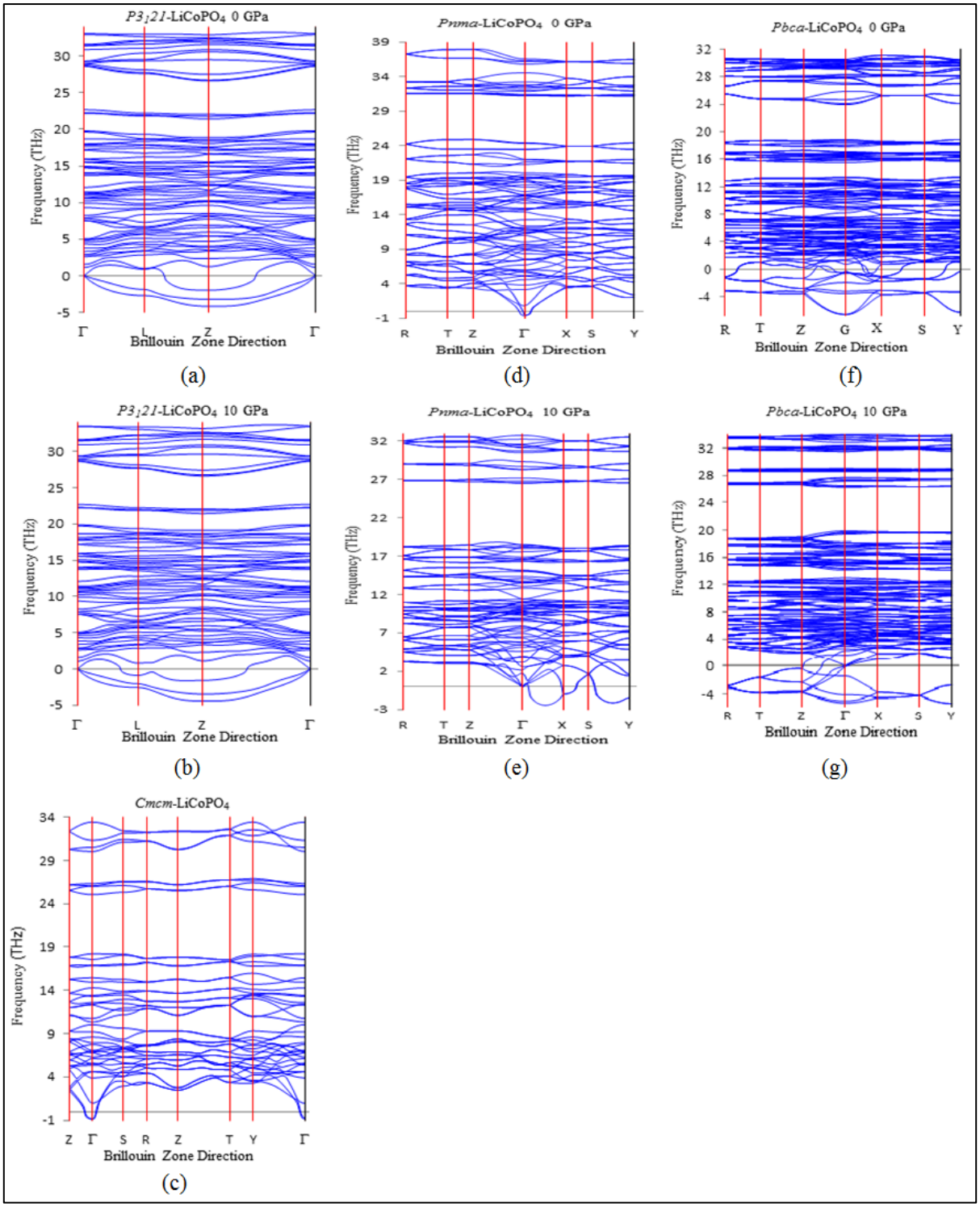

Figure 5-17 Phonon dispersion curves for $LiCoPO_4$ polymorphs at 0 GPa and 10 GPa.

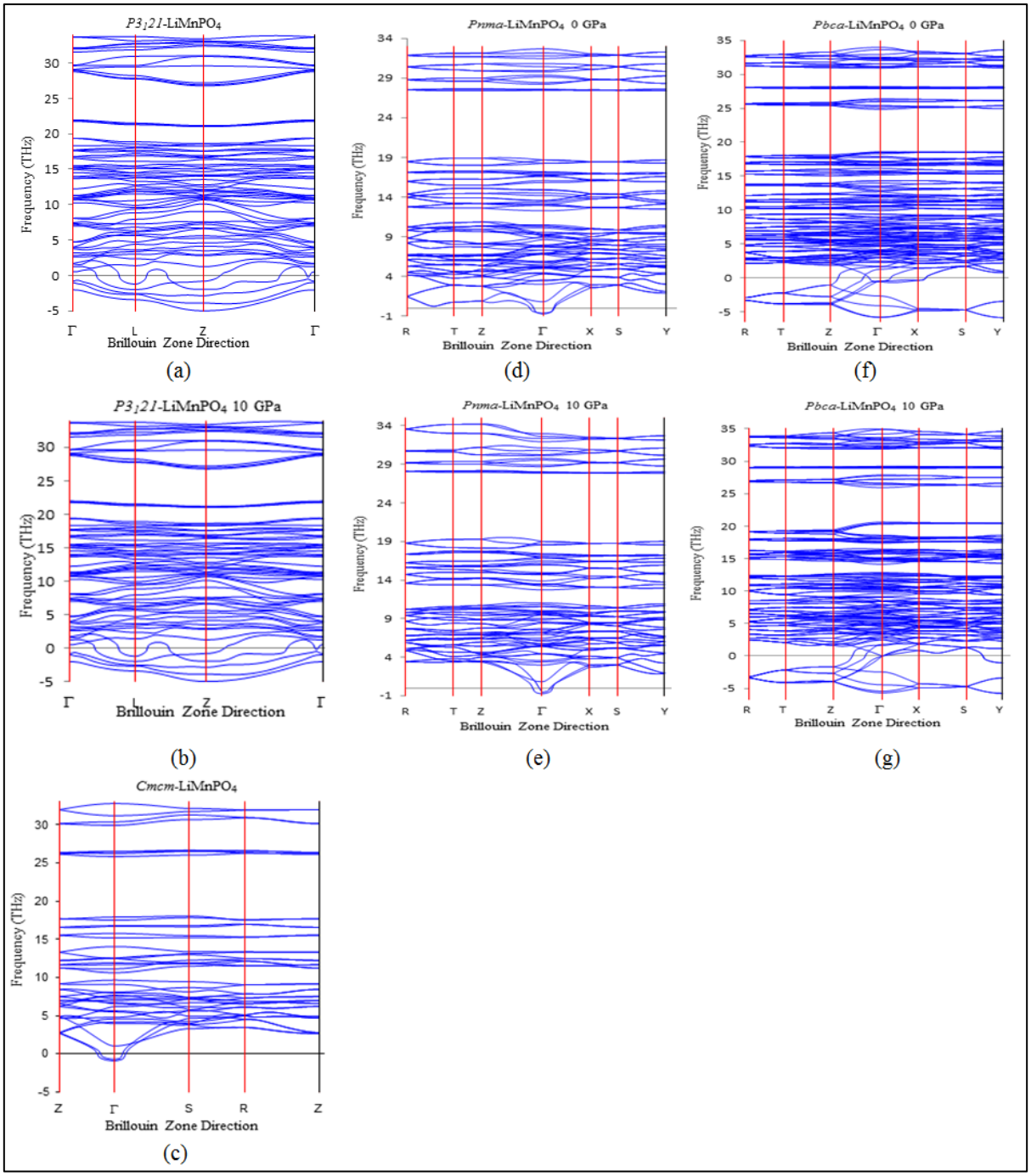

Figure 5-18 Phonon dispersion curves for $LiMnPO_4$ polymorphs at 0 GPa and 10 GPa.

5.3.2 Elastic Properties $LiMPO_4$ polymorphs

5.3.2.1 Elastic Properties of $LiFePO_4$ Polymorphs

In table 5-7 we list the calculated elastic constants (C_{ij}), bulk moduli, shear moduli, Young's moduli and Pugh ratio for $LiFePO_4$ polymorphs.

Table 5-7 DFT+*U* results on elastic constants (C_{ij}), bulk (B), shear (G), and Young's (E) moduli, Pugh ratio (B/G) for $LiFePO_4$ polymorphs in 0 GPa and 10 GPa.

	0 GPa					10 GPa			
C_{ij} (GPa)	*$P3_121$*	*Pnma*	*Pbca*	*$P2_1/c$*	*Cmcm*	*$P3_121$*	*Pnma*	*Pbca*	*$P2_1/c$*
C_{11}	106.83	209.56	95.33	90.83	283.78	111.33	198.50	169.19	232.83
C_{12}	58.92	117.29	32.75	64.25	136.18	54.83	122.67	82.75	109.00
C_{13}	62.67	99.83	28.00	54.17	115.85	62.33	108.08	68.58	88.67
C_{14}	-3.00					2.25			
C_{15}				7.17					9.50
C_{22}		270.49	154.83	61.17	290.74		277.67	199.83	187.83
C_{23}		80.53	45.58	36.67	154.01		88.92	106.17	139.83
C_{25}				2.67					-2.92
C_{33}	82.83	249.58	58.50	124.17	254.86	82.83	249.00	137.83	231.50
C_{35}				7.92					16.67
C_{44}	48.50	56.89	24.00	33.00	56.13	48.33	55.00	398.33	51.67
C_{46}				7.67					10.83
C_{55}		72.27	10.00	23.83	68.08		70.33	233.33	35.33
C_{66}	23.94	62.40	32.33	13.67	58.23	28.23	60.67	51.00	22.00
B_V	73.89	147.21	57.93	65.15	182.38	73.83	151.61	113.54	147.46
B_R	72.76	146.39	48.53	53.69	180.76	72.65	149.88	108.11	145.51
B_H	73.32	146.80	53.23	59.42	181.57	73.24	150.74	110.82	146.49
G_V	31.68	67.11	26.76	22.17	64.71	33.38	64.23	153.16	42.78
G_R	24.86	64.83	20.08	12.51	63.37	26.81	61.42	62.60	32.79
G_H	28.27	65.97	23.42	17.34	64.04	30.10	62.83	107.88	37.78
E_V	83.14	174.78	69.56	59.74	173.60	87.03	168.85	316.95	117.02
E_R	66.95	169.48	52.94	34.83	170.22	71.62	162.12	157.41	91.50
E_H	75.05	172.13	61.25	47.29	171.91	79.32	165.49	237.18	104.26
B/G_V	2.33	2.19	2.16	2.94	2.82	2.21	2.36	0.74	3.45
B/G_R	2.93	2.26	2.42	4.29	2.85	2.71	2.44	1.73	4.44
B/G_H	2.59	2.23	2.27	3.43	2.84	2.43	2.39	1.03	3.79

We note that $LiFePO_4$ polymorphs have relatively large positive C_{ij} values with the exception of C_{14} of *P3₁21*-$LiFePO_4$ at both 0 GPa and 10 GPa. The relatively low C_{14} values i.e. -3.00 GPa and 2.25 GPa in 0 GPa and 10 GPa, respectively are in good agreement with the observed negative vibrations. The other elastic constants satisfy the necessary conditions for stability as discussed in details in section 2.6.4.1. Similarly, we note that the orthorhombic *Pnma*-$LiFePO_4$, *Pbca*-$LiFePO_4$ and *Cmcm*-$LiFePO_4$ and the monoclinic *P2₁/c*-$LiFePO_4$ also satisfy the necessary stability conditions. These suggest mechanical stability of $LiFePO_4$ polymorphs at both ambient and high pressures. We observe that elastic constants change randomly with lithium intercalation, as we note an increment and decrease in elastic constants. However, all calculated elastic constants of *P2₁/c*-$FePO_4$ decrease with lithium intercalation. Furthermore, we notice an irregular change of C_{ij} values when 10 GPa pressure is applied. According to previous report [196], calculated C_{ij} in high pressure are closer to experimental values; however for these polymorphs there no experimental C_{ij} values recorded yet. Hence, we cannot make robust conclusion as to whether the C_{ij} in 10 GPa are considerable. However, there are previously recorded calculations of elastic properties of Pnma-$LiFePO_4$. As observed with delithiated form of *Pnma*-$LiFePO_4$, our LDA+*U* elastic constants and moduli in ambient pressure overestimate GGA+*U* results by Maxisch and Ceder [53]. However, there are some similarities between the two calculations with both showing C_{22} to be the largest C_{ij} value (198.0 GPa for GGA+*U* and 270.49 GPa for LDA+*U*) and C_{44} being the smallest C_{ij} value (36.8 GPa for GGA+*U* and 56.89 GPa for LDA+*U*).

The $FePO_4$ polymorphs are isostructural to $LiFePO_4$ polymorphs where all lithium sites are unoccupied, thus $FePO_4$ polymorphs are expected to be softer than $LiFePO_4$ polymorphs [53]. However, there are some irregularities observed. In the case of

P3₁21 symmetry we observe that elastic constants C_{14} and C_{33} are smaller in $LiFePO_4$ than in $FePO_4$; while for *Pnma* symmetry, C_{11} and C_{44}, C_{55} and C_{66} are smaller in $LiFePO_4$ than in $FePO_4$, suggesting that the PO_4 tetrahedrons move rotationally towards interstitial lithium sites along *a*-axis under compressions and weak shear resistance along {100}, {010} and {001} planes. This is consistence with previous observations [53, 55]. It should also be noted that C_{44} and C_{66} are smaller in $LiFePO_4$ than in $FePO_4$ in *Cmcm* symmetry. These irregularities are noted at both ambient and high pressure conditions.

The corresponding bulk, shear and Young's moduli and the Pugh ratio of trigonal and orthorhombic $LiFePO_4$ systems have also been calculated on the basis of Voigt-Reuss-Hill method (section 2.6.4.1 equations 2.54 to 2.59). The bulk modulus (B) suggests that *Pnma*-$LiFePO_4$ is the hardest material; that is not easily broken in ambient pressure over *P3₁21*-$LiFePO_4$, *P2₁/c*-$LiFePO_4$ and *Pbca*-$LiFePO_4$, respectively. However, the *Cmcm*-$LiFePO_4$ polymorph shows hardness over *Pnma*-$LiFePO_4$, *P2₁/c*-$LiFePO_4$, *Pbca*-$LiFePO_4$ and *P3₁21*-$LiFePO_4$ in high pressure. The Young's (E) modulus suggest the same trend as of bulk modulus, but in terms of stiffness, that is not easily stretchable.

Lithium intercalation enhances the hardness of *P3₁21*-$FePO_4$, *Pnma*-$FePO_4$ and *Pbca*-$FePO_4$ in ambient pressure; that is bulk moduli increase. The bulk modulus of *P2₁/c*-$FePO_4$ decreases from 96.09 GPa to 59.42 GPa when lithium is intercalated. The hardness of all $FePO_4$ polymorphs is enhanced when 10 GPa pressure is applied, that is bulk moduli increase. Moreover, lithium intercalation intensifies the stiffness of *P3₁21*-$FePO_4$ and *Pbca*-$FePO_4$, while diminishes the stiffness of *Pnma*-$FePO_4$ and *P2₁/c*-$FePO_4$ in ambient pressure. This is made evident by the increase and decrease of the Young's modulus values, respectively. The same change is observed in 10 GPa

pressure, as we also note a slight decline of stiffness of *Cmcm*-$FePO_4$ when lithium is intercalated. Our results show that $LiFePO_4$ is a harder material than $FePO_4$ which correspond well with the prediction that lithium transportation is faster in $FePO_4$ than in $LiFePO_4$ [59, 60]. We also observe that the average bulk moduli are greater than the average shear modulus ($B_H > G_H$), implying that the parameter limiting the stability of these polymorphs is the shear modulus [53].

According to the Pugh brittle/ductility criterion [195], all $LiFePO_4$ polymorphs are considered ductile since all B/G values are greater than 1.75 in ambient and high pressures, except *Pbca*-$LiFePO_4$ which is brittle (B/G<1.75) in high pressure. It is noted that lithium intercalation improves ductility of $FePO_4$ polymorphs, while enhances the brittleness of *Pbca*-$FePO_4$ and reduces the ductility of *P3₁21*-$FePO_4$ in 10 GPa pressure. The Pugh ratio value of *Pbca*-$FePO_4$ decreases from 2.80 to 1.03 when lithium is intercalated in 10 GPa pressure.

Table 5-8 Anisotropy factors and Poisson ratio of $LiFePO_4$ polymorphs in 0 GPa and 10 GPa.

	0 GPa					10 GPa			
Anisotropy	*P3₁21*	*Pnma*	*Pbca*	*P2₁/c*	*Cmcm*	*P3₁21*	*Pnma*	*Pbca*	*P2₁/c*
A_1	0.91	0.88	0.46		0.73	1.71	0.95	3.59	
A_2	0.78	0.81	0.33		1.15	0.74	0.81	4.66	
A_3	0.94	1.02	0.70		0.77	0.88	1.05	0.72	
A_B *(%)*		0.31	8.83		0.44		0.56	0.24	
A_G *(%)*		1.69	14.26		1.05		2.24	0.42	
A^U	1.39	0.18	4.86	4.07	0.12	1.24	0.24	7.29	1.54
U_H	0.38	0.31	0.29	0.38	0.34	0.38	0.32	0.26	0.40

Table 5-8 lists the anisotropy factors and Poison ratio of $LiFePO_4$ polymorphs. Effects of lithium insertion in anisotropy factors are essential to determine the susceptibility of materials to cracks during battery operation [208]. Elastic anisotropy is essential in

inducing such cracks and dislocations [157, 209]. Similarly to $FePO_4$ polymorphs, $LiFePO_4$ polymorphs are moderately anisotropic, except for *Pbca*-$LiFePO_4$ at both 0 GPa and 10 GPa. Furthermore, we note that the percentage shear modulus anisotropy (A_G) is greater than the percentage bulk modulus anisotropy (A_B) for all polymorphs at all pressures. Thus, $LiFePO_4$ polymorphs are less in compressibility than in shear. This corresponds well with the GGA+*U* calculations by Maxisch and Ceder [53].

We note that lithium insertion either enhances isotropic or anisotropic character. In ambient pressure, we note that lithium insertion generally enhances isotropy of the trigonal *P3₁21*-$FePO_4$ and anisotropy of the orthorhombic *Pnma*-$FePO_4$ and *Pbca*-$FePO_4$. This is in good agreement with the GGA+*U* calculations done by Maxisch and Ceder [53]. Anisotropy factors in high pressure show that *P3₁21*-$LiFePO_4$ and *Pnma*-$LiFePO_4$ approaches isotropy while *Cmcm*-$LiFePO_4$ and *Pbca*-$LiFePO_4$ are further anisotropic when lithium is inserted.

The percentage anisotropy in compressibility and shear for orthorhombic systems shows that lithium insertion generally improves isotropy for *Cmcm*-$FePO_4$ and anisotropy of *Pbca*-$FePO_4$ and *Pnma*-$FePO_4$, particularly in high pressure. We note that A_B *d*ecreases from 0.80 % to 0.31 % while A_G increases from 1.16 % to 1.69 % when lithium is inserted in *Pnma*-$FePO_4$ in 0 GPa pressure, while increase respectively from 0.33 % to 8.83 % and 0.113 % to 14.26 % when lithium is inserted in *Pbca*-$FePO_4$. On the other, we note that both A_B and A_G decrease for *Cmcm*-$LiFePO_4$. In 10 GPa pressure, we note that both A_B and A_G increase with lithium intercalation on *Pbca*-$FePO_4$ and *Pnma*-$FePO_4$, further increasing anisotropy.

The universal anisotropy factor shows that *P3₁21*-$FePO_4$, *Cmcm*-$FePO_4$ and *P2₁/c*-$FePO_4$ approach unity with lithium insertion, while *Pnma*-$FePO_4$ and *Pbca*-$FePO_4$ are

anisotropic. The change in anisotropy factors is significant, thus suggesting that $LiFePO_4$ polymorphs are susceptible to crack propagating during battery operation as recorded by Wang *et al*. [208]. However, as a way to minimise the phase transformation crackings, Maxisch and Ceder [53] suggested that the usage of small $LiFePO_4$ particles. The poison ratio has also been calculated, and it was found that it generally increase with lithium insertion.

5.3.2.2 Elastic Properties of $LiCoPO_4$ Polymorphs

In table 5-9 we list the calculated elastic constants, bulk, shear, Young's moduli and Pugh ratio for $LiCoPO_4$ polymorphs. There are currently no experimental or theoretical findings recorded on the elastic properties of $LiCoPO_4$ to the best of our knowledge. We note that the necessary stability criteria are satisfied in ambient pressure for trigonal, monoclinic and orthorhombic systems, suggesting mechanical stability. However, we note a negative C_{ij} value (C_{14}=-3.50 GPa) for *P3₁21*-$LiCoPO_4$ in 0 GPa, corresponding well with observed negative phonon vibrations. We further observe that C_{ij} values slightly increase with 10 GPa pressure, with an exception of C_{12} for *Pnma*-$LiCoPO_4$.

The macroscopic bulk, shear, and Young's moduli were also calculated and presented in table 5-9. In 0 GPa, we note that the bulk and Young's moduli suggest hardness and stiffness of *Pnma*-$LiCoPO_4$ over *Cmcm*-$LiCoPO_4$, *P3₁21*-$LiCoPO_4$, *Pbca*-$LiCoPO_4$ and *P2₁/c*-$LiCoPO_4$, respectively. However, the hardness and stiffness trend is slightly altered in 10 GPa, as we observe *P2₁/c*-$LiCoPO_4$ to be harder and stiffer than *P3₁21*-$LiCoPO_4$ and *Pbca*-$LiCoPO_4$. The Pugh ratio has predicted ductility on *P3₁21*-

$LiCoPO_4$, *P2₁/c*-$LiCoPO_4$, *Cmcm*-$LiCoPO_4$ and *Pnma*-$LiCoPO_4$ and brittleness on *Pbca*-$LiCoPO_4$.

Table 5-9 DFT+*U* results on elastic constants (C_{ij}), bulk (B), shear (G), and Young's (E) moduli, Pugh ratio (B/G) for $LiCoPO_4$ polymorphs in 0 GPa and 10 GPa.

	0 GPa					10 GPa			
C_{ij} (GPa)	*P3₁21*	*Pnma*	*Pbca*	*P2₁/c*	*Cmcm*	*P3₁21*	*Pnma*	*Pbca*	*P2₁/c*
C_{11}	119.00	209.83	93.33	59.83	219.96	120.00	212.00	177.33	200.17
C_{12}	77.67	114.58	35.17	43.33	65.82	81.00	104.33	81.67	90.67
C_{13}	95.83	89.25	25.25	22.75	65.50	96.75	97.17	48.17	111.08
C_{14}	-3.50					4.67			
C_{15}				8.080					2.33
C_{22}		252.67	138.50	54.83	233.24		261.33	261.67	293.67
C_{23}		78.58	32.67	30.08	74.44		86.17	99.00	91.67
C_{25}				1.17					15.00
C_{33}	169.17	255.83	54.33	117.67	185.67	169.17	270.33	177.00	133.00
C_{35}				5.83					19.50
C_{44}	43.17	62.67	28.00	27.67	66.57	46.50	63.00	-32.67	67.33
C_{46}				4.50					7.83
C_{55}		78.00	26.00	22.83	46.15		78.67	25.67	98.17
C_{66}	20.67	66.67	45.33	20.00	56.51	19.50	67.33	33.67	62.67
B_V	105.09	142.57	52.48	47.19	116.71	106.46	146.56	119.30	134.85
B_R	98.25	142.08	44.36	44.28	115.75	100.32	145.64	110.08	120.24
B_H	101.67	142.33	48.42	45.73	116.23	103.39	146.10	114.69	127.55
G_V	30.59	70.53	32.74	23.18	62.72	31.48	72.20	31.14	67.86
G_R	26.68	68.52	29.31	15.32	60.55	26.18	70.61	70.89	51.77
G_H	28.63	69.52	31.02	19.25	61.63	28.83	71.41	51.02	59.81
E_V	83.65	181.63	81.31	59.75	159.58	85.96	186.05	85.95	174.34
E_R	73.39	177.09	72.06	41.21	154.67	72.26	182.36	175.10	135.81
E_H	78.52	179.36	76.68	50.48	157.12	79.11	184.20	130.52	155.07
B/G_V	3.44	2.02	1.60	2.04	1.86	3.38	2.03	3.83	1.98
B/G_R	3.68	2.07	1.51	2.89	1.91	3.83	2.06	1.55	2.32
B/G_H	3.55	2.05	1.56	2.38	1.89	3.59	2.05	2.25	2.12

We note that all elastic constants values increase with lithium insertion for *P3₁21*-$LiCoPO_4$ at both 0 GPa and 10 GPa, suggesting that *P3₁21*-$CoPO_4$ is softer than *P3₁21*-$LiCoPO_4$ [53]. Elastic constants for orthorhombic *Pnma*-$LiCoPO_4$, *Pbca*-

$LiCoPO_4$ and *Cmcm*-$LiCoPO_4$ change randomly with lithium insertion at both ambient and high pressures. Interestingly, we observe that lithium eradicates the negative C_{ij} values on *P2₁/c*-$CoPO_4$ polymorph; thus enhancing mechanical stability. We also note that lithium insertion increases hardness and stiffness of $LiCoPO_4$ polymorphs as bulk and Young moduli increase at both ambient and high pressures. Furthermore, the Pugh ratio increase for all $LiCoPO_4$ except for *Pbca*-$LiCoPO_4$ when lithium is inserted, further increasing ductility of the respective polymorphs. Hence, lithium transportation is faster in $CoPO_4$ than in $LiCoPO_4$.

Table 5-10 lists the calculated anisotropy factors and Poison ratio of $LiCoPO_4$ polymorphs. The anisotropy factors show that *P3₁21*-$LiCoPO_4$ is relatively anisotropic; A_1, A_2 and A_3 diverge from unity by 70.51 %, 34.64 % and 20.99 %, respectively in ambient pressure. The application of 10 GPa pressure has minimal effect on the anisotropy factors; A_1 differ from unity by 81.83 %, A_2 by 34.02 % and A_3 by 17.75 %. On the other hand, we note that *Pbca*-$LiCoPO_4$, *Pnma*-$LiCoPO_4$ and *Cmcm*-$LiCoPO_4$ are moderately anisotropic, thus harder than *P3₁21*-$LiCoPO_4$.

Table 5-10 Anisotropy factors and Poisson ratio of $LiCoPO_4$ polymorphs in 0 GPa and 10 GPa.

	0 GPa					10 GPa			
Anisotropy	*P3₁21*	*Pnma*	*Pbca*	*P2₁/c*	*Cmcm*	*P3₁21*	*Pnma*	*Pbca*	*P2₁/c*
A_1	2.09	0.87	0.57		0.97	2.39	0.88	-0.30	
A_2	1.42	0.89	0.82		0.68	1.41	0.88	0.43	
A_3	0.81	1.14	1.12		0.70	0.84	1.02	0.49	
A_B (%)		0.18	8.38		0.39		0.34	4.01	
A_G (%)		1.45	5.53		1.76		0.01	-39.34	
A^U	0.80	0.15	0.77	2.63	0.19	1.07	0.12	0.32	1.66
U_H	0.49	0.29	0.24	0.35	0.28	0.48	0.29	-2.72	0.41

The percentage anisotropy shows that *Pnma*-$LiCoPO_4$ is less in compressibility than in shear in ambient pressure, since we observe that A_B is less than A_G. However, in 10 GPa, A_G is less than A_B; thus lower in shear than in compressibility. On the other hand, *Pbca*-$LiCoPO_4$ is less in shear than in compressibility, since A_G is less than A_B at both 0 GPa and 10 GPa. The *Cmcm*-$LiCoPO_4$ shows low compressibility and higher shear. Generally, we observe that *Pnma*-$LiCoPO_4$ and *Cmcm*-$LiCoPO_4$ show relatively low values of percentage bulk modulus anisotropy A_B and shear modulus anisotropy A_G, with 1.76 % being the largest possible value of anisotropy, while *Pbca*-$LiCoPO_4$ shows high bulk modulus anisotropy A_B (8.38 %) and percentage shear modulus anisotropy A_G (5.53 %), in 10 GPa. The universal anisotropy index shows that *Pnma*-$LiCoPO_4$ (A^U =0.15) is least in anisotropic compared *to Pbca*-$LiCoPO_4$ (0.77), *P3₁21*-$LiCoPO_4$ (0.80) and *P2₁/c*-$LiCoPO_4$ (2.63), respectively in 0 GPa. Similarly, in 10 GPa, *Pnma*-$LiCoPO_4$ (A^U =0.12) is less anisotropic than *Cmcm*-$LiCoPO_4$ (A^U =0.19), *Pbca*-$LiCoPO_4$, *P3₁21*-$LiCoPO_4$ (A^U =1.07) and *P2₁/c*-$LiCoPO_4$, respectively.

The effect of lithium insertion on the anisotropy of $LiCoPO_4$ polymorphs was also analysed. We note that lithium intercalation generally favours the isotropy of $LiCoPO_4$ polymorphs at both ambient and high pressures. Anisotropy factors A_1, A_2 and A_3 change by 64.18 %, 51.77 % and 100.36 % for *P3₁21*-$LiCoPO_4$ when lithium is intercalated in ambient pressure i.e. diverging from unity by 70.51 %, 34.64 % and 20.99 %. The anisotropy factors for *Pnma*-$LiCoPO_4$ change by 5.89 %, 35.33 % and 34.46 % when lithium is intercalated in ambient pressure, consequently diverging from unity by 13.56 %, 11.86 % and 13.34 %. On the other hand, the anisotropy factors for *Pbca*-$LiCoPO_4$ change by 44.35 %, 5.03 % and 15.13 % when lithium is intercalated and diverge from unity by 55.59 %, 20.26 % and 11.59 %. We observe a

relatively similar change when 10 GPa pressure is inserted. Anisotropy is also relatively reduced when lithium is inserted in *Cmcm*-$LiCoPO_4$.

The change in anisotropy factors is relatively remarkable, suggesting that $LiCoPO_4$ polymorphs are subject to cracks during the cycling of the battery, particularly *P3₁21*-$LiCoPO_4$ [157, 158]. Interestingly, we also note that lithium insertion has a positive impact on percentage modulus anisotropy of $CoPO_4$ polymorphs. We note that all percentage bulk modulus anisotropy A_B and percentage shear modulus anisotropy A_G values decrease when lithium is intercalated and universal anisotropy index values further approaches zero. Thus, lithium intercalation enhances isotropy behaviour of $LiCoPO_4$ polymorphs. Moreover, Poison ratio increases during intercalation, except for *Pbca*-$LiCoPO_4$ in 0 GPa.

5.3.2.3 Elastic Properties of $LiMnPO_4$ Polymorphs

In table 5-11, we present the calculated elastic properties of $LiMnPO_4$ polymorphs in ambient and high pressures. Similarly to $LiCoPO_4$ polymorphs, there are no recorded experimental and calculated values on elastic properties of $LiMnPO_4$ to the best of our knowledge. We observe that *Pbca*-$LiMnPO_4$ has negative C_{44} value (-205.33 GPa) in ambient pressure, which does not satisfy the necessary mechanical stability criteria $C_{44}>0$. This suggests that *Pbca*-$LiMnPO_4$ is mechanical unstable. The other polymorphs satisfy the necessary stability criterion. On the other hand, we note that *P3₁21*-$LiMnPO_4$ shows relatively low C_{14} values in 0 GPa and 10 GPa, corresponding well with the observed negative phonon vibrations; we observe -4.08 GPa and 4.25 GPa for 0 GPa and 10 GPa, respectively. For *P3₁21*-$LiMnPO_4$, the elastic constants C_{33} and C_{44} decrease with pressure, while C_{11}, C_{12}, C_{13} and C_{14} increase with pressure. Similarly to the trigonal *P3₁21*-$LiMnPO_4$, the monoclinic *P2₁/c*-$LiMnPO_4$ shows an

irregular change of C_{ij} in high pressure. Moreover C_{25} (-6,75 GPa), C_{35} (-11.67 GPa) and C_{46} (-1.83 GPa) become negative for *P2₁/c*-$LiMnPO_4$, suggesting a decrease in mechanical stability. The orthorhombic *Pnma*-$LiMnPO_4$ shows larger C_{ij} values in 10 GPa than 0 GPa. *Pbca*-$LiMnPO_4$ also shows larger C_{ij}'s in 10 GPa, except for C_{55} and C_{66}.

Table 5-11 DFT+*U* results on elastic constants (C_{ij}), bulk (B), shear (G), and Young's (E) moduli, Pugh ratio (B/G) for $LiMnPO_4$ polymorphs in 0 GPa.

	0 GPa					10 GPa			
C_{ij} (GPa)	*P3₁21*	*Pnma*	*Pbca*	*P2₁/c*	*Cmcm*	*P3₁21*	*Pnma*	*Pbca*	*P2₁/c*
C_{11}	113.33	167.61	108.17	98.00	216.84	125.00	192.00	163.33	322.00
C_{12}	79.92	82.33	43.25	30.92	61.61	89.08	110.42	77.08	111.67
C_{13}	90.67	79.07	25.42	26.83	67.32	97.25	87.58	51.92	97.25
C_{14}	-4.08					4.25			
C_{15}				12.00					1.58
C_{22}		199.84	185.00	122.50	218.46		218.50	258.67	192.00
C_{23}		63.41	55.25	16.58	71.08		86.33	97.08	114.17
C_{25}				13.50					-6.75
C_{33}	159.50	200.78	101.33	73.50	176.40	158.83	229.33	186.17	285.83
C_{35}				7.83					-11.67
C_{44}	40.83	49.99	-205.33	29.00	60.18	39.83	55.67	57.00	43.00
C_{46}				15.33					-1.83
C_{55}		62.56	19.00	45.00	51.64		70.00	18.00	74.50
C_{66}	16.69	54.79	31.67	28.00	49.05	17.96	57.67	27.00	19.00
B_V	100.96	113.09	71.37	49.19	112.41	108.44	134.28	117.81	160.67
B_R	96.15	112.90	63.41	44.44	111.69	105.70	133.90	109.21	153.85
B_H	98.56	113.00	67.39	46.81	112.05	107.07	134.09	113.51	157.26
G_V	28.00	56.36	-12.89	35.04	59.60	27.88	60.37	45.87	59.08
G_R	23.25	55.17	39.28	27.68	58.01	23.94	58.83	35.01	42.24
G_H	25.63	55.77	13.19	31.36	58.81	25.91	59.60	40.44	50.66
E_V	76.90	145.00	-41.16	84.96	151.99	77.03	157.50	121.81	157.90
E_R	64.56	142.33	97.66	68.77	148.35	66.77	153.94	94.89	116.10
E_H	70.73	143.67	28.25	76.86	150.17	71.90	155.72	108.35	137.00
B/G_V	3.61	2.01	-5.54	1.40	1.89	3.89	2.23	2.57	2.72
B/G_R	4.14	2.05	1.61	1.61	1.93	4.42	2.28	3.12	3.64
B/G_H	3.85	2.03	5.11	1.49	1.91	4.13	2.25	2.81	3.11

The macroscopic bulk modulus shows that *Pnma*-$LiMnPO_4$ is a harder material over *P3₁21*-$LiMnPO_4$ and *Pbca*-$LiMnPO_4$ and *P2₁/c*-$LiMnPO_4$, respectively in ambient pressure. The Young's modulus also predicts stiffness of *Pnma*-$LiMnPO_4$ over *P2₁/c*-$LiMnPO_4$, *P3₁21*-$LiMnPO_4$ and *Pbca*-$LiMnPO_4$. The Pugh ratio predicts ductility (B/G>1.75) of *P3₁21*-$LiMnPO_4$, *Pnma*-$LiMnPO_4$ and *Pbca*-$LiMnPO_4$ and brittleness (B/G<1.75) of *P2₁/c*-$LiMnPO_4$ in ambient pressure. In high pressure, the bulk modulus predicts that the *P2₁/c*-$LiMnPO_4$ is harder than *Pnma*-$LiMnPO_4$, *Pbca*-$LiMnPO_4$, *Cmcm*-$LiMnPO_4$ and *P3₁21*-$LiMnPO_4$, respectively. On the other hand, the Young's modulus suggests that the *Pnma*-$LiMnPO_4$ is the stiffest polymorph over *Cmcm*-$LiMnPO_4$, *P2₁/c*-$LiMnPO_4$, *Pbca*-$LiMnPO_4$ and *P3₁21*-$LiMnPO_4$, respectively in high pressure. The Pugh ratio predicts that all polymorphs are ductile in high pressure. Moreover, the shear modulus is less than the bulk modulus, suggesting that the Shear is the limiting parameter for stability [53].

The effect of lithium intercalation on $MnPO_4$ has also been determined. *P3₁21*-$MnPO_4$ shows smaller C_{ij} values than *P3₁21*-$LiMnPO_4$ with an exception of C_{14} at both 0 GPa and 10 GPa, suggesting free lithium transportation in *P3₁21*-$MnPO_4$. On the other hand, C_{11}, C_{22}, and C_{55} are smaller in *Pnma*-$LiMnPO_4$ than in *Pnma*-$MnPO_4$ while C_{11} and C_{44} are smaller in *Cmcm*-$LiMnPO_4$ than in *Cmcm*-$MnPO_4$. The elastic constants of *Pbca*-$LiMnPO_4$ generally increase, except C_{44} and C_{66} at both ambient and high pressures. Lastly, the elastic constants of *P2₁/c*-$MnPO_4$ generally decrease, except C_{22}, C_{46} and C_{55} in ambient pressure and randomly change in high pressure.

The hardness and ductility of *P3₁21*-$LiMnPO_4$, *Pnma*-$LiMnPO_4$ and *Pbca*-$LiMnPO_4$ increase and decreased for *P2₁/c*-$MnPO_4$ in ambient pressure when lithium is intercalated. On the other hand, stiffness increases for *P3₁21*-$LiMnPO_4$ and *Pnma*-$LiMnPO_4$ while it decreases for *Pbca*-$MnPO_4$ and *P2₁/c*-$MnPO_4$ when lithium is

intercalated in ambient pressure. However, in high pressure, we note that lithium insertion increases hardness, stiffness and ductility of all $LiMnPO_4$ polymorphs. Elastic anisotropy, percentage anisotropy and Poison ratio of $LiMnPO_4$ polymorphs are listed in table 5-12. We note that the trigonal *$P3_121$*-$LiMnPO_4$ is substantially anisotropic at both 0 GPa and 10 GPa. Anisotropy factors A_1, A_2 and A_3 deviate from unity by 83.92 %, 33.89 % and 12.65 % respectively at 0 GPa. However, in high pressure 10 GPa, A_1, A_2 and A_3 deviate from unity by 75.51 %, 23.79 % and 8.77 %, respectively. This implies that 10 GPa minimises anisotropy of *$P3_121$*-$LiMnPO_4$ polymorph.

Table 5-12 Anisotropy factors and Poisson ratio of $LiMnPO_4$ polymorphs in 0 GPa and 10 GPa.

0 GPa						10 GPa			
Anisotropy	*$P3_121$*	*Pnma*	*Pbca*	*$P2_1/c$*	*Cmcm*	*$P3_121$*	*Pnma*	*Pbca*	*$P2_1/c$*
A_1	2.45	0.92	-3.15		0.93	2.21	0.91	0.50	
A_2	1.41	0.91	0.43		0.82	1.27	1.02	0.29	
A_3	0.88	1.08	0.61		0.63	0.92	1.22	0.40	
A_B *(%)*		0.09	5.91		0.31		0.15	3.79	
A_G *(%)*		1.07	-188		1.35		1.29	13.4	
A^U	1.07	0.11	-6.51	1.44	0.14	0.85	0.13	1.63	2.04
U_H	0.47	0.29	0.41	0.25	0.28	0.45	0.31	0.34	0.36

On the other hand, we note that the orthorhombic *Pnma*-$LiMnPO_4$ and *Cmcm*-$LiMnPO_4$ show anisotropy factors values close to unity; hence moderately anisotropic.. Anisotropy factors of *Cmcm*-$LiMnPO_4$ deviate from unity by 7.15 %, 20.14 % and 45.55 %, suggesting moderate anisotropy. The anisotropic factors A_1, A_2 and A_3 for *Pbca*-$LiMnPO_4$ deviate from unity by 103.74 %, 79.33 % and 47.98 % and 66.13 %, 110.81 % and 85.10 % at a 0 GPa and 10 GPa respectively, indicating a significant degree of anisotropy.

The percentage anisotropy for compressibility and shear for orthorhombic systems further suggest that the *Pnma*-$LiMnPO_4$ and *Cmcm*-$LiMnPO_4$ polymorphs are moderately anisotropic. *Pbca*-$LiMnPO_4$ is relatively anisotropic, particularly in 0 GPa. The percentage bulk (A_B) and shear (A_G) modulus anisotropy are A_B=5.91 % and A_G=-187.93 % in ambient pressure and A_B=3.79 % and A_G=13.43 % in high pressure. A_B is smaller than A_G, implying that orthorhombic forms of $LiMnPO_4$ are less anisotropic in compressibility than in shear [53]. Universal anisotropy index show that *Pnma*-$LiMnPO_4$ is more isotropic (A^U values are close to zero) over *Cmcm*-$LiMnPO_4$, *P3₁21*-$LiMnPO_4$, *P2₁/c*-$LiMnPO_4$ and *Pbca*-$LiMnPO_4$ at both ambient and high pressures. The Poison ratio was also calculated and was found to decrease with pressure for *P3₁21*-$LiMnPO_4$ and *Pbca*-$LiMnPO_4$ increase with pressure for *P2₁/c*-$LiMnPO_4$ and *Pnma*-$LiMnPO_4$.

The effect of lithium on anisotropy behaviour of $MnPO_4$ polymorphs has also been analysed. We note that lithium intercalation brings about a substantial effect on $MnPO_4$ polymorphs. The trigonal *P3₁21*-$LiMnPO_4$ and orthorhombic *Pbca*-$MnPO_4$ anisotropy factors further deviate from unity, while orthorhombic *Pnma*-$LiMnPO_4$ and *Cmcm*-$LiMnPO_4$ anisotropy factors converge towards unity at both ambient and high pressures. A_B and A_G also converge towards zero for *Pnma*-$LiMnPO_4$ and *Cmcm*-$LiMnPO_4$ and diverge further from zero for *Pbca*-$MnPO_4$. However, irrespective of moderate anisotropy, the change in anisotropy factors is remarkable large when lithium is intercalated, thus $LiMnPO_4$ polymorphs are susceptible to cracks during battery operation [157, 158]. The universal anisotropy index, A^U, suggest that lithium intercalation enhances isotropic behaviour of *Pnma*-$LiMnPO_4$ and *Cmcm*-$LiMnPO_4$ polymorphs and enhance anisotropy of *P3₁21*-$LiMnPO_4$, *Pbca*-$LiMnPO_4$ and *P2₁/c*-$LiMnPO_4$.

Chapter 6

Structural, Electronic, and Mechanical Properties of *Pnma*-$NaMPO_4$

In this chapter we present the structural, thermodynamic, electronic and mechanical properties of olivine *Pnma*-$NaMPO_4$ structures to deduce their stability and prospect of being future cathode materials in sodium ion batteries. In the previous chapters, we have shown that the olivine system displays good stability over other polymorphs. Thus, in this study we consider only the olivine $NaMPO_4$ polymorph. The effect of sodium intercalation on MPO_4 will also be discussed and their stability will be compared with that of olivine $LiMPO_4$.

6.1. $NaMPO_4$ Structural and Thermodynamic Properties

The calculated and experimental cell parameters of $NaMPO_4$ are listed in table 6-1. We note that the cell parameters of $NaMnPO_4$, $NaFePO_4$ and $NaCoPO_4$ are in good agreement with the experimentally reported results to within 3 %. The cell volumes of $NaFePO_4$, $NaCoPO_4$ and $NaMnPO_4$ contracts by almost the same factor when the external pressure 10 GPa is applied, that is, 27.67 $Å^3$, 26.04 $Å^3$ and 27.60 $Å^3$, respectively. Moreover, we note 13.77 %, 11, 54 % and 12.74 % volume changes upon sodiation from $FePO_4$ to $NaFePO_4$, $CoPO_4$ to $NaCoPO_4$ and $MnPO_4$ to $NaMnPO_4$ in ambient pressure, respectively. These large volume changes may contribute to poor

performance [22]. They are also larger than those of $LiFePO_4$ (5 %), $LiCoPO_4$ (4.47 %) and $LiMnPO_4$ (6.68 %). It was also indicated previously that $LiMnPO_4$ often shows poor performance due to the large lattice misfit between $MnPO_4$ and $LiMnPO_4$ [22, 77]. Now, when a 10 GPa is applied, the volumes changes by even a larger percentage: 17.38 %, 18.96 % and 18.42 % for $NaFePO_4$, $NaCoPO_4$ and $NaMnPO_4$, respectively. These large volume changes induce strain and may cause cracks during the charge/discharge cycles, increasing the contact resistance and also hindering the phase transition kinetics, especially during Na-ion extraction [208].

Table 6-1 Calculated and experimental lattice parameters, cell volume and heats of formation of *Pnma*-$NaMPO_4$ structures in 0 GPa and 10 GPa. The experimental values are given for comparison.

0 GPa					
Structure	*a* (Å)	*b* (Å)	*c* (Å)	V (Å^3)	H_f (kJ/mol)
$NaFePO_4$	9.07	6.90	5.08	318.26	-1143.58
Exp.	8.99	6.86	5.05	311.35[a]	
$NaCoPO_4$	8.95	6.86	5.07	311.68	-1085.48
Exp.	8.88	6.79	5.03	303.28 [b]	-1547.50[b]
$NaMnPO_4$	9.16	6.92	5.14	326.38	-1292.57
Exp.	10.56	6.34	4.99	334.24 [c]	
10 GPa					
Structure	*a* (Å)	*b* (Å)	*c* (Å)	V (Å^3)	H_f (kJ/mol)
$NaFePO_4$	8.83	6.68	4.93	290.56	-685.71
$NaCoPO_4$	8.74	6.65	4.92	285.66	-635.85
$NaMnPO_4$	8.95	6.71	4.97	298.78	-819.52

[a] [67] [b] [68] [c] [66]

The thermodynamic properties of $NaMPO_4$ structures in 0 GPa and 10 GPa were investigated and the corresponding heats of formation are also listed in tables 6-1. The heats of formation are calculated using the expression;

$$\Delta H_f\left(NaMPO_4\right)=\left[E_{Total}-\left(E_{Na}+E_M+E_P+4E_O\right)\right], \quad 6.1$$

where E_{total} is the total energy of the system ($NaMPO_4$) which subtract the individual elemental energies E_{Na}, E_M, E_P and E_O of sodium, transition metal, phosphorous and oxygen, respectively in the system. We note that $NaMPO_4$ structures show relatively low heats of formation, where $NaMnPO_4$ shows the lowest values at both ambient (-1292.57 kJ/mol) and high (-819.52 kJ/mol) pressure. This suggests that the structure is more stable compared to the other two structures. Furthermore, we note that our calculated heats of formation value for $NaCoPO_4$ (-1085.48 kJ/mol) overestimate the experimental value (-1547.50 kJ/mol) reported by Le *et al.* using differential scanning calorimetry, X-ray diffraction, and high-temperature oxide melt drop solution calorimetry [68]. The heats of formation of $NaMPO_4$ are lower than those of MPO_4 (see tables 3-1; 3-8; 3-15), suggesting that sodium intercalation enhance thermodynamic stability of MPO_4. In comparison to $LiMPO_4$, we note that heats of formation values of $NaMPO_4$ are slightly higher than those of $LiMPO_4$ (see tables 5-1; 5-3; 5-5), indicating that $LiMPO_4$ is energetically favourable over $NaMPO_4$. This may be attributed to the fact that interactions of oxides are stronger in $LiMPO_4$ than in $NaMPO_4$ [68].

6.2 Electronic DOS of $NaMPO_4$

The calculated total and partial densities of states (DOS) of $NaMPO_4$ structures are presented in Figure 6-1 to 6-3. Our spin polarised DOS calculations show that $NaFePO_4$ has a semi-metallic behaviour, since the Fermi level falls on the Fe 3*d* band. On the other hand, $NaMnPO_4$ and $NaCoPO_4$ show insulating behaviour, since the

Fermi level is located on the edge of the upper valence band. Similar characteristics were observed on $LiMPO_4$ structures. Similarly to the olivine $LiMPO_4$, we note that the energy band gaps become wider as pressure is increased. $NaFePO_4$ shows energy band gaps of 1.17 eV and 1.18 eV in 0 GPa and 10 GPa, respectively. $NaMnPO_4$ shows energy band gaps of 3.51 eV and 3.90 eV, while $NaCoPO_4$ shows 1.87 eV and 1.90 eV. Sodium intercalation on the $NaFePO_4$ leads to the creation of spin-down Fe 3*d* band near E_F and narrowing of the energy band gap at both 0 GPa and 10 GPa. The creation of spin-down band is mainly due to sodium electrons which are essentially transferred to Fe atoms (see Figure 6-2). On the other hand, sodium interaction on *Pnma*-$NaCoPO_4$ and *Pnma*-$NaMnPO_4$ does not show the spin-down band, but a band gap is observed. Furthermore, we note that $NaFePO_4$ shows three spin-down Fe 3*d* peaks at about 0 eV, 4 eV and 6 eV, the $NaMnPO_4$ has only one spin-down Mn 3*d* peak at about 5 eV, while two Co 3*d* peaks contribution in $NaCoPO_4$ are observed around 3-5 eV (see Figure 6-3). Generally, we observe that there are insignificant differences on the electronic properties of $NaMPO_4$ and $LiMPO_4$ structures, as contribution of P and O are basically indistinguishable.

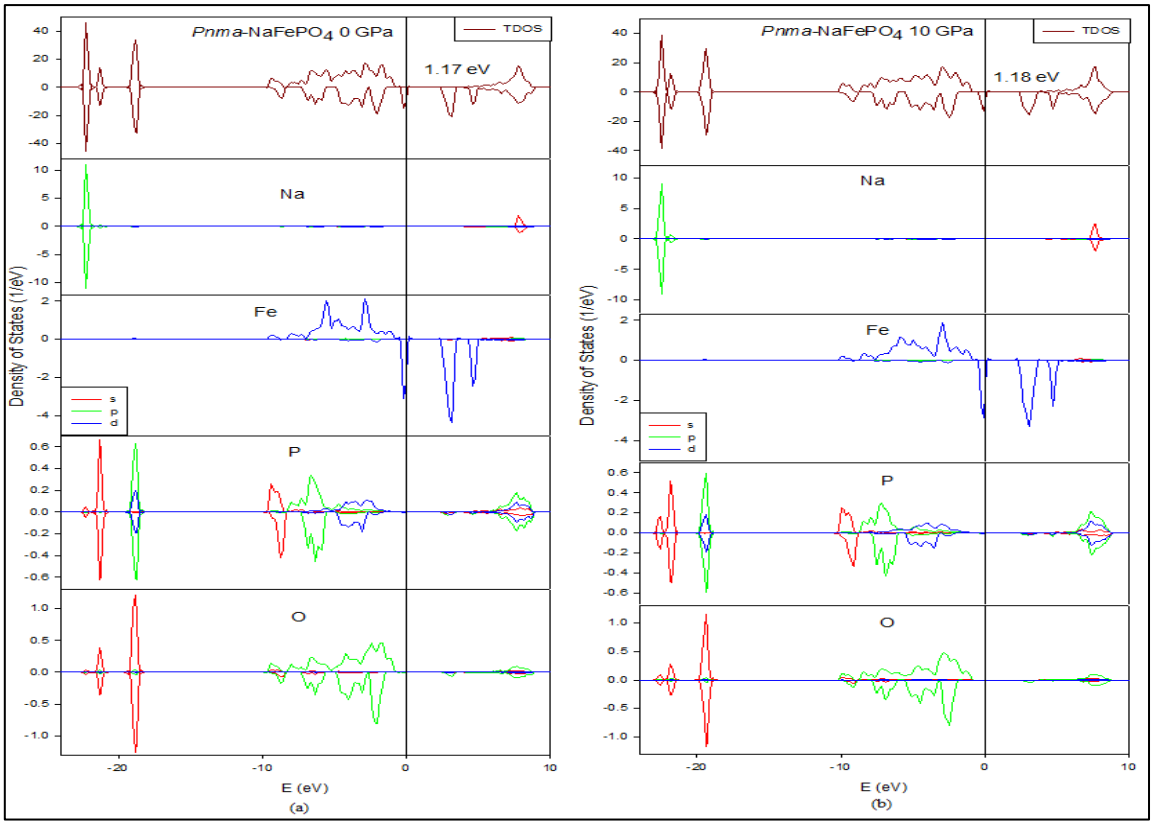

Figure 6-1 Total and partial DOS of *Pnma*-$NaFePO_4$, in (a) 0 GPa and (b) 10 GPa. The Fermi level is taken as the energy zero ($E-E_F=0$).

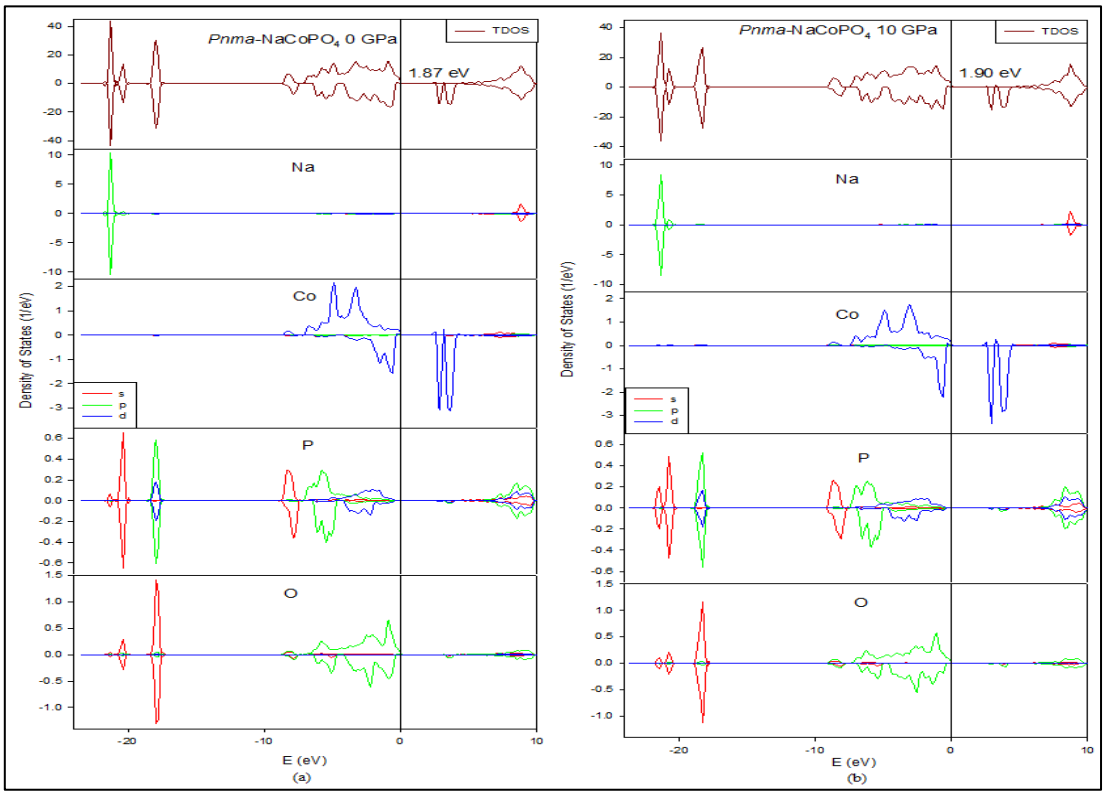

Figure 6-2 Total and partial DOS of *Pnma*-$NaCoPO_4$, in (a) 0 GPa and (b) 10 GPa. The Fermi level is taken as the energy zero ($E-E_F=0$).

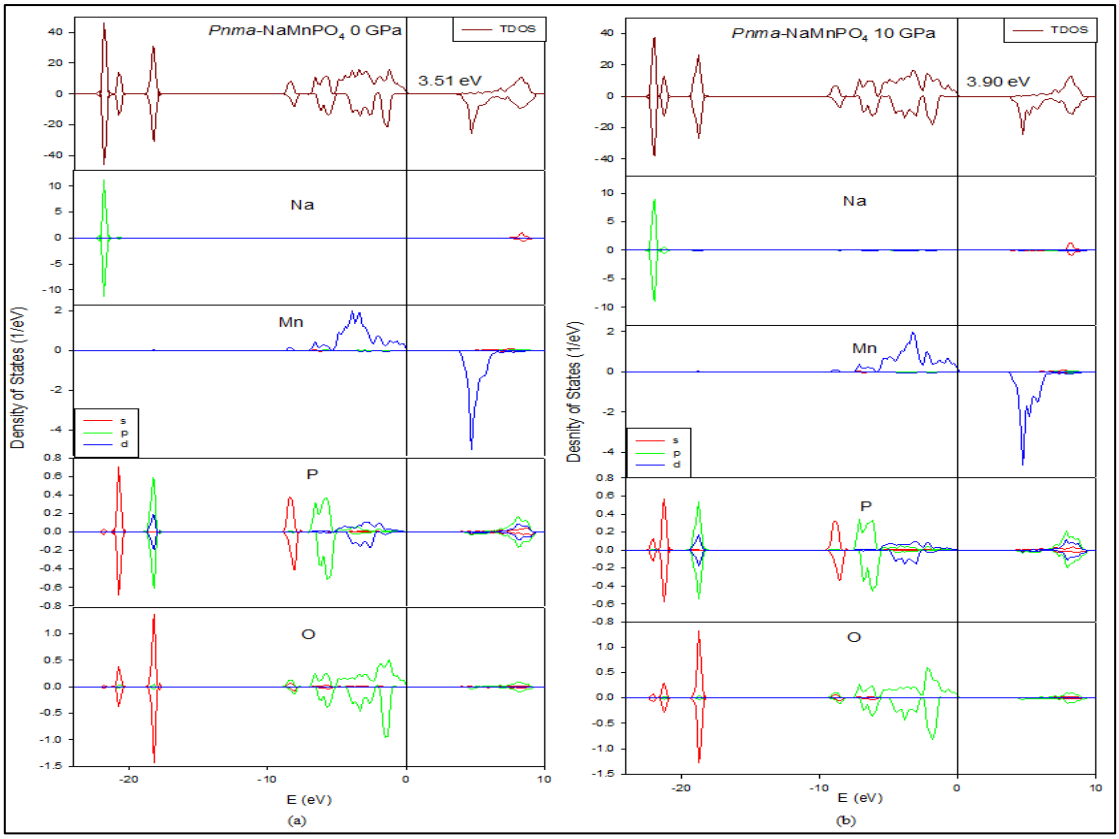

Figure 6-3 Total and partial DOS of *Pnma*-$NaMnPO_4$, in (a) 0 GPa and (b) 10 GPa. The Fermi level is taken as the energy zero ($E-E_F=0$).

6.3 Mechanical Properties of $NaMPO_4$

6.3.1 Phonons Dispersion Curves of $NaMPO_4$

In this section, we present the calculated phonon dispersion spectra and phonon density of states (DOS) for *Pnma*-$NaMPO_4$ in 0 GPa and 10 GPa along high symmetry directions in the Brillouin zone. We note that the dispersion curves are composed of two distinctive modes, the optical and acoustic modes corresponding to the upper and lower sets of curves in the diagram, respectively. The phonon curves show the longitudinal and transverse acoustic and optical phonon branches which show a total of 84 branches. $NaMPO_4$ contains 28 atoms in a unit cell, so there are 3 acoustic

branches (1 longitudinal and 2 transverse) shown at the lower part of the phonon dispersion curve, and 81 optical branches (27 longitudinal and 54 transverse).

In Figure 6-4 we show the phonon dispersion curves and DOS for *Pnma*-$NaFePO_4$ in 0 GPa and 10 GPa. Figure 6-4(a) shows that the frequencies of optical phonon branches start at about 3 THz, while the acoustic start at about -2 THz. Moreover, we observe that negative phonon vibration extend to -4 THz. The presence of negative phonon frequencies suggests vibrational instability. The application of 10 GPa pressure (Figure 6-4(b)) slightly affects the vibrational frequencies. We observe that the optical phonon branches start at about 4 THz, while the acoustic branches starts just below 0 THz. However, the negative phonon dispersion curves along high symmetry directions R (1/2,1/2,1/2), T (0,1/2,1/2), and Z (0,0,1/2) in the Brillouin zone extend down to -3 THz, suggesting vibrational instability. The absence of negative vibrations at Γ (Center of the Brillouin zone) suggests that vibrational instability is not severe, which is consistent with the elastic properties that satisfy the mechanical stability conditions. Furthermore, we note that sodium insertion slightly destabilises *Pnma*-$FePO_4$ as no soft modes are observed and not favourable compared to lithium insertion.

In addition to the phonon dispersion curves, we have calculated the phonon density of states for the completeness of lattice dynamics. The total and partial phonon densities of states in 0 GPa and 10 GPa are presented in Figure 6-4(c) and Figure 6-4(d), respectively. We observe relatively high density of states for Na and Fe atoms below 12 THz, whereas for P and O atoms high densities of states are dominant above 15 THz. This suggests that Na and Fe atoms vibrate in modes of the same low frequencies, while P and O atoms vibrate in modes of high frequencies. Moreover, Fe atoms also show density of states below 0 THz, suggesting that Fe is mainly

responsible for negative acoustic modes in the phonon dispersion curves at both 0 GPa and 10 GPa. Furthermore, the high densities of states for Na and Fe below 12 THz suggest high contribution on the acoustic modes and low on optical. Similarly, P and O contribute more on the optical and less on the acoustic modes.

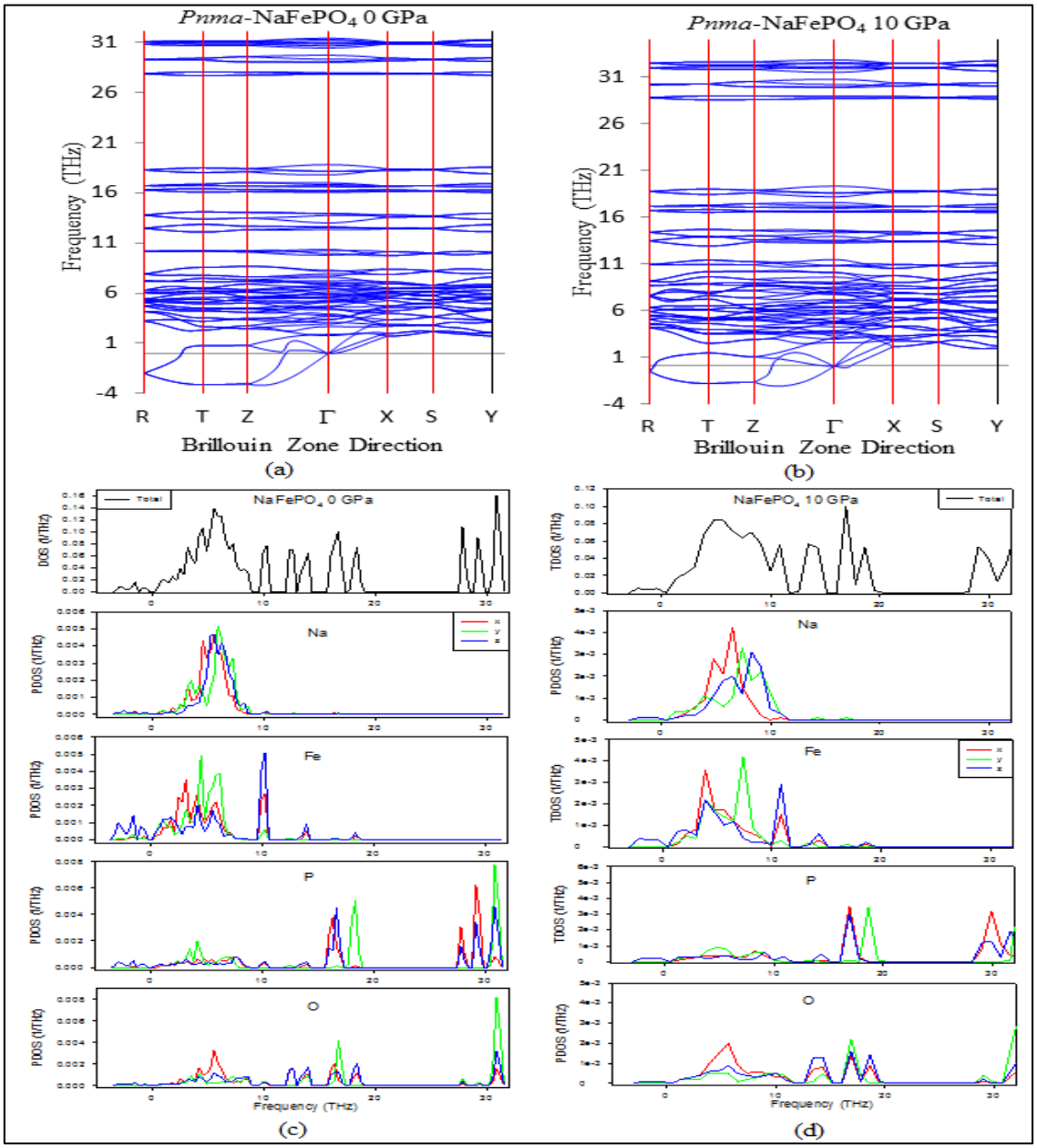

Figure 6-4 Phonon dispersion curves and phonon density of states of $NaFePO_4$ polymorphs in 0 GPa and 10 GPa.

Figure 6-5 shows the phonon dispersion curves and DOS for *Pnma*-$NaCoPO_4$ in 0 GPa and 10 GPa. In ambient pressure (0 GPa), the frequencies of optical phonon modes starts slightly below 3 THz, while the acoustic modes starts below -3 THz. The application of 10 GPa pressure slightly pushes the phonon modes to higher frequencies; the optical modes are observed above 4 THz and acoustic modes above -2 THz. However, the phonon dispersion curves in 0 GPa (Figure 6-5(a) and 10 GPa (Figure 6-5(b)) show negative vibrational modes, suggesting instability. Similarly to *Pnma*-$NaFePO_4$, *Pnma*-$NaCoPO_4$ shows no negative vibrations along Γ, which suggests minimal instability. Similarly to *Pnma*-$NaFePO_4$, we observe that sodium insertion slightly destabilises *Pnma*-$CoPO_4$ and not vibrationally favourable over lithium insertion.

The total and partial DOS in 0 GPa and 10 GPa were also plotted and presented in Figures 6-5(c) and 6-5 (d), respectively. Similarly to $NaFePO_4$, we note that Na and Co show low partial phonon density of states (below 12 THz) while P and O have high density of states (above 12 THz), suggesting that Na and Co atoms vibrate in low acoustic frequency modes, while P and O vibrates in high. Furthermore, we observed that the partial phonon density of states for Co shows negative frequencies, suggesting that Co atoms are predominantly responsible for the negative phonon vibrations observed in the phonon dispersion curves. The negative frequencies are observed at both ambient and high pressures.

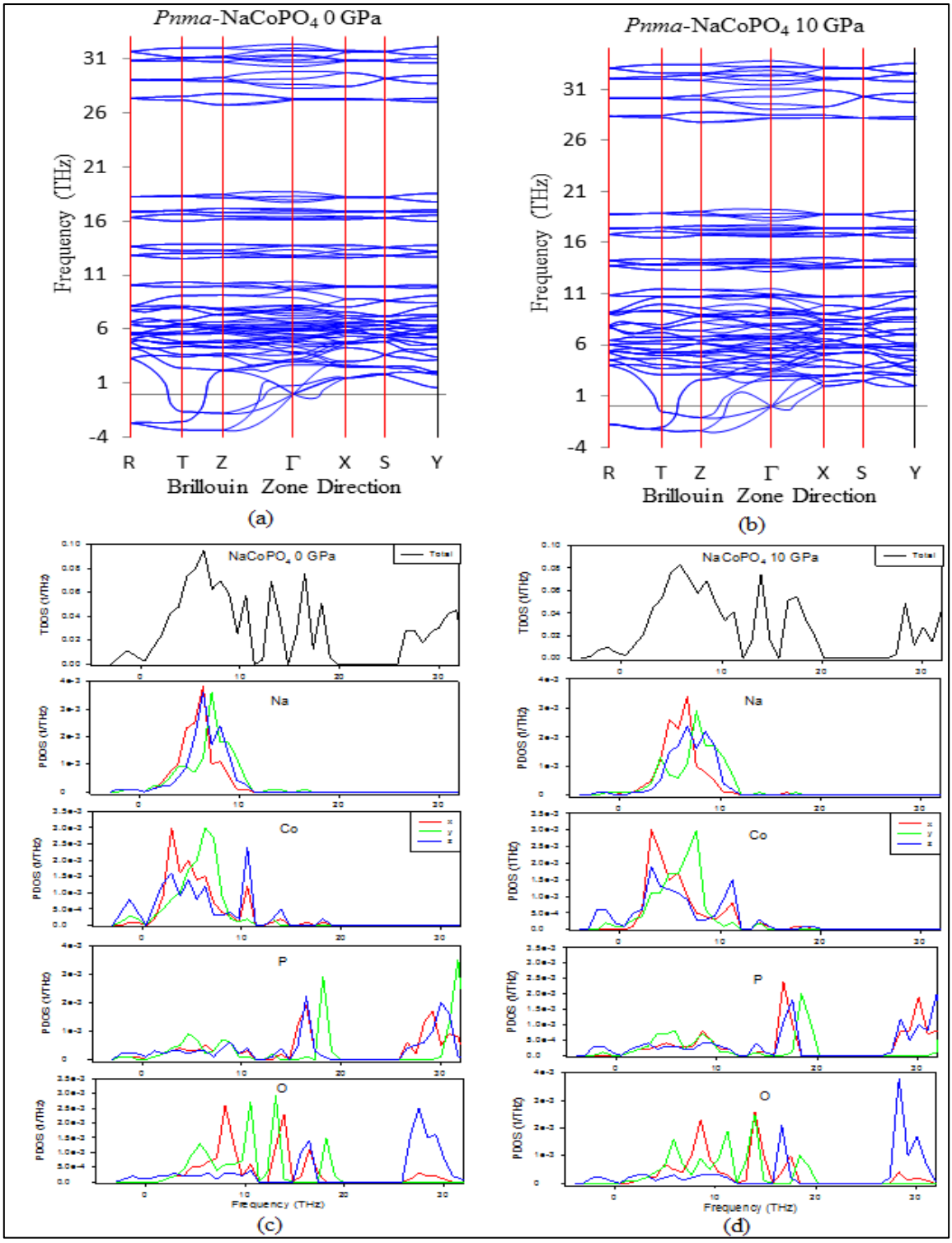

Figure 6-5 Phonon dispersion curves and phonon density of sates of $NaCoPO_4$ polymorphs in 0 GPa and 10 GPa.

In figure 6-6, we present the phonon dispersion curves and DOS for the $NaMnPO_4$ structure in 0 GPa and 10 GPa. The phonon dispersion curves for $NaMnPO_4$ shows negative vibration frequencies down to -3 THz along high symmetry directions R, T and Z in the Brillouin zone in ambient pressure. The application of 10 GPa pressure slightly pushes the negative vibrations to -2 THz, indicating enhancement in stability. On the other hand, the presence of negative vibrations suggests vibrational instability. However, we note that the negative vibrations are absent along symmetry directions Γ, X, S and Y, which is attributed to minimal instability.

In ambient pressure (Figure 6-6 (a)), the frequencies of acoustic modes starts above -3 THz, while the optical modes start above 3 THz. In 10 GPa (Figure 6-6(b)) the acoustic and optical modes start at 1 THz and 4 THz, respectively. The total and partial phonon density of states in 0 GPa and 10 GPa were also calculated and presented in Figure 6-6(c) and Figure 6-6(d), respectively. Similarly to $NaFePO_4$ and $NaCoPO_4$, we note that the partial density of states for Na and Mn show high density of states below 10 THz while P states are dominant above 15 THz. The O states are dominant throughout the frequency range of 0 THz to 32 THz. The partial density of states for Fe shows that the negative acoustic vibrational frequencies emanate from the Fe 3*d*-states at both 0 GPa and 10 GPa.

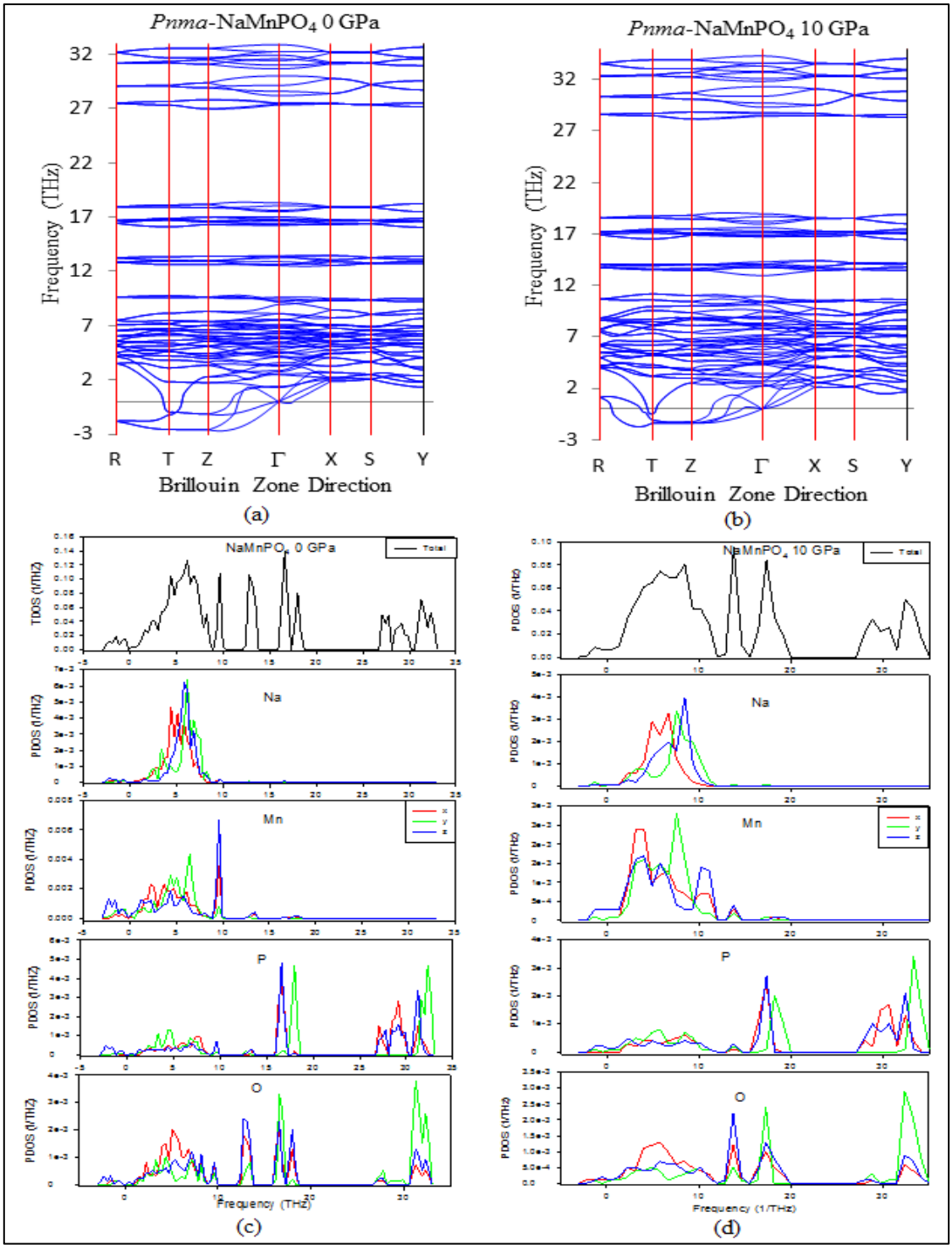

Figure 6-6 Phonon dispersion curves and phonon density of states of $NaMnPO_4$ polymorphs in 0 GPa and 10 GPa.

6.3.2 Elastic Properties of $NaMPO_4$

In table 6-2 we present the elastic constants, moduli and Pugh ratio on $NaMPO_4$ structures.

Table 6-2 Elastic constants (C_{ij}), bulk (B), shear (G), and Young's (E) moduli, Pugh ratio (B/G) for olivine $NaMPO_4$ polymorphs in 0 GPa and 10 GPa.

	0 GPa			10 GPa		
C_{ij} (GPa)	$NaFePO_4$	$NaMnPO_4$	$NaCoPO_4$	$NaFePO_4$	$NaMnPO_4$	$NaCoPO_4$
C_{11}	166.83	178.17	184.83	231.83	241.67	252.00
C_{12}	59.67	59.83	50.00	103.00	99.50	96.75
C_{13}	80.58	70.17	75.25	115.25	105.33	121.33
C_{22}	161.17	163.67	178.33	232.33	239.00	256.00
C_{23}	65.83	61.50	55.58	105.42	104.00	103.67
C_{33}	175.17	163.33	168.33	213.00	204.83	225.33
C_{44}	53.00	50.33	47.67	66.67	62.33	61.00
C_{55}	61.67	62.33	65.67	72.33	67.33	74.00
C_{66}	49.33	51.33	41.67	65.00	67.00	61.00
B_V	101.70	98.69	99.24	147.17	144.80	152.98
B_R	101.04	98.41	98.95	147.03	144.17	152.79
B_H	101.37	98.55	99.10	147.10	144.48	152.89
G_V	52.61	53.71	54.38	64.37	64.44	66.64
G_R	51.98	53.28	52.49	63.64	63.91	65.51
G_H	52.29	53.49	53.43	64.00	64.18	66.07
E_V	134.61	136.39	137.94	168.53	168.36	174.57
E_R	133.12	135.40	133.81	166.84	167.05	171.96
E_H	133.86	135.89	135.87	167.69	167.70	173.26
B/G_V	1.93	1.84	1.83	2.29	2.25	2.30
B/G_R	1.94	1.85	1.89	2.31	2.26	2.33
B/G_H	1.94	1.84	1.86	2.30	2.25	2.31

We note that all calculated elastic constants are positive and satisfy the necessary stability conditions for orthorhombic systems (as discussed in section 2.6.4.1) at both ambient and high pressures, suggesting that the structure is mechanical stable. When

sodium is intercalated in $FePO_4$, C_{ij} values decreases, except of C_{23} which increases by 22.50 GPa. These anomalies suggest weak resistance to linear compression and shear along *a*, *b* and *c* and {100}, {010} and {001} planes, respectively. It is also noted that the C_{ij} values increase as pressure is increased to 10 GPa, suggesting that the $NaMPO_4$ structures are softer in ambient pressure.

The resultant macroscopic moduli are also presented in table 6-2. We note that the three olivine $NaMPO_4$ structures give moduli values that are closer to one another. The bulk modulus suggests that $NaFePO_4$ (101.37 GPa) is slightly harder than $NaCoPO_4$ (99.10 GPa) and $NaMnPO_4$ (98.55 GPa) in ambient pressure. We also note that the bulk moduli values increase in 10 GPa pressure, where $NaCoPO_4$ (152.89 GPa) is harder than $NaFePO_4$ (147.10 GPa) and $NaMnPO_4$ (144.48 GPa). The shear is less that bulk moduli, thus the shear is the parameter limiting stability [53] and we observe that all structures give positive values, suggesting stability. The Young's modulus suggests that $NaMnPO_4$ (135.89 GPa) is slightly stiffer than $NaCoPO_4$ (135.87 GPa) and $NaFePO_4$ (133.86 GPa) in ambient pressure. However, $NaCoPO_4$ is slightly stiffer than $NaMnPO_4$ (167.69 GPa) and $NaFePO_4$ (167.70 GPa) in high pressure of 10 GPa. The Pugh ratio of ductility and brittleness shows that $NaMPO_4$ structures are ductile ($B/G>1.75$) at both ambient and high pressures. Furthermore, we note that ductility increases with pressure.

The effect of sodium intercalation on the elastic properties of olivine MPO_4 has also been investigated. Sodium transportation is expected to be easier on MPO_4 structures than in $NaMPO_4$ structures, since they are isostructural and Na atoms occupy empty sites in MPO_4 [53]. However, we found that $NaFePO_4$ and $NaCoPO_4$ are softer than $FePO_4$ and $CoPO_4$, respectively, since C_{ij} are larger in $FePO_4$ and $CoPO_4$ (see tables 4-

1; 4-3). On the other hand, sodium intercalation on $NaMnPO_4$ corresponds to the theory, since the C_{ij}'s are generally smaller than on $NaMnPO_4$ at both 0 GPa and 10 GPa. The bulk, shear and Pugh ratio show that hardness, stiffness and ductility are enhanced with sodium intercalation. In comparing olivine $NaMPO_4$ and $LiMPO_4$, we note that $LiMPO_4$ structures are generally harder, stiffer and ductile over $NaMPO_4$, due to higher moduli and Pugh ratio.

The elastic anisotropic factors of the olivine $NaMPO_4$ have been calculated to determine susceptibility of the material to cracks during battery operation. The anisotropy factors A_1, A_2, and A_3 must equate to unity; while the percentage bulk modulus (A_B) and shear modulus (A_G) anisotropy must show zero percentage [162, 165]. At both ambient and high pressures, we note that the anisotropy factor A_1 is clearly far from unity by a factor greater than 0.5 for all systems, indicating higher degree of anisotropy. On the other hand, the A_2 and A_3 approach unity, and 10 GPa pressure slightly enhancing isotropy. We note that A_2 diverge from unity by 18.59 %, 19.98 % and 10.87 % for $NaFePO_4$, $NaMnPO_4$ and $NaCoPO_4$, respectively in 0 GPa, while it diverges by 20.95 %, 13.26 % and 7.69 % in 10 GPa. A_3 diverge from unity by 5.55 %, 7.90 % and 44.95 % for $NaFePO_4$, $NaMnPO_4$ and $NaCoPO_4$, respectively for 0 GPa. In 10 GPa, degree of anisotropy is greatly reduced as A_3 diverge from unity by 0.70 %, 5.02 % and 25.22 % for $NaFePO_4$, $NaMnPO_4$ and $NaCoPO_4$, respectively. The olivine $NaMPO_4$ structures show greater degree of anisotropic as compared to $LiMPO_4$ structures. Thus olivine $NaMPO_4$ systems may be more susceptible to cracks during battery operation than $LiMPO_4$ systems.

A_B and A_G further confirm that $NaMPO_4$ structures have high degree of anisotropy, since we note none zero percentage values. A_B is lesser than A_G, indicating that

$NaMPO_4$ structures are less anisotropic in compressibility than in shear. The universal anisotropy factor A^U also show none zero value, indicating the degree of anisotropy.

Table 6-3 Anisotropy factors and Poisson ratio of $NaMPO_4$ polymorphs in 0 GPa and 10 GPa.

	0 GPa			10 GPa		
Anisotropy	$NaFePO_4$	$NaMnPO_4$	$NaCoPO_4$	$NaFePO_4$	$NaMnPO_4$	$NaCoPO_4$
A_1	0.42	0.42	0.38	0.40	0.38	0.34
A_2	1.21	1.22	1.12	1.23	1.14	1.08
A_3	0.95	0.92	0.63	1.01	0.95	0.78
A_B	0.15	0.14	0.15	0.05	0.22	0.06
A_G	0.60	0.40	1.77	0.57	0.41	0.86
A^U	0.07	0.04	0.18	0.06	0.05	0.09

6.4. Voltage Profile for Li/$NaMPO_4$

In this section we present the predicted Li and Na intercalation/deintercalation potentials of $LiMPO_4$ polymorphs and $NaMPO_4$ olivines. The aspect of intercalation potential is of great essential when determining the competence of new materials as positive electrodes in rechargeable lithium and sodium ions batteries. A high potential increases the energy density of the material, however, Li/Na may not be removed from host structure and the battery may experience electrolyte breakdown if the potential is too high. On the other hand, a very low potential can lead to moisture sensitivity of the electrode material [1]. It has been reported that 2.7 V per cell is the predefined limit for discharge and 3.9 V per cell for charge; thus end of discharge/charge limit is reached when these terminal cell voltages are established [210]. The average potential, V when removing and inserting Li/Na on the host material MPO_4 is calculated by [211]:

$$V = -\frac{\left[E(A_{x_2}MPO_4) - E(A_{x_1}MPO_4) - (x_2 - x_1)E(A)\right]}{(x_2 - x_1)e} \qquad 6.2$$

where E is the total VASP energy, A is Li and Na, and e is an absolute electron charge. The average removal/insertion potentials of the olivine $LiMPO_4$ and $NaMPO_4$ are shown in Table 6-4 and plotted in Figure 6-7. Experimental values are also shown where available. The DFT+*U* calculations show that Co-based olivine has higher potential compared to Mn-based and Fe-based, respectively. This is in good agreement to the experimental and previous calculations [1, 2, 5, 9]. We note that $LiFePO_4$, $LiCoPO_4$ and $LiMnPO_4$ have insertion/removal potentials of 3.43 V, 4.34 V and 4.20 V, respectively. This suggests that Li may not be removed from MPO_4 and the battery may experience electrolyte breakdown in $LiCoPO_4$ and $LiMnPO_4$, since the potentials exceed the maximum limit of 3.9 V. On the other hand a 3.43 V potential for $LiFePO_4$ suggests that the negative electrode may be protected from lithium deposition side reaction during charge in a cell [210]. The insertion potentials for $LiFePO_4$, $LiCoPO_4$ and $LiMnPO_4$ compare well to the experimental values to within 2.02 %, 10.07 % and 2.41 %, respectively. Studies by Zhou *et al*. on the lithium intercalation potential of $LiMPO_4$ have shown that the potential generally increases with the atomic number of the 3*d*-metal series, except for $LiFePO_4$ [1]. The lowest potential for $LiFePO_4$ is believed to be related to the particular electron structure of Fe^{3+}.

Furthermore, the sodium intercalation potentials for the olivine $NaMPO_4$ were calculated and presented in Table 6-4 and Figure 6-7. The experimental intercalation potentials for olivine $NaMPO_4$ are not known to our knowledge. We note that the predicted sodium intercalation potentials are lower than those of the lithium intercalation potentials. Similarly to $LiMPO_4$ olivines, Co-based structure shows high potential over Mn and Fe, respectively. We note that $NaFePO_4$, $NaCoPO_4$ and

$NaMnPO_4$ show the potentials of 3.00 V, 4.22 V and 3.70 V, respectively. The calculated potentials for $NaFePO_4$ and $NaMnPO_4$ fall within the minimum and maximum limits of 2.7 V and 3.9 V, respectively, suggesting that the cell will be safe from moisture sensitivity of the cathode material, side reactions and minimal solid-state diffusion [210]. The high potential for $NaCoPO_4$ suggests that Na may not be removed and side reactions may occur in the cell leading to capacity fading of the battery.

The intercalation potentials of $LiMPO_4$ and $NaMPO_4$ were also calculated in high pressure (10 GPa). We note that the potentials increase with pressure, suggesting that the energy density is enhanced with pressure [212]. Furthermore, we note that the potential for $NaMnPO_4$ exceeds the maximum charge limit, suggesting that Na may not be removed and side reactions may occur in the cell in 10 GPa. On the other hand, the potentials for $LiFePO_4$ and $NaFePO_4$ remain within the discharge and charge potential, while $LiCoPO_4$ and $NaCoPO_4$ further surpasses the maximum limit. This suggests that $LiFePO_4$ and $NaFePO_4$ can operate at a pressure range of 0 to 10 GPa without side reactions in the cell.

Table 6-4 Voltage profiles of olivine *Pnma*-Li/$NaMPO_4$ in 0 GPa and 10 GPa.

Structure	$LiFePO_4$	$NaFePO_4$	$LiCoPO_4$	$NaCoPO_4$	$LiMnPO_4$	$NaMnPO_4$
0 GPa	3.43	3.00	4.34	4.22	4.20	3.70
Exp.	3.5 [212]		4.8 [5]		4.1 [9]	
10 GPa	3.68	3.38	4.75	4.77	4.68	4.10

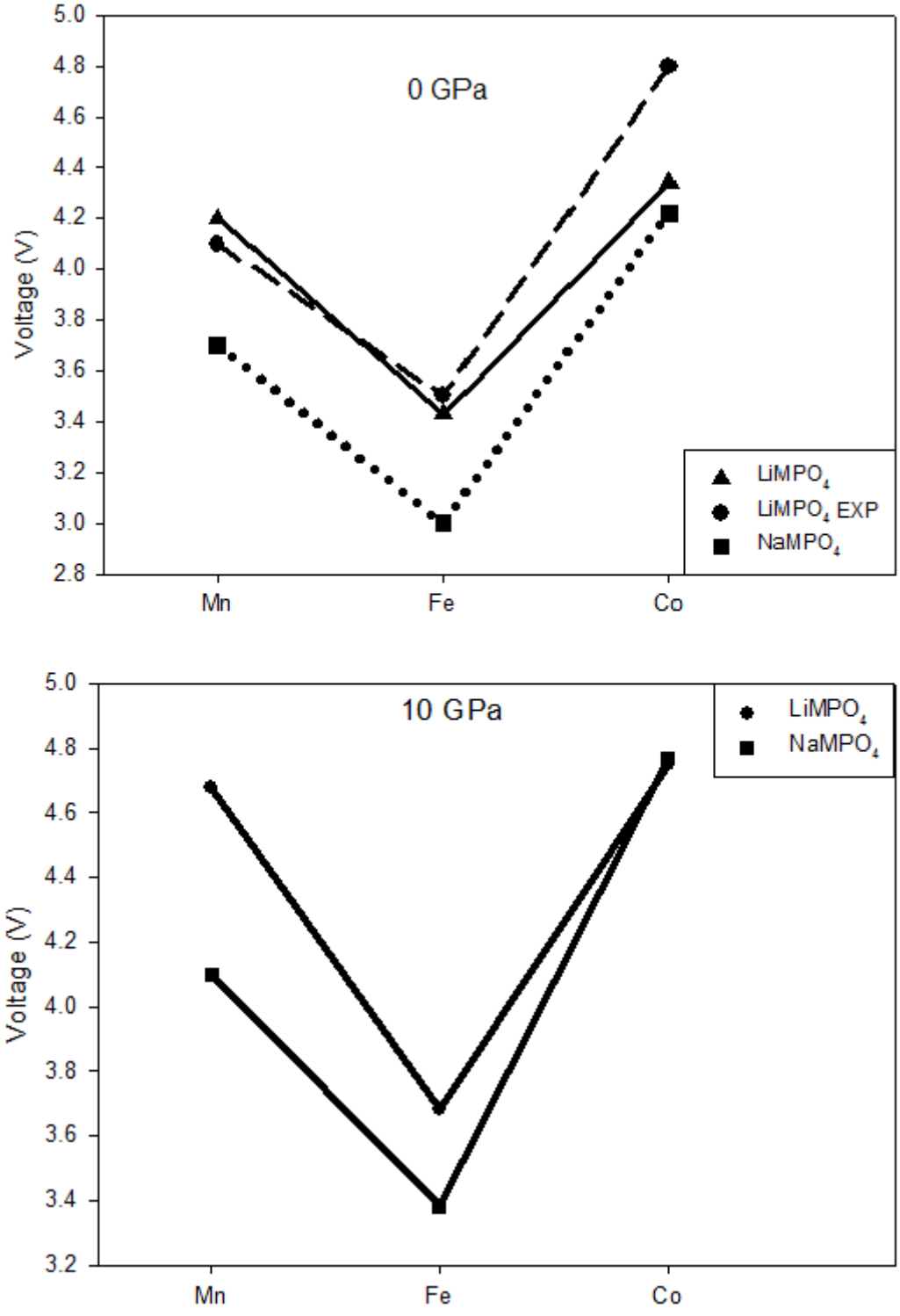

Figure 6-7 Voltage profiles for olivine Li/$NaMPO_4$ in 0 GPa and 10 GPa.

The intercalation potentials of $LiMPO_4$ polymorphs in 0 GPa and 10 GPa are presented in Table 6-5 and plotted in Figure 6-8 below. We note that *$P3_121$*-$LiFePO_4$ (2.45 V), *Pbca*-$LiFePO_4$ (2.48 V) and *$P2_1/c$*-$LiFePO_4$ (2.47 V) show potentials that are less than the minimum limit of 2.7 V in ambient pressure (0 GPa), indicating that solid-state diffusion is the limiting mechanism and a potential moisture sensitivity of the cathode material may take place in a cell [1, 210]. On the other hand, *Pnma*-$LiFePO_4$ and *Cmcm*-$LiFePO_4$ show potentials that are within the cell terminal voltages range. The increase of pressure increases the potentials of $LiFePO_4$ polymorphs to within the cell terminal voltages range, except for *$P2_1/c$*-$LiFePO_4$, suggesting good operation in 10 GPa. In contrast to $LiFePO_4$, we note that $LiCoPO_4$ polymorphs show intercalation potentials that are above the maximum limit per unit cell, except for *$P3_121$*-$LiCoPO_4$, suggesting that lithium may not be removed and side reactions may occur in the cell. The increase of pressure further increases the intercalation potentials above the maximum limit, thus $LiCoPO_4$ batteries may undergo cell breakdown in high pressures. The $LiMnPO_4$ polymorphs show that only *$P2_1/c$*-$LiMnPO_4$ gives a potential that allows lithium insertion/removal with the intercalation potential of 2.96 V per cell, while *$P3_121$*-$LiMnPO_4$ (3.91 V) potential is slightly above the maximum limit. Similarly to ambient pressure, $P2_1/c$-$LiMnPO_4$ (3.89 V) is the only polymorph that allows lithium insertion/removal in a cell.

Table 6-5 Voltage profiles for $LiMPO_4$ polymorphs in 0 GPa and 10 GPa.

Voltages (V)						
0 GPa				10 GPa		
Symmetry	$LiFePO_4$	$LiCoPO_4$	$LiMnPO_4$	$LiFePO_4$	$LiCoPO_4$	$LiMnPO_4$
$P3_121$	2.45	3.88	3.91	2.89	4.28	4.30
Pnma	3.43	4.34	4.20	3.68	4.75	4.68
Pbca	2.48	3.99	4.23	3.19	4.54	4.70
$P2_1/c$	2.47	4.10	2.96	2.60	4.42	3.89
Cmcm	3.21	4.48	4.12	3.14	4.90	4.30

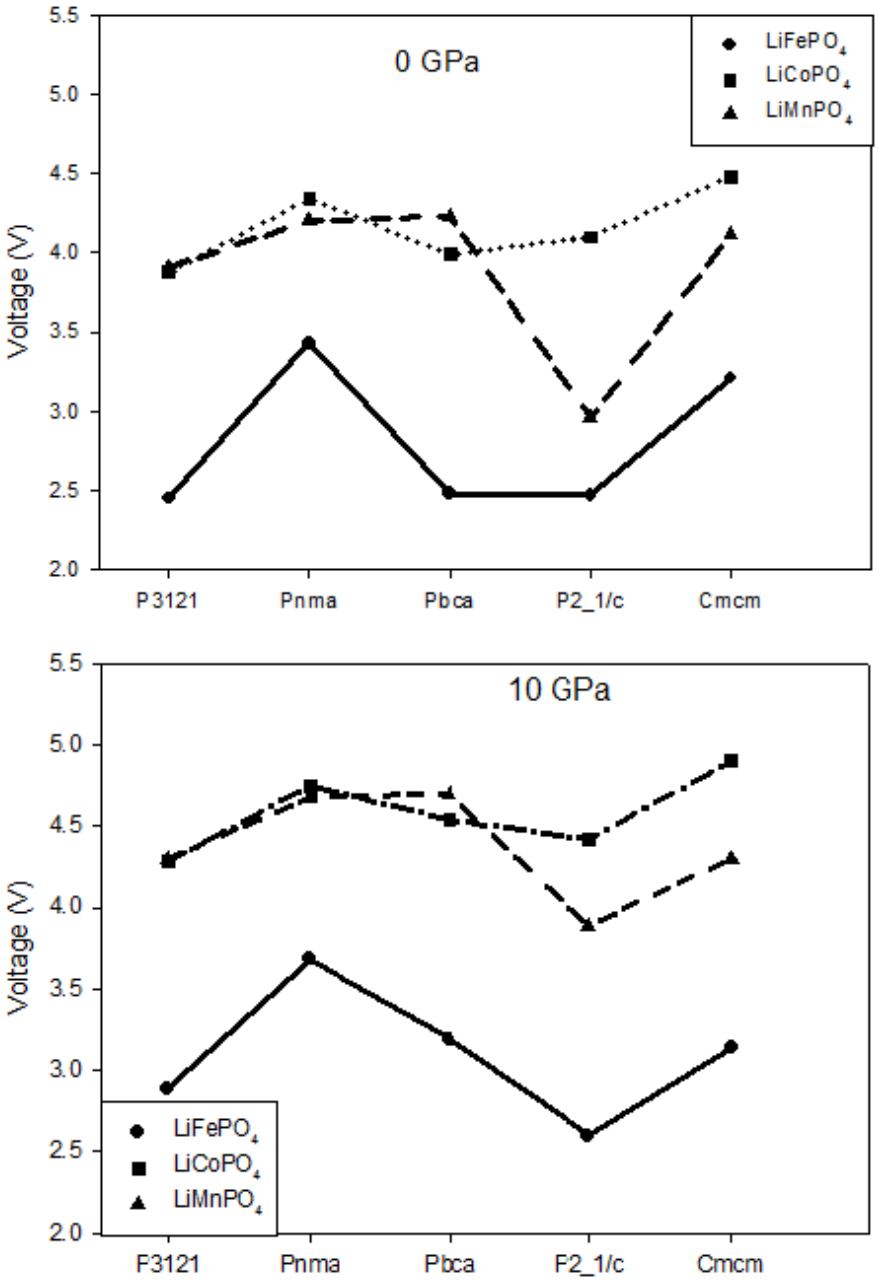

Figure 6-8 Voltage profiles for $LiMPO_4$ polymorphs in 0 GPa and 10 GPa.

Chapter 7

Summary and Conclusions

Density functional theory was used to investigate the structural, electronic and mechanical properties as well as voltage profiles of MPO_4 and Li/$NaMPO_4$ polymorphs. We employed DFT with Hubbard correction *U* calculation within the exchange correlation of GGA-PBE as embodied in the VASP code, and the PHONON codes. Five different structural polymorphs with different space groups were considered; namely, $P3_121$, *Pnma*, *Pbca*, $P2_1/c$ and *Cmcm*. Full structure optimisation has been performed to determine the equilibrium cell parameters and heats of formation. Spin polarised local density approximation calculation was also undertaken to calculate the electronic total and partial densities of states. Mechanical properties were determined by calculating the elastic properties and phonon dispersion curves. The effect of pressure on the calculated properties has been determined, particularly in 10 GPa.

The equilibrium lattice parameters and cell volumes for MPO_4 structural polymorphs are in good agreement with the available experimental and theoretical data. $FePO_4$ and $CoPO_4$ polymorphs were accurate with the experimental values to within 3 % and 4 %, respectively, while $MnPO_4$ are in good correspondence to theoretical values to within 3 %, which is typical for DFT+*U* transition metal phosphates calculations [177, 178, 180]. The heats of formation for $FePO_4$ suggested that the berlinite $P3_121$-$FePO_4$ is the most stable polymorph over the orthorhombic *Pbca*-$FePO_4$, monoclinic $P2_1/c$-$FePO_4$, heterosite *Pnma*-$FePO_4$ and high pressure *Cmcm*-$FePO_4$, respectively. However, the

introduction of external pressure shows that $P3_121$-$FePO_4$ polymorph is most stable up to 4 GPa, while the *Cmcm*-$FePO_4$ is most stable above 4 GPa. On the other hand, heats of formation of $CoPO_4$ polymorphs shows that *Cmcm*-$CoPO_4$ is the most stable throughout the pressure range of 0 – 10 GPa. *Pnma*-$CoPO_4$ is least stable in ambient pressure; however second most stable at pressures above 2.5 GPa. The heats of formation of $MnPO_4$ polymorphs predicted that *Pnma*-$MnPO_4$ is the most stable in ambient pressure, while the application of pressure favours *Cmcm*-$MnPO_4$ in pressures above 4 GPa.

We have also calculated the densities of states (DOS) of MPO_4 polymorphs to investigate their electronic structure behaviour. $FePO_4$ polymorphs show relatively wide band gaps (ranging from 0.35 eV to 2.69 eV) and the Fermi level is located on the edge of the valence band. This suggests that there may be a dilute number of thermally excited carriers residing near the band gap edge. The presence of energy band gap and the location of the Fermi level suggest that $FePO_4$ polymorphs are either semiconductors or insulators, hence low in electronic conductivity at both ambient and high pressures.

The $CoPO_4$ polymorphs show different electronic behaviour. $P3_121$-$CoPO_4$, *Pnma*-$CoPO_4$ and *Cmcm*-$CoPO_4$ show semiconducting behaviour, where the energy band gaps ranging from 0.34 eV to 0.83 eV were observed and the Fermi level lies on the edge of the upper valence band at both ambient and high pressures. These suggest low electronic conductivity. On the other hand, *Pbca*-$CoPO_4$ and $P2_1/c$-$CoPO_4$ show no band gap, but a continuous flow of electrons from the valence to the conduction band, suggesting metallic behaviour and good electrochemical conductivity. The electronic DOS on $MnPO_4$ polymorphs show a shallow pseudo gap, indicating that $MnPO_4$

polymorphs have good conducting and metallic characteristics in ambient and high pressures.

Furthermore, the mechanical properties of MPO_4 were determined by calculating phonon dispersion curves and elastic properties. The phonon dispersion curves for $FePO_4$ and $CoPO_4$ polymorphs suggest that *Pnma*-Fe/$CoPO_4$ and *Cmcm*-Fe/$CoPO_4$ are most stable polymorphs in ambient and high pressures, respectively. These polymorphs show no soft modes or negative vibrational branches. *$P3_121$*-Fe/$CoPO_4$, *Pbca*-Fe/$CoPO_4$ and *$P2_1/c$*-Fe/$CoPO_4$ have soft modes down to -5 THz in ambient and high pressures, indicating vibrational instability. Furthermore, the phonon dispersion curves for $MnPO_4$ polymorphs show that all polymorphs are vibrationally unstable, due to the presence of soft modes. The negative vibrations on *Cmcm*-$MnPO_4$ are consistent with the negative elastic constant C_{55}, suggesting that $MnPO_4$ may not be feasible as a high pressure phase.

The mechanical properties of MPO_4 polymorphs were validated by further calculating the elastic properties. The elastic constants of $FePO_4$ polymorphs satisfy the necessary conditions for mechanical stability at both ambient and high pressures. Moreover, the shear moduli are positive, further indicating mechanical stability. The elastic properties of *$P3_121$*-$FePO_4$ are in good agreement with the experimental and calculated results found by Mittal *et al*. [54] and Labeguerie *et al*. [193]. For the well-studied *Pnma*-$FePO_4$, we noted that our DFT+*U* calculations overestimate the previous calculations by Maxisch and Ceder [53]. This may be due to the use of different choice of Hubbard *U* parameter: 5.5 eV and 4.7 eV were used, respectively. However, the trend of elastic constants is the same for these *U* values. The macroscopic bulk and Young's moduli indicate that *Pnma*-$FePO_4$ (B_H=119.63 GPa;

E_H=204.70 GPa) is the hardest and stiffest polymorph, while *Pbca*-$FePO_4$ (B_H=26.74 GPa; E_H=40.83 GPa) is the least in hardness and stiffness. The Pugh ratio (for ductility and brittleness) suggested that the trigonal *P3₁21*-$FePO_4$ and monoclinic *P2₁/c*-$FePO_4$ are ductile i.e. B/G>1.75, while the orthorhombic *Pnma*-$FePO_4$, *Pbca*-$FePO_4$ and *Cmcm*-$FePO_4$ are brittle i.e. B/G>1.75. The increase of pressure up to 10 GPa enhances the hardness, stiffness and brittleness for the trigonal *P3₁21*-$FePO_4$ polymorph. On the other hand, hardness and ductility increase, while stiffness decreases for the orthorhombic *Pnma*-$FePO_4$ and *Pbca*-$FePO_4$. Furthermore, the hardness of *P2₁/c*-$FePO_4$ decreases, while brittleness and stiffness are enhanced. The anisotropic factors have suggested that $FePO_4$ polymorphs have the degree of anisotropic i.e. the anisotropy factors are not equal to unity and the percentage bulk and shear modulus are not zero.

The elastic constants for $CoPO_4$ showed that the orthorhombic (space groups; *Pnma*, *Pbca* and *Cmcm*) systems satisfy the necessary condition for stability, while the negative C_{14} value on *P3₁21*-$CoPO_4$ correspond well with the negative vibrations observed on the phonon dispersion curves. Furthermore, the monoclinic *P2₁/c*-$CoPO_4$ polymorph does not satisfy the stability criteria $(C_{35}C_{55} - C_{35}^2) > 0$, hence the system is mechanical unstable. The bulk and Young's moduli suggest that *Pnma*-$CoPO_4$ is the hardest and stiffest polymorph, while *P3₁21*-$CoPO_4$ is the least in hardness and stiffness, respectively. The Pugh ratio showed that *P3₁21*-$CoPO_4$, *Pnma*-$CoPO_4$ and *Cmcm*-$CoPO_4$ are easy to break (brittle), while *Pbca*-$CoPO_4$ and *P2₁/c*-$CoPO_4$ are malleable (ductile). Interestingly, the application of 10 GPa pressure stabilises *P2₁/c*-$CoPO_4$, since stability criteria $(C_{35}C_{55} - C_{35}^2 > 0$ is satisfied.

The necessary stability criterion on trigonal, orthorhombic and monoclinic $MnPO_4$ systems showed mechanical stability in all the polymorphs, since all the stability criterion were satisfied. However, *Cmcm*-$MnPO_4$ did not satisfy the criteria where the elastic constant $C_{55}>0$, indicating mechanical instability consistent well with the phonon soft modes (Figure 4-14). The macroscopic bulk and Young's modulus suggested hardness on *Pnma*-$MnPO_4$ (84.94 GPa) over *P2₁/c*-$MnPO_4$ (73.96 GPa), *P3₁21*-$MnPO_4$ (40.51 GPa) and *Pbca*-$MnPO_4$ (39.58 GPa), respectively. On the other hand, the Young's modulus suggested stiffness on *Pnma*-$MnPO_4$ (131.63 GPa) over *P2₁/c*-$MnPO_4$ (101.86 GPa), *Pbca*-$MnPO_4$ (65.59 GPa) and *P3₁21*-$MnPO_4$ (42.47 GPa), respectively. The Pugh ratio for ductility and brittleness showed that the trigonal and monoclinic systems are ductile, while the orthorhombic systems are brittle. The application of 10 GPa pressure generally increases the elastic constants of $MnPO_4$ polymorphs and macroscopic moduli; consequently enhancing hardness, stiffness and ductility. Similarly to the $FePO_4$ and $CoPO_4$ structural polymorphs, $MnPO_4$ polymorphs are relatively anisotropic.

Furthermore, the structural, thermodynamic, electronic and mechanical properties of lithium intercalation on MPO_4 have been determined in ambient and high pressures. The effect of lithium intercalation on the respective properties has also been analysed. The equilibrium cell parameters of $LiMPO_4$ are in good agreement to available experimental data. *Pnma*-$LiFePO_4$ polymorph compared well with the experimental findings to within 1 %, while *Cmcm*-$LiFePO_4$, *Pnma*-$LiCoPO_4$ and *Pnma*-$LiMnPO_4$ agree to within 8 %, 3 % and 8 %, respectively [5, 36, 42, 201]. The equilibrium cell volume as expected changed minimally during lithium intercalation as lithium atoms occupy interstitial sites. The cell volume for *P3₁21*-$LiFePO_4$, *Pnma*-$LiFePO_4$ and *Cmcm*-$LiFePO_4$ slightly changed by 0.97 %, 4.86 % and 3.52 %, respectively, which

suggests good reversibility during the charge/discharge process and long life cycle. However, *Pbca*-$LiFePO_4$ and *P2₁/c*-$LiFePO_4$ display poor reversibility and short life cycle as the respective volumes change by larger amounts. The introduction of 10 GPa pressure brings about a significant change on the reversibility and life cycle. We noted that the *P3₁21*-$LiFePO_4$ is not preferred in high pressure with a large volume change of about 26 % during lithium intercalation. On the other hand, *Pbca*-$LiFePO_4$ and *P2₁/c*-$LiFePO_4$ are preferred in 10 GPa, since they display a minimal volume change of 11.8 % and 2.12 %. *Pnma*-$LiFePO_4$ and *Cmcm*-$LiFePO_4$ remain relatively stable, as volume changes of 10.4 % and 2.51 % were recorded.

Similarly to $LiFePO_4$ polymorphs, *P3₁21*-$LiCoPO_4$, *Pnma*-$LiCoPO_4$ and *Cmcm*-$LiCoPO_4$ are potentially good in reversibility and long life cycle, as they display volume changes of 0.58 %, 4.47 % and 7.19 %, respectively, while *Pbca*-$LiCoPO_4$ and *P2₁/c*-$LiCoPO_4$ display poor reversibility and short life cycle. All $LiMnPO_4$ polymorphs show good reversibility and long life cycle as the equilibrium cell volumes change to within 7 %.

Thermodynamic stability has been investigated for all $LiMPO_4$ structural polymorphs and stability trend has been deduced for the respective three structures under study. For the $LiFePO_4$ polymorphs, *Pbca*-$LiFePO_4$ and *P2₁/c*-$LiFePO_4$ are the most stable polymorphs in ambient and high pressures, respectively; while *P3₁21*-$LiFePO_4$ is the least stable polymorph at both ambient and high pressures. The intermediates, *Pnma*-$LiFePO_4$ and *Cmcm*-$LiFePO_4$ are respectively metastable at either pressure condition. Similarly to $LiFePO_4$ polymorphs, LiCo/$MnPO_4$ polymorphs showed that *Pbca*-LiCo/$MnPO_4$ is the most thermodynamic stable polymorph in ambient pressure and *P3₁21*-LiCo/$MnPO_4$ is the least stable at any pressure. In 10 GPa pressure, we noted that *P2₁/c*-$LiCoPO_4$ is the most stable polymorph, while stability trend remained

unaltered for $LiMnPO_4$ polymorphs. *Pnma*-LiCo/$MnPO_4$ and *Cmcm*-LiCo/$MnPO_4$ are intermediately metastable through all pressure range.

Generally, we note that lithium insertion has significant role in enhancing the stability of MPO_4 structural polymorphs. $LiMPO_4$ polymorphs also show good reversibility during charge/discharge process and long life cycle. It is also apparent that $LiMnPO_4$ polymorphs are more energetically favourable over $LiFePO_4$ and $LiCoPO_4$ polymorphs, respectively.

In addition, the electronic properties were determined to deduce their band gap as well as conductivity, in particular the density of states. It was observed that lithium intercalation enhances the electronic conductivity of all $LiFePO_4$ polymorphs due to the creation of spin-down 3*d* band. It was also observed that the Fermi level falls on 3*d* band; hence the structure has a metallic behaviour at both ambient and high pressures. $LiCoPO_4$ polymorphs showed poor electronic conductivity as the Fermi level falls on the edge of the upper valence band. Moreover, the relatively wide band gaps supplement the insulator behaviour. Similarly, observations have been made for $LiMnPO_4$ which also displays insulator behaviour. *Pbca*-$LiMnPO_4$ and *$P2_1/c$*-$LiMnPO_4$ have electrons overlapping from the valence band to the conduction band, suggesting metallic characteristics. Furthermore, it was noted that lithium intercalation show reduced states around the Fermi level for all $LiMPO_4$ structural polymorph, indicating stability enhancement at all pressures up to 10 GPa.

The mechanical properties were investigated by calculating the phonon dispersion curves and elastic properties. The phonon dispersion curves showed that trigonal systems, possessing space group *$P3_121$*, are vibrational unstable as soft modes (negative vibrations) are observed. The existence of soft modes corresponds well with

the presence and low value of the hexagonal-trigonal elastic constant C_{14}. On the other hand, the orthorhombic systems with space groups *Pnma* and *Cmcm* showed no soft modes, indicating vibrational stability. This is in good agreement with the elastic constants, where all orthorhombic systems satisfied the necessary conditions for stability. Furthermore, lithium intercalation enhanced the stability of *Pnma*-$MnPO_4$ and *Cmcm*-$MnPO_4$, since the delithiated polymorphs showed negative vibrations.

The macroscopic bulk and Young's moduli suggested that *Pnma*-$LiFePO_4$ is the hardest and stiffest material in ambient pressure, while *Cmcm*-$LiFePO_4$ shows greater hardness and stiffness in high pressure. The *Pbca*-$LiFePO_4$ polymorph is least, while *$P3_121$*-$LiFePO_4$ and *$P2_1/c$*-$LiFePO_4$ are intermediately harder and stiffer throughout the designated pressure range. Lithium intercalation intensifies the hardness of *$P3_121$*-$FePO_4$, *Pnma*-$FePO_4$ and *Pbca*-$FePO_4$ in ambient pressure, as the bulk moduli increase when lithium is inserted. On the other hand, hardness reduces for *$P2_1/c$*-$FePO_4$. Interestingly, the hardness is enhanced in high pressure for all $FePO_4$ polymorphs. Lithium intercalation increases stiffness of *$P3_121$*-$FePO_4$ and *Pbca*-$FePO_4$, while decreases stiffness of *Pnma*-$FePO_4$ and *$P2_1/c$*-$FePO_4$ in 0 GPa and 10 GPa while we also noted decrease for the high pressure *Cmcm*-$FePO_4$ polymorph. The Pugh ratio showed that all $LiFePO_4$ polymorphs are ductile (B/G>1.75) i.e. easy to bend in ambient and high pressures, except *Pbca*-$LiFePO_4$ in high pressure (B/G=1.03). Generally, $LiFePO_4$ is a harder and ductile material than $FePO_4$; corresponding well with the prediction that lithium transference is faster in $FePO_4$ than in $LiFePO_4$.

The macroscopic bulk and Young's moduli suggested hardness and stiffness for *Pnma*-$LiCoPO_4$ (B=142.3 GPa; E=179.36 GPa) over *Cmcm*-$LiCoPO_4$ (B=116.23 GPa; E=157.12 GPa), *$P3_121$*-$LiCoPO_4$ (B=106.67 GPa; E=78.52 GPa), *Pbca*-$LiCoPO_4$

(B=48.42 GPa; E=76.68 GPa) and *$P2_1/c$*-$LiCoPO_4$ (B=45.73 GPa; E=50.48 GPa), in ambient pressure, respectively. However, the hardness and stiffness trend is slightly altered in 10 GPa, as we observe *$P2_1/c$*-$LiCoPO_4$ to be harder and stiffer than *$P3_121$*-$LiCoPO_4$ and *Pbca*-$LiCoPO_4$. Lithium intercalation improved ductility, stiffness and ductility of $CoPO_4$ polymorphs, as we observed an increase in the bulk modulus, Young's modulus and Pugh ratio, suggesting that lithium transportation is faster in $CoPO_4$ than in $LiCoPO_4$. On the other hand, the bulk and Young's moduli suggested greatest hardness and stiffness on the *Pnma*-$LiMnPO_4$ polymorph in ambient pressure. However, *$P2_1/c$*-$LiMnPO_4$ showed greatest hardness in high pressure. Generally, the $LiMnPO_4$ polymorphs are ductile (B/G>0) and are not easy to break, except *$P2_1/c$*-$LiMnPO_4$ in ambient pressure. Lithium intercalation has no uniform effect on hardness, stiffness and ductility/brittleness of $MnPO_4$ polymorphs as we note an irregular change of values. Similarly to MPO_4 structural polymorphs, the shear modulus remains the limiting stability parameter of $LiMPO_4$, since it's less than the bulk modulus.

The structural, thermodynamic, electronic and mechanical properties of the olivine *Pnma*-$NaMPO_4$ and the effect of sodium intercalation on the *Pnma*-MPO_4 were investigated. The calculated lattice constants are in good agreement with the experimental data to within 3 % for $NaFePO_4$ and $NaCoPO_4$, while agree to within 16 % for $NaMnPO_4$. Sodium intercalation increases the cell volume of $NaFePO_4$, $NaCoPo_4$ and $NaMnPO_4$ by 13.77 %, 11.54 % and 12.74 %, respectively. These volume changes are higher in comparison to $LiFePO_4$ (4.86 %), $LiCoPO_4$ (4.47 %) and $LiMnPO_4$ (6.68 %), suggesting that $NaMPO_4$ has poor performance compared to $LiMPO_4$. The heats of formation have suggested that $NaMPO_4$ structures are relatively stable and sodium intercalation enhance stability, since we observed lower values. In

comparison to $LiMPO_4$, we have observed that the heats of formation of $NaMPO_4$ are slightly higher, suggesting that $NaMPO_4$ is less stable.

The electronic densities of states suggested that $NaFePO_4$ shows semi-metallic characteristics, while $NaCoPO_4$ and $NaMnPO_4$ showed insulator characteristics. Sodium intercalated $FePO_4$ displayed spin-down Fe 3*d* band at E_F, making the material semi-metallic. Similarly to $LiMPO_4$, we have seen that the application of 10 GPa pressure widens the energy band gap. However, in comparing conductivity, we noted that $LiMPO_4$ systems have better electronic conductivity, since all display semi-metallic behaviour. The phonon dispersion spectra have shown that the $NaMPO_4$ systems are slightly vibrational unstable, due to the presence of the acoustic soft modes, indicating that the olivine $NaMPO_4$ systems are less stable compared to $LiMPO_4$ systems. The elastic constants suggested that all the $NaMPO_4$ systems are mechanically stable, since they satisfy the necessary stability condition criteria. The resultant bulk and Young's moduli have suggested that $NaMPO_4$ systems are relatively hard and stiff, with $NaFePO_4$ (B=101.37 GPa) slightly the hardest and $NaMnPO_4$ (E=135.89 GPa) stiffest in ambient pressure. Similarly to MPO_4 and $LiMPO_4$ systems, we noted that the moduli increase with pressure. The Pugh ratio have suggested that all $NaMPO_4$ systems are ductile (B/G>1.75). $LiMPO_4$ systems have been found to be generally harder and more ductile than $NaMPO_4$. $NaMPO_4$ systems are also more anisotropic than $LiMPO_4$, further suggesting the superiority of the latter.

Finally, the Li and Na intercalation/deintercalation potentials (voltage profiles) for $LiMPO_4$ polymorphs and $NaMPO_4$ olivines were determined. Our DFT+*U* calculations have shown that the Co-based olivines have higher operating voltages than the Mn and Fe based, respectively, which is in good agreement with theoretical

and experimental observations. We have also noted that $LiFePO_4$, $NaFePO_4$ and $NaMnPO_4$ olivines display potential voltage profiles that fall within the minimum and maximum limits of 2.7 V to 3.9 V in ambient and high pressures. These may suggest a safer cell during battery operation. The intercalation/deintercalation potentials of other four $LiMPO_4$ polymorphs were also calculated in 0 GPa and 10 GPa. It was noted that $LiFePO_4$ polymorphs are more favourable in 10 GPa than in 0 GPa, while $LiCoPO_4$ and $LiMnPO_4$ generally exceeds the maximum limits throughout the pressure range. Furthermore, we have noted that the potentials increase with pressure for all systems.

Suggestions for Future Work

Nanomaterials, in which one or more dimensions exist at the nanoscale, offer the ability to change the properties of the material or proffer new properties by adjusting the size. Atomistic simulations, i.e. amorphisation recrystallisation methods, have played an important role in growing nano MnO_2 as electrodes in lithium batteries [213], which corresponded well with experimental results [214]. This approach offers a unique window of explanation into structural features that exist at the nanoscale that are difficult to characterise experimentally. It will be of great importance in future studies to develop simulation strategies for generating full atomistic models for nanomaterials, in particular MPO_4 and $Li/NaMPO_4$ polymorphs [215]. In the future work, we intend to employ amorphisation recrystallisation methods to generate nanostructural models of $LiMPO_4$ and MPO_4, which are important materials for energy storage. Recently, it has been discovered that maricite $NaFePO_4$ can function as an excellent cathode material for Na ion batteries [216]. Hence, it will be of great interest to perform first-principle calculations on the maricite polymorph.

References

[1] F. Zhou, M. Cococcioni, K. Kang, and G. Ceder, “The Li Intercalation Potential of $LiMPO_4$ and $LiMSiO_4$ Olivines with M = Fe, Mn, Co, Ni,” *Electrochem. Commun.,* vol. 6, p. 1148, 2004.

[2] A.K. Padhi, K.S. Nanjundaswamy, and J.B. Goodenough, “Phospho-Olivines as Positive-Electrode Materials for Rechargeable Lithium Batteries,” *J. Electrochem. Soc.,* vol. 144, p. 1194, 1997.

[3] A.K. Padhi, K.S. Nanjundaswamy, and J.B. Goodenough, “$LiFePO_4$: A Novel Cathode Material for Rechargeable Batteries,” *Electrochem. Soc.,* vol. 96, p. 73, 1996.

[4] K. Mizushima, P.C. Jones, P.J. Wiseman, and J.B. Goodenough, “A New Cathode Material for Batteries of High Energy Density,” *Mater. Res. Bull.,* vol. 15, p. 799, 1980.

[5] K. Amine, H. Yashuda, and M. Yamachi, “Olivine $LiCoPO_4$ as 4.8 V Electrode Material for Lithium Batteries,” *Electrochem. Solid State Lett.,* vol. 31, p. 179, 2000.

[6] V. Aravindan, J. Gnanaraj, Y.S. Lee, and S. Madhavi, “$LiMnPO_4$ – A next Generation Cathode Material for Lithium-ion Batteries,” *J. Mater. Chem.,* vol. 1, p. 3518, 2013.

[7] J.S. Yun, S. Kim, B.W. Cho, K.Y. Lee, K.Y. Chung, and W. Chang, “Synthesis and Electrochemical Properties of $Li_3V_2(PO_4)_3$-$LiMnPO_4$ Composite Cathode Material for Lithium-ion Batteries,” *Bull. Korean Chem. Soc.,* vol. 34, p. 433, 2013.

[8] A. Yamada, and S.C. Chung, “Crystal Chemistry of Olivine-Type Li $(Mn_yFe_{1-y})PO_4$ and $(Mn_yFe_{1-y})PO_4$ as Possible 4 V Cathode Materials for Lithium Batteries,” *J. Electrochem. Soc.,* vol. 148, p. A960, 2001.

[9] G.H. Li, H. Azuma, and M. Tohda,, “$LiMnPO_4$ as the Cahode Lithium Batteries,” *Electrochem. Solid State Lett.,* vol. 5, p. A135, 2002.

[10] S.Y. Chung, J.T. Bloking, and Y.M. Chiang, “Electronically Conductive Phospho-Olivines as Lithium Storage Electrodes,” *Nat. Mat.,* vol. 1, p. 128, 2002.

[11] A. Yamada, M. Hosoya, S.C. Chung, Y. Kudo, K. hinokuma, K.Y. Liu, and Y. Nishi, "Olivine-Type Cathodes: Achievements and Problems," *J. Power Sources,* vol. 119, p. 238, 2003.

[12] D. Wang, H. Buqa, M. Crouzet, G. Deghenghi, T. Drezen, I. Exnar, N.H. Kwon, J.H Miners, L. Poletto, and M. Gratzel, "High-Performance, Nano-Structured $LiMnPO_4$ Synthesized Via a Polyol Method," *J. Power Sources,* vol. 189, p. 628, 2009.

[13] H. Huang, S.C. Yin, and L.F. Nazar, "Approaching Theoretical Capacity of $LiFePO_4$ at Room Temperature at High Rates," *Electrochem Solid State Lett.,* vol. 4, p. A172, 2001.

[14] M.S. Islam, and C.A.J. Fisher, "Lithium and Sodium Battery Cathode Materials: Computational Insights into Voltage, Diffusion and Nanostructural Properties," *Chem. Soc. Rev.,* vol. 43, p. 185, 2014.

[15] P.S. Herle, B. Ellis, N. Coombs, and L.F. Nazar, "Nano-Network Electronic Conduction in Iron and Nickel Olivine Phosphates," *Nat. Mat,* vol. 3, p. 147, 2004.

[16] P.G. Patil, "Advanced Battery Technology for Electronic Two-Wheelers in the People's Republic of China," *Energy Systems Division, Argonne National Laboratary ,* 2009.

[17] P. Tang, N.A.W. Holzwarth, and Y.A. Du, "Comparison of the Electronic Structure of Four Crystalline Phases of $FePO_4$," *Phys. Rev. B,* vol. 76, p. 174118, 2007.

[18] H.D. Megaw, "Crystal Structures - A Working Approach," *Acta Cryst.,* vol. 30, p. 1887, 1974.

[19] L. Arthouel, F. Moser, R. Dugas, O. Crosnier, D. Belanger, and T. Brusse, "Variation of the MnO_2 Birnessite Structure upon Charge/Discharge in an Electrochemical Supercapacitor Electrode in Aqueous Na_2SO_4 Electrolyte," *J. Phys. Chem. C,* vol. 112, p. 7270, 2008.

[20] Q.T. Qu, Y. Shi, S. Tian, Y.H. Chen, Y.P. Wu, and R. Holze, "A New Cheap Asymmetric Aqueous Supercapacitor: Activated Carbon//$NaMnO_2$," *J. Power Sources,* vol. 194, p. 1222, 2009.

[21] J.P. Whitacre, A. Tevar, and S. Sharma, "$Na_4Mn_9O_{18}$ as a Positive Electrode Material for an Aqueous Electrolyte Sodium-Ion Energy Storage Device," *Electrochem. Com.,* vol. 12, p. 463, 2010.

[22] R.A. Shakoor, Y.U. Park, J. Kim, S.W. Kim, D.H. Seo, H. Gwon, and K. Kang, "Synthesis of $NaFePO_4$/$NaCoPO_4$ and their Application to Sodium Batteries," *J. Korean Battery Soc.,* vol. 3, p. 00, 2010.

[23] A.S. Anderson, and J.O. Thomas, "The Source of First-cycle Capacity Loss in $LiFePO_4$," *J. Power Sources,* vol. 97, p. 498, 2001.

[24] G. Rousse, J. Rodriguez-Carvajal, S. Patoux, and C. Masquelier, "Magnetic Structures of the Triphylite $LiFePO_4$ and of its Delithiated Form $FePO_4$," *Chem. Mater.,* vol. 15, p. 4082, 2003.

[25] R.G. Iyer, C. Delacourt, C. Masquelier, J.M Tarascon, and A. Navrotsky, "Energetics of $LiFePO_4$ and Polymorphs of Its Delithiated Form, $FePO_4$," *Electrochem. Solid State Lett.,* vol. 9, p. A46, 2006.

[26] S. Yang, Y. Song, P.Y. Zavalij, and M.S. Whittingham, "Reactivity, Stability and Electrochemical Behavior of Lithium Iron Phosphates," *Electrochem. Commun.,* vol. 4, p. 239, 2002.

[27] N. Kinomura, M. Shimada, and M. Koizumi, "Synthesis of a High Pressure Phase of $FePO_4$," *Mater. Res. Bull.,* vol. 11, p. 457, 1976.

[28] C. Murli, S.M. Sharma, S.K. Kulshreshtha, and S.K. Sikka, "High Pressure Study of Phase Transitions in α-$FePO_4$," *Pramana,* vol. 49, p. 285, 1997.

[29] Y. Song, P.Y. Zavalij, M. Suzuki, and M.S. Whittingham, "New Iron(III) Phosphate Phases: Crystal Structure and Electrochemical and Magnetic Properties," *Inorg. Chem.,* vol. 41, p. 5778, 2002.

[30] M.E. Arroyo-de Dompablo, J.M. Gallardo-Amores, and U.Amador, "Lithium Insertion in the High-Pressure Polymorphs of $FePO_4$," *Electrochem. Solid State Lett.,* vol. 8, p. A564, 2005.

[31] A. Fedorkova, A. Nacher-Alejos, P. Gomez-Romero, R Orinakova, and D. Kaniansky, "Structural and Electrochemical Studies of PPy/PEG-$LiFePO_4$ Cathode Material for Li-ion Batteries," *Electrichem. Acta.,* vol. 55, p. 947, 2010.

[32] D. Fujimoto, Y. Lei, Z.H. Huang, F. Kang, and J. Kawamura, "Synthesis and Electrochemical Performance of $LiMnPO_4$ by Hydrothermal Method," *Int. J. Electrochem.,* vol. 2014, p. 768912, 2014.

[33] H. Fang, L. Li, and G. Li, "Hydrothermal Synthesis of Electrochemically Active $LiMnPO_4$," *Chem. Lett.,* vol. 36, p. 436, 2007.

[34] G. Meligrana, C. Gerbaldi, A. Tuel, S. Bodoardo, and N. Penazzi,

"Hydrothermal Synthesis of High Surface $LiFePO_4$ Powders as Cathode for Li-ion Cells," *J. Power Sources,* vol. 160, p. 516, 2006.

[35] H.N. Ng, and C. Calvo, "Refinement of the Crystal Structure of the Low-quartz Modification of Ferric Phosphate," *Can. J. Chem.,* vol. 53, p. 2064, 1975.

[36] O. Garcia-Moreno, M. Alvarez-Vega, F. Garcia-Avarado, J. Garcia-Jaca, J.M. Gallardo-Amores, M.L. Sanjuan, and U. Amador, "Influence of the Structure on the Electrochemical Performance of Open Framework Phosphates as Cathodic Materials in Rechargeable Lithium Batteries: A New High Pressure Form of $LiMPO_4$ (M= Mn, Fe and Ni)," *Chem. Matter.,* vol. 13, p. 1576, 2001.

[37] H. Ehrenberg, N.N. Bramnik, A. Senyshyn, and H. Fuess, "Crystal and Magnetic Structures of Electrochemically Delithiated $Li_{1-x}CoPO_4$ phases," *Solid State Sci.,* vol. 11, p. 18, 2009.

[38] Y. Dong, L. Wang, S. Zhang, Y. Zhao, J. Zhou, H. Xie, and J.B. Goodenough, "Two-phase Interface in $LiMnPO_4$ Nanoplates," *J. Power Sources,* vol. 215, p. 116, 2012.

[39] R.D. Shannon, and C.T. Prewitt, "Effective Ionic Radii in Oxides and Fluorides," *Acta Crystallogr., Sec. B,* vol. 25, p. 925, 1969.

[40] F. Kubel, and Z. Kristallogr, "Crystal Structure of Lithium Cobalt Double Orthophosphate, $LiCoPO_4$," *Z. Kristallogr.,* vol. 209, p. 755, 1994.

[41] P. Tang, and N.A.W. Holzwarth, "Electronic Structure of $FePO_4$, $LiFePO_4$, and Related Materials," *Phys. Rev. B,* vol. 68, p. 165107, 2003.

[42] J.M. Osorio-Guillén, B. Holm, R. Ahuja, and B. Johansson, "A Theoretical Study of Olivine $LiMPO_4$ Cathodes," *Solid State Ionics,* vol. 167, p. 221, 2004.

[43] H.T. Lai, Y.S. Kang, and W.E. Stumph, "Subunit Stoichiometry of the Drosophila Melanogaster Small Nuclear RNA Activating Protein Complex (SNAPc)," *FEBS. Lett.,* vol. 582, p. 3734, 2008.

[44] S.B. Lee, S.H. Cho, S.J. Cho, G.J. Park, S.H. Park, and Y.S. Lee, "Synthesis of $LiFePO_4$ Material with Improved Cycling Performance under Harsh Conditions," *Electrochem. Commun.,* vol. 10, p. 1221, 2008.

[45] Y.N. Xu, and W.Y. Ching, "Comparative Studies of the Electronic Structure of $LiFePO_4$, $FePO_4$, Li_3PO_4, $LiMnPO_4$, $LiCoPO_4$, and $LiNiPO_4$," *J. App. Phys.,* vol. 95, p. 11, 2004.

[46] R.P. Santoro, and R.E. Newnham, "Antiferromagnetic in $LiFePO_4$," *Acta*

Crystallogr., vol. 22, p. 344, 1967.

[47] N.H. Kwon, and K.M. Fromm, "Enhanced Electrochemical Performance of <30 nm Thin $LiMnPO_4$ Nanorods with a Reduced Amount of Carbon as a Cathode for Lithium Ion Batteries," *Food Chem.,* vol. 133, p. 1435, 2012.

[48] D. Vaknin, J.L. Zarestky, L.L. Miller, J.P. Rivera, and H. Schmid, "Weakly Coupled Antiferremagnetic Planes in Single-Crystal $LiCoPO_4$," *Phys. Rev. B,* vol. 65, p. 224414, 2002.

[49] I. Kornev, M. Bichurin, J.P. Rivera, S. Gentil, H. Schmid, A.G.M. Jansen, and P. Wyder, "Magnetoelectronic Properties of $LiCoPO_4$ and $LiNiPO_4$," *Phys. Rev. B,* vol. 62, p. 12247, 2000.

[50] F. Zhou, K. Kang, T. Maxisch, G. Ceder, and D. Morgan, "The Electronic Structure and Band Gap of $LiFePO_4$ and $LiMnPO_4$," *Solid State Comm.,* vol. 132, p. 181, 2004.

[51] O. Le Bacq, and A. Pasturel, "First-Principles Study of $LiMPO_4$ Compounds (M=Mn, Fe, Co, Ni) as Electrode Material for Lithium Batteries," *Philos. Mag.,* vol. 85, p. 1754, 2005.

[52] M. Yonemura, A. Yamada, Y. Takei, N. Sonoyama, and R. Kanno, "Comparative Kinetic Study of Olivine Li_xMPO_4 (M = Fe, Mn)," *J. Electrochem. Soc.,* vol. 151, p. A1352, 2004.

[53] T. Maxisch, and G. Ceder, "Elastic Properties of Olivine Li_xFePO_4 from First-Principles," *Phys Rev. B,* vol. 73, p. 174112, 2006.

[54] R. Mittal, S.L. Chaplot, A.I. Kolenikov, C.K. Loong, O.D. Jayakumar, and S.K. Kulshreshtha, "Inelastic Neutron Scattering, Lattice Dynamics, and Synchrotron X-ray Diffraction Study of $FePO_4$," *Phys. Rev. B,* vol. 66, p. 174304, 2002.

[55] Y.Xie, H.T. Yu, T.F. Yi, and Y.R. Zhu, "Understanding the Thermal and Mechanical Stabilities of Olivine-Type $LiMPO_4$ (M = Fe, Mn) as Cathode Materials for Rechargeable Lithium Batteries from First Principles," *Appl. Mater. Interfaces,* vol. 6, p. 4033, 2014.

[56] J. Wolfenstine, J.L. Allen, T.R. Jowa, T. Thompson, J. Sakamoto, H. Jo, and H.Choe, "$LiCoPO_4$ Mechanical Properties Evaluated by Nanoindentation," *Ceram. Int.,* vol. 40, p. 13673, 2014.

[57] R.M. Hazen, R.T. Downs, and C.T. Prewitt, "Comparative Crystal Chemistry. Washington: Mineralogical Society of America," *Rev. Mineral. Geochem.,* vol. 41, p. 1, 2000.

[58] J.R. Smyth, S.D. Jacobsen, and R.M. Hazen, "Comparative Crystal Chemistry of Dense Oxides Minerals," *Rev. Mineral. Geochem.,* vol. 41, p. 157, 2001.

[59] D. Morgan, A. Van der Ven, and G. Ceder, "Li Conductivity in Li_xMPO_4 (M=Mn, Fe, Co, Ni) Olivine Materials," *Electrochem. Solid-State Lett.,* vol. 7, p. A30, 2004.

[60] T. Maxisch, F. Zhou, and G. Ceder, "Ab Initio Study of the Migration of Small Polarons in Olivine Li_xFePO_4 and their Association with Lithium Ions and Vacancies," *Phys. Rev. B,* vol. 73, p. 104301, 2006.

[61] M.P. Pasternak, G.K. Rozenberg, A.P. Milner, M. Amanowicz, T. Zhou, and U. Schwarz, "Pressure-Induced Concurrent Transformation to an Amorphous and Crystalline Phase in Berlinite-Type $FePO_4$," *Phys. Rev. Lett.,* vol. 79, p. 4409, 1997.

[62] G.G. Amatucci, and N. Pereira, "Fluoride Based Electrode Materials for Advanced Energy Storage Devices," *J. Flourine Chem.,* vol. 128, p. 243, 2007.

[63] B.L. Ellis, W.R.M. Makahnouk, W.N.R. Weetaluktuk, D.H. Ryan, and L.F. Nazar, "Crystal Structure and Electrochemical Properties of A_2MPO_4 Fluorophosphates (A = Na, Li; M = Fe, Mn, Co, Ni)," *J. Chem. Mater.,* vol. 22, p. 1059, 2010.

[64] J. Barker, M.Y. Saidi, and J. Swoyer, "A Sodium-Ion Cell Based on the Fluorophosphate Compound $NaVPO_4F$," *J. Electrochem. Solid State Lett.,* vol. 6, p. A1, 2003.

[65] H. Zhou. X. Wang. A. Tang, Z. Liu, S. Gamboab, and P.J. Sebastian, "The Preparation of $NaV_{1-x}Cr_xPO_4F$ Cathode Materials for Sodium-Ion Battery," *J. Power Sources,* vol. 160, p. 698, 2006.

[66] J. Moring, and E. Kostiner, "The Crystal Structure of $NaMnPO_4$," *J. Solid State Chem.,* vol. 61, p. 379, 1986.

[67] J.N. Bridson, S.E. Quinlan, and P.R. Tremaine, "Synthesis and Crystal Structure of Maricite and Sodium Iron(III) Hydroxyphosphate," *J. Chem. Mater.,* vol. 10, p. 763, 1998.

[68] S.N. Le, W. Eng, and A. Navrotsky, "Energetics of Cobalt Phosphate Frameworks: α, β, and Red $NaCoPO_4$," *Solid State Chem.,* vol. 179, p. 3731, 2006.

[69] C. Delacourt, P. Poizot, M. Morcrette, J.M. Tarascon, and C. Masquelier, "One-Step Low-Temperature Route for the Preparation of Electrochemically Active

$LiMnPO_4$," *Chem. Mater.,* vol. 16, p. 93, 2004.

[70] S. Sauvage, E. Quarez, J.M. Tarascon, and E. Baudrin, "Crystal Structure and Electrochemical Properties Vs. Na+ of the Sodium Fluorophosphate $Na_{1.5}VOPO_4F_{0.5}$," *Solid state sciences,* vol. 8, p. 1215, 2006.

[71] R.A. Shakoor, D.H. Seo, Y.U. Park, J. Kim, S.W. Kim, H. Gwon, S. Lee, and K. Kang, "A Combined First principles and Experimental Study on $Na=V_2(PO_4)_2F3$ for Rechargeable Na Batteries," *J. Mater. Chem.,* vol. 22, p. 20535, 2012.

[72] P. Moreau, D. Guyomard, J. Gaubicher, and F. Boucher, "Structure and Stability of Sodium Intercalated Phases in Olivine $FePO_4$," *Chem. Mater.,* vol. 22, p. 4126, 2010.

[73] A.J. Fernandez, D. Saurel, B. Acebedo, T. Rojo, and M. Casas-Cabanas, "Electrochemical Characterization of $NaFePO_4$ as Positive Electrode in Aqueous Sodium-ion Batteries," *J. Power Sources,* vol. 291, p. 40, 2015.

[74] A. Sun, and A. Manivannam, "Structural Studies on $NaFePO_4$ as a Cathode Material for Na^+/Li^+ Mixed-ion Batteries," *ASC Transactions,* vol. 35, p. 3, 2011.

[75] L. Zyga, "Sodium-Ion Battery Cathode has Highest Enegry Density to Date," Phys. Org., 2013.

[76] Y.U. Park, D.H. Seo, H.S. Kwon, B. Kim, J. Kim, H. Kim, I. Kim, H.I. Yoo, and K. Kang, "A New High-Energy Cathode for a Na-Ion Battery with Ultrahigh Stability," *J. Am. Chem. Soc. ,* vol. 135, p. 13870, 2013.

[77] Y. Zhu, Y. Xu, Y. Liu, C. Luo, and C. Wang, "Comaprison of Electrochemical Performance of Olivine $NaFePO_4$ in Sodium-Ion Batteries and Olivine $LiFePO_4$ in Lithium-Ion Batteries," *Nanoscale,* vol. 780, p. 5, 2013.

[78] H.H. Kim, I.H. Yu, H.S. Kim, H.J. Koo, and M.H. Whangbo, "On Why the Two Polymorphs of $NaFePO_4$ Exhibit Widely Different Magnetic Structures: Density Functional Analysis," *Inorg Chem.,* vol. 54, p. 4966, 2015.

[79] D. Li, and H.K. Liu, "Synthesis and Electrochemical Performance of Olivine $NaFePO_4$/Grahene Composite As Cathode Materials for Sodium Ion Batteries," in *17th International Meeting on Lithium Batteries,* Como, Italy, 2014.

[80] K. Parlinski, "PHONON Software," Last update: January 2, 2014.

[81] F. Zhou, C.A. Marianetti, M. Cococcioni, D. Morgan, and G. Ceder, "Phase Separation in $LixFePO_4$ Induced by Correlation Effects," *Phys. Rev. B,* vol. 69,

p. 201101, 2004.

[82] K. Zaghib, A. Mauger, J. B. Goodenough, F. Gendron, and C. M. Julien, "Electronic, Optical, and Magnetic Properties of $LiFePO_4$: Small Magnetic Polaron Effects," *Chem. Mater.,* vol. 19, p. 3740, 2007.

[83] V. Antonov, B. Harmon, and A. Yaresko, Electronic Structure and Magneto\Optical Properties of Solids, New York, Boston, Dordrecht, London, Moscow: Kluwer Academic Publishers, 2004, p. 4.

[84] K. Capelle, "A Bird's-Eye View of Density-Functional Theory," *Brazilian J. Phys.,* vol. 36, p. A4, 2006.

[85] L.H. Thomas, "The Calculation of Atomic Fields," *Proc. Camb. Phil. Soc.,* vol. 23, p. 542, 1927.

[86] E. Fermi, "Un Metodo Statistico per la Determinazione di Alcune Priorieta Dell'atome," *Rend. Accad. Naz. Lincei,* vol. 6, p. 602, 1927.

[87] P. Hohenberg, and W. Kohn, "Inhomogeneous Electron gas," *Phys. Rev,* vol. 136, p. B871, 1964.

[88] W. Kohn, and L.J. Sham, "Self-Consistent Equations Including Exchange and Correlation Effects," *Phys. Rev.,* vol. 140, p. A1133, 1965.

[89] R.A. Evarestov, "The LCAO First-Principles Treatment of Crystals," *Quantum Chemistry of Solids,* vol. 153, p. 232, 2007.

[90] R.G. Parr, and W.T. Yang, "Density-Functional Theory of Atoms and Molecules," *Oxford University Press, New York,,* 1994.

[91] W. Koch, and M.C. Holthausen, A Chemist's Guide to Density Functional Theory, 2nd ed., Willey-VCH, 2001.

[92] L.J. Sham, and W. Kohn, "One-Particle Properties of an Inhomogeneous Interacting Electron Gas," *Phys. Rev.,* vol. 145, p. 531, 1966.

[93] D.C. Langreth, and J.P. Perdew, "The Exchange Correlation Energy of a Metallic Surface," *Solid State Commun.,* vol. 17, p. 1425, 1975.

[94] O. Gunnarsson, and B.I. Lundqvist, "Exchange and Correlation in Atoms, Molecules and Solids by the Spin-Density-Functional Formalism," *Phys. Rev. B ,* vol. 13, p. 4274, 1976.

[95] A.E. Mattsson, P.A. Schultz, M.P. Desjarlais, T.R. Mattsson, and K. Leung,, "Designing Meaningful Density Functional Theory Calculations in Materials

Science—a Primer," *Modelling Simul. Mater. Sci. Eng.,* vol. 13, p. R1, 2005.

[96] H.R. Chauke, " PhD Thesis, Unpublished," *University of Limpopo,* p. 26, 2005.

[97] M. Chakraverty, H.M. Kittur, and P.A. Kumar, "First Principle Simulations of Various Magnetic Tunnel Junctions for Applications in Magnetoresistive Random Access Memories," *IEEE Trans. Nanotechnol.,* vol. 12, p. 971, 2013.

[98] K. Horn, and M. Scheffler, In Electronic Structure (Handbook of Surface Science), vol. 2, Amsterdam: North Holland, 2000.

[99] D.J.W. Geldart, and M. Rasolt, "Exchange and Correlation Energy of an Inhomogeneous Gas at Metallic Densities," *Phys. Rev. B,* vol. 13, p. 1477, 1976.

[100] G.P. Robert, and Y. Weitao, "Density-Functional Theory of Atoms and Molecules," *Oxford: Oxford University Press,* 1994.

[101] P.A.M. Dirac, "Note on Exchange Phenomena in the Thomas-Fermi Atom," *Proc. Cambridge Phil. Roy. Soc.,* vol. 26, p. 385, 1930.

[102] R.M. Dreizler, and E.K.U. Gross, Density Functional Theory, Berlin: Springer-Verlag, 1990.

[103] R.G. Parr, and W. Yang, Density Functional Theory of Atoms and Molecules, New York: Oxford, 1989.

[104] S.H. Vosko, L. Wilk, and M. Nusair, "Accurate Spin-Dependent Electron Liquid Correlation Energies for Local Spin Density Calculations: A Critical Analysis," *Can. J. Phys.,* vol. 58, p. 1200, 1980.

[105] J.P. Perdew, and A. Zunger, "Self-Interaction Correction to Density-Functional Approximations for Many-Electron Systems," *Phys. Rev. B,* vol. 23, p. 5048, 1981.

[106] J.P. Perdew, and Y. Wang, "Accurate and Simple Analytic Representation of the Electron Gas Correlation Energy," *Phys. Rev. B,* vol. 45, p. 13244, 1992.

[107] J.P. Perdew, "Generalized Gradient Approximations for Exchange and Correlation: A Look Forward and Backward," *Phys. Rev. B,* vol. 172, p. 6, 1991.

[108] A. St-Amant, W.D. Cornell, P.A. Kollman, and T.A. Halgren , "A Study of Geometries, Conformational Energies, Dipole Moments and Electrostatic Potential Fitted Charges Using Density Functional Theory," *J. Comput. Chem.,* vol. 16, p. 1483, 1995.

[109] J.P. Perdew, J.A. Chevary, S.H. Vosko, K.A. Jackson, M.R. Pederson, D.J. Singh, and C. Fiolhais, "Atoms, Molecules, Solids, and Surfaces: Applications of the Generalized Gradient Approximation for Exchange and Correlation," *Phys. Rev. B,* vol. 46, p. 6671, 1992.

[110] P. Politzer, and J.M. Seminario, Modern Density Functional Theory: A Tool for Chemistry, Amsterdam: Elsevier Science, 1995.

[111] A.D. Becke, "Density-functional Exchange-Energy Approximation with Correct Asymptotic Behaviour," *Phys. Rev. A,* vol. 38, p. 3100, 1988.

[112] J.P. Perdew, "Density-Functional Approximation for the Correlation Energy of the Inhomogeneous Electron Gas," *Phys. Rev. B,* vol. 33, p. 8824, 1986.

[113] J.P. Perdew, and Y. Wang, "Accurate and Simple Density Functional for the Electronic Exchange Energy: Generalized Gradient Approximation," *Phys. Rev. B,* vol. 33, p. 8800, 1986.

[114] J.P. Perdew, P. Ziesche, and H. Eschrig, In Electronic Structure of Solids, Berlin: Akademie Verlag, 1991.

[115] M.C. Payne, M.P. Teter, D.C. Allan, T.A. Arias, and J.D. Joannopoulos, "Iterative Minimization Techniques for Ab iIitio Total-Energy Calculations: Molecular Dynamic and Conjugate Gradients," *Rev. Mod. Phys.,* vol. 64, p. 1045, 1992.

[116] B. Meyer, "The Pseudopotential Plane Wave Approach," *NIC Series,* vol. 31, p. 71, 2006.

[117] N.W. Ashcroft, and N.D. Mermin, "On Introductory Concepts," in *Solid State Physics*, Philadelphia, Saunders College Publishing, 1976.

[118] J.S. Blakemore, Solid State Physics, 2nd ed, Cambrige: Cambrige University Press, 1985.

[119] J.C. Phillips, and L. Kleinman, "New Method for Calculating Wave Functions in Crystal and Molecules," *Phys. Rev.,* vol. 116, p. 287, 1959.

[120] M.L. Cohen, and V. Heine, "The Fitting of Pseudopotentials to Experimental Data and their Subsequent Application," *Solid State Phys.,* vol. 24, p. 37, 1970.

[121] H. Hans, "A New Approximation Method in the Problem of Many Electrons," *J. Chem. Phys.,* vol. 3, p. 61, 1935.

[122] W.E. Pickett, "Pseudopotential Methods in Condensed Matter Applications,"

Comput. Phys. Rep, vol. 9, p. 197, 1989.

[123] H. Volker, "The Pseudopotential Concept," *Solid State Physics (Academic Press),* vol. 24, 1970.

[124] D. Brust, and B. Alder, , "The Pseudopotential Method and the Single-Particle Electronic Excitation Spectra of Crystals, Methods in Computational Physics," *Academic Press,* vol. 8, p. 61, 1968.

[125] W.A. Harrison, Pseudopotentials in the Theory of Metals, Frontiers in Physics, Virginia: University of Virginia, 1966.

[126] G.P. Srivastava, and D. Weaire, "The Theory of the Cohesive Energies of Eolids," *Adv. Phys.,* vol. 26, p. 463, 1987.

[127] G.B. Bachelet, D.R. Hamann, and M. Schluter, "Pseudopotentials that Work: From H to Pu," *Phys. Rev. B,* vol. 26, p. 4199, 1982.

[128] D.R. Hamann, M. Schluter, and C. Chiang, "Norm-Conserving Pseudopotentials," *Phys. Rev. Lett.,* vol. 43, p. 1494, 1979.

[129] D.R. Hamann, "Generalised Norm-conserving Pseudopotentials," *Phys. Rev. B,* vol. 40, p. 2980, 1989.

[130] D. Vanderbilt, "Soft Self-Consistent Pseudopotentials in Generalized Eigenvalue Formalism," *Phys. Rev. B,* vol. 41, p. 7892, 1990.

[131] G. Kresse, M. Marsman, and J. Furthmuller, "VASP the GUIDE, Computational Physics," Vienna, 2009.

[132] K. Parlinski, Z.Q. Li, and Y. Kawazoe, "First-Principles Determination of the Soft Mode in Cubic ZrO2," *Phys. Rev. Lett.,* vol. 78, p. 4063, 1997.

[133] http://www.materialsdesign.com.

[134] F.S. Pierce, D.N. Basov, P. Volkov, S.J. Poon, and T. Timusk, "Optical Conductivity of Insulating Al-Based Alloys: Comparison of Quasiperiodic and Periodic Systems," *Phys. Rev. Lett.,* vol. 73, p. 1865, 1994.

[135] A. Matsuda, S. Sugita, T. Fujii, and T. Watanabe, "Study of Pseudogap Phenomena by STM and Other Probes," *J.Phys. Chem. Solids,* vol. 62, p. 65, 2001.

[136] T. Matsuda, I Ohara, H. Satoi, S. Ohashi, and U. Mizutani, "Electronic Properties for Icosahedral and Amorphous Phases in the Mg-Zn-Al Alloy

System," *J. Phys. Condens. Matter,* vol. 1, p. 4087, 1989.

[137] T. Inoshita, K. Nakao, and H. Kamimura,, "Electronic Structure of Potassium-Graphite Intercalation Compound: C8K," *J. Phys. Soc. Jpn.,* vol. 43, p. 1237, 1977.

[138] P.A. Bancel, and P.A. Heiney, "Icosahedral Aluminum-Transition Metal Alloys," *Phys. Rev. B,* vol. 88, p. 7917, 1986.

[139] L.S. Bartell, "Molecular Geometry: Bonded Versus Nonbonded interactions," *J. Chem. Educ,* vol. 45, p. 754, 1968.

[140] Y.N. Gornostyrev, O.Y. Kontsevoi, A.F. Maksyutov, A.J. Freeman, M.I. Katsnelson, A.V. Trefilov, and A.I. Lichtenstein, "Negative Yield Stress Temperature Anomaly and Structural Istability of Pt3Al," *Phys. Rev. B,* vol. 70, p. 014102, 2004.

[141] D.A. Pankhurst, D. Nguyen-Manh, and D.G. Pettifor, "Electronic Origin of Structural Trends Across Early Transition-Metal Disilicides: Anomalous Behaviour of CrSi2," *Phys Rev B,* vol. 69, p. 075113, 2004.

[142] S.J. Blundell, and K.M. Blundell, Concepts in Thermal Physics, 2nd ed, New York: Oxford University Press, 2010.

[143] C. Kittel, Introduction to Solid States Physics, 8th ed, New york: Wiley, 2004.

[144] I. Harald, and H. Lüth, Solid-State Physics: An Introduction to Principles of Materials Science 2nd ed., New York: Springer-Verlag, 1996.

[145] D. Vasileska, S.M. Goodnick, and G. Klimeck, Computational Electronics: Semiclassical and Quantum Device Modelling and Simulation, Boca Raton: CRC Press, 2010.

[146] Z. Zhou, and B. Joos, "Stability Criteria for Homogeneously Stressed Materials and the Calculation of Elastic Constants," *Phys. Rev. B, 54,* vol. 54, p. 3850, 1996.

[147] O. Beckstein, J.E. Klepeis, G.L.W. Hart, and O. Pankratov, "First-Principles Elastic Constants and Electronic Structure of α-Pt2Si and PtSi," *Phys. Rev. B,* vol. 63, p. 134112, 2001.

[148] M. Born, and K. Huang, "Dynamical Theory of Crystal Lattices," *Acta Cryst.,* vol. 9, p. 837, 1956.

[149] R. Hill, H. G. Hopkins, and M. J. Sewell, Mechanics of Solids 1st ed, Oxford:

Pergamon Press Ltd., 1982.

[150] M. Tang, and S. Yip, "Lattice Instability in β-SiC and Simulation of Brittle Fracture," *J. App. Phys*, vol. 76, p. 2719, 1994.

[151] J. Wang, J. Li, S. Yip, S.R. Phillpot, and D. Wolf, "Mechanical Instabilities of Homogeneous Crystals," *Phys. Rev. B,* vol. 52, p. 627, 1995.

[152] T.H.K. Barron, and M.L. Klein, "Second-Order Elastic Constants of a Solid under Stress," *Proc. Phys. Soc.*, vol. 85, p. 523, 1965.

[153] C. Kittle, Introduction to Solid State Physics, 5th ed., New York: John Wiley & Sons, 1976.

[154] M.L. Cohen, "Calculation of Bulk Moduli of Diamond and Zinc-Blende Solids," *Phys. Rev. B,* vol. 32, p. 7988, 1985.

[155] S.F. Pugh, "Relations Between Elastic Moduli and Plastic Properties of Polycrystalline Pure Metals," *Philos. Mag.,* vol. 45, p. 843, 1954.

[156] W. Voigt, "Lehrbuch der Kristallphysik," Leipzig, Teubner, 1928.

[157] V. Tvergaard, and J.W. Hutchinson, "Microcracking in Ceramics Induced by Thermal Expansion or Elastic Anisotropy," *J. Am. Chem. Soc.*, vol. 71, p. 157, 1988.

[158] S. Goumri-Said, and M.B. Kanoun, "Theoretical Investigations of Structural, Elastic, Electronic and Thermal Properties of Damiaoite $PtIn_2$," *Comput. Mat. Sci.*, vol. 43, p. 243, 2008.

[159] Y. Qiao, H. Zhang, C. Hong, and X. Zhang, "Phase Stability, Electronic Structure and Mechanical Properties of Molybdenum Disilicide: A First-Principles Investigation.," *J. Phys. D: Appl. Phys.*, vol. 42, p. 105413, 2009.

[160] S.O. Kasap, P. Capper, and C. Koughia, Handbook of Electronic and Photonic Materials, New York: Springer, 2006, p. 758.

[161] S.K.R. Patil, S.V. Khare, B.R. Tuttle, J.K. Bording, and S. Kodambaka, "Investigation of Mechanical Stability of Possible Structure of PtN Using First-Principles Computations," *Phys. Rev. B,* vol. 73, p. 104118, 2006.

[162] P. Ravindran, L. Fast, P.A. Korzhavyi, B. Johansson, J. Wills, and O. Eriksson, "Density Functional Theory for Calculation of Elastic Properties of Orthorhombic Crystals: Application to $TiSi_2$," *J. App. Phys.*, vol. 84, p. 4904, 1998.

[163] H.S. Chen, Anisotropy of Elasticity about Metal, Beijing: Metallurgy Industry Press, 1996.

[164] B. Mayer, H. Anton, E. Bott, M. Methfessel, J. Sticht, and P.C. Schmidt, "*Ab-Initio* Calculation of the Elastic Constants and Thermal Expansion Coefficients of Laves Phases," *Interm.,* vol. 11, p. 23, 2003.

[165] D.H. Chung, and W.R. Buessem, "The Elastic Anisotropy of Crystals," *J. Appl. Phys.,* vol. 38, p. 2010, 1967.

[166] P. Heyliger, H. Ledbetter, and S. Kim, "Elastic Constants of Natural Quartz," *J. Acoust. Soc. Am.,* vol. 114, p. 644, 2003.

[167] M. Carpenter, and E. Salje, "High-Pressure Elasticity of Stishovite and the P42/mnm ⇌ Pnnm Phase Transition," *Eur. J. Mineral,* vol. 10, p. 693, 1998.

[168] R.W. Terhune, T. Kushida, and G.W. Ford, "Soft Acoustic Modes in Trigonal Crystals," *Phys. Rev. B,* vol. 32, p. 8416, 1985.

[169] A. Bulou, "On Considering the Elastic Constant Table as the Matrix of an Operator; Consequences in Ferroelasticity," *J. Phys. I France,* vol. 2, p. 1445, 1992.

[170] E. Schneider, O.L. Anderson, and N. Soga, "Elastic Constants and their Measurement," McGraw-Hill, New York, 1974.

[171] J.F. Nye, "Physical Properties of Crystals," Oxford: Oxford University Press, 1985.

[172] S.I. Ranganathan, and M. Ostoja-Starzewski, "Universal Elastic Anisotropy Index," *Phys. Rev. Lett.,* vol. 101, p. 055504, 2008.

[173] M.E. Arroyo y de Dompablo, N. Biskup, J.M. Gallardo-Amores, E. Moran, H. Ehrenberg, and U. Amador, "Gaining Insights into the Energetics of $FePO_4$ Polymorphs," *Chem. Mater.,* vol. 22, p. 994, 2010.

[174] A.S. Andersson, B. Kalska, L. Haggstrom, J.O. Thomas, "Lithium Extraction/Insertion in $LiFePO_4$: An X-ray Diffraction and Mossbauer Spectroscopy Study," *Solid State Ionics,* vol. 130, p. 41, 2000.

[175] O. Le Bacq, and A. Pasturel, "Impact on Electronic Correlations on the Structural Stability, Magnetism, and Voltage of $LiCoPO_4$ Battery," *Phys. Rev. B,* vol. 69, p. 245107, 2004.

[176] J. Haines, O. Cambon, and S. Hull, "Neutron Diffraction Study of Quartz-Type $FePO_4$: High-Temperature Behavior and Alpha-Beta Phase Transition,"

Zeitschrift fuer Kristallographie, vol. 218, p. 193, 2003.

[177] U. Amador, J.M. Gallardo-Amores, G. Heymann, H. Huppertz, E. Moran, and M.E. Arroyo y de Dompablo, "High Pressure Polymorphs of $LiCoPO_4$ and $LiCoAsO_4$," *Solid State Sci.,* vol. 11, p. 343, 2009.

[178] F. Zhou, M. Cococcioni, C.A. Marianetti, D. Morgan, and G. Ceder, "First-Principles Prediction of Redox Potentials in Transition-Metal Compounds with LDA+U," *Phys. Rev. B,* vol. 70, p. 235121, 2004.

[179] M.E. Arroyo-de Dompablo, J.M. Gallardo-Amores, M.T. Azcondo, F. Garcia-Alvarado, and U. Amador, "Towards Innovative Electrode Materials Obtained by High-Pressure: Experimental and Computational Study of HP-$FePO_4$," *J. Phys. Chem. Soc.,* vol. 67, p. 1243, 2006.

[180] G. Li, H. Azuma, and M. Tohda, "$LiMnPO_4$ as the Cathode for Lithium Batteries," *Electrochem. Solid State Lett.,* vol. 5, p. A135, 2002.

[181] M. Hanfland, K. Syassen, N.E. Christensen, and D.L. Novikov, "New High-Pressure Phase of Lithium," *Nature,* vol. 408, p. 174, 2000.

[182] A. Hunt, W.Y. Ching, Y.M. Chiang, and A. Moewes, "Electronic Structures of $LiFePO_4$ and $FePO_4$ Studied Using Resonant Inelastic X-ray Scattering," *Phys. Rev. B,* vol. 73, p. 205120, 2006.

[183] V.I. Anisimov, J. Zaanen, and O.K. Andersen, "Band theory and Mott insulators: Hubbard U Instead of Stoner I," *Phy. Rev. B,* vol. 44, p. 943, 1991.

[184] A. Bouhemadou, R. Khenata, M. Chegaar, and S. Maabed, "First-Principles Calculations of Structural, Elastic, Electronic and Optical Properties of the Antiperovskite $AsNMg_3$," *Phys. Lett,* vol. 337, p. A371, 2007.

[185] S. Tian, Materials Physical Properties, Beijing: Beijing University of Aeronautics and Astronautics Press, 2004.

[186] L.Q. Zhang, Y. Cheng, and W. Niu, "Elastic Properties and Phonon Dispersion of BCC Vanadium under Pressure from First-Principles," *J. At. Mol. Sci.,* vol. 5, p. 91, 2014.

[187] L. Fast, J.M. Wills, B. Johansson, and O. Eriksson, "Elastic Constants of Hexagonal Transition Metals: Theory," *Phys. Rev. B,* vol. 51, p. 17431, 1995.

[188] P.E. Blöchl, "Projector Augmented-Wave Method," *Phys. Rev. B,* vol. 50, p. 17953, 1994.

[189] J.P. Perdew, K. Burke, and M. Ernzerhof, "Generalized Gradient Approximation Made Simple," *Phys. Rev. Lett.*, vol. 77, p. 3865, 1996.

[190] A. Yamada, H. Koizumi, N. Sonoyama, and R. Kanno, "Phase Change in Li_xFePO_4," *Electrochem. Solid State Lett.*, vol. 8, p. A409, 2005.

[191] I.R. Shein, and A.L. Ivanovskii, "Elastic Properties of Mono- and Polycrystalline Hexagonal AlB_2-Like Diborides of s, p and d Metals from First-Principles Calculations," *J. Phys. Condens. Matter.*, vol. 20, p. 415218, 2008.

[192] J. Jiang, C. Ouyang, H. Li, Z. Wang, X. Huang, and L. Chen,, "First-Principles Study on Electronic Structure of $LiFePO_4$," *Solid State Commun.*, vol. 143, p. 144, 2007.

[193] P. Labéguerie, M. Harb, I. Baraille and M. Rérat, "Structural, Electronic, Elastic, and Piezoelectric Properties of α-quartz and MXO_4 (M=Al, Ga, Fe; X=P, As) isomorph Pompounds: A DFT Study," *Phys. Rev. B,* vol. 81, p. 045107, 2010.

[194] E. Gregoryanz, R.J. Hemley, H. Mao, and P. Gillet, "High-Pressure Elasticity of α-Quartz: Instability and Ferroelastic Transition," *Phys. Rev. Lett.*, vol. 84, p. 3117, 2000.

[195] B.B. Karki, G.J. Ackland, and J. Crain, "Elastic Instability in Crystal from ab initio Stress-Strain Relations," *J. Phys. Conden. Matter.*, vol. 9, p. 8579, 1997.

[196] A.M. Walker, "The Effect of Pressure on the Elastic Properties and Seismic Anisotropy of Diopside and Jadeite from Atomic Scale Simulation," *Phys. Earth Plan. Int.*, vol. 192, p. 91, 2012.

[197] O.V. Yakubovich, M.A. Simonov, and N.V. Belov, "The Crystal Structure of a Synthetic Triphylite $LiFe(PO_4)$," *Doklady Akademii Nauk,* vol. 235, p. 93, 1977.

[198] C. Wolverton, and A. Zunger, "First-Principles Prediction of Vacancy Order-Disorder and Intercalation Battery Voltages in Li_xCoO_2," *Phys. Rev. Lett.*, vol. 81, p. 606, 1998.

[199] Z. Gong, and Y. Yang, "Recent Advances in the Research of Polyanion-Type Cathode Materials for Li-ion Batteries," *Energy Environ. Sci.*, vol. 4, p. 3223, 2011.

[200] A. Pujana, J.L. Pizarro, A. Goni, T. Rojo, and M.I. Arriortu, "Synthesis and Structural Study of the $Li_{1-3x}Fe_xCoPO_4$ (x=0-0.10) Solid Solution Related to the Litiophylite-Triphylite Family," *Ann. Quim. Int. Ed.*, vol. 94, p. 383, 1998.

[201] S.Q. Shi, L.J. Liu, C.Y. Ouyang, D.S. Wang, Z.X. Wang, L.Q. Chen, and X.

Huang, “Enhancement of Electronic Conductivity of $LiFePO_4$ by Cr Doping and its Identification by First-Principles Calculations,” *Phys. Rev. B,* vol. 68, p. 195108, 2003.

[202] Y.N. Xu, W.Y. Ching, and Y.M. Chiang, “Comparative Studies of the Electronic Structure of $LiFePO_4$, $FePO_4$, Li_3PO_4, $LiMnPO_4$, $LiCoPO_4$ and $LiNiPO_4$,” *J. Appl. Phys.*, vol. 95, p. 6583, 2004.

[203] W.Y. Ching, “Theoretical Studies of the Electronic Properties of Ceramic Materials,” *J. Am. Ceram. Soc.,* vol. 73, p. 3135, 1990.

[204] D. Wang, X. Wu, Z. Wang, and L. Chen, “Cracking Causing Cyclic Instability of $LiFePO_4$ Cathode Material,” *J. Power Sources,* vol. 140, p. 125, 2005.

[205] J.R. Rice, “Dislocation Nucleation from a Crack Tip: An Analysis Based on the Peierls Concept,” *J. Mech. Phys. Solids,* vol. 40, p. 239, 1992.

[206] K. Smith, and C.Y. Wang, “Power and Thermal Characterization of a Lithium-Ion Battery Pack for Hybrid-Electric Vehicles,” *J. Power Sources,* vol. 160, p. 662, 2006.

[207] M.K. Aydinol, A.F. Kohan, and G. Ceder, “*Ab Initio* Calculation of the Intercalation Voltage of Lithium-Transition-Metal Oxide Electrodes for Rechargeable Batteries,” *J. Power Sources,* vol. 68, p. 664, 1997.

[208] A.K. Padhi, K.S. Nanjundaswamy, and J.B. Godenough, “Phospho-olivines as Positve-Electrode Materials for Rechargeable Lithium Bateries,” *J. Electrochem. Soc.,* vol. 14, p. 1188, 1977.

[209] T.X.T. Sayle, R.R. Maphanga, C.R.A. Catlow, P.E. Ngoepe, and D.C. Sayle, “Predicting the Electrochemical Properties of MnO_2 Nanomaterials Used in Rechargeable Li Batteries: Simulating Nanostructure at the Atomistic Level,” *J. Am. Chem. Soc.,* vol. 131, p. 6161, 2009.

[210] T. Ogasawara, A. Debart, M. Holfazel, P. Novak, and P.G. Bruce, “Rechargeable Li_2O_2 Electrode for Lithium Batteries,” *J. Am. Chem. Soc.,* vol. 131, p. 1390, 2006.

[211] C. Li, X. Miao, W. Chu, P. Wu, and D.G. Tong, “Hollow Amorphous $NaFePO_4$ Nanospheres as a High-Capacity and High-Rate Cathode for Sodium-ion Batteries,” *J. Mater. Chem. A,* vol. 3, p. 8265, 2015.

[212] J. Kim, D.H. Seo, H. Kim, I. Park, J.K. Yoo, S.K. Jung, Y.U. Park, W.A. Goddard III, and K. Kang, “Unexpected Discovery of the Low-Cost Maricite $NaFePO_4$ as a High-Performance Electrolyte for Na-ion Batteries,” *Energy*

Environ. Sci., vol. 8, p. 540, 2015.

[213] M. Minakshi, P. Singh, N. Sharma, M. Blackford, and M. Ionescu, "Lithium Extraction-Insertion from/into $LiCoPO_4$ in Aqueous Batteries," *Ind. Eng. Chem. Res.,* vol. 50, p. 1905, 2011.

[214] J.M. Lloris, C.P. Vicente, and J.L. Tirado, "Improvement of the Electrochemical Performance of $LiCoPO_4$ 5 V Material Using a Novel Synthesis Procedure," *Electrochem Solid-State Lett.,* vol. 5, p. A234, 2002.

[215] S. Okada, S. Sawa, M. Egashira,. Yamaki, M. Tabuchi, H. Kageyama, T. Konishi, and A. Yoshino, "Cathode Properties of Phospho-olivine $LiMPO_4$ for Lithium Secondary Batteries," *J. Power Sources,* vol. 98, p. 430, 2001.

[216] N.N. Bramnik, K. Nikolowski, D.M. Trots, and H. Ehrenberg, "Thermal Stability of $LiCoPO_4$ Cathodes," *Electrochem. Solid State Lett.,* vol. 11, p. A89, 2008.

Appendix A: Tables

Table 7-1 Experimental and calculated fractional coordinates of $P3_121$-$FePO_4$.

	Experimental [35]			Calculated		
Atoms	X	Y	Z	X	Y	Z
Fe	0.458	0.000	0.833	0.4610	0.0000	0.8333
P	0.458	0.000	0.333	0.4606	0.0000	0.3333
O1	0.419	0.318	0.369	0.4167	0.3105	0.3974
O2	0.413	0.264	0.875	0.4127	0.2597	0.8768

Table 7-2 Experimental and calculated fractional coordinates of *Pnma*-$FePO_4$.

	Experimental [24]			Calculated		
Atoms	X	Y	Z	X	Y	Z
Fe	0.2755	0.250	0.9482	0.2736	0.2500	0.9524
P	0.0939	0.250	0.3950	0.0935	0.2500	0.4006
O1	0.1215	0.250	0.7089	0.1200	0.2500	0.7123
O2	0.4391	0.250	0.1595	0.4415	0.2500	0.1573
O3	0.1660	0.0449	0.2498	0.1674	0.0439	0.2509

Table 7-3 Experimental and calculated fractional coordinates of *Pbca*-$FePO_4$.

	Experimental [29]			Calculated		
Atoms	X	Y	Z	X	Y	Z
Fe	0.3995	0.5645	0.2841	0.3995	0.5644	0.2836
P	0.1764	0.3794	0.1168	0.1760	0.3794	0.1161
O1	0.3190	0.3929	0.1914	0.3193	0.3939	0.1932
O2	0.1065	0.2270	0.1558	0.1547	0.2269	0.1547
O3	0.0820	0.5157	0.1641	0.0822	0.5144	0.1646
O4	0.1982	0.3854	-0.0486	0.1998	0.3856	0.9508

Table 7-4 Experimental and calculated fractional coordinates of $P2_1/c$-$FePO_4$.

	Experimental [29]			Calculated		
Atoms	X	Y	Z	X	Y	Z
Fe	0.388	0.806	0.060	0.3897	0.8096	0.0598
P	0.590	0.458	0.266	0.5859	0.4574	0.2698
O1	0.481	0.640	0.228	0.4918	0.6471	0.2346
O2	0.828	0.463	0.384	0.8359	0.4755	0.3832
O3	0.641	0.358	0.116	0.6278	0.3602	0.1097
O4	0.410	0.343	0.368	0.4148	0.3508	0.3688

Table 7-5 Experimental and calculated fractional coordinates of *Cmcm*-$FePO_4$.

	Experimental [30]			Calculated		
Atoms	X	Y	Z	X	Y	Z
Fe	0.000	0.000	0.000	0.0000	0.0000	0.0000
P	0.000	0.354	0.250	0.0000	0.3482	0.2500
O1	0.000	0.246	0.050	0.0000	0.2408	0.0494
O2	0.247	0.465	0.250	0.2432	0.4662	0.2500

Table 7-6 Calculated fractional coordinates of $P3_121$-$CoPO_4$.

Atoms	X	Y	Z
Co	0.4698	0.0000	0.3333
P	0.4805	0.0000	0.8333
O1	0.3993	0.2929	0.3958
O2	0.4344	0.2561	0.8783

Table 7-7 Experimental and calculated fractional coordinates of *Pnma*-$CoPO_4$.

	Experimental [37]			Calculated		
Atoms	X	Y	Z	X	Y	Z
Co	0.2684	0.2500	0.9444	0.2705	0.2500	0.9480
P	0.0928	0.2500	0.3820	0.0949	0.2500	0.3932
O1	0.1178	0.2500	0.7016	0.1239	0.2500	0.7059
O2	0.4339	0.2500	0.1590	0.4364	0.2500	0.1475
O3	0.1595	0.0414	0.2334	0.1635	0.0452	0.2436

Table 7-8 Calculated fractional coordinates of *Pbca*-$CoPO_4$.

Atoms	X	Y	Z
Co	0.5644	0.2836	0.3933
P	0.3796	0.1134	0.1729
O1	0.3959	0.1837	0.3214
O2	0.2249	0.1538	0.1027
O3	0.5169	0.1625	0.0796
O4	0.3849	0.9514	0.1943

Table 7-9 Calculated fractional coordinates of $P2_1/c$-$CoPO_4$.

Atoms	X	Y	Z
Co	0.3416	0.3115	0.0488
P	0.2913	0.9510	0.2703
O1	0.2541	0.1356	0.2220
O2	0.4461	0.9651	0.3797
O3	0.4480	0.8325	0.1206
O4	0.0151	0.8642	0.3801

Table 7-10 Calculated fractional coordinates of *Cmcm*-$CoPO_4$.

Atoms	X	Y	Z
Co	0.0000	0.0000	0.0000
P	0.5000	0.1519	0.2500
O1	0.7423	0.0375	0.2500
O2	0.0000	0.2350	0.5518

Table 7-11 Calculated fractional coordinates of *$P3_121$*-$MnPO_4$.

Atoms	X	Y	Z
Mn	0.5628	0.0000	0.3333
P	0.5739	0.0000	0.8333
O1	0.8995	0.3472	0.2693
O2	0.8816	0.2685	0.7945

Table 7-12 Experimental and calculated fractional coordinates of *Pnma*-$MnPO_4$.

	Previous [42]			Calculated		
Atoms	X	Y	Z	X	Y	Z
Mn	0.29013	0.25000	0.92949	0.2861	0.2500	0.9196
P	0.10391	0.25000	0.42600	0.0985	0.2500	0.4008
O1	0.12533	0.25000	0.73506	0.1216	0.2500	0.7130
O2	0.45064	0.25000	0.13504	0.4428	0.2500	0.1493
O3	0.17377	0.05014	0.28537	0.1679	0.0489	0.2537

Table 7-13 Calculated fractional coordinates of *Pbca*-$MnPO_4$.

Atoms	X	Y	Z
Mn	0.5161	0.2474	0.4014
P	0.3205	0.0678	0.1844
O1	0.3343	0.1358	0.3511
O2	0.1513	0.0826	0.1312
O3	0.4357	0.1519	0.0794
O4	0.3561	0.8978	0.1907

Table 7-14 Calculated fractional coordinates of $P2_1/c$-$MnPO_4$.

Atoms	X	Y	Z
Mn	0.3773	0.8144	0.0560
P	0.5772	0.4661	0.2692
O1	0.4766	0.6604	0.2401
O2	0.8226	0.4911	0.3879
O3	0.6311	0.3795	0.1082
O4	0.4224	0.3494	0.3645

Table 7-15 Calculated fractional coordinates of *Cmcm*-$MnPO_4$.

Atoms	X	Y	Z
Mn	0.0000	0.0000	0.0000
P	0.5000	0.1525	0.2500
O1	0.7402	0.0363	0.2500
O2	0.0000	0.2392	0.55521

Table 7-16 Calculated fractional coordinates of $P3_121$-$LiFePO_4$.

Atoms	X	Y	Z
Li	0.4703	0.0000	0.3333
Fe	0.9722	0.0000	0.3333
P	0.4941	0.0000	0.8333
O1	0.3869	0.2706	0.3931
O2	0.4147	0.2117	0.8985

Table 7-17 Experimental and calculated fractional coordinates of *Pnma*-$LiFePO_4$.

	Experimental [36]			Calculated		
Atoms	X	Y	Z	X	Y	Z
Li	0.00000	0.00000	0.000	0.0000	0.0000	0.0000
Fe	0.282	0.250	0.973	0.2820	0.2500	0.9732
P	0.095	0.250	0.419	0.0948	0.2500	0.4193
O1	0.099	0.250	0.744	0.0963	0.2500	0.7455
O2	0.455	0.250	0.211	0.4566	0.2500	0.2071
O3	0.163	0.048	0.284	0.1660	0.0458	0.2854

Table 7-18 Calculated fractional coordinates of *Pbca*-$LiFePO_4$.

Atoms	X	Y	Z
Li	0.0000	0.0000	0.0000
Fe	0.5453	0.2738	0.3883
P	0.3496	0.0882	0.1998
O1	0.3553	0.1507	0.3772
O2	0.1868	0.1112	0.1116
O3	0.4865	0.1625	0.1055
O4	0.3838	0.9344	0.2216

Table 7-19 Calculated fractional coordinates of *P2₁/c*-$LiFePO_4$.

Atoms	X	Y	Z
Li	0.0000	0.0000	0.0000
Fe	0.4885	0.7621	0.0941
P	0.5300	0.3942	0.2364
O1	0.5497	0.5569	0.1627
O2	0.7295	0.3833	0.3544
O3	0.5487	0.2612	0.1202
O4	0.2880	0.3891	0.3396

Table 7-20 Experimental and calculated fractional coordinates of *Cmcm*-$LiFePO_4$.

	Experimental [36]			Calculated		
Atoms	X	Y	Z	X	Y	Z
Li	0.000	0.676	0.250	0.0000	0.1656	0.2500
Fe	0.000	0.000	0.000	0.0000	0.0000	0.0000
P	0.000	0.3504	0.250	0.0000	0.3525	0.2500
O1	0.000	0.247	0.043	0.0000	0.2466	0.0384
O2	0.228	0.467	0.250	0.2261	0.4711	0.2500

Table 7-21 Calculated fractional coordinates of *$P3_121$*-$LiCoPO_4$.

Atoms	X	Y	Z
Li	0.4726	0.0000	0.3333
Co	0.9726	0.0000	0.3333
P	0.4904	0.0000	0.8333
O1	0.3869	0.2666	0.3998
O2	0.4071	0.2153	0.8961

Table 7-22 Experimental and calculated fractional coordinates of *Pnma*-$LiCoPO_4$.

	Experimental [37]			Calculated		
Atoms	X	Y	Z	X	Y	Z
Li	0.0000	0.0000	0.0000	0.0000	0.0000	0.0000
Co	0.2775	0.2500	0.9780	0.2771	0.2500	0.9874
P	0.0943	0.2500	0.4190	0.0948	0.2500	0.4227
O1	0.0972	0.2500	0.7420	0.0948	0.2500	0.7457
O2	0.4543	0.2500	0.2037	0.4589	0.2500	0.2094
O3	0.1663	0.0446	0.2817	0.1694	0.0424	0.2888

Table 7-23 Calculated fractional coordinates of *Pbca*-$LiCoPO_4$.

Atoms	X	Y	Z
Li	0.0000	0.0000	0.0000
Co	0.5430	0.2754	0.3890
P	0.3485	0.0886	0.1329
O1	0.3541	0.1571	0.3629
O2	0.1847	0.1111	0.1070
O3	0.4884	0.1553	0.0968
O4	0.3805	0.9331	0.2212

Table 7-24 Calculated fractional coordinates of *$P2_1/c$*-$LiCoPO_4$.

Atoms	X	Y	Z
Li	0.0000	0.0000	0.0000
Co	0.4845	0.7618	0.0980
P	0.5325	0.3915	0.2326
O1	0.5591	0.5543	0.1569
O2	0.7263	0.3821	0.3577
O3	0.5594	0.2577	0.1168
O4	0.2860	0.3884	0.3297

Table 7-25 Calculated fractional coordinates of *Cmcm*-$LiCoPO_4$.

Atoms	X	Y	Z
Li	0.5000	0.1707	0.2500
Co	0.0000	0.0000	0.0000
P	0.0000	0.3508	0.2500
O1	0.0000	0.2463	0.0464
O2	0.2288	0.4672	0.2500

Table 7-26 Calculated fractional coordinates of $P3_121$-$LiMnPO_4$.

Atoms	X	Y	Z
Li	0.4741	0.0000	0.3333
Mn	0.9741	0.0000	0.3333
P	0.4895	0.0000	0.8333
O1	0.3943	0.2695	0.4017
O2	0.4131	0.2180	0.8938

Table 7-27 Experimental and calculated fractional coordinates of *Pnma*-$LiMnPO_4$.

	Experimental [42]			Calculated		
Atoms	X	Y	Z	X	Y	Z
Li	0.00000	0.00000	0.00000	0.0000	0.0000	0.0000
Mn	0.21822	0.25000	0.52039	0.2204	0.2500	0.5264
P	0.40635	0.25000	0.08453	0.4091	0.2500	0.0915
O1	0.33865	0.04818	0.21525	0.3395	0.0481	0.2251
O2	0.04323	0.25000	0.28378	0.0462	0.2500	0.2860
O3	0.40635	0.25000	0.76076	0.4046	0.2500	0.7698

Table 7-28 Calculated fractional coordinates of *Pbca*-$LiMnPO_4$.

Atoms	X	Y	Z
Li	0.0000	0.0000	0.0000
Mn	0.5318	0.2717	0.3810
P	0.3511	0.0913	0.1972
O1	0.3447	0.1382	0.3865
O2	0.1935	0.1100	0.0965
O3	0.4853	0.1909	0.1283
O4	0.4121	0.9493	0.1997

Table 7-29 Calculated fractional coordinates of $P2_1/c$-$LiMnPO_4$.

Atoms	X	Y	Z
Li	0.0000	0.0000	0.0000
Mn	0.4020	0.8093	0.0647
P	0.6715	0.4693	0.2026
O1	0.6557	0.6361	0.1091
O2	0.8463	0.4936	0.3640
O3	0.7992	0.3367	0.0833
O4	0.4080	0.4167	0.2875

Table 7-30 Calculated fractional coordinates of *Cmcm*-$LiMnPO_4$.

Atoms	X	Y	Z
Li	0.0000	0.1653	0.2500
Mn	0.0000	0.0000	0.0000
P	0.0000	0.3540	0.25000
O1	0.2231	0.4687	0.2500
O2	0.0000	0.2523	0.0477

Table 7-31 Calculated fractional coordinates of *Pnma*-$NaFePO_4$.

Atoms	X	Y	Z
Na	0.3492	0.2500	0.9679
Fe	0.0000	0.0000	0.0000
P	0.1744	0.2500	0.4614
O1	0.1192	0.0673	0.3147
O2	0.3473	0.2500	0.4507
O3	0.1152	0.2500	0.7488

Table 7-32 Calculated fractional coordinates of *Pnma*-$NaCoPO_4$.

Atoms	X	Y	Z
Na	0.8517	0.2500	0.5312
Co	0.0000	0.0000	0.0000
P	0.1771	0.2500	0.4624
O1	0.1168	0.2500	0.7511
O2	0.3533	0.2500	0.4516
O3	0.1225	0.0657	0.3165

Table 7-33 Calculated fractional coordinates of *Pnma*-$NaMnPO_4$.

Atoms	X	Y	Z
Na	0.3512	0.2500	0.9770
Mn	0.0000	0.0000	0.0000
P	0.1765	0.2500	0.4730
O1	0.1218	0.0675	0.3318
O2	0.3484	0.2500	0.4585
O3	0.1208	0.2500	0.7607

Appendix B: Publication

N.L. Lethole, H.R. Chauke and P.E. Ngoepe, "Structural, electronic and mechanical stability study of olivine $LiMPO_4$ (M: Mn, Fe, Co)", Material Modeling Centre, Department of Physics, University of Limpopo, SA. SAIP 2013 Conference proceedings

N.L. Lethole, H.R. Chauke and P.E. Ngoepe, "Computer Simulations of $FePO_4$ Polymorphs", Material Modeling Centre, Department of Physics, University of Limpopo, SA. To be published

N.L. Lethole, H.R. Chauke and P.E. Ngoepe, “Comparison of Lithium and Sodium Iron Phosphates as Future Battery Material”, Material Modeling Centre, Department of Physics, University of Limpopo, SA. To be published

Appendix C: Papers presented at conferences

Local

N.L. Lethole, H.R. Chauke and P.E. Ngoepe, “Stabilities of Low and High Pressure Structures of $FePO_4$” FSA Research Day, University of Limpopo, Polokwane (SA), 16-17 September 2010

N.L. Lethole, H.R. Chauke and P.E. Ngoepe, “Stabilities of $CoPO_4$ and $MnPO_4$ polymorphs”, South African Institute of Physics Conference, CSIR, Pretoria (SA), 27 September- 1 October 2010

N.L. Lethole, H.R. Chauke and P.E. Ngoepe, “Stabilities of $CoPO_4$ and $MnPO_4$ polymorphs”, South African Institute of Physics Conference, University of South Africa, Pretoria (SA), 12-15 July 2011

N.L. Lethole, H.R. Chauke and P.E. Ngoepe, “First-principles stability study of $FePO_4$ and $LiFePO_4$ polymorphs”, South African Institute of Physics Conference, University of Pretoria, Pretoria (SA), 9-13 July 2012

N.L. Lethole, H.R. Chauke and P.E. Ngoepe, “Effect of Li Intercalation on $FePO_4$ Polymorphs Stabilities” FSA Research Day, Bolivia Lodge, Polokwane (SA), 4-5 October 2012

N.L. Lethole, H.R. Chauke and P.E. Ngoepe, “First-principles stability study of $LiFePO_4$ polymorphs as future battery material”, ASSAf Third Annual South African Young Scientists’ Conference, CSIR International Convection Centre, Pretoria (SA), 16-18 October 2012

N.L. Lethole, H.R. Chauke and P.E. Ngoepe, “First-principles stability study of $LiFePO_4$ polymorphs as future battery material”, South African Institute of Physics Conference, University of Zululand, Richard’s Bay (SA), 8-12 July 2013

N.L. Lethole, H.R. Chauke and P.E. Ngoepe, “Stability comparison of olivine $LiFePO_4$ in Lithium-ion batteries and olivine $NaFePO_4$ in Sodium-ion batteries” FSA Research Day, Bolivia Lodge, Polokwane (SA), 2-3 October 2014

N.L. Lethole, H.R. Chauke and P.E. Ngoepe, “Thermodynamic, structural, electronic and mechanical stability study of olivine $NaMPO_4$ (M: Mn, Fe, Co)”, South African Institute of Physics Conference, University of Johannesburg, Johannesburg (SA), 7-11 July 2014

International

N.L. Lethole, H.R. Chauke and P.E. Ngoepe, “Stabilities of Low and High Pressure Structures of $FePO_4$”, International Battery Association, Cape Town (SA), 12-15 April 2011

N.L. Lethole, H.R. Chauke and P.E. Ngoepe, "Thermodynamic, Electronic and Mechanical Stability of $FePO_4$ Polymorphs", RSC Solid State Chemistry Group Christmas Meeting, Scotland, UK, 18 - 19 December 2012.

N.L. Lethole, H.R. Chauke and P.E. Ngoepe, "Thermodynamic, Electronic and Mechanical Stability of $FePO_4$ Polymorphs", Institute of Physics, London, UK, 17 - 18 December 2012.

N.L. Lethole, H.R. Chauke and P.E. Ngoepe, "Investigation of the Structural, Electronic and Mechanical Stability of Olivine $FePO_4$ and $LiFePO_4$", 7^{th} International Conference of the Africa Materials Research Society, 8-13 December 2013, Addis Ababa, Ethiopia

N.L. Lethole, H.R. Chauke and P.E. Ngoepe, "First-principles study of olivine $LiMPO_4$ and $NaMPO_4$ (M: Mn, Fe, Co) for energy storage application" ASME Power and Energy Conference, 28 June- 02 July , San Diego, CA, US